Effects of dopants and trace elements at the Ni / ScYSZ interface

Schmidt, Michael Stenbæk

Publication date:
2008

Document Version
Publisher's PDF, also known as Version of record

UNIVERSITY OF SOUTHERN DENMARK
Risø DTU
National Laboratory for Sustainable Energy

Effects of dopants and trace elements at the Ni / ScYSZ interface

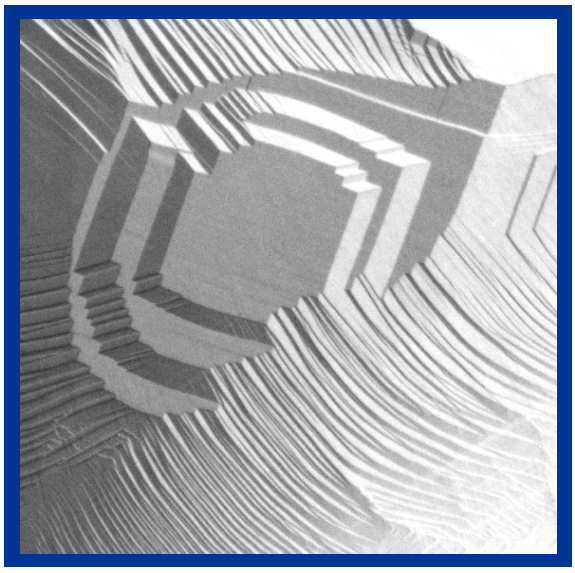

Michael Stenbæk Schmidt
Ph.D. thesis
2008

Author: Michael Stenbæk Schmidt
Title: Effects of dopants and trace elements at the Ni / ScYSZ interface
Division: Fuel Cells and Solid StateChemistry Division

Risø-PhD-44(EN)
2008

ISBN 978-87-550-3708-3

Abstract (max. 2000 char.):

The interfaces between the various materials and phases in solid oxide fuel cells (SOFCs) play a fundamental role, when optimizing SOFC performance. The industrial grade materials commonly used in SOFCs contain numerous impurities. At the catalyst / electrolyte interfaces in SOFC cermet anodes, these impurities are believed to be responsible for losses in electrochemical performance. Impurities such as silica have been shown to segregate to the three phase boundary (TPB) in SOFC cermet anodes.

A three-electrode configuration, with a high purity (99.999 %) nickel point-electrode acting as the working electrode, was used as a simplified model of the SOFC cermet anode. Electrochemical impedance spectroscopy was used to characterise the electrode polarisation resistances on selected electrolyte materials at 850 °C in humidified hydrogen atmospheres. Electrode reactions were characterized on two types of scandia and yttria co-doped zirconia electrolytes (ScYSZ) with different purity levels, a ScYSZ electrolyte doped with alumina and an yttria stabilized zirconia (YSZ) electrolyte.

A point electrode setup provided a well defined electrode / electrolyte interface (EEI) and TPB during electrochemical characterisation, which, after lifting the electrode off the electrolyte, could be studied by surface analysis techniques. Surface analysis was performed using low acceleration voltage scanning electron microscopy (SEM), atomic force microscopy (AFM), time of flight secondary ion mass spectrometry (ToF-SIMS) and x-ray photoelectron spectroscopy (XPS).

For all electrolyte materials the electrode polarization resistances dropped rapidly during the first 50 hours of measurements at 850 °C before stabilising. From ToFSIMS and SEM analysis, rim zones with relatively low impurity concentrations were identified at the outer perimeter of the EEI on the electrolyte surfaces. It was suggested that the rim zones were formed, as the nickel electrode expanded, due to metallic creep. The subsequent drops in polarization resistance are believed to be a direct consequence of fewer impurities in the reaction path at the anode. Chemical analysis of the various EEIs showed that larger impurity concentrations measured in the EEIs resulted in larger electrode polarization resistances.

It was found that prolonged anodic polarisations activated the electrodes. This effect was suggested to be caused by the removal of impurities by water, which formed at the TPB. The electrodes slowly deactivated when the anodic polarization was lifted which was believed to be a result of renewed impurity segregation and concentrations at the TPB.

Dynamic processes occurred on the electrodes when they were subjected to anodic polarization. Chronoamperometry revealed a sawtooth oscillation pattern in the current signal which was hypothesised to be caused by formation and subsequent reduction of Ni(OH)2 on the electrode surface. Increasing the water content in the atmosphere promoted the dynamic process. Nickel was transported away from the electrode which could be a possible cause for the degradation observed in SOFC anodes.

Contract no.:

Group's own reg. no.:

Sponsorship:

Cover :

Pages: 151
Tables:
References:

Information Service Department
Risø National Laboratory for Sustainable Energy
Technical University of Denmark
P.O.Box 49
DK-4000 Roskilde
Denmark
Telephone +45 46774005
bibl@risoe.dtu.dk
Fax +45 46774013
www.risoe.dtu.dk

List of Abbreviations

AFM	Atomic force microscope
ASR_p	Area specific polarisation resistance
EDS	Energy dispersive X-ray spectroscopy
EEI	Electrode / Electrolyte Interface
EGI	Electrolyte / Gas Interface
EIS	Electrochemical Impedance Spectroscopy
GDMS	Glow discharge mass spectrometry
LSR_p	Length specific polarisation resistance
OCV	Open circuit voltage
R_p	Polarisation resistance
R_s	Series resistance
ScYSZ	Scandia and yttria stabilised zirconia
SEM	Scanning electron microscope
SOFC	Solid Oxide Fuel Cell
SZ	Stabilised zirconia
ToF-SIMS	Time-of-flight secondary ion mass spectrometry
XPS	X-ray photoelectron spectroscopy
YSZ	Yttria stabilised zirconia
σ	Ion conductivity

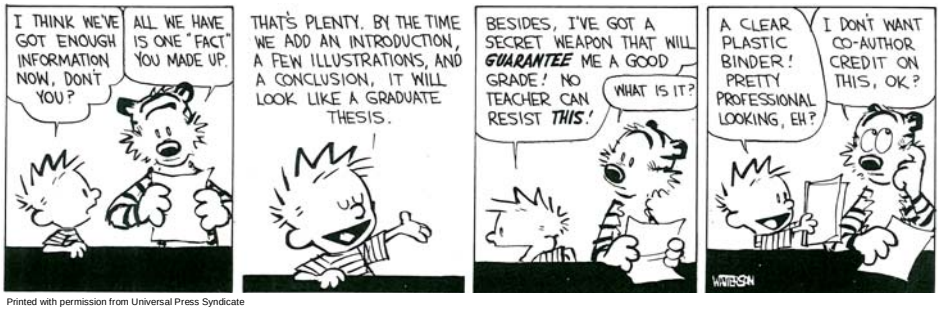

Preface

This thesis was submitted to the University of Southern Denmark as one of the requirements to obtain the Ph.D. degree. The work presented in this work was carried out from August 2005 to July 2008 at the Fuel Cells and Solid State Chemistry Department which is part of the National Laboratory for Sustainable Energy, Risø-DTU. The work was funded by the Danish Ministry of Science, Technology and Innovation.

I would like to thank my thesis advisors, in no particular order, for their time, highly skilled guidance and positive input throughout the course of the project:

Associate Professor *Eivind Skou*, Department of Chemistry, University of Southern Denmark

Senior Scientist *Karin Vels Hansen*, Fuel Cells and Solid State Chemistry Dept., Risø-DTU

Senior Scientist *Kion Norrman*, Polymer Department, Risø-DTU

Research Professor *Mogens Mogensen*, Fuel Cells and Solid State Chemistry Dept., Risø-DTU

Special thanks are also due to *Dorthe Lybye* for her guidance at the beginning of the project. I would also like to thank Associate Professor *Per Morgen* of the Physics Department, SDU. Furthermore, I would like to acknowledge the assistance of Ph.D. student *Rasmus Munksgård Nielsen* and Post doc. *Shane Murphy* from the Center for Individual Nanoparticle Functionality, DTU. I would also like to thank *Danish Micro Engineering A/S* for their time.

Finally I would like to thank all of my colleagues at the Fuel Cells and Solid State Chemistry Department for providing a great work environment and the chance to experience world class researchers at work. I would especially like to thank the members of *CECC* and my office partners *Jens Sunshine Rasmussen* and *Jimmi Midnight Nielsen* for interesting, fruitful and (not always) relevant discussions.

Michael Stenbæk Schmidt
Roskilde, August 2008.

Abstract

The interfaces between the various materials and phases in solid oxide fuel cells (SOFCs) play a fundamental role, when optimizing SOFC performance. The industrial grade materials commonly used in SOFCs contain numerous impurities. At the catalyst / electrolyte interfaces in SOFC cermet anodes, these impurities are believed to be responsible for losses in electrochemical performance. Impurities such as silica have been shown to segregate to the three phase boundary (TPB) in SOFC cermet anodes.

A three-electrode configuration, with a high purity (99.999 %) nickel point-electrode acting as the working electrode, was used as a simplified model of the SOFC cermet anode. Electrochemical impedance spectroscopy was used to characterise the electrode polarisation resistances on selected electrolyte materials at 850 °C in humidified hydrogen atmospheres. Electrode reactions were characterized on two types of scandia and yttria co-doped zirconia electrolytes (ScYSZ) with different purity levels, a ScYSZ electrolyte doped with alumina and an yttria stabilized zirconia (YSZ) electrolyte.

A point electrode setup provided a well defined electrode / electrolyte interface (EEI) and TPB during electrochemical characterisation, which, after lifting the electrode off the electrolyte, could be studied by surface analysis techniques. Surface analysis was performed using low acceleration voltage scanning electron microscopy (SEM), atomic force microscopy (AFM), time of flight secondary ion mass spectrometry (ToF-SIMS) and x-ray photoelectron spectroscopy (XPS).

For all electrolyte materials the electrode polarization resistances dropped rapidly during the first 50 hours of measurements at 850 °C before stabilising. From ToF-SIMS and SEM analysis, rim zones with relatively low impurity concentrations were identified at the outer perimeter of the EEI on the electrolyte surfaces. It was suggested that the rim zones were formed, as the nickel electrode expanded, due to metallic creep. The subsequent drops in polarization resistance are believed to be a direct consequence of fewer impurities in the reaction path at the anode. Chemical analysis of the various EEIs showed that larger impurity concentrations measured in the EEIs resulted in larger electrode polarization resistances.

It was found that prolonged anodic polarisations activated the electrodes. This effect was suggested to be caused by the removal of impurities by water, which formed at the TPB. The electrodes slowly deactivated when the anodic polarization was lifted which was believed to be a result of renewed impurity segregation and concentrations at the TPB.

Dynamic processes occurred on the electrodes when they were subjected to anodic polarization. Chronoamperometry revealed a sawtooth oscillation pattern in the current signal which was hypothesised to be caused by formation and subsequent reduction of $Ni(OH)_2$ on the electrode surface. Increasing the water content in the atmosphere promoted the dynamic process. Nickel was transported away from the electrode which could be a possible cause for the degradation observed in SOFC anodes.

Dansk resumé

Grænsefladerne mellem de forskellige materialer og faser i fastoxid brændselsceller (SOFCer) spiller en fundamental rolle i arbejdet med at optimere SOFC ydeevne. De industrielle materialer der ofte bliver brugt i SOFC'er indeholder signifikante mængder urenheder. Ved katalysator / elektrolyt grænsefladen af SOFC cermet anoder er disse urenheder sandsynligvis ansvarlige for tab af elektrokemisk ydeevne. Det er tidligere blevet vist at urenheder så som silikat segregerer til tre-fase-grænsen i SOFC cermet anoder.

En tre-elektrode konfiguration med en nikkel elektrode af høj renhed (99.999 %) fungerende som arbejdselektrode blev brugt som en simplificeret model af SOFC cermet anoden. Elektrokemisk impedansspektroskopi blev brugt til at karakterisere elektrodepolarisationsmodstanden målt på udvalgte elektrolytter ved 850 °C i befugtede brint atmosfærer. Elektrodereaktionerne blev karakteriseret på forskellige typer af skandia og yttria co-doteret zirkonia (ScYSZ) med forskellige urenhedsgrader, en ScYSZ elektrolyt doteret med alumina og en yttria stabiliseret zirkonia elektrolyt (YSZ).

Målinger med punktelektroder skabte veldefinerede elektrode / elektrolyt grænseflader og tre-fase-grænser som efter elektrokemisk karakterisering kunne undersøges ved hjælp af diverse overfladeanalyse tekniker så som SEM, AFM, ToF-SIMS og XPS.

For alle elektrolytmaterialer faldt den målte elektrodepolarisationsmodstand stærkt i løbet af de først 50 timer ved 850 °C. Fra ToF-SIMS og SEM blev en ring i udkanten af elektrode / elektrolyt grænsefladerne fundet med et relativt svagt urenheds niveau. Det foreslås at den lavere urenheds koncentration i disse områder skyldes ekspansionen af nikkel elektroden på grund af metallisk krybning. De markante fald i elektrodepolarisationsmodstande menes at kunne forklares ved, at der er færre urenheder i reaktionsvejen efter områderne med færre urenheder blev dannet. Analyser af kontakt områderne viste at højere urenheds koncentrationer resulterede i højere elektrode polarisationsmodstande.

Længerevarende anodisk polarisation aktiverede elektroderne. Denne effekt menes at skyldes de urenheder der var samlet ved tre-fase-grænsen blev fjernet af det vand som dannedes ved tre-fase-grænsen. Elektroderne deaktiverede da den anodiske polarisation blev fjernet, hvilket foreslås at skyldes fornyet segregering af urenheder og forurening af tre-fase-grænsen.

Dynamiske processer fandt sted på elektroderne når elektroderne blev udsat for stærk anodisk polarisation. Kronoamperometri viste et savtakket oscillationsmønster i det målte strøm signal. Dette menes at ske på grund af dannelse og efterfølgende reduktion af $Ni(OH)_2$ på elektrode overfladen. Forhøjelse af dampindholdet i måleatmosfæren fremhævede den dynamiske proces. Nikkel partikler blev også observeret rundt om punktelektroden, hvilket var et tegn på at nikkel kunne transporteres væk fra elektroden. Denne form for nikkel transport menes at være en mulig årsag til den observerede degradering af SOFC anoder.

Table of Contents

1 INTRODUCTION 1

1.1 MOTIVATION 1
1.2 MATERIALS USED IN SOLID OXIDE FUEL CELLS 3
1.2.1 Electrolyte 3
1.2.2 Cathode 3
1.2.3 Anode 3
1.3 THE ANODE / ELECTROLYTE INTERFACE 4
1.3.1 The three phase boundary 4
1.4 THESIS OBJECTIVE 5
1.5 THESIS LAYOUT 6
1.6 REFERENCES 6

2 EXPERIMENTAL 7

2.1 SAMPLE PREPARATION 7
2.1.1 Electrolyte sample preparation 7
2.1.2 Electrode sample preparation 8
2.2 ELECTROCHEMICAL CHARACTERISATION SETUP 9
2.3 MICROSCOPY 12
2.4 CHEMICAL SURFACE ANALYSIS 12
2.4.1 Time-of-flight secondary ion mass spectrometry 12
2.4.2 X-ray photoelectron spectroscopy 14
2.5 REFERENCES 14

3 CHARACTERISATION ON *YSZ* 15

3.1 ELECTROCHEMICAL CHARACTERISATION ON *YSZ* 15
3.2 MICROSTRUCTURE OF *YSZ* 18
3.3 CONCLUSION 20
3.4 REFERENCES 20

4 EFFECTS OF IMPURITIES 21

4.1 ELECTROCHEMICAL CHARACTERISATION 21
4.1.1 Pure ScYSZ 22
4.1.2 Impure ScYSZ 24
4.1.3 EIS summary 25
4.2 MICROSTRUCTURAL CHARACTERISATION 26
4.2.1 Pure ScYSZ 26
4.2.2 Impure ScYSZ 28
4.3 CHEMICAL CHARACTERISATION 30
4.3.1 ToF-SIMS of Pure ScYSZ 30
4.3.2 ToF-SIMS of Impure ScYSZ 34
4.4 XPS ON *PURE SCYSZ* AND *IMPURE SCYSZ* 38
4.4.1 Summary chemical characterisation 40
4.5 DISCUSSION 40
4.6 CONCLUSION 43
4.7 REFERENCES 44

5 FLATTENED ELECTRODES 45

5.1 SAMPLE PREPARATION 45
5.2 EIS USING FLATTENED ELECTRODES 46
5.3 MICROSTRUCTURE 48
5.4 CHEMICAL ANALYSIS 49
5.5 DISCUSSION 49
5.6 CONCLUSION 50

6 EFFECTS OF ALUMINA DOPING 51

6.1 ALUMINA ADDITION TO *IMPURE SCYSZ* 51
6.2 ELECTROCHEMICAL CHARACTERISATION OF *AL-SCYSZ* 52
6.3 MICROSTRUCTURE OF *AL-SCYSZ* 54
6.4 CHEMICAL CHARACTERISATION 58
6.5 DISCUSSION AND CONCLUSION 62
6.6 REFERENCES 63

7 ELECTRODE DYNAMICS 64

7.1 MOTIVATION 64
7.2 EXPERIMENTAL 64
7.2.1 Measurement setup 64
7.2.2 Electrochemical impedance spectroscopy 65
7.2.3 Chronoamperometry 66
7.2.4 Microscopy 66
7.2.5 Chemical analysis 66
7.3 RESULTS 67
7.3.1 Impedance at OCV and during anodic polarisation 67
7.3.2 Chronoamperometry in constant atmosphere 68
7.3.3 Chronoamperometry in atmospheres with varying H_2O levels 70
7.3.4 Potential sweeps at different temperatures 71
7.3.5 Microstructure 72
7.3.6 Chemical analysis of Pure ScYSZ 76
7.3.7 Chemical analysis of Impure ScYSZ 79
7.4 DISCUSSION 81
7.5 CONCLUSION 85
7.6 REFERENCES 86

8 SUMMARY & DISCUSSION 87

8.1 ELECTROCHEMICAL CHARACTERISATION 87
8.2 MICROSTRUCTURAL AND CHEMICAL CHARACTERISATION 88
8.3 MECHANISTIC CONSIDERATIONS 89
8.4 REFERENCES 91

9 CONCLUSIONS 92

10 OUTLOOK 93

APPENDIX A 97

APPENDIX B 98

APPENDIX C 101

APPENDIX D 103

APPENDIX E 104

APPENDIX F 106

APPENDIX G 113

APPENDIX H 129

1 Introduction

In this chapter the motivation for the choice of this thesis' subject matter is given. A very brief introduction to the vast field of solid oxide fuel cells (SOFCs) is given with special focus on the anode / electrolyte interface, which has been studied in the present work. Finally an outline of the thesis structure is given.

1.1 Motivation

Presently the demand for electrical power is increasing on a global scale as the economies of developing countries such as India and China continue their rapid economic growth. These growing economies rely, to a large extent, on fossil fuels such as coal and oil as a source of energy. Fossil fuels are technologically easy to convert into electricity and heat by means of combustion, but have a major drawback in being major sources of greenhouse gases such as CO_2, SO_2 and NO_x. The United Nations Intergovernmental Panel on Climate Change states that the increase in human generated greenhouse gases since the mid-20^{th} century is very likely the cause of the observed increase in global temperatures [1]. In the face of this problem the prospect of finding a CO_2 neutral energy source has become ever more interesting in recent years. Simultaneously the cost of crude oil has increased dramatically giving the market for electricity production an additional incentive to look into alternative production methods.

Fuel cells are good candidates for more efficient electricity production. Generally speaking, fuel cells convert chemical energy into electrical energy. There are several types of fuel cells and depending on the type, they have a wide range of operation characteristics such as operation temperature, requirements to fuels etc. This thesis focuses on the solid oxide fuel cell (SOFC). In an SOFC chemical energy in the form of a fuel such as hydrogen, methane, carbon monoxide or ammonia is converted directly into electrical energy [2]. When using hydrogen as a fuel, electricity is produced as shown in Figure 1.1. As there are no moving parts involved in the conversion reaction inside the SOFC itself, the conversion efficiency is much higher than for example combustion engines which are generally thermodynamically limited as described by the Carnot cycle. As the overall conversion reaction in the fuel cell is exothermic, heat is produced as a fortunate by-product. In an SOFC the heat produced can be used to keep the cell at operation temperature and excess heat can be used, for example as domestic heating.

An SOFC consists of three major components, an anode, a cathode and an electrolyte. The fuel is continuously added to the anode where the fuel is oxidised

i.e. losses electrons. At the cathode, air or oxygen is continuously added and electrons reduce the oxygen forming negatively charged oxide ions. The electrolyte is an oxide ion conductor through which the oxide ions migrate towards the anode. Oxide ion transport is driven by a difference in the oxygen activity, between the anode and cathode sides of the electrolyte, which can be calculated by applying the Nernst equation. A single cell generates a potential difference of ~ 1 V which is insufficient for most applications. However if the cells are connected in series in a so called *stack* an arbitrary voltage can be generated by simply increasing the number of cells in the stack.

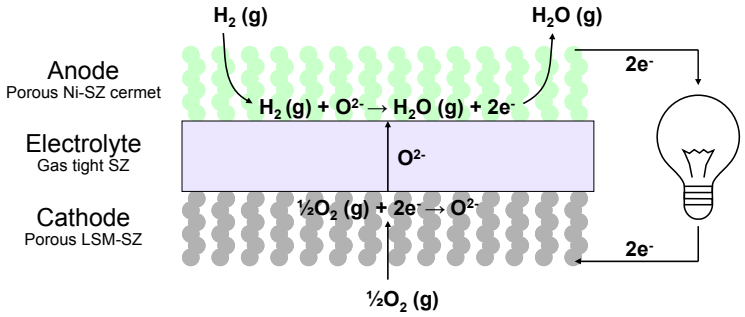

Figure 1.1: A schematic illustration of the principle behind SOFC operation.

When hydrogen is used as a fuel the only by-product of the electricity production is water. If natural gas, which primarily consists of methane, is used, the fuel cell will also emit CO_2 but the fuel to electricity conversion efficiency is better (~60 %) than conventional combustion techniques (~30 %). If, however, the methane is formed by a renewable technique such as e.g. anaerobic digestion used in 2nd generation biogas production [3], the net CO_2 emission is zero as the amount of CO_2 emitted from the SOFC is equal to the amount of CO_2 absorbed by the plants by photosynthesis while growing. Hydrogen is the most abundant element in the universe. On earth hydrogen is bound to other elements so that hydrogen is not freely available as an energy source in nature as for example natural gas and oil are, and is therefore often called an energy carrier. Therefore, hydrogen must be separated from the compounds to which it is bound before it can be used as a zero CO_2 emission SOFC fuel. Today steam reforming of methane is the technique which produces the largest quantities of industrial hydrogen [4] and many other methods of hydrogen production exist. Most industrial hydrogen production methods rely on electricity which is often produced by fossil fuels. Hence using hydrogen produced by essentially burning fossil fuels as an electricity source will not reduce global CO_2 emissions.

By supplying electricity to an electrolysis cell, hydrogen and oxygen can be produced from water. An electrolysis cell is essentially a fuel cell running in reverse. By supplying an electrolysis cell with electricity produced by a renewable energy source such as wind power, tidal power, and solar power etc. hydrogen can be produced without CO_2 emissions. However, a large disadvantage with renewable energy sources is their unreliability which is perhaps best illustrated with wind power. It is envisioned that hydrogen produced by electrolysis when excess renewable energy is available, acts as a means to store energy chemically when the electricity produced by renewable sources exceeds the momentary demand. When renewable energy sources cannot supply enough electricity, i.e. when the wind isn't

blowing or the sun isn't shining, the hydrogen which has been produced previously is used to fuel a fuel cell in order to meet electricity demands.

1.2 Materials used in Solid Oxide Fuel Cells

Solid oxide fuel cells operate in a temperature range of 600 – 1000 °C at which oxide conductivity through the electrolyte occurs. Due to the elevated temperatures necessary for ion transport through the electrolyte some critical requirements must be met by the components of the SOFC. In general the components must have chemical and mechanical stability at the elevated temperatures of SOFC operation. The components should thus not react with each other to form unwanted phases at the interfaces. Also, components should have similar coefficients of thermal expansion to avoid mechanical stress in the cell when the cell undergoes thermal cycling. Finally, the cost of the materials should be as low as possible. In the following brief descriptions of some of the materials used in SOFCs are given.

1.2.1 Electrolyte

The electrolyte must be a gas tight ion conducting membrane. Ideally the electrolyte is infinitely thin but to avoid gas leaks through the electrolyte it is usually applied in ~15 μm thick layers. An electrolyte commonly used today is zirconium dioxide (ZrO_2) also known as zirconia. In order to increase its ion conductivity zirconia can be doped with yttrium oxide (Y_2O_3), also called yttria, to form a compound called yttria stabilized zirconia (YSZ) which is stable at high temperatures. Recently zirconia co-doped with yttria and scandia (Sc_2O_3) has been used as an electrolyte and is referred to as ScYSZ.

1.2.2 Cathode

Cathode materials should be electrically conductive as well as chemically and mechanically stable in oxidising atmospheres at high temperatures. The thermal expansion coefficient of the cathode material should match that of the electrolyte and anode. Presently ceramic materials such as strontium doped lanthanum manganite, $La_xSr_{1-x}MnO_{3+\delta}$ (LSM) and strontium doped lanthanum cobaltate, $La_xSr_{1-x}CoO_{3+\delta}$ (LSC) are used as cathode materials. To allow gas transport to the electrolyte these materials are mixed with YSZ to form a porous structure.

1.2.3 Anode

Presently the most commonly used anode design consists of a ceramic-metal mixture (cermet) where metallic nickel is interdispersed in YSZ. The cermet structure is porous to allow gas transport of fuel to the electrolyte. Nickel is used due to its catalytic ability to dissociate hydrogen as well as being stable in a reducing atmosphere at SOFC operation temperatures. Nickel particles form percolating networks and fulfil the task of transporting electrons from the reaction sites at the electrolyte to the exterior circuit. The YSZ component in the cermet acts as a mechanical support for the nickel as well as an oxide ion conductor, as in the electrolyte, to increase the number of reaction sites.

1.3 The anode / electrolyte interface

At present a major barrier for introducing mass produced SOFCs to the marketplace is production cost and durability. The longer a SOFC stack can operate the lower the kW/h running cost becomes for the end costumer. Long term testing of SOFCs have shown degradation in performance over time [5]. Long term stability is fundamental to SOFC becoming technologically viable thus continuous efforts are being put into illuminating the causes and finding solutions for long term degradation. One of the causes of SOFC performance degradation is found at the anode / electrolyte interface where the anode cermet meets the electrolyte [6]-[8]. For the commercialisation of SOFCs it is sought to reduce the operation temperature in order to reduce the cost of auxiliary equipment around the stack itself, i.e. gas manifolds, as these must otherwise be made of expensive steel alloys. However, as the operation temperature is lowered, effects limiting the conversion reaction such as decreasing ion conductivity through the electrolyte become more significant.

1.3.1 The three phase boundary

Although there are many suggestions for reaction mechanisms at the anode it is acknowledged that the three phase boundary (TPB) is the site around which electrochemical charge transfer reactions take place, Figure 1.2. As the name suggests, the TPB is the intersection of the electrolyte, electrode and gas phase. The length of the TPB is thought to be a measure of the number of reaction sites. Therefore SOFC anode cermets are designed to have the smallest size nickel particles possible to increase the TPB length to nickel mass ratio. Changes to the microstructure such as coarsening of nickel particles in the cermet i.e. a reduction of the three phase boundary length has been connected with a decrease in SOFC performance [5]. Studies have also documented that impurities from the raw materials (nickel and electrolyte) segregate to the free surfaces in the anode / electrolyte interface [9]-[12]. It is believed that if the TPB is blocked by non-conducting impurities the electrochemical charge transfer reaction is inhibited resulting in poor SOFC performance. When lowering the operation temperature the relative detrimental effects of impurities increase, hence the study of impurities becomes relevant for the further development of SOFC technology.

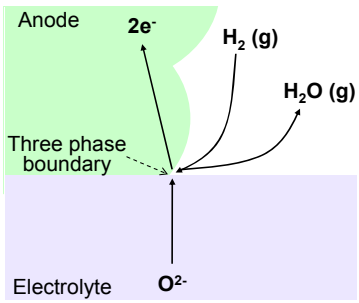

Figure 1.2: Schematic illustration of the three phase boundary at the SOFC anode and the chemical species which converge there to produce electricity and water.

1.4 Thesis objective

Numerous studies of the nickel / YSZ interface have been reported in literature, but these have often been inconsistent. It has been suggested that impurities at the Ni / YSZ interface and changes in microstructure could explain the disagreements found in literature [13]. This thesis is the continuation of the study of the anode / electrolyte interface that has been conducted at *Risø-DTU* since 1999. Vels Hansen (formerly Vels Jensen) [9] studied the Ni / YSZ interface at 1000 °C using point electrodes with purities of 99.8 % Ni and 99.995 % Ni and found that impurities from both the electrodes and electrolytes segregated to the TPB forming ridges of impurities. The impure electrodes created the largest ridges at the TPB and subsequently the electrode polarisation resistance using the 99.995 % Ni electrodes was 10-100 times lower than that measured using less pure 99.8% Ni electrodes. It was also found that the YSZ interface was dynamic at 1000 °C in that topographical changes on the Ni / YSZ interface were observed.

In an attempt to characterise the electrode / electrolyte interface without the influence of impurity species Høgh [12] used a higher purity nickel electrode (99.999 % Ni) and a point electrode setup for electrochemical measurements on one ScYSZ and three YSZ and single crystals at 500-700 °C. Impurities are typically removed by zone melting when producing single crystals and these are therefore usually much cleaner with respect to impurities than the polycrystalline electrolytes used in commercial SOFCs. However, Høgh found that impurities still segregated to the surfaces of the single crystal electrolytes during electrochemical testing at relatively low temperatures and that the area specific electrode polarisation resistance increased by a factor of 5-19 over time. The degradation of electrode performance was attributed to the segregation impurities to the electrolyte surface and the formation of a ridge of impurities at the TPB.

This study investigates the interface between a high purity (99.999 % Ni) nickel electrodes and scandia and yttria co-doped zirconia electrolytes at 850 °C. Scandia doped electrolytes were selected since scandia has been shown to significantly increase ion conductivity through the electrolyte and are prime candidates for the next generation of commercial SOFCs. Furthermore recent studies have shown that Sc-doped zirconia is less vulnerable than YSZ to sulphur poisoning which is a common problem when using biogas as a fuel in SOFCs [14]. 850 °C lies between the temperature ranges studied by Høgh and Vels Hansen, and is also a temperature at which single cells and stacks are commonly tested at *Risø-DTU*.

In order to evaluate the effect of impurities in Sc-doped YSZ an electrolyte with few impurities was tested and compared to a ScYSZ electrolyte with higher impurity levels. Addition of alumina has been shown to increase the ion conductivity in YSZ by acting as a scavenger of impurity species such as silica [15][16]. To evaluate this effect and the consequence on the electrode reaction, alumina was added to a ScYSZ electrolyte with high impurity levels.

Electrochemical characterisation was performed using electrochemical impedance spectroscopy (EIS) and chronoamperometry at 850°C in H_2 / H_2O atmospheres. Using a nickel point-electrode in a three-electrode configuration enabled the investigation of the electrode / electrolyte interface after electrochemical characterisation as the electrode was easily lifted off the electrolyte exposing the electrode / electrolyte interface. Scanning electron microscopy (SEM) and atomic

force microscopy (AFM) was used to study the microstructural topography of the electrode / electrolyte interface. X-ray photoelectron spectroscopy (XPS) was used for quantitative chemical measurements on electrolyte surfaces and time-of-flight secondary ion mass spectrometry (ToF-SIMS) was used to map the lateral distribution of chemical species on the electrolyte surfaces.

1.5 Thesis layout

The thesis is built up to best describe the experimental process and the subsequent conclusions from each experiment. Chapter 2 describes the experimental setup used for electrochemical characterisation and the methods used in the following microstructural- and chemical characterisations. Chapter 3 evaluates a reference YSZ electrolyte commonly used in SOFCs. In chapter 4 and 5 the effects of varying impurity levels are investigated by comparing two ScYSZ electrolytes with different impurity levels. The effects of alumina addition to a ScYSZ electrolyte are documented in chapter 6. Chapter 7 studies the electrode kinetics during prolonged anodic polarisations of nickel electrodes placed on ScYSZ electrolytes. The results of chapters 3 through 7 are discussed in chapter 8 and final conclusions drawn in chapter 9. Finally, thoughts on directions for future work are given in chapter 10. Supplementary data referred to in the text is attached in Appendices A to E. Appendices F to H comprises two papers that have been accepted for publication and one submitted manuscript.

1.6 References

[1] Intergovernmental Panel on Climate Change. Climate change 2007: Mitigation. Contribution of Working Group III to the Fourth Assessment Report of the IPCC, B. Metz, O.R. Davidson, P.R. Bosch, R. Dave, L.A. Meyer (eds), Cambridge University Press, 2007.

[2] N.Q. Minh, T. Takahashi, Science and Technology of Ceramic Fuel Cells, Elsevier Science B.V., 1995.

[3] Biofuels for Fuelcells, Renewable energy from biomass fermentation, P. Lens, P. Westermann, M. Haberbauer, A. Moreno (eds) IWA publishing, 2005.

[4] I. Chorkendorff, J.W. Niemantsverdriet, Concepts of Modern Catalysis and Kinetics, Wiley-VCH, 2003.

[5] A. Hagen, R. Barfod, P.V. Henriksen, Y-L. Liu, S. Ramousse, Jour. Electrochem. Soc. 153 (2006) A1165.

[6] H.Y. Tu, U. Stimming, Journal of Power Sources, 127 (2004) 284.

[7] T. Iwata, Jour. Electrochem. Soc. 143 (1996) 1521.

[8] P. Metzger, K.A. Friedrich, H. Muller-Steinhagen, G. Schiller, Solid State Ionics, 177 (2006) 2045.

[9] K.V. Jensen, Ph.D. thesis, Risø National Laboratory, Denmark, 2002.

[10] Y.-L. Liu, C.G. Jiao, Solid State Ionics, 176 (2005) 435.

[11] Y-L. Liu, S. Primdahl, M. Mogensen, Solid State Ionics, 161 (2003) 1.

[12] J.V.T. Høgh, Ph.D. thesis, Risø National Laboratory, Denmark, 2005.

[13] M. Mogensen, J. Høgh, K. V. Hansen, T. Jacobsen, ECS Transactions 7 (1) (2007) 1329.

[14] O. Yamamoto, Y. Takeda, R. Kanno, K. Kohno, T. Kamiharai, Journal of Materials Science Letters 8 (1989) 198.

[15] J. Drennan, E. P. Butler, Proceedings of Science of Ceramics 12 (1984) Faenza, Italy, 267.

[16] D. Lybye, Y-L. Liu, J. Eur. Ceramic Soc. 26 (2006) 599.

2 Experimental

This chapter describes the experimental methods used to produce the data presented and analysed in the rest of the thesis. The experimental work can be divided into three parts, sample preparation, electrochemical characterisation and surface analysis. Unless stated otherwise in the following chapters the samples were prepared and the experiments performed as stated in the following.

2.1 Sample preparation

2.1.1 Electrolyte sample preparation

Electrolyte powders were acquired from three commercial suppliers, *Tosoh Corporation*, *Daiichi Kigenso Kagaku Kogyo Co.*, *Ltd*., and *Viking Chemicals*. These powders were analysed by glow discharge mass spectrometry (GDMS) by *Evans Analytical Group*, France, to determine the exact levels of impurity species, Table 2.1. Based on the GDMS analysis the electrolyte powders were dubbed *Pure ScYSZ*, *Impure ScYSZ* and *YSZ*. The difference in Sc_2O_3 content between the Scandia doped electrolytes was only 1.1 weight %, and thus only small differences in ionic conductivity based on doping levels were expected [1].

Table 2.1: Glow discharge mass spectrometry results in ppm by weight. Note the large Si content in *Impure ScYSZ*.

	Na	Al	Si	K	Ca	Mg	Cr	Mn	Fe	Li	Ni
Pure ScYSZ $Sc_{0.18}Y_{0.02}Zr_{0.80}O_{1.9}$	39	6.9	10	16	9.6	0.43	1.8	0.52	10	0.74	21
Impure ScYSZ $Sc_{0.16}Y_{0.04}Zr_{0.80}O_{1.9}$	370	12	380	22	80	310	10	1.5	51	0.15	8.8
YSZ $Y_{0.14}Zr_{0.86}O_{1.9}$	470	12.3	9	1.5	3.5	1.5	0.56	0.7	1.0	1.6	0.71

When preparing the electrolyte samples, care was taken to ensure identical processing of the different powders. The electrolyte powders were pressed uniaxially in a 20 mm diameter tool for 20 seconds with a pressure of 1 ton to form rods. Thereafter the rods were isostatically pressed for 20 seconds with a pressure of 55 tons. The isostatically pressed rods were heated to 1315 °C at a ramp speed of 100 °C/h and sintered in air for 12 hours. After sintering the rods were ~5 cm in length and ~16 mm in diameter.

AlO(OH) powder (Catapal®, *Sasol*) corresponding to an aluminium content of 2 % of the metal cations in the electrolyte, was added to one batch of *Impure ScYSZ* powder and ball milled to ensure uniform distribution. This batch of *Impure ScYSZ*

with added alumina was dubbed *Al-ScYSZ*. Besides ball milling, the impure ScYSZ powder (*Al-ScYSZ*) with added AlO(OH) was processed exactly like the other electrolytes as described above. The AlO(OH) powder was also analysed by GDMS the results of which are presented in Table 2.2. The AlO(OH) powder had low impurity levels relative to *Impure ScYSZ*.

Table 2.2: Glow discharge mass spectrometry results in ppm by weight of the AlO(OH) added to a batch of *Impure ScYSZ* to create *Al-ScYSZ*.

	Na	Al	Si	K	Ca	Mg	Cr	Mn	Fe	Li	Ni
Catapal AlO(OH)	74	-	15	0.38	52	6.3	0.70	0.63	9.8	0.05	1.1

After sintering, the rods were cut into 3.1 mm thick pellets using a 0.75 mm thick diamond blade (*Norton*) fixed in a *Struers* Accutom-5 saw with digital feed. The digital feed system made it possible to reproduce the thickness of the cut pellets to within ± 0.01 mm. 6 pellets were fixed to a 16 cm diameter steel sample holder using wax. The pellets were ground and polished, using the procedure shown in Appendix A, down to 0.25 µm diamond particles, using a RotoPol (*Struers*) polishing system with mechanical force application, ensuring that all samples were identically polished. The pellets were polished to remove any impurity concentrations at the surface as well as easing microstructural characterisation following electrochemical testing. Separate polishing cloths were used for each electrolyte material in order to prevent cross contamination. The samples were removed from the steel sample holder by heating it to ~120 °C at which temperature the wax softened and the samples could be lifted off the sample holder. The samples were ultrasonically cleaned in acetone to remove any adhering wax and rinsed with ethanol. Finally the samples were ultrasonically cleaned and rinsed using deionised water (*Millipore*).

2.1.2 Electrode sample preparation

It has previously been shown that impure nickel greatly contributes to observed microstructures and electrochemical performance at the electrode / electrolyte interface [2]. Therefore nickel wire with as high a purity as possible was used in order to reduce the risk of the electrode acting as a contamination source. Thus, the point electrodes were constructed from high purity (99.999 % Ni) nickel wire supplied by *Alfa Aesar*, Table 2.3.

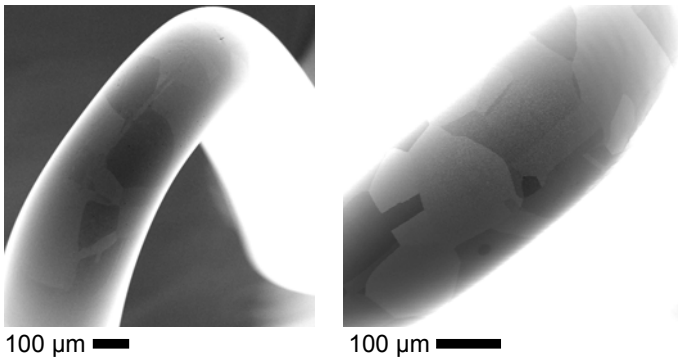

Figure 2.1: Scanning electron microscopy images using the secondary electron detector of two electro-polished Ni-electrodes prior to electrochemical testing. Individual grains can be distinguished from each other.

40 mm long pieces of the 0.5 mm diameter wire were bent to form a point and annealed for 24 hours at 1000 °C in 9 % H_2 / Ar. Annealing was performed in order to restore the Ni crystals (grains) that were damaged by deformation when the wire was bent. Finally, the nickel tips were electropolished for 4 minutes in an electrolyte solution (120 mL water, 700 mL ethanol, 100 mL 2-butoxy ethanol, 78 mL perchloric acid) cooled to -5 °C. A platinum cathode was used and a voltage of 10 V was applied resulting in a current of ~0.38 A. The electropolished electrode tips were examined with optical and scanning electron microscopes to ensure that a smooth surface had been obtained as shown in Figure 2.1.

Table 2.3: Results of glow discharge mass spectrometry of the nickel wire given in ppm.

Ag	0.7	Cs	< 0.01	Ir	< 0.05	Pr	< 0.01	Tb	< 0.01
Al	0.005	Cu	0.15	K	< 0.05	Pt	< 0.05	Te	< 0.05
As	< 0.05	Dy	< 0.01	La	< 0.005	Rb	< 0.05	Th	< 0.001
Au	< 0.05	Er	< 0.01	Li	< 0.005	Re	< 0.05	Ti	0.2
B	< 0.005	Eu	< 0.01	Lu	< 0.01	Rh	< 0.1	Tl	< 0.01
Ba	< 0.05	F	< 0.05	Mg	0.02	Ru	< 0.5	Tm	< 0.01
Be	< 0.005	Fe	1.5	Mn	< 0.005	S	0.06	U	< 0.001
Bi	< 0.01	Ga	< 0.05	Mo	< 0.05	Sb	< 0.01	V	< 0.001
Br	< 0.05	Gd	< 0.01	Na	0.85	Sc	< 0.001	W	< 0.05
Ca	< 0.05	Ge	< 0.05	Nb	< 0.01	Se	< 0.05	Y	< 0.05
Cd	< 0.1	Hf	< 0.01	Nd	< 0.01	Si	0.2	Yb	< 0.01
Ce	< 0.05	Hg	< 0.05	Os	< 0.05	Sm	< 0.01	Zn	0.2
Cl	2.1	Ho	< 0.01	P	< 0.005	Sn	0.04	Zr	< 0.05
Co	1.2	I	< 0.01	Pb	0.9	Sr	< 0.05		
Cr	0.01	In	< 0.05	Pd	< 0.05	Ta	< 1		

2.2 Electrochemical characterisation setup

A custom made rig was used for electrochemical characterisation. The rig parts consisted of alumina (99.8 % purity) and all electrical leads were platinum. The rig fitted four, three-electrode cells in which the Ni point electrodes were the working electrodes, Figure 2.2. Figure 2.3 gives the principle and the dimensions of the three-electrode configuration. Porous counter and reference electrodes were painted onto the bottom of the electrolyte pellets with platinum paste (*Degussa*). The painted electrode areas of each cell were placed on two separate platinum meshes to ensure gas access to the entire area of the painted electrodes and to connect the painted electrodes to the measurement equipment. The mounting of the electrode / electrolyte pairs into the rig took place in a laminar air flow bench (*Holten*) where particles down to 0.3 µm were filtered out. This effectively reduced dust contamination of the rig and its contents.

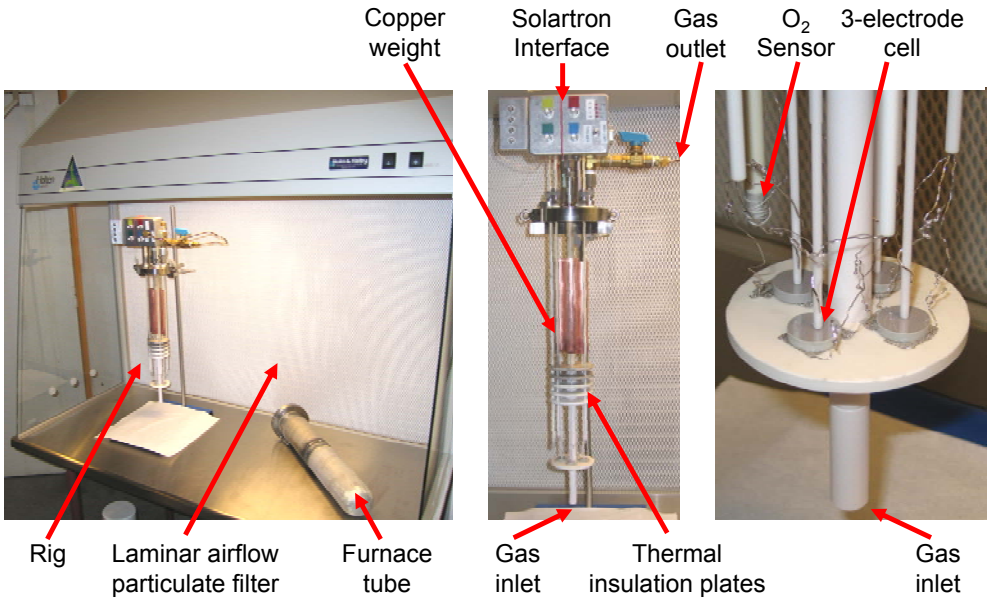

Figure 2.2: The laminar air flow, dust filtering work station at which the rig was prepared for electrochemical testing.

The nickel wires acting as working electrodes were set onto the centre of the polished electrolyte surface and pressed down by 315 g copper weights via two-bore alumina tubes. Weights were necessary to ensure good physical contact between the electrodes and electrolytes. While still placed inside the laminar air flow bench the rig, with mounted samples and copper weights, was inserted into an alumina furnace tube after which dust contamination was no longer possible. The oven tube with the rig sitting inside was then placed in an oven where connections to the gas supply were attached. The gas inlet was at the bottom of the rig minimizing possible contamination from the copper weights as these were downstream from the three-electrode cells. Furthermore, a study of YSZ samples placed downstream from a copper weight in 9 % H_2 / 3 % H_2O / N_2 for 7 days at 1000 °C and analysed by X-ray photoelectron spectroscopy showed that copper contamination of the YSZ did not occur [3] hence copper contamination was not an issue.

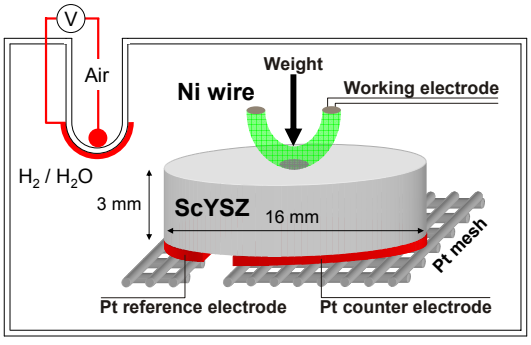

Figure 2.3: Schematic of the three-electrode setup and oxygen sensor measuring pO_2 voltage in the measurement atmosphere.

Electrochemical measurements were performed in a one-atmosphere setup. Inlet hydrogen was bubbled through a water bottle placed in a refrigerator, hence the water content in the measurement atmosphere could be controlled by varying the

refrigerator temperature. The oxygen potential in the measurement atmosphere versus air was monitored by a platinum electrode pair on two sides of an alumina tube closed at one end, inserted in the measurement atmosphere, Figure 2.3. To avoid stagnant air at the closed end of the alumina tube, air was constantly pumped into the tube from the open end. The water bottle could be bypassed to create a "dry" measurement atmosphere by closing Wet gas valves 1 and 2 and opening the Dry gas valve, Figure 2.4. Some moisture was, however, present in the gas supply and based on the oxygen potential, the "dry" atmosphere had a water content calculated to 54 ppm.

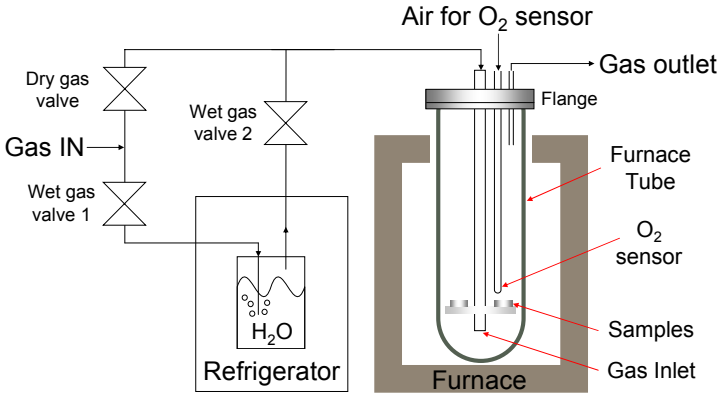

Figure 2.4: Schematic of the gas connections and the furnace with rig inserted in the furnace tube. The water content in the measurement atmosphere could be controlled by varying the temperature of the refrigerator or eliminated by bypassing the water bottle.

With the samples mounted, the rig was heated to 850 °C at a rate of 5 °C / minute in 89 % Ar / 9 % H_2 / 2 % H_2O where after the atmosphere was switched to 97.6 % H_2 / 2.4 % H_2O (pO_2 = -1104 mV vs. Pt / air). Electrochemical impedance spectroscopy (EIS) was performed at open circuit voltage (OCV) with an applied RMS amplitude of 7.07 mV using a *Solartron* 1250 frequency response analyser coupled with a *Solartron* SI 1287 potentiostat controlled by *Elchemea* software [4]. The obtained impedance spectra were fitted with the equivalent circuit $R_s(R_{p1}Q_1)(R_{p2}Q_2)$ [5] using *ZView* version 2.90. From the impedance spectra values for the ohmic losses in the electrolyte and electrode (R_s) and the electrode polarisation resistance (R_p) could be obtained, Figure 2.5. Upon completion of electrochemical measurements the furnace was cooled to room temperature in 91 % Ar / 9 % H_2 over the course of 7 hours.

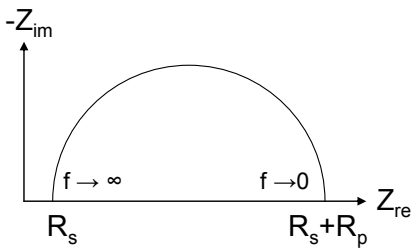

Figure 2.5: Schematic of an impedance spectrum labelled with the series- (R_s) and electrode polarisation resistances (R_p).

2.3 Microscopy

Following electrochemical measurements, the nickel electrodes were lifted off the electrolytes. The electrodes and electrolytes were examined with a field emission gun scanning electron microscope (SEM) (Supra 35, *Zeiss*). Secondary electrons with a 1 keV acceleration voltage and working distance of 4 mm were used to examine the surface microstructures on the electrolytes without necessitating carbon coating. From SEM images of the electrolytes and electrodes the electrode / electrolyte interface areas were quantified using an image analysis tool (*Scion Corporation*).

A DualScope atomic force microscope (AFM)(*DME Danish Micro Engineering A/S*) was used in tapping mode to obtain three-dimensional images of the electrode / electrolyte interfaces and to quantify the microstructural features observed with SEM.

2.4 Chemical surface analysis

2.4.1 Time-of-flight secondary ion mass spectrometry

The lateral distribution of chemical species on electrodes and electrolytes was analysed by time-of-flight secondary ion mass spectrometry (ToF-SIMS) (TOF-SIMS IV, *ION-TOF GmbH*). ToF-SIMS is a qualitative measurement technique, where a focused beam of pulsed primary ions (Bi^+) is scanned across an analyte surface. The incoming ions have a high kinetic energy and cascade through the sample surface transferring kinetic energy to the surface and subsurface regions. As cascading atoms transfer kinetic energy to surface atoms these overcome the surface binding energy and are emitted from the sample surface as both neutral species and charged ions, Figure 2.6. The majority of species emitted from the surface are neutral, but it is the charged secondary ions which are detected and analysed. ToF-SIMS is surface specific with over 95 % of the secondary particles originating from the top two layers of the solid [6]. In an electric field and at the same kinetic energy, heavy ions travel slower than light ions, so the time it takes for the ion to reach the detector determines the mass of the ion. Since the primary ion beam is scanned across the sample surface, a two-dimensional image of the lateral distribution of species on the sample surface can be obtained. Each pixel corresponds to a mass spectrum which is why ToF-SIMS imaging data is usually presented by showing the intensity of a single individual mass peak converted to a colour code. During the flight time of emitted secondary ions the extraction field is switched off and low energy electrons are used to compensate for surface charging due to primary or secondary ions. For this reason all types of bulk insulators including ScYSZ can be analysed. Depth profiling of the analyte surface can be performed using an ion source (Xe^+) to remove surface layers by sputtering followed by analysis of the sputtered area.

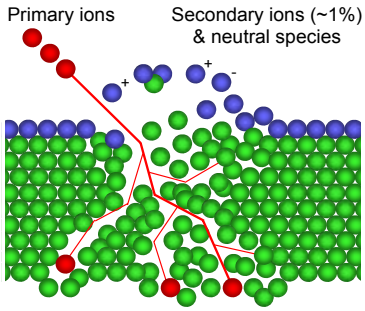

Figure 2.6: Schematic of the principle behind time-of-flight secondary ion mass spectrometry (ToF-SIMS). Primary ions with high kinetic energy impact the analyte sample and cause a cascade around the impact point. Secondary ions with sufficient kinetic energy escape the sample surface and are accelerated to the same kinetic energy and subsequently mass analysed in a time-of-flight (ToF) analyser.

Two ToF-SIMS analysis modes were used, bunch mode and burst alignment mode. In bunch mode the primary ions were focused so that they impacted the sample surface at more or less the same time resulting in high mass resolution. In burst alignment mode the primary ions were focused in a narrower beam (spot size ~150 nm) resulting in high lateral resolution, but compromising mass resolution. A qualitative illustration of the two modes is given in Figure 2.7.

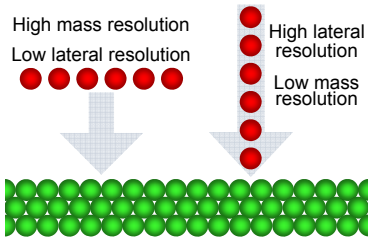

Figure 2.7: Schematic of the different way primary ions can be focused using ToF-SIMS. High mass resolution compromises lateral resolution of the created secondary ion signal and vice versa.

ToF-SIMS images with high mass resolution, but low lateral resolution were acquired using 30 ns pulses of 25 keV Bi^+, bunched to form ion packets with a nominal temporal extent of < 0.9 ns at a repetition rate of 10 kHz yielding a target current of 500 fA. These primary ion conditions were used to scan 500 × 500 μm^2 areas of the sample surface. Images with low mass resolution but high lateral resolution (primary ion spot size ~150 nm) were acquired covering 20 × 20 μm^2 to 75 × 75 μm^2 areas of the sample surface using 100-ns pulses of 25 keV Bi^+ at a repetition rate of 10 kHz yielding a target current of ≤ 10 fA. High lateral resolution images enabled the correlation between ToF-SIMS and SEM images. Following the 20 × 20 μm^2 to 75 × 75 μm^2 area scans a 1000 × 1000 μm^2 area of the surface was sputtered using 3 kV Xe^+ (sputter ions) resulting in a target current of 20 nA. After sputtering, the same areas were scanned again. Electron bombardment (20 eV) was used to minimize charge build-up at the surface. Desorbed secondary ions were accelerated to 2 keV, mass analyzed in the flight tube, and post-accelerated to 10 keV before detection.

2.4.2 X-ray photoelectron spectroscopy

For quantitative measurements of element concentrations on the electrolyte surfaces X-ray photoelectron spectroscopy (XPS)(K-Alpha, *Thermo Scientific*) was used. XPS takes advantage of the photoelectric effect, where electrons are liberated from well defined core levels of atoms, when they absorb energy from electromagnetic radiation in the form of X-rays [7]. The kinetic energy and the number of the emitted electrons is measured allowing quantification of the element composition of the top 1-10 nm of the sample. Energy scans were performed with a spot size of 400 µm outside the electrode / electrolyte interfaces and with at spot size of 100 µm inside the electrode / electrolyte interface; which was located with a built in optical microscope. The spectra were quantified using *Thermo Avantage* v3.91, software.

2.5 References

[1] O. Yamamoto, Y. Arati, Y. Takeda, N. Imanishi, Y. Mitzutani, M. Kawai, Y. Nakamura, Solid State Ionics 79 (1995) 137.

[2] K. V. Jensen, S. Primdahl, I. Chorkendorff, M. Mogensen, Solid State Ionics 144 (2001) 197.

[3] J.V.T. Høgh, Ph.D. thesis, Risø National Laboratory, Denmark, 2005.

[4] S. Koch, K.V. Hansen, B.S. Johansen, Risø-DTU, Denmark, Elchemea (2005).

[5] B.A. Boukamp, Solid State Ionics 18-9 (1986) 136.

[6] J.C. Vickerman, D. Briggs (eds) ToF-SIMS: Surface Analysis by Mass Spectrometry, Surface Spectra Ltd., 2001.

[7] J.M Thomas, W.J. Thomas, Principles and Practice of Heterogeneous Catalysis, VCH Publishers Inc., 1997.

3 Characterisation on *YSZ*

This chapter presents results from a preliminary experiment performed to evaluate the electrode reaction on a standard YSZ electrolyte material (*YSZ*), currently used in SOFC production at *Risø-DTU*. In this chapter *YSZ* is compared with *Pure ScYSZ*. The electrochemical performance of electrodes measured on *YSZ* will later be compared with the scandia and yttria co-doped zirconia electrolytes. The *YSZ* powder was prepared and tested under identical conditions using the same measurement setup as the scandia doped electrolytes. Furthermore, as it has been shown that scandia doping will generally improve ion conductivity in zirconia [1] this is also evaluated here.

3.1 Electrochemical characterisation on *YSZ*

After preparing the electrolyte pellets and Ni electrodes as described in chapter 2 electrochemical impedance spectroscopy (EIS) measurements were performed at 850 °C in a 2.4 % H_2O / H_2 atmosphere. EIS was performed at open circuit voltage (OCV) for up to 360 hours on eight samples of *YSZ*. Examples of impedance spectra measured on *YSZ* and *Pure ScYSZ* electrolytes at the beginning of the measurements (t = 0 h) are shown in Figure 3.1. More impedance spectra of *Pure ScYSZ* will be presented in chapter 4. It is seen that the electrode polarisation resistance (R_p) measured on *YSZ* was much larger than that measured on *Pure ScYSZ*. The contact area between the electrode and electrolyte are not known at the start of the measurement, hence R_p, is not converted to an area specific notation. However, the contact area is assumed to be similar as identical electrodes and weights were used. It should also be noted that the high frequency series resistance (R_s) measured on both electrolytes was several orders of magnitude smaller than R_p.

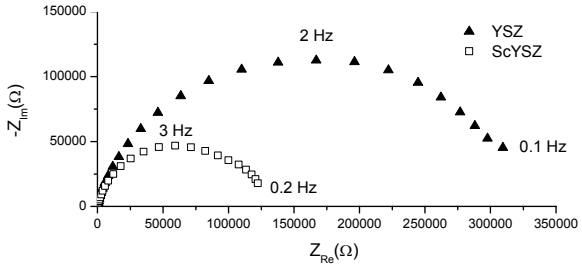

Figure 3.1: Impedance spectra recorded on *YSZ* and *Pure ScYSZ* electrolytes at 850 °C in a 2.4 % H_2O / 97.6 % H_2 atmosphere using Ni electrodes, at the beginning of the measurement (t = 0). The contact areas are assumed to be similar in size.

The development of R_s and R_p as a function of time for four representative samples are presented in Figure 3.2 and Figure 3.3 respectively. Newman [2] described the relationship between the radius of the contact area and R_s by:

$$r = \frac{1}{4\,\sigma\,R_s} \qquad (1)$$

Where r is the radius of a circular contact area and σ is the ion conductivity of the electrolyte. When substituting with the area $A = \pi\, r^2$ the relationship between R_s and contact area can be written:

$$A = \frac{\pi}{16\,\sigma^2\,R_s^{\,2}} \qquad (2)$$

Figure 3.2 shows that the high frequency series resistance describing the ohmic losses in the electrolyte and nickel electrode decreased rapidly during the first 50 hours at 850 °C. The initial rapid decrease in R_s was attributed to an increase in the electrode / electrolyte contact area by metallic creep. Once the initial rapid decrease in R_s was over the rate of decrease in R_s on both electrolytes slowed significantly.

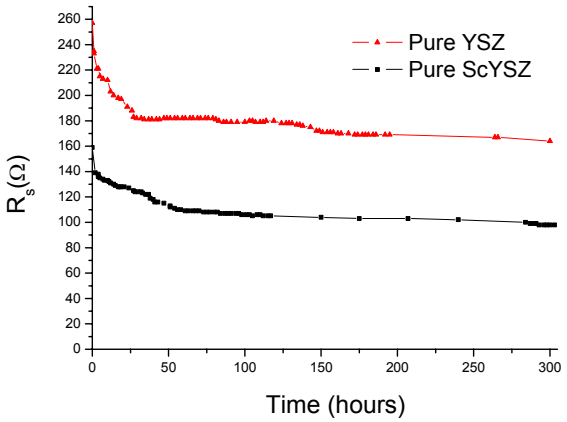

Figure 3.2: Plot of the series resistance (R_s) over the first 300 hours of measurements at 850 °C measured on YSZ and ScYSZ electrolytes. The initial rapid decreases in R_s were attributed to an increase in the electrode / electrolyte interface areas due to metallic creep of the nickel electrodes.

Over the first 50 hours large initial decreases in the electrode polarisation resistance were measured on both YSZ and ScYSZ electrolytes, Figure 3.3. After the initial rapid decreases, the R_p values stabilised. It should be added that the measured R_s values were much more regular than the measured R_p values, which were less stable as seen in Figure 3.3.

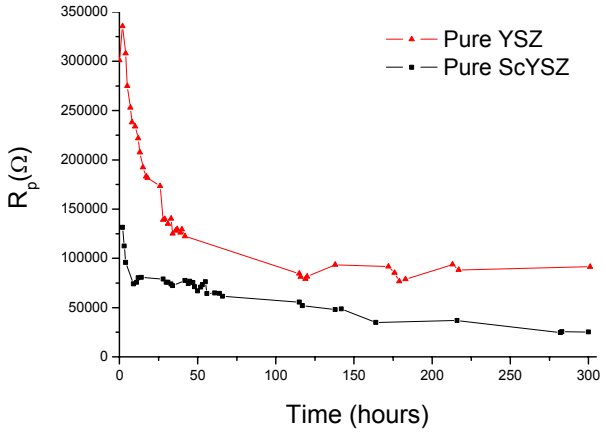

Figure 3.3: Plot of the electrode polarisation resistance (R_p) over the first 300 hours of measurements at 850 °C measured on YSZ and ScYSZ electrolytes. After initial rapid decreases, the R_p values levelled out for the remainder of the measurements.

Impedance spectra recorded after 300 hours at 850 °C on the same samples also shown in Figure 3.1 and Figure 3.3 are shown in Figure 3.4. Here it can be seen that R_p had decreased compared to that measured at t = 0, Figure 3.1. After 300 hours at 850 °C there was a significant difference in R_p between YSZ and ScYSZ despite not being plotted with area specific axis.

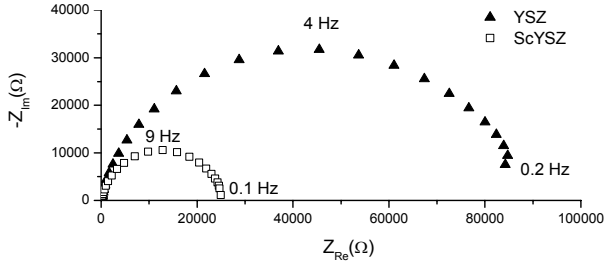

Figure 3.4: Impedance spectra recorded on YSZ and ScYSZ electrolytes after 300 hours at 850 °C. The contact areas are assumed to be similar in size.

After 360 hours at 850 °C the *YSZ* cells were cooled and the electrode / electrolyte interfaces of the electrolytes and Ni electrodes were examined with SEM to quantify the contact areas, Figure 3.5.

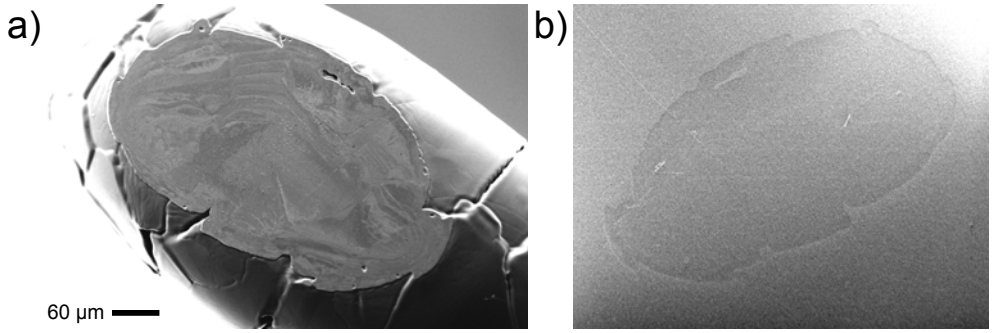

Figure 3.5: a) Secondary electron SEM image of a Ni electrode after electrochemical characterisation. b) SEM image, using the InLens detector, of a *YSZ* surface after electrochemical characterisation. The electrode / electrolyte interface area was measured using image analysis software for high accuracy.

From the measured contact areas and the final measured values of R_p, the area specific electrode polarisation resistances (ASR_p) were determined. The lengths of the electrode / electrolyte interfaces (EEIs) were also determined by SEM and used to calculate the length specific polarisation resistances (LSR_p). In Table 3.1 the results of the electrochemical characterisation of the electrode reaction on *YSZ* are presented. As will be shown in chapter 4, the average ASR_p and LSR_p values for *YSZ* (75 Ωcm^2 / 12.8 k Ωcm) were significantly larger than for *Pure ScYSZ* (42 Ωcm^2 / 5.6 kΩcm).

From the contact areas and the final R_s measurements the electrolyte conductivities, σ, were calculated. It is seen that there was a relatively low scatter in the obtained ion conductivity values. Furthermore, a lower average ion conductivity was calculated for *YSZ* compared to *Pure ScYSZ* (148 $mScm^{-1}$).

Table 3.1: Results of the electrochemical characterisation on the *YSZ* electrolyte. The areas and the lengths of the electrode / electrolyte interfaces were measured by SEM. $R_{p\ start}$ were the electrode polarisation resistances measured at the beginning of the measurements and $R_{p\ final}$ were the final stabilised electrode polarisation resistances measured. The area specific- and length specific electrode polarisation resistances (ASR_p and LSR_p) were calculated from the final polarisation resistance values and SEM measurements. The ion conductivity, σ, was calculated from $R_{s\ final}$ and the EEI area.

	Area (μm^2)	Length (μm)	R_s *start* (Ω)	R_s *final* (Ω)	R_p *start* (kΩ)	R_p *final* (kΩ)	ASR_p (Ωcm^2)	LSR_p (kΩcm)	σ ($mScm^{-1}$)
1	122899	1754	200	162	125	98	120	17.2	72
2	101272	1949	238	181	301	89	90	17.3	69
3	113905	2233	226	166	150	39	44	8.6	70
4	114887	1924	211	169	149	40	46	7.6	69
5	100224	1590	257	167	221	76	76	12.0	67
6	100246	1437	234	167	107	67	67	9.6	77
7	81072	1815	286	176	172	97	78	17.5	76
8	95120	1499	258	172	122	83	79	12.4	73
					Average		**75**	**12.8**	**72**
					Standard deviation		24	4.1	4
					%		33	32	5

3.2 Microstructure of *YSZ*

A closer look at the electrolyte surface revealed that the electrode / electrolyte interface had a distinct surface microstructure. The microstructure has previously been described as the *hill and valley* surface microstructure [3][4] and that term will be adopted throughout this work. Surrounding the electrode / electrolyte interface, a ridge rose up to 20 nm from the surface. This microstructural feature is designated as the *rim ridge*. SEM and AFM images of the hill and valley surface microstructure and rim ridge on an *YSZ* electrolyte sample after electrochemical testing is shown in Figure 3.6, Figure 3.7 and Figure 3.8.

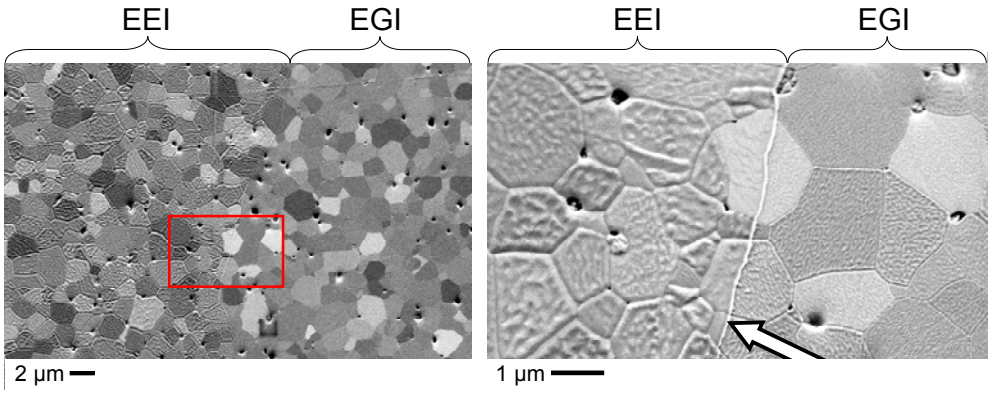

Figure 3.6: Secondary electron SEM images of an *YSZ* electrolyte after 360 hours at 850 °C in H_2 atmosphere. A distinct surface microstructure was seen inside the electrode / electrolyte interface (EEI) compared to the electrolyte / gas interface (EGI). A rim ridge (marked with an arrow) separated the EEI from the EGI.

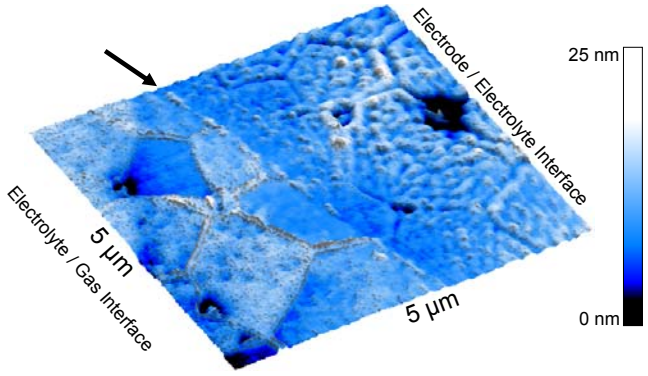

Figure 3.7: Atomic force microscopy image of an *YSZ* electrolyte after 360 hours at 850 °C in H_2 atmosphere. The electrode / electrolyte interface was separated from the electrolyte / gas interface by a rim ridge (marked with an arrow) of heights up to 20 nm.

The hill and valley microstructure was also seen to fade out towards the outer perimeter of the electrode / electrolyte interface as illustrated by Figure 3.8. A coarse topography was observed on the electrolyte / gas interfaces as shown in Figure 3.6, Figure 3.7 and Figure 3.8.

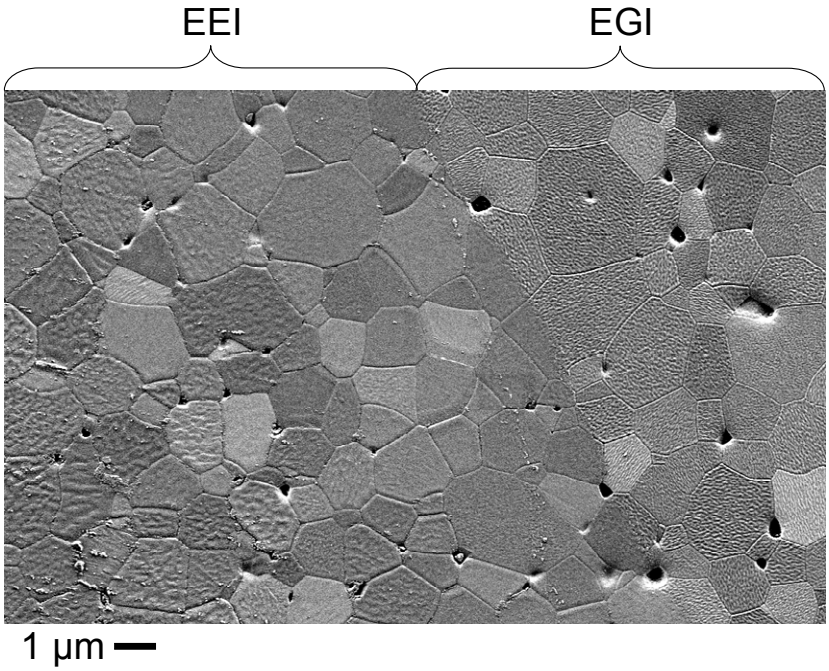

Figure 3.8: SEM image of an *YSZ* electrolyte after 360 hours at 850 °C in H_2 atmosphere. The hill and valley surface microstructure in the electrode / electrolyte interface (EEI) faded out towards the border to the electrolyte / gas interface (EGI).

3.3 Conclusion

It was found that the YSZ material commonly used as electrolyte material in SOFC displays inferior electrochemical performance when compared to a Sc and Y co-doped Zr electrolyte at 850 °C. ASR_p and LSR_p values were slightly larger on *YSZ* compared to *Pure ScYSZ*. The Si content of *YSZ* and *Pure ScYSZ* were 9 and 10 ppm respectively. However there were 470 ppm Na in *YSZ* compared to 39 ppm Na in *Pure ScYSZ*. The measured differences in ASR_p and LSR_p are most likely a consequence of the larger Na content in *YSZ*. The calculated ion conductivity through *Pure ScYSZ* was larger than through *YSZ* and was thus in agreement with literature as to the advantageous effects of scandia doping.

3.4 References

[1] O. Yamamoto, Y. Arati, Y. Takeda, N. Imanishi, Y. Mitzutani, M. Kawai, Y. Nakamura, Solid State Ionics 79 (1995) 137.

[2] J. Newman, J. Electrochem. Soc. 113 (1966) 501.

[3] K. V. Jensen, S. Primdahl, I. Chorkendorff, M. Mogensen, Solid State Ionics 144 (2001) 197.

[4] K.V. Hansen, Ph.D. thesis, Risø National Laboratory, Denmark, 2002.

4 Effects of Impurities

The aim of the experiments presented in this chapter was to investigate the influence of impurities in ScYSZ electrolytes on electrode performance using three-electrode cells. One ScYSZ electrolyte powder with relatively low impurity contents and one with relatively high impurity contents were electrochemically characterised by impedance spectroscopy followed by various surface analysis techniques to illuminate the caused for the measured differences in electrochemical performance. Parts of the results presented in this chapter have been published in Solid State Ionics, appendix F and G.

4.1 Electrochemical characterisation

Two scandia and yttria co-doped zirconia electrolyte powders were selected and analysed by glow discharge mass spectrometry (GDMS) to determine their impurity levels, Table 4.1. Based on the GDMS analysis the powders were dubbed *Pure ScYSZ* and *Impure ScYSZ*. The two powders were processed into pellets by an identical process and sintered at 1315 °C in the same oven at the same time as described in chapter 2. The electrolyte pellets were also polished by an identical process. Polishing the electrolyte pellets had two advantages, firstly it removed any impurity concentrations at the surface so that the Ni point electrodes were placed on a surface representative of the bulk material, and secondly it made the following microstructural characterisation easier as changes in microstructure are better observed on smooth surfaces.

Table 4.1: Glow discharge mass spectrometry results in ppm by weight. Note the large Si and Na content in *Impure ScYSZ* compared to *Pure ScYSZ*.

	Na	Al	Si	K	Ca	Mg	Cr	Mn	Fe	Li	Ni
Pure ScYSZ $Sc_{0.18}Y_{0.02}Zr_{0.80}O_{1.9}$	39	6.9	10	16	9.6	0.43	1.8	0.52	10	0.74	21
Impure ScYSZ $Sc_{0.16}Y_{0.04}Zr_{0.80}O_{1.9}$	370	12	380	22	80	310	10	1.5	51	0.15	8.8

16 cells with *Impure ScYSZ* electrolyte and 16 cells with *Pure ScYSZ* electrolyte were tested at 850 °C in a 97.6 % H_2 / 2.4 % H_2O atmosphere (pO_2 = -1104 mV vs. Pt / air). Electrochemical impedance spectroscopy was performed as soon as the temperature of the measurement atmosphere had stabilised (~30 min).

Examples of impedance spectra measured on *Pure ScYSZ* and *Impure ScYSZ* cells, recorded after 483 hours at 850 °C, are shown in Figure 4.1. The obtained impedance spectra were fitted to the equivalent circuit $R_s(R_{p1}Q_1)(R_{p2}Q_2)$ [1]. From the fitted circuits, average values for the exponential *n* in the constant phase

element Q° ($j\ \omega$)^n were obtained for each RQ pair. These average *n*-values were locked and used to re-evaluate R_{p1} and R_{p2} for each cell during the course of the measurement.

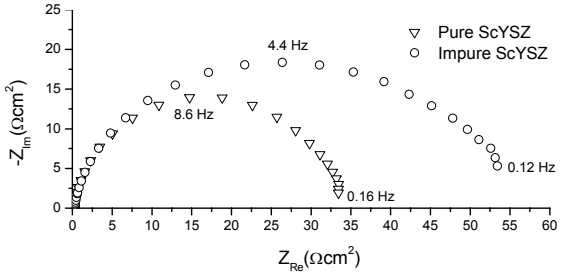

Figure 4.1: Representative Nyquist plots of impedance spectra recorded on samples of pure (Δ) and impure (○) ScYSZ electrolytes after 483 hours at 850 °C, when the electrode response had stabilised. The electrode on the pure electrolyte has a significantly lower electrode polarisation resistance.

4.1.1 *Pure ScYSZ*

Large drops in electrode polarisation resistances, R_p, at OCV, of the Ni electrodes on *Pure ScYSZ* were observed over the first 50 hours from ~110-160 kΩ at t = 0 hours to ~50-70 kΩ at t = 50 hours, Figure 4.2 and Figure 4.3a). The polarisation resistance values fluctuated during the course of the measurements but stabilised around 40 kΩ after 350 hours. Similarly, the series resistances, R_s, decreased from initial values of ~115 Ω at rates of ~0.5 Ω/hour during the first 50 hours to ~100 Ω, Figure 4.3b). Note, however, that R_s was 3 orders of magnitude lower than R_p. After this initial rapid decrease the series resistances reached a steady rate of decrease of ~0.02 Ω/hour.

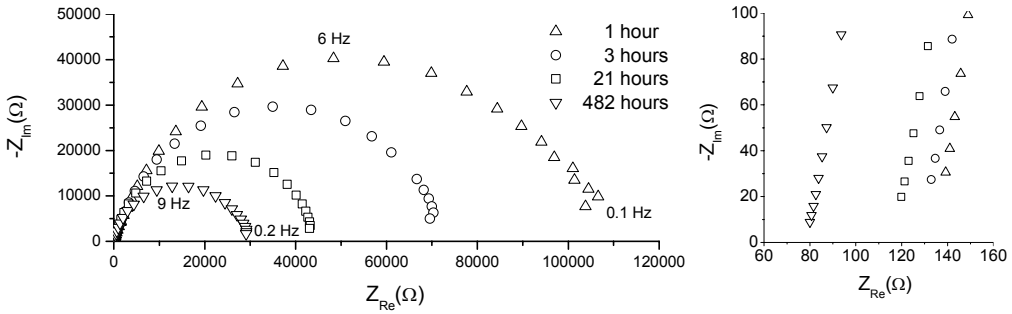

Figure 4.2: Examples of impedance spectra measured on a *Pure ScYSZ* electrolyte as a function of time. During the first 50 hours large drops in electrode polarisation resistance were measured. The series resistance also decreased over time.

When the polarisation resistances of the equivalent circuit $R_s(R_{p1}Q_1)(R_{p2}Q_2)$ (with locked *n*-values) were split up into R_{p1} and R_{p2} a common trend was found for all the *Pure ScYSZ* cells. An example is shown in Figure 4.3a), where it is seen that the resistance corresponding to the high frequency arc (R_{p1}) after an initial stabilisation period, was about 40 kΩ larger than the low frequency arc (R_{p2}). The fluctuations in the total electrode polarisation resistance were mainly due to changes in R_{p1}.

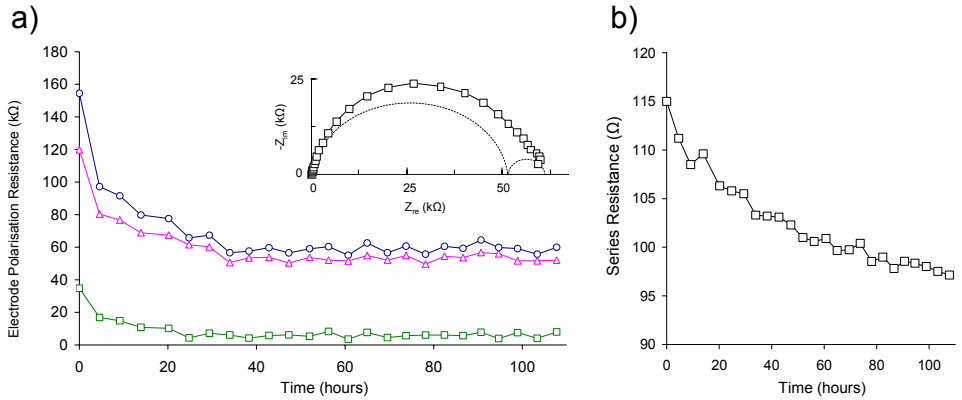

Figure 4.3: The total polarisation resistance of a Ni point-electrode at OCV on a *Pure ScYSZ* electrolyte (○) split up into two components R_{p1} (Δ) and R_{p2} (□) corresponding to the equivalent circuit model $R_s(R_{p1}Q_1)(R_{p2}Q_2)$. The *n*-values for this sample were locked at n_1 = 0.94 and n_2 = 0.61. The lines are simple connections between the measured values. b) The series resistance, which mainly originates from the electrolyte, as a function of time during the first 100 hours of measurements.

A summary of the results of the three-electrode measurements using *Pure ScYSZ* is presented in Table 4.2. There was a relatively narrow spread in the measured values of area- and length specific electrode polarisation resistances as well as the calculated ion conductivities.

Table 4.2: Results of the electrochemical characterisation on the *Pure ScYSZ* electrolyte. The areas and the lengths of the electrode / electrolyte interfaces were measured by SEM. $R_{p\ start}$ were the electrode polarisation resistances measured at the beginning of the measurements and $R_{p\ final}$ were the final stabilised values. The area specific- and length specific electrode polarisation resistances (ASR_p and LSR_p) were calculated from the final polarisation resistance values and SEM measurements.

	Area (μm^2)	Length (μm)	R_s *start* (Ω)	R_s *final* (Ω)	R_p *start* ($k\Omega$)	R_p *final* ($k\Omega$)	ASR_p (Ωcm^2)	LSR_p ($k\Omega cm$)	σ ($mScm^{-1}$)
1	122016	1642	102	81	113	37.8	46	6.2	157
2	125645	1750	127	112	124	18.7	23	3.3	112
3	69782	1233	136	112	121	31.7	22	3.9	150
4	151952	1959	109	73	131	22.1	34	4.3	156
5	125373	1677	159	80	141	46.1	58	7.7	156
6	135863	1520	120	75	113	38.4	52	5.8	160
7	129699	1778	124	79	120	47.5	62	8.4	156
8	112095	1520	125	79	111	33.5	38	5.1	168
9	163079	1800	108	79	71	28.7	47	5.2	139
10	188782	1919	99	78	101	29.9	56	5.7	131
11	154138	2392	154	80	63	25.1	39	6.0	141
12	174663	1813	95	78	77	34.1	60	6.2	136
13	92844	1601	104	90	126	52.9	49	8.5	162
14	95027	1508	115	97	155	59.9	57	9.0	148
15	100261	1641	122	91	171	53.0	53	8.7	154
16	89386	1433	118	98	236	85.1	76	12.2	151
					Average		**48**	**6.6**	**148**
					Standard deviation		14	2	14
					%		30	35	9

4.1.2 *Impure ScYSZ*

The electrode polarisation resistances at OCV of the Ni point-electrodes on *Impure ScYSZ* initially showed large drops from ~500-600 kΩ at t = 0 hours to ~ 80-160 kΩ at t = 50 hours, Figure 4.4 and Figure 4.5a). After 400 hours the R_p values had stabilised at ~60 kΩ. Series resistances of ~350 Ω were measured on the impure electrolytes initially, but in contrast to the case of the pure electrolyte these values did not decrease immediately. On the contrary, the R_s values were stable or even increased slightly during a 20 hour period, Figure 4.5b). After this initial 20 hour lag period the series resistances started to decrease at an initial rate of 0.7 Ω/h. The rate of decrease in series resistances slowed down throughout the measurements, reaching rates of decrease of ~0.4 Ω/h at the end of the measurements.

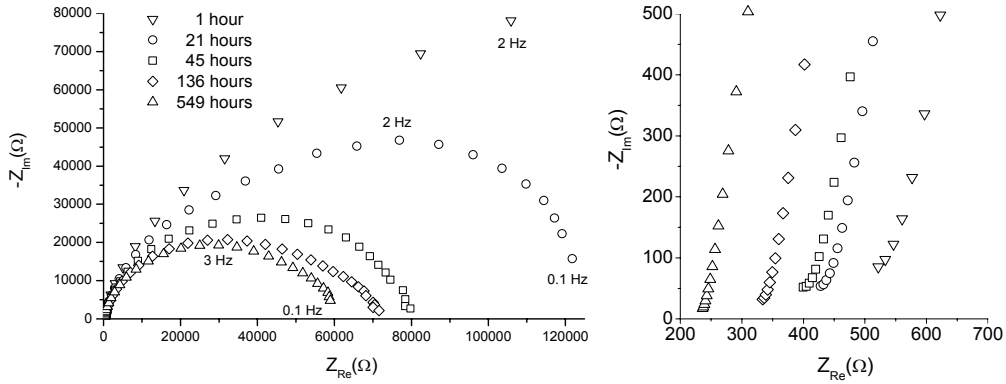

Figure 4.4: Examples of impedance spectra measured on an *Impure ScYSZ* electrolyte as a function of time. During the first 50 hours large drops in electrode polarisation resistance were measured. The series resistance also decreased over time after an initial lag period (not shown here).

The polarisation resistances of the equivalent circuit $R_s(R_{p1}Q_1)(R_{p2}Q_2)$ were split up into R_{p1} and R_{p2}, and the same common trend was found for all 16 cells, of which an example is given in Figure 4.5a). At t = 0 hours the resistance corresponding to the high frequency R_{p1} was four times larger than the low frequency resistance R_{p2}.

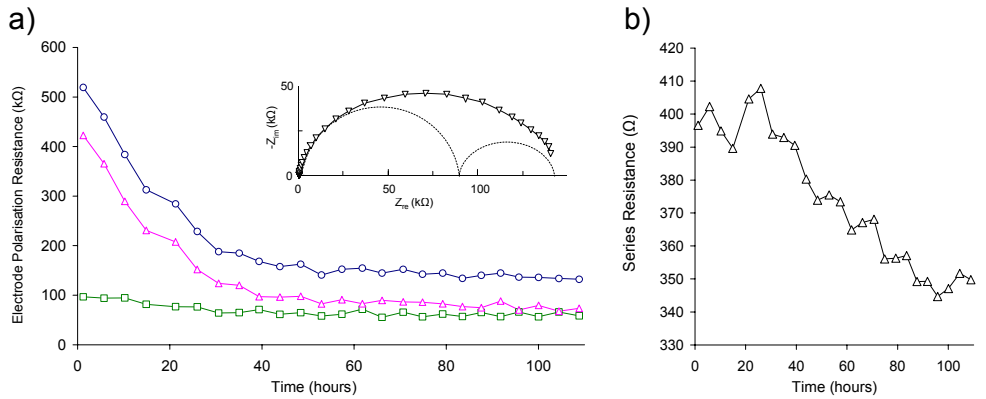

Figure 4.5: The total electrode polarisation resistance of a Ni point-electrode on an *Impure ScYSZ* electrolyte (○) split up into two components R_{p1} (Δ) and R_{p2} (□) corresponding to the equivalent circuit model $R_s(R_{p1}Q_1)(R_{p2}Q_2)$. The n-values for this sample were locked at n_1 = 0.85 and n_2 = 0.69. The lines are simple connections between the measured values. b) The series resistance, which mainly originates from the electrolyte, as a function of time.

R_{p1} dropped during the first 50 hours while the magnitude of the low frequency R_{p2}, remained stable during the course of the experiment. After 400 hours R_{p1} and R_{p2} had stabilised and were approximately the same size. A summary of the results of the three-electrode measurements using *Impure ScYSZ* are presented in Table 4.3.

Table 4.3: Results of the electrochemical characterisation of the *Impure ScYSZ* electrolyte. The area and the lengths of the electrode / electrolyte interfaces were measured by SEM. $R_{p\ start}$ were the electrode polarisation resistances measured at the beginning of the measurements and $R_{p\ final}$ were the final stabilised values.. The area specific- and length specific electrode polarisation resistances (ASR_p and LSR_p) were calculated from the final polarisation resistance values and SEM measurements. Sample 6 is marked with a *p* as this sample has a porous surface microstructure described in the following section.

	Area (μm^2)	Length (μm)	R_s *start* (Ω)	R_s *final* (Ω)	R_p *start* ($k\Omega$)	R_p *final* ($k\Omega$)	ASR_p (Ωcm^2)	LSR_p ($k\Omega cm$)	σ ($mScm^{-1}$)
1	155552	1861	532	225	387	71.1	111	13.2	50
2*p*	145362	1878	404	225	333	64.9	94	12.2	52
3	183486	1707	403	232	317	72.2	133	12.3	45
4	191924	1796	341	210	224	58.4	112	10.5	48
5	150385	1875	674	247	398	120.0	180	22.5	46
6	138245	2059	619	254	415	62.7	87	12.9	47
7	170984	2118	536	232	517	62.1	106	13.1	46
8	165950	2174	613	215	419	52.6	87	11.4	51
9	276920	2127	228	210	409	32.4	90	6.9	40
10	144037	1921	508	307	432	81.6	117	15.7	38
11	114724	1749	662	330	325	97.4	112	17.0	40
12	172083	1720	502	268	514	60.6	104	10.4	40
13	71169	1169	397	350	519	132.0	94	15.4	47
14	80348	1461	468	342	315	76.4	61	11.2	46
15	107256	1772	508	317	234	91.5	98	16.2	43
16	104098	1831	520	357	294	81.5	85	14.9	38
					Average		**104**	**13.5**	**45**
					Standard deviation		26	3.5	4
					%		25	26	10

4.1.3 EIS summary

The average values for ASR_p, LSR_p for *Pure ScYSZ* and *Impure ScYSZ* are summarised in Table 4.4. The results from the characterisation of *YSZ* from chapter 3 are also listed. There is a significant difference between *Pure ScYSZ* and *Impure ScYSZ* when considering ASR_p, LSR_p. Furthermore, the relative scatter of the results for both electrolytes were approximately the same.

Table 4.4: Summary of the electrochemical characterisation by electrochemical impedance spectroscopy at 850 °C of *Pure ScYSZ*, *Impure ScYSZ* and *YSZ*.

	ASR_p (Ωcm^2)	LSR_p ($k\Omega cm$)
Pure ScYSZ	48	7
Impure ScYSZ	104	13
YSZ	75	13

4.2 Microstructural characterisation

After electrochemical impedance measurements the electrodes and electrolytes were separated and examined with SEM and AFM to characterise the surface microstructures of the electrode / electrolyte interfaces (EEIs) and the surrounding electrolyte / gas interfaces (EGIs).

4.2.1 *Pure ScYSZ*

Identical microstructural features were found on all the high purity electrolyte samples. The surfaces of the EEIs were covered by an undulating microstructure that has previously been dubbed the *hill and valley microstructure* [2], and exemplified by Figure 4.6 and Figure 4.7 from *Pure ScYSZ*. The hill and valley microstructure was clearly dependent on the crystallographic orientation of the individual zirconia grains as the microstructure of neighbouring grains could have different amplitudes. It should be noted that the hill and valley microstructure became less distinct towards the outer perimeter of the EEI as also seen on *YSZ* as shown in chapter 3. The pure electrolyte had not sintered to completion at 1315 °C, as porosities were observed at triple points on the polished surfaces, Figure 4.7. Inside the EEI, Ni from the electrode had crept into the porosities in the electrolyte. When separating the electrode and electrolyte some of the Ni remained in the porosities and in other areas continued to adhere to the electrode thus protruding from the flat electrode surface.

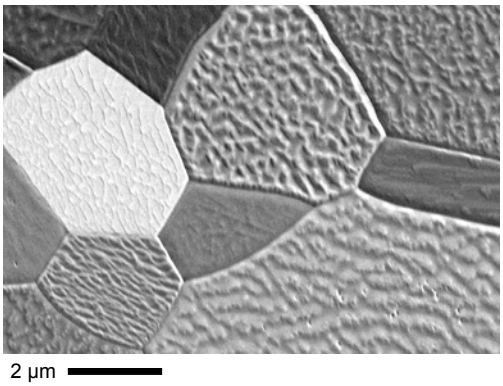

Figure 4.6: Secondary electron SEM image of the hill and valley surface microstructure found on *Pure ScYSZ* electrolytes inside the electrode / electrolyte interfaces. The surface microstructure varied from grain to grain.

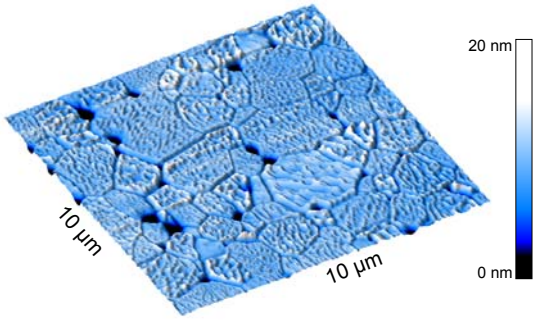

Figure 4.7: Atomic force microscopy image of the hill and valley surface microstructure found on *Pure ScYSZ* electrolytes inside the electrode / electrolyte interfaces. Porosities due to incomplete sintering (black) were found at triple points.

The electrolyte areas, which had not come into contact with the Ni electrode (the electrolyte / gas interface), showed only very subtle microstructural changes to the polished surface. The surface structure of the EGI could be described as a very low amplitude variation of the hill and valley structure. The surfaces of the EEIs on *Pure ScYSZ* were not as rough as that of the EGIs on *YSZ*. The EEIs were delimited by a 5-20 nm tall ridge, which clearly defined the border between the EEIs hill and valley microstructure and the smoother EGI surface. The ridge will be referred to as the *rim ridge* in the following. The ridge was measured by AFM to have local variations in height in the order of 5 nm over a ridge section of 50 µm length.

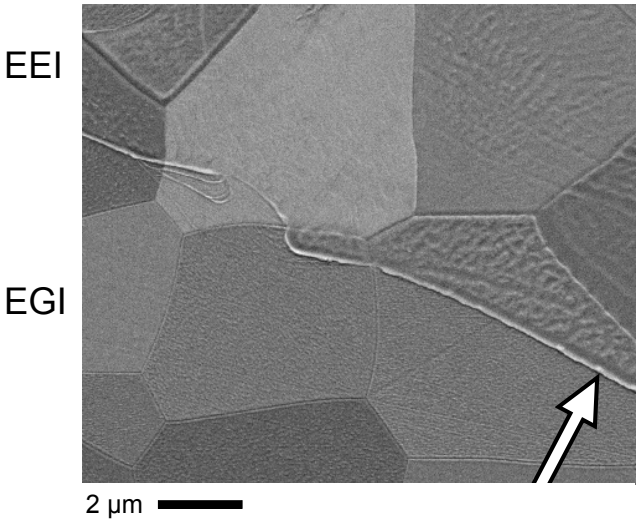

Figure 4.8: Secondary electron SEM image of a *Pure ScYSZ* electrolyte sample. The electrode / electrolyte interface (EEI) with the hill and valley surface microstructure was separated from the electrolyte / gas interface (EGI) by a rim ridge (arrow).

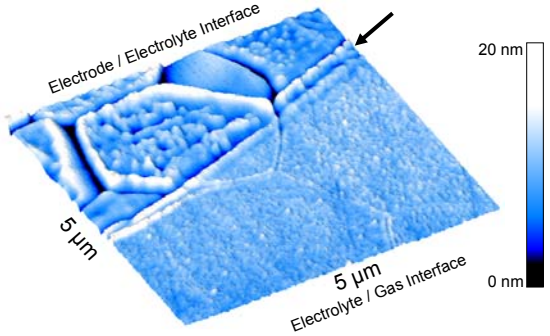

Figure 4.9: Atomic force microscopy image of the rim ridge (5-20 nm tall) surrounding the electrode / electrolyte interface of *Pure ScYSZ*. The electrolyte / gas interface was smooth in comparison to the hill and valley surface microstructure in the electrode / electrolyte interface.

Examination of the Ni electrodes showed that the hill and valley microstructures had been replicated on the electrode surfaces. Outside the contact areas the Ni electrodes had retained the smooth surface created by electropolishing, Figure 4.10.

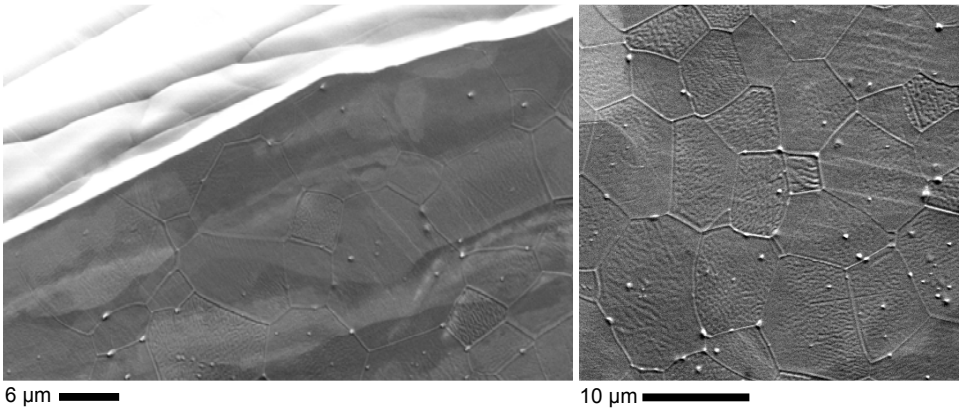

Figure 4.10: Secondary electron SEM images of two different nickel electrodes that were lifted off a *Pure ScYSZ* electrolyte after impedance measurements. The hill and valley surface microstructure found inside the electrode / electrolyte interface on the electrolyte has been moulded into the nickel electrode.

4.2.2 *Impure ScYSZ*

The EEIs of the impure ScYSZ electrolytes were also covered by the hill and valley surface microstructure. Unlike the pure electrolyte, small porosities were observed inside individual grains of *Impure ScYSZ* and not only at triple points, Figure 4.11 and Figure 4.12.

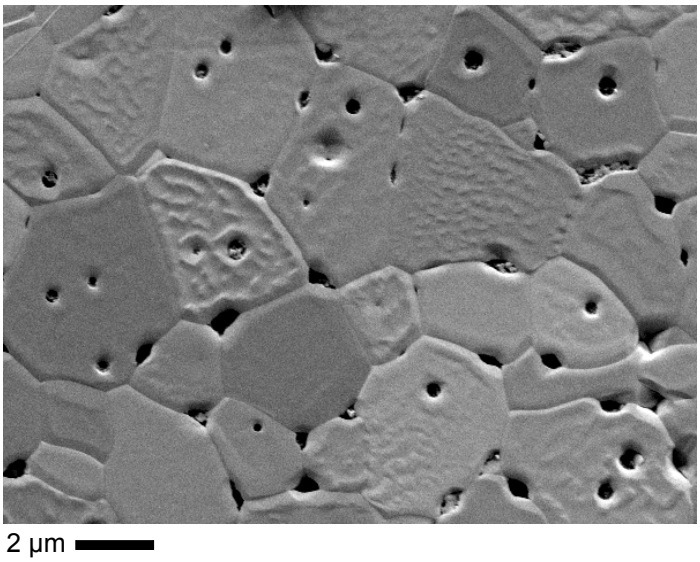

Figure 4.11: Secondary electron SEM image of the hill and valley surface microstructure found on *Impure ScYSZ* electrolytes inside the electrode / electrolyte interface. The surface microstructure varies from grain to grain. Porosities were located inside individual grains.

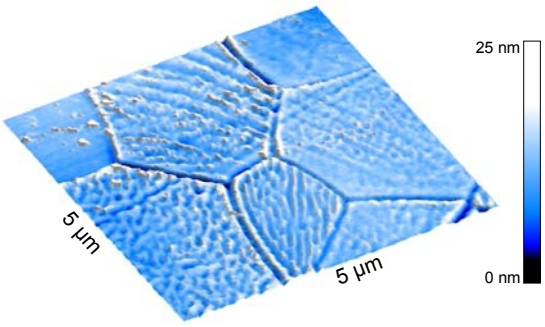

Figure 4.12: Atomic force microscopy image of the hill and valley surface microstructure found on *Impure ScYSZ* electrolytes inside the electrode / electrolyte interface.

A 5–20 nm tall rim ridge was observed around the EEI perimeters on all *Impure ScYSZ* samples, Figure 4.13 and Figure 4.14. The ridges measured on the impure samples did not differ significantly in height from those measured on the pure electrolytes. As on the pure electrolytes the hill and valley microstructure became less distinct towards the outer perimeter of the EEI found on the impure electrolytes.

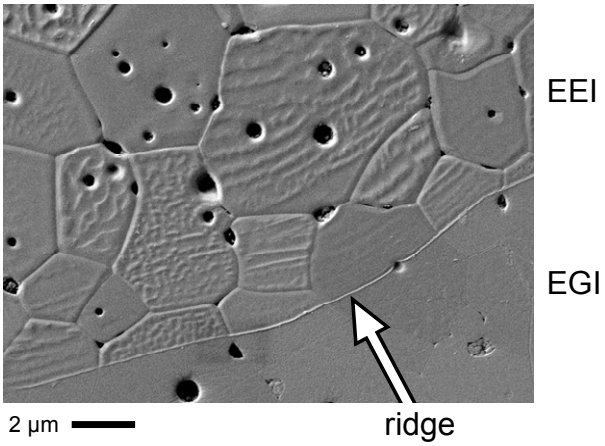

Figure 4.13: Secondary electron SEM image of an *Impure ScYSZ* electrolyte sample. The electrode / electrolyte interface (EEI) with the hill and valley surface microstructure was separated from the electrolyte / gas interface (EGI) by a rim ridge (arrow). Porosities can be found inside individual grains.

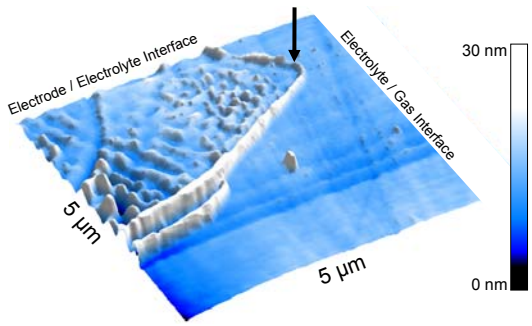

Figure 4.14: Atomic force microscopy image of the rim ridge (5-20 nm tall) surrounding the electrode / electrolyte interface of *Impure ScYSZ*. The electrolyte / gas interface was smooth in comparison to the hill and valley surface microstructure in the electrode / electrolyte interface.

In addition to the hill and valley microstructure one sample of the impure electrolyte also contained large areas of a layer with a porous microstructure. The layer rose approximately 40 nm above the plane of the hill and valley structure. The porous layer had flaked off in some areas exposing a very rough and coarse surface. In the corresponding areas on the nickel electrode, pieces of electrolyte were found attached. The porous structure was separated from the rim ridge by a 5-20 µm wide hill and valley belt referred to here as the *EEI rim zone*. In a few areas the EEI rim zone was not visible and the porous layer directly bordered the electrolyte / gas interface. Figure 4.15 shows the porous layer found on the impure ScYSZ samples.

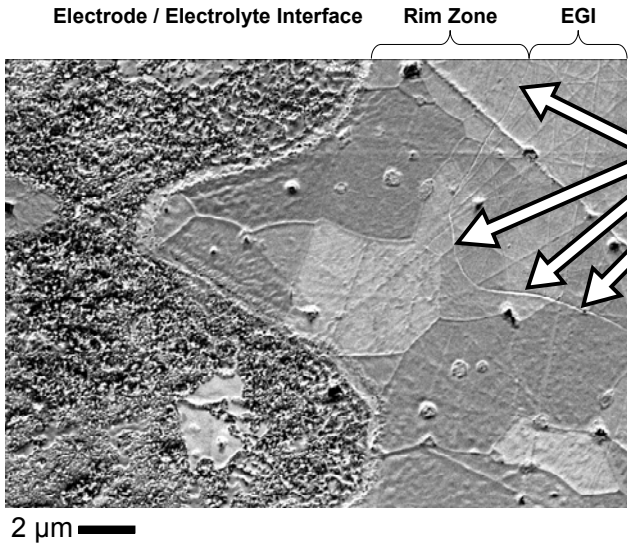

Figure 4.15: On one *Impure ScYSZ* electrolyte a porous microstructure was observed (left). A hill and valley belt (*EEI rim zone*) surrounded the porous microstructure. A 5-20 nm tall rim ridge separated the electrode / electrolyte interface from the electrolyte / gas interface (EGI).

4.3 Chemical characterisation

4.3.1 ToF-SIMS of *Pure ScYSZ*

ToF-SIMS analysis of the surfaces of *Pure ScYSZ* identified the presence of Na, Mg, Al, K, Ca, Mn, Ni, La, Si in addition to Zr, Y and Sc. The lateral distribution of the Si signal was representative of the Na, Mg, Al, K and Ca signals, and thus Si will be used to describe the location of impurity species in the following.

An area of 500 × 500 µm^2 was scanned on a pure electrolyte prior to sputtering. Figure 4.16 shows the lateral distribution of Si signal intensities. The Si signal intensity was strongest in the electrolyte / gas interface. From the spectra shown in Figure 4.16 the Si signal strength was evaluated in lines drawn across the EEI. The Si signal strength from one of these lines is plotted in Figure 4.16. Here it is clearly seen that the Si signal was strongest in the centre of the EEI and faded out towards the perimeter of the EEI. The electrode / electrolyte interface outline of the corresponding electrode, Figure 4.17, matched that of the EEI found on the electrolyte with ToF-SIMS.

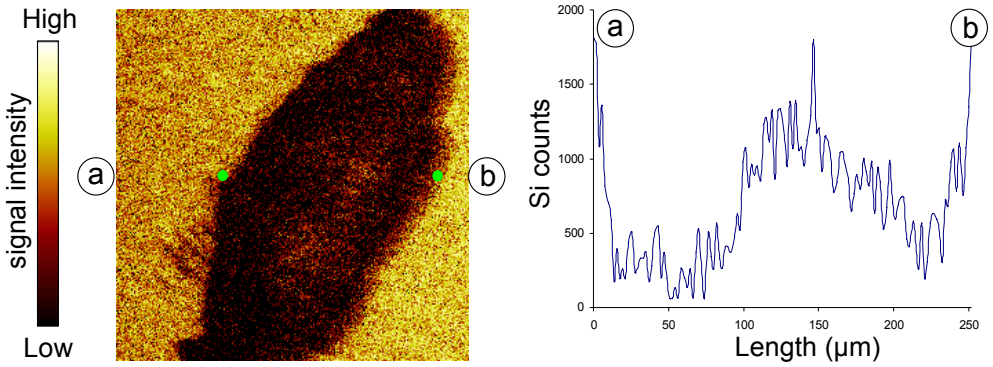

Figure 4.16: 500 × 500 µm^2 area ToF-SIMS logarithmic data representations of the silicon signal on a *Pure ScYSZ* electrolyte. The white colour corresponds to the most intense signal and black corresponds to the weakest signal. Inside the electrode / electrolyte interface (EEI) the Si signal was strongest in the centre, *EEI core*. Surrounding the EEI core was a rim zone with a weaker Si signal.

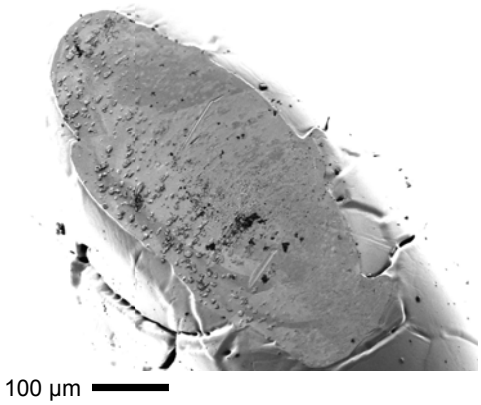

Figure 4.17: SEM image of the nickel electrode after impedance measurements on a *Pure ScYSZ* electrolyte. Nickel had moulded into porosities in the electrolyte creating protrusions upon lifting the electrode off the electrolyte. The electrode / electrolyte interface outline matched that found on the electrolyte using ToF-SIMS.

The area with the strong impurity signal inside the EEI is called the *EEI core* and the surrounding area with the weaker impurity signal is designated as the *EEI rim zone* in the following, Figure 4.18.

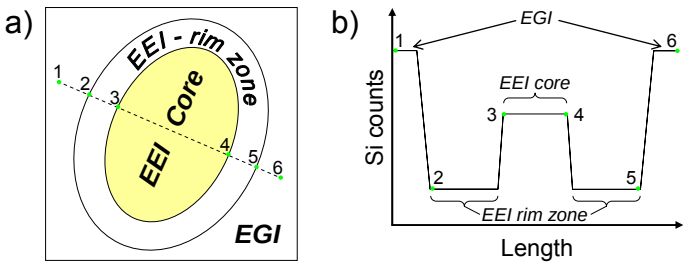

Figure 4.18: Schematic of the electrode contact area and the terms used in this work. Electrode / electrolyte interface rim zone: The area with a weak impurity signal surrounding the EEI core with a strong impurity signal.

The ToF-SIMS data analysis software enabled separate regions of interest of the same scan to be evaluated individually. The EEI core could thus be singled out and

compared with rim zone and the EGI with respect to their signals of Si and other impurity species. As the data was obtained in the same scan a semi-quantitative analysis of the relative impurity concentrations in the EEI and EGI could thus be made. The Si intensity in the whole EEI was 0.09 counts/μm^2 compared to 1.03 counts/μm^2 in the EGI, Table 4.5. When evaluating the Si counts from the EEI core it was found that this area had a stronger Si signal (0.13 counts/μm^2) than the EEI rim zone (0.07 counts/μm^2). The ratio between the Si signal intensity in the EEI and the Si signal intensity from the EGI was a measure of the silicon concentration in the EEI relative to the EGI and was found to be 0.09 on the pure electrolyte, Table 4.5.

Table 4.5: The Si signal intensity from various areas measured on a *Pure ScYSZ* sample.

	Si counts / μm^2 EEI_{Core}	Si counts / μm^2 $EEI_{Rim\ Zone}$	Si counts / μm^2 EEI_{Total}	Si counts / μm^2 EGI	(Si counts / $\mu m^2{}_{EEI}$) / (Si counts/ $\mu m^2{}_{EGI}$)
Pure ScYSZ	0.13	0.07	0.09	1.03	0.09

After the entire EEI had been analysed by ToF-SIMS optimised for high mass resolution, a 50 × 50 μm^2 area at the perimeter of the EEI was selected and analysed with the analysis optimised for high lateral resolution. As the analysed area was at the perimeter of the EEI, the EEI signal represented the EEI rim zone. As the area scan was optimised for high lateral resolution it was possible to distinguish the EEI from the EGI and to correlate the ion image with SEM images of the same area. A SEM image of an area analysed with high lateral resolution with ToF-SIMS is shown in Figure 4.19. From the SEM image it is seen that nickel had crept into some of the pores in the electrolyte. The rim ridge separating the EEI from the EGI is marked by a yellow dotted line.

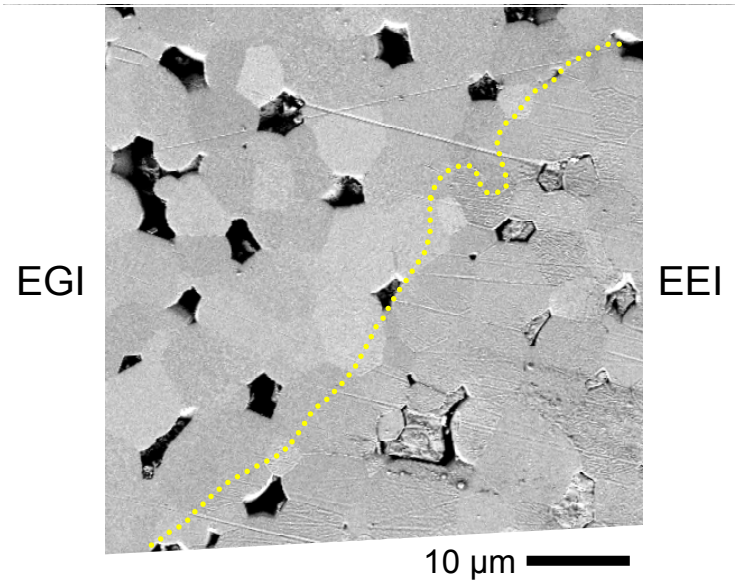

Figure 4.19: SEM image of a *Pure ScYSZ* sample analysed by ToF-SIMS. In the electrode / electrolyte interface (EEI) nickel had crept into pores in the electrolyte. The border between the electrolyte / gas interface (EGI) and the EEI is marked by a line.

After obtaining an image of the 50 × 50 μm^2 area the sample was sputtered by Xe^+ for 4 seconds. Sputtering removed the species located at the surface and by alternating between sputtering and analysing the chemical composition down

through the top surface layers of the electrolyte could be monitored. Organic species will always absorb to the surface once exposed to air, hence 4 seconds of sputtering had the effect of "sharpening" the ToF-SIMS data representations. After the initial 4 seconds of Xe^+ sputtering, the surface was sputtered for at total of 16, 40 and 120 seconds with subsequent analysis. ToF-SIMS data representations of the lateral distribution of the strongest impurity species, Si and Na in addition to the Ni signals are shown in Figure 4.20 as a function of sputter time. The ion signals can be correlated with the SEM images of the same area shown in Figure 4.19.

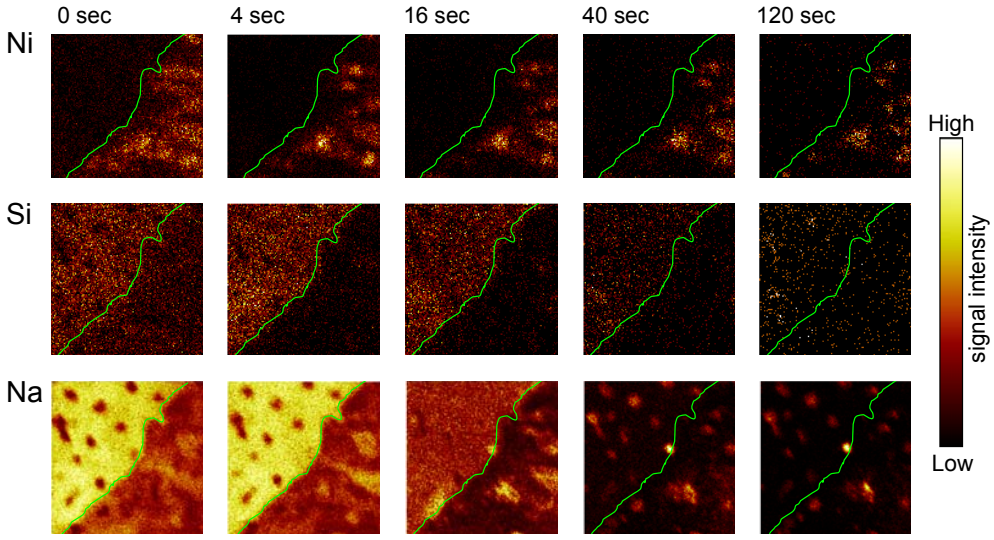

Figure 4.20: *Pure ScYSZ*. ToF-SIMS data representations of the lateral distributions of the Ni, Si and Na signal intensities as a function of Xe^+ sputtering time. The Si and Na signals from the EEI (bottom right) were weaker than those from the EGI (top left).

The signal intensities in the EEI and EGI areas analysed in Figure 4.20 were extracted from the spectra and plotted in Figure 4.21 as a function of sputter time. Figure 4.21 shows that the Si and Na signal intensities decreased in both the EEI and EGI areas as a function of Xe^+ sputter time. However, the Si and Na signals inside the EEI were found to be lower than outside as also seen on the 500 × 500 μm^2 area scan, Figure 4.16 and Table 4.5. The fact that the Si and Na signals in both EEI and EGI rapidly decreased as a function of sputter time showed that the impurities had accumulated in a surface layer.

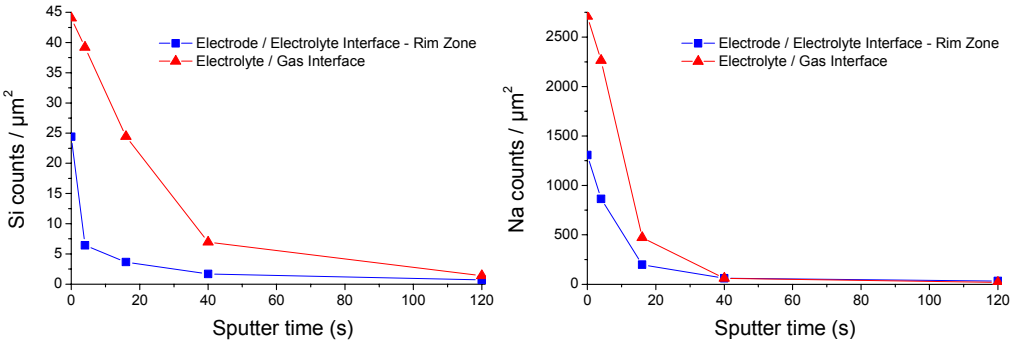

Figure 4.21: The Si and Na signal intensities obtained from a 50 × 50 μm^2 area scan at the electrode / electrolyte perimeter, inside the EEI rim zone (□) and outside, on the EGI (Δ), as a function of Xe^+ sputter time on *Pure ScYSZ*.

ToF-SIMS analysis of the corresponding nickel electrode also shown in Figure 4.17, did not show any concentrations of impurities on the parts of the electrode which had been placed on top of the EEI rim zones, Figure 4.22. It should be noted that the nickel signal was very well defined indicating that the lack of impurities on the electrodes were not due to edge effects.

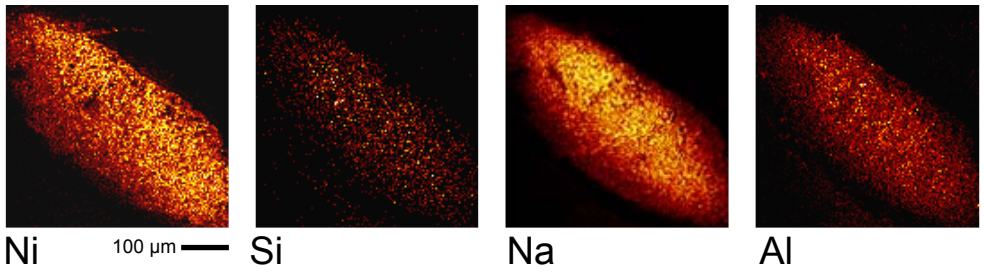

Figure 4.22: ToF-SIMS analysis of the nickel electrode placed on a *Pure ScYSZ* electrolyte did not show any concentrations of impurity species in the areas corresponding to the EEI rim zone on the electrolyte.

4.3.2 ToF-SIMS of *Impure ScYSZ*

ToF-SIMS analysis measured significant amounts of Na, Mg, Al, Si, K, Ca, Ni, Mn, La in addition to Zr, Y and Sc on the surface of the impure electrolytes. As on the pure electrolytes the in-plane distribution of signals from the impurity species Na, Mg, Al, K, Ca and Si overlapped and the location of impurity species are thus described here by the representative Si signal. A 500 × 500 µm^2 area scan of an impure electrolyte, without the porous microstructure, is shown in Figure 4.23. The Si signal from the electrode contact area was slightly distorted, most likely caused by scraping of the electrode upon dissembling the electrode / electrolyte pair. The electrode / electrolyte interface is marked with a line in Figure 4.23. SEM investigation of the area outside the marked line with the weak Si signal did not show any signs of the hill and valley microstructure or ridges. This, as well as the fact that the outline of the scraped area matches that of the electrode, Figure 4.24, signified that the electrode was not situated there at high temperature.

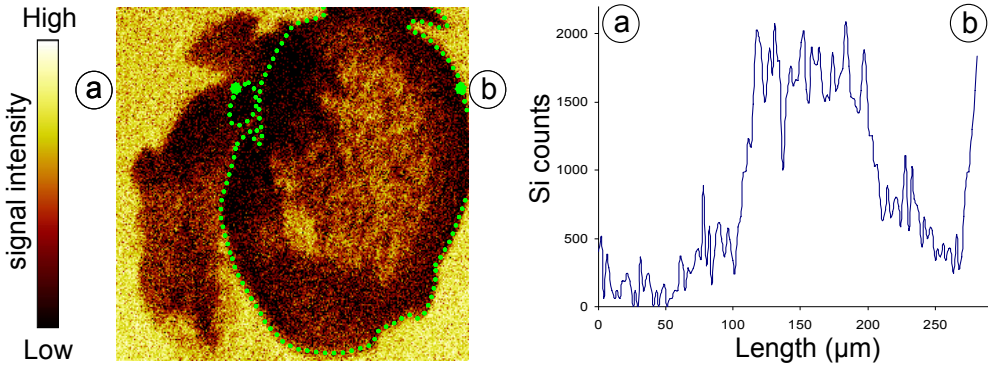

Figure 4.23: 500 × 500 µm^2 area ToF-SIMS logarithmic data representations of the silicon signal on the pure, impure and alumina added electrolytes. The white colour corresponds to the most intense signal and black corresponds to the weakest signal. Inside the electrode / electrolyte interface the Si signal was strongest in the centre, EEI core. Surrounding the EEI core was an EEI rim zone with a weaker Si signal.

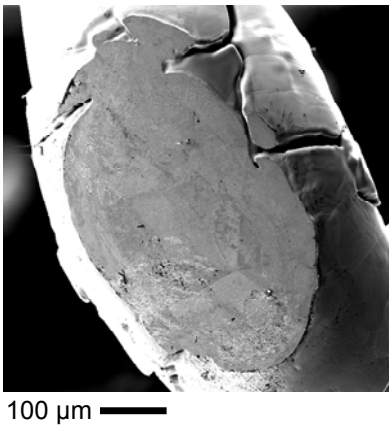

Figure 4.24: SEM image of the nickel electrode after impedance measurements on an *Impure ScYSZ* electrolyte. Nickel had moulded into porosities in the electrolyte creating protrusions upon lifting the electrode off the electrolyte. The electrode / electrolyte interface outline matched that found on the electrolyte using ToF-SIMS.

From the spectra shown in Figure 4.23 the Si signal strength was evaluated in lines drawn across the EEI. The Si signal strength from one of these lines is plotted in Figure 4.23. Here it is clearly seen that the Si signal was strongest in the centre of the EEI and faded out towards the perimeter of the EEI. As with *Pure ScYSZ* the area with the strong impurity signal in the centre of the EEI is designated the *EEI core* and the belt with the much weaker impurity signals surrounding the EEI core is designated the *EEI rim zone*. From the line profiles the Si signals from the EEI core and EEI rim zone were identified and evaluated. A Si signal intensity of 0.40 counts/µm^2 was measured in the EEI compared to 1.77 counts/µm^2 in the EGI, Table 4.6. The Si signal intensity in the EEI core was 0.66 counts/µm^2 compared to 0.22 counts/µm^2 for the EEI rim zone. The ratio between the Si signals of the EEI and the EGI from *Impure ScYSZ* was 2.5 times larger than measured on *Pure ScYSZ*. This indicates that a relatively high impurity level existed inside the EEI of the impure electrolyte compared to that of the pure electrolyte. The 50 × 50 µm^2 area scan shown in Figure 4.25 clearly shows the EEI rim zone and its lack of impurities exemplified by the Si and Na signals.

Table 4.6: The Si signal intensity from various areas measured on a *Impure ScYSZ* sample.

	Si counts / µm^2 EEI_{Core}	Si counts / µm^2 $EEI_{Rim\ Zone}$	Si counts / µm^2 EEI_{Total}	Si counts / µm^2 EGI	$\frac{(Si\ counts / \mu m^2_{EEI})}{(Si\ counts / \mu m^2_{EGI})}$
Impure ScYSZ	0.66	0.22	0.40	1.77	0.22

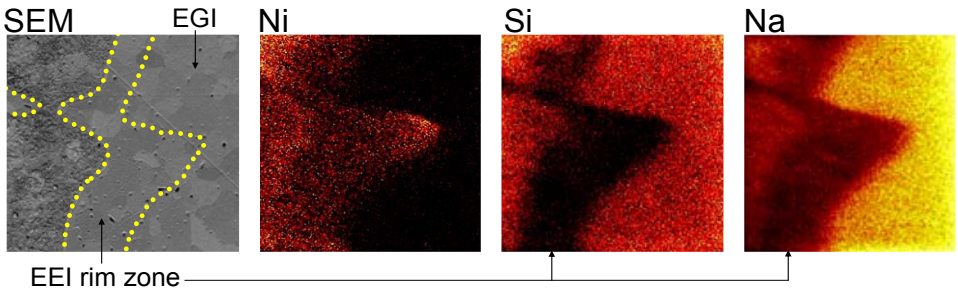

Figure 4.25: SEM image and ToF-SIMS data representations of a 50 × 50 µm^2 area the electrode / electrolyte interface rim zone which is relatively free of impurities. The perimeter ridge separating the EEI and the EGI has been marked with a line.

The electrode shown in Figure 4.24 was analysed by ToF-SIMS. No impurity concentrations were found in the parts of the electrode which corresponded to the EEI rim zone. It could thus be concluded that the weak impurity signal measured from the EEI rim zone was not due to impurities adhering to the electrodes. The nickel signal was very well defined indicating that the lack of impurity signals was not due to edge effects.

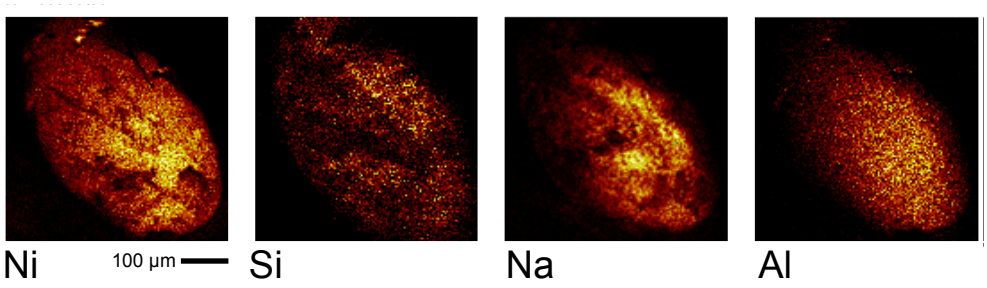

Figure 4.26: ToF-SIMS analysis of the nickel electrode placed on a *Impure ScYSZ* electrolyte did not show any concentrations of impurity species in the areas corresponding to the EEI rim zone on the electrolyte.

A ToF-SIMS analysis of the *Impure ScYSZ* sample with the porous microstructure, shown in Figure 4.15 was also performed. SEM images of the area analysed are shown in Figure 4.27 and at a higher magnification in Figure 4.28. An interesting feature which appeared to be a concentric accumulation of rim ridges was observed, as seen in Figure 4.28. A cavity was found in the corresponding area on the Ni-electrode. As the ridges were concentrated there was a possibility for ToF-SIMS to determine the chemical composition of ridges. A high lateral resolution analysis of the 20×20 µm^2 area was performed with subsequent Xe^+ sputtering. The scan included a section with the porous layer, a hill and valley structured rim zone, and an section of the EGI. It was found that the silicon, sodium and potassium signal from the porous layer in the EEI became stronger relative to the EGI as a function of sputter time, Figure 4.29.

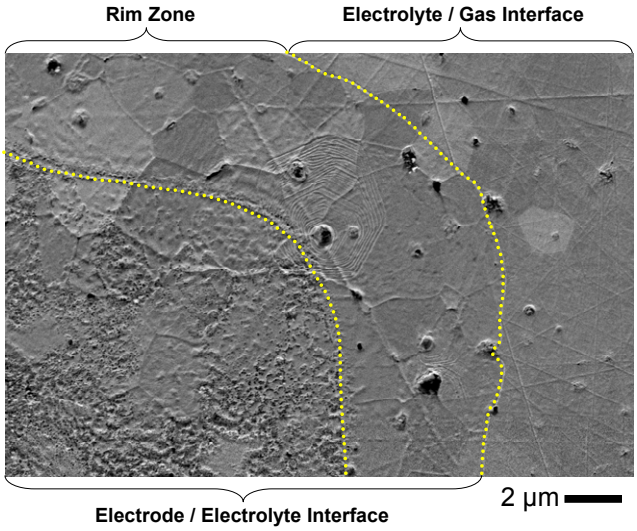

Figure 4.27: SEM image of the *Impure ScYSZ* sample with a porous microstructure. The electrode / electrolyte interface (EEI) consisted of the EEI core and the EEI rim zone. The ridge separating the EEI rim zone and the electrolyte / gas interface is marked by a line. In the centre of the image a concentration of ridges can be seen.

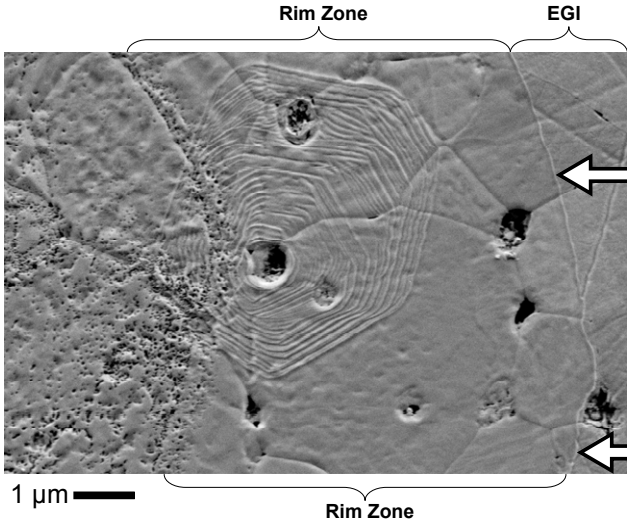

Figure 4.28: Magnification of Figure 4.27. SEM image of the *Impure ScYSZ* sample with the porous microstructure. In the centre of the image a concentration of ridges can be seen.

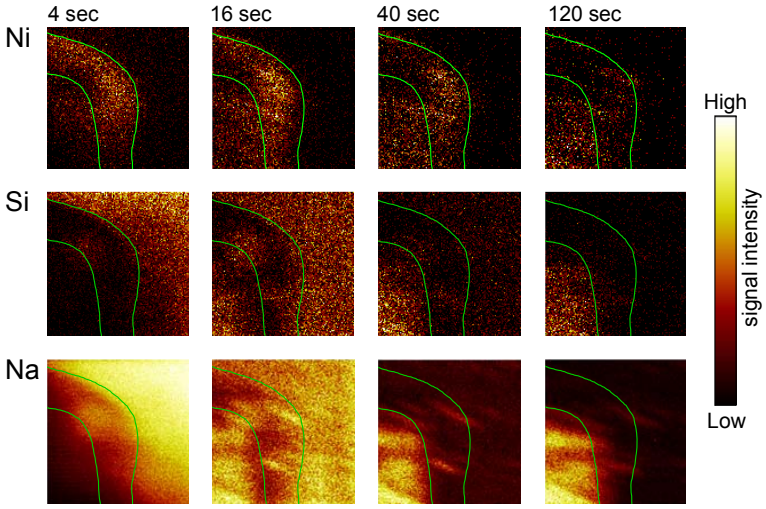

Figure 4.29: 20 × 20 µm^2 area scan of *Impure ScYSZ* with porous microstructure. ToF-SIMS data representations of the lateral distributions of the Ni, Si and Na signal intensities as a function of Xe^+ sputtering time. The Si and Na signals from the EEI (bottom left) were weaker than those from the EGI (top right).

The Ni and Si signals are plotted in the same data representations in Figure 4.30, where it is seen that the Ni signal defined the entire EEI throughout the sputtering process. The Si signal was most intense outside the EEI after 4 seconds of sputtering but after 120 seconds the Si signal was strongest from the porous microstructure of the EEI. The concentration of ridges can also be distinguished and a strong Si signal, relative to the rim zone, was measured after 4 seconds of sputtering. After 120 seconds sputter the Si signal from the ridge concentration had disappeared. SEM investigation after ToF-SIMS showed that the ridge concentration had not been removed by 120 seconds of sputtering and therefore it is difficult to conclude that the ridges were impurity concentrations. It is, however, clear that impurities were found on the surface of the ridge concentration.

The number of detected Si and Na counts within the EEI core, EEI rim zone and EGI were normalized by the respective areas and the results of the semi-quantitative analysis are shown in Figure 4.31. Here it is seen that the Si and Na signals in both the EEI rim zone and EGI decreased rapidly as a function of sputter time signifying that impurities had accumulated in a surface layer.

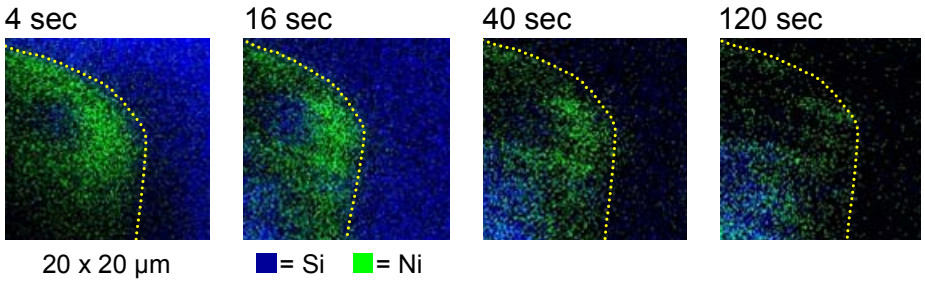

Figure 4.30: ToF-SIMS data representations of a 20 × 20 µm^2 area of *Impure ScYSZ* electrolyte sample with the porous microstructure in the EEI core. The lateral distributions of the Ni and Si are shown together, and represented by the colours green and blue respectively, as a function of Xe^+ sputtering time.

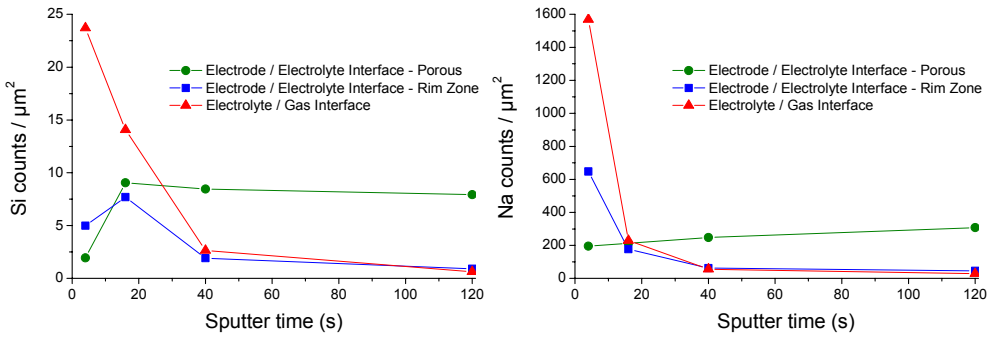

Figure 4.31: The Si and Na signal intensities from a 20 × 20 µm^2 area scan at the electrode / electrolyte interface perimeter including the porous layer (○), the hill and valley rim zone inside the EEI (□) and the EGI (Δ) on *Impure ScYSZ* as a function of Xe^+ sputter time.

4.4 XPS on *Pure ScYSZ* and *Impure ScYSZ*

X-ray photoelectron spectroscopy was performed on four samples each of *Pure ScYSZ* and *Impure ScYSZ* electrolyte. Using a spot size of 400 µm the electrolyte / gas interface was analysed and the chemical species present quantified. A representative spectrum is shown in Figure 4.32, which was obtained from an *Impure ScYSZ* electrolyte sample.

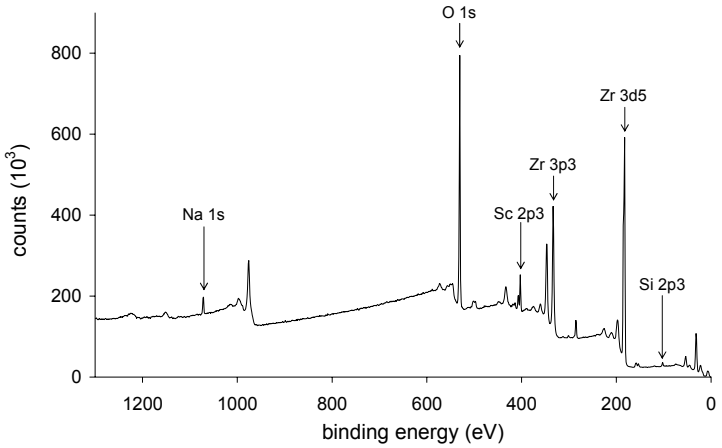

Figure 4.32: Typical XPS spectrum obtained from the electrolyte / gas interface of both electrolytes, here *Impure ScYSZ*.

The results of the element quantification from the electrolyte / gas interfaces are shown in Figure 4.33, where it is seen that there was a significant difference in the measured Na and Si contents between *Impure ScYSZ* and *Pure ScYSZ*.

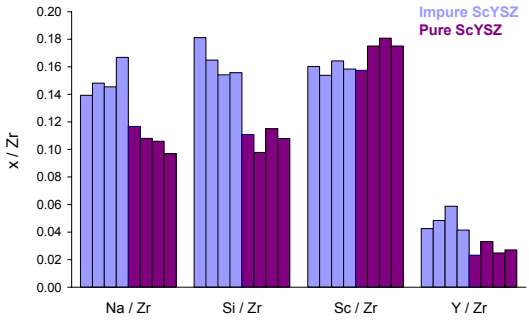

Figure 4.33: Quantitative results of XPS analysis showed a significant difference in the amounts of Na and Si impurities found in the electrolyte / gas interface on *Impure ScYSZ* (blue) and *Pure ScYSZ* (purple) electrolytes.

The Si and Na content in the electrode / electrolyte interface was quantified on both electrolytes using a spot size of 100 µm which fitted inside the electrode contact areas without risking measuring the electrolyte / gas interface. Using a smaller spot size resulted in a weaker total signal thus necessitating a prolonged measurement time. One EEI on a *Pure ScYSZ* electrolyte pellet could not be satisfactorily located hence only three measurements from the pure electrolyte were obtained. Nickel residue was measured inside all EEIs. The quantitative results of the XPS measurements inside the EEI on the pure and impure ScYSZ electrolytes are shown in Figure 4.34. As measured in the EGI there was a significant difference in the Na and Si content between *Pure-* and *Impure ScYSZ*. One *Impure ScYSZ* had an artificially low Si and Na content as large parts of the EEI was covered with Ni residue on this sample, which can also be seen from the XPS Ni signal. This sample was not included when calculating the average values in Table 4.8.

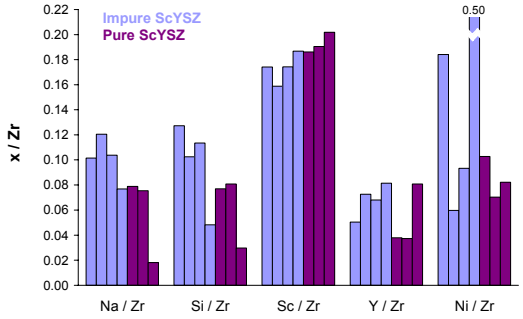

Figure 4.34: Quantitative results of XPS analysis showed a significant difference in the amounts of Na and Si impurities found in the electrode / electrolyte interface on *Impure ScYSZ* (blue) and *Pure ScYSZ* (purple) electrolytes.

4.4.1 Summary chemical characterisation

Table 4.7: Summary of ToF-SIMS results on *Pure ScYSZ* and *Impure ScYSZ*.

	Si counts / μm^2 EEI_{Core}	Si counts / μm^2 $EEI_{Rim\ Zone}$	Si counts / μm^2 EEI_{Total}	Si counts / μm^2 EGI	$\frac{(Si\ counts / \mu m^2_{EEI})}{(Si\ counts / \mu m^2_{EGI})}$
Pure ScYSZ	0.13	0.07	0.09	1.03	0.09
Impure ScYSZ	0.66	0.22	0.40	1.77	0.22

Table 4.8: Average values of XPS results on *Pure ScYSZ* and *Impure ScYSZ* inside and outside the electrode / electrolyte interface.

	Si / Zr EEI	Si / Zr EGI	Na / Zr EEI	Na / Zr EGI
Pure ScYSZ	0.06	0.11	0.06	0.11
Impure ScYSZ	0.11	0.16	0.11	0.15

4.5 Discussion

The ToF-SIMS measurements presented in this chapter documented the existence of an impurity layer on the electrolyte / gas interface on the pure as well as the impure electrolyte. Although this layer need not necessarily have the same thickness and composition on both electrolytes, the layer could be removed by 120 seconds of Xe^+ sputtering on both electrolytes. It was not possible to quantify the thickness of the impurity layer in the EGI, but the relatively short time of sputtering required to remove the layer indicated that the layer thickness is to be measured in the order of monolayers [3]. Subtle differences in the chemical composition of glass phases, such the Na content, will affect the viscosity [4]. Since ToF-SIMS is not a quantitative method the exact chemical compositions of the detected impurity layers of the EGI are not known. However, it is noted that it is mainly the impurities that were present in the original electrolyte powders, Table 4.1, which were found by ToF-SIMS. Thus, it is assumed that the impurities segregated from the interior of the electrolyte to the surface, and no significant amount of the impurities originated from the cell assembly, measurement rig or from the hydrogen gas.

Both electrolytes displayed impurity layers similar in both composition and thickness on the free surfaces, i.e. on the EGIs. Thus, the large differences in electrode polarisation resistance between the electrodes on the pure and the impure electrolytes cannot be explained by a rate determining step of the electrode reaction occurring through the EGI. It seems reasonable to assume that the rim ridges at the TPBs also had similar compositions and a consequence of this assumption is that the TPB is not the main place at which the electrode reaction takes place. This in turn means that the only important reaction path for charge transfer is by diffusion of protons through the Ni to the EEI near the rim ridge and further into the ScYSZ by a mechanism described previously by Mogensen et al. [5][6].

Also, in the EEI the same elements were detected on both the pure and impure electrolytes, so the measured differences in electrode polarisation resistance must be explained in terms of surface concentration rather than chemical composition of impurity species. A relatively weaker Si signal was found in the pure electrolyte EEI compared to the EEI of the impure electrolyte. This supports the hypothesis that impurity species affect the reaction kinetics occurring through the EEI.

In the EEI of both types of electrolytes the Si signal was found to be most intense in the core of the EEI. The Si signal faded out towards the perimeter of the EEI, and a contrast between the EEI core and the rim zone was documented with Figure 4.16 and Figure 4.23 and summarised in Table 4.7. A possible explanation for the differences in electrochemical performance summarised in Table 4.4 is attempted in the following and illustrated schematically in Figure 4.35. At room temperature, when the electrode is set onto the electrolyte the EEI is essentially a point contact between a sphere and a flat surface, although, slight plastic deformation of the Ni will occur, when placing the polished electrode onto the electrolyte due to the mechanical load. Nevertheless, the EEI is only a relative small fraction (ca. 25 % in case of the Ni on *Pure ScYSZ*) of the final area as estimated from the course of the ohmic resistances using the Newman formula, $r = 1/4\sigma R_s$ [7]. This situation is indicated in Figure 4.35a). Figure 4.35b), as the cell is heated to the test temperature of 850 °C over a period of four hours, impurities start to segregate to the electrolyte surface and in particular to the TPB [8]. During heating to 850 °C the Ni begins to creep causing the EEI area to increase. Through the creep process the first formed rim ridge impurity (glassy) phase is caught under the Ni, which is slowly pressed down almost vertically, and in this way the high concentration (particles) of impurities in the EEI core was formed, Figure 4.35c). If the impurity segregation is fast relative to the Ni creep rate then the EEI may be blocked to an extent that R_s increases (or decreases much slower than the actual contact area increases, Figure 4.5, R_s vs. time). Furthermore, the results indicate that the glassy impurities do not tend to segregate to the EEI interface. This means that the interface free energy of the EEI (Ni to ScYSZ) is more negative than the total energy of the Ni to glass and glass to gas interfaces. Thus, when the TPB has scavenged most of the impurities and these were "embedded" under the Ni, Figure 4.35c), the further creep of the Ni will come down on an electrolyte surface with only maybe a monolayer of silica based glass, and as this is on an unstable interface some mobile impurities may migrate to the TPB outside the EEI. In this way a relatively clean EEI rim zone was formed, and outside this zone only a rather modest rim ridge was observed as sketched in Figure 4.35e). The fact that the EEI and TPB of the corresponding Ni electrode surfaces did not show signs of concentrations of glassy impurities of the type found on the electrolyte gives

evidence that especially the interface energy of the Ni-glassy impurity interface is very high here, i.e. a free energy is gained by making interfaces to the gas instead. Thus, it is hypothesised that the EEI at the onset of the impedance measurements corresponds to the EEI core area later measured by ToF-SIMS. The first electrode polarisation resistance measurements yielded relatively large values for both electrolytes. The large R_p values are a result of an impurity concentration at the TPB and inside the EEI, Figure 4.35d). The rapid decrease of R_p is seen as a consequence of the formation of the EEI rim zone, Figure 4.35e). It is interesting to note that the time scale of the initial decrease in R_p was similar for both electrolytes even though the detailed course was not identical. This is likely to be a consequence of the identical force applied to all of the electrodes resulting in equal creep rates. The relative rate of R_p decrease was largest for the Ni on the impure electrolyte. This electrode had a very large initial R_p, so as soon as just a small area of relatively clean EEI rim zone was formed, R_p dropped drastically.

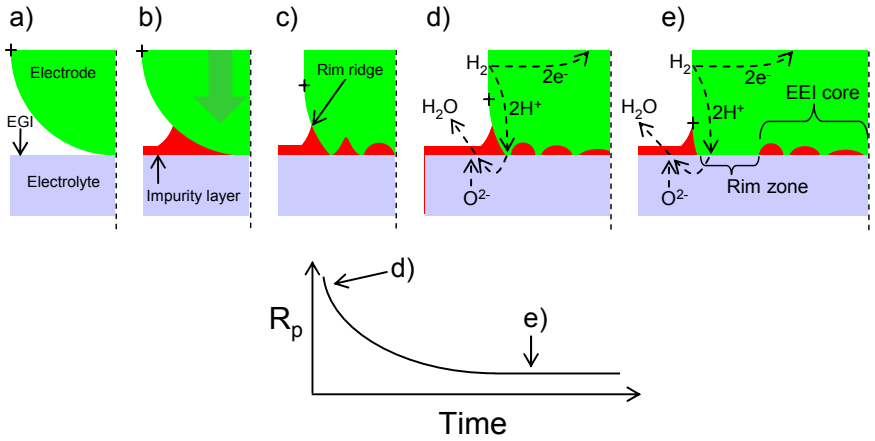

Figure 4.35: The proposed mechanism that created rim zones during electrode / electrolyte interface expansion due to nickel creep. a) The electrode is set on to the electrolyte at room temperature. b) During heating to operation temperature impurities (red) segregate to the surface of the electrolyte. c) While heating, electrode area expansion also occurs but is not able to displace impurities at low temperatures. d) At operation temperature EIS measurements are started. The EEI at the TPB is blocked by impurities resulting in a large electrode polarisation resistance (R_p). e) The electrode area continues to expand and, at the high temperature, impurities are displaced resulting in a decrease in the measured R_p.

The EIS revealed two arcs, i.e. two processes contributing to the limitation of the electrode reaction rate. The fact that the high frequency arc underwent the largest changes indicates that it was related to the expanding electrode and the formed rim zone. A hypothesis is that the high frequency arc, which seemed very dependent on the size of the EEI rim zone, is associated with proton transport across the electrode / electrolyte interface. The low frequency arc is believed to be due to the diffusion of protons through the Ni bulk metal. Proton diffusion is expected to be less dependent, but certainly not independent on the size of the EEI rim zone. The low frequency arc only changes slightly as the proton diffusion through the nickel electrode is not influenced by impurities the EEI surface. However the proton diffusion length could perhaps be influenced by the height of the rim ridge.

The rim ridges observed at the perimeters of the EEI, Figure 4.35e), are expected to consist of accumulated impurity species. In prior work, glassy types of impurities were found on larger ridges using energy dispersive X-ray spectroscopy (EDS) [8].

Appendix C shows similar ridges on *Pure ScYSZ* surfaces when using the same nickel electrode as [8] at 850 °C. Unfortunately, the ridges observed in this work using high purity nickel electrodes were too small to analyse with EDS and ToF-SIMS.

The reason for the occurrence of the layer with the porous microstructure found on one of the impure electrolyte samples cannot be satisfactorily explained at the present moment. As with the other samples it is interesting to note that the Si signal from the porous EEI core was relatively stronger than the Si signal from the rim zone, which surrounded the porous microstructures. The fact that EEI rim zones with hill and valley structures surrounded the porous EEI cores indicated that the porous microstructures were formed at the beginning of the measurement and that the hill and valley structures in the rim zone formed later as the electrode slowly expanded across the electrolytes over time.

The layers with porous microstructures, although rich in impurities, did not appear to have a negative influence on the area specific electrode polarisation resistance as seen from the samples marked with a *p* in Table 3.1. It is speculated that the formation of the porous microstructure greatly increased the three phase boundary length, hence diminishing the role of impurities.

From the continuing decrease in R_s throughout the measurements it was clear that the EEI areas were constantly increasing throughout the measurement while the electrode polarisation resistances stabilised over time. Relative to the EEI area the EEI perimeter length does not increase as quickly when the electrode expands. This may be a further indication that it is the three phase boundary length or rim zone length rather than the EEI area which defines reaction kinetics. This suggests that the width of the active EEI rim zone is relatively narrow compared to the size of the total area of the EEI. Thus, based on the above reasoning it can be argued that the anode reaction in these cells takes place through a rim zone of the Ni / ScYSZ interface at the inner side of the TPB as described in [6] and is therefore not influenced much by the higher impurity levels located in the centre of the EEI.

4.6 Conclusion

Electrochemical impedance spectroscopy showed that the electrode polarisation resistance in a model SOFC anode greatly depends on the amount of impurities found in the electrode / electrolyte interface near the three phase boundary. As impurity layers of similar compositions accumulated in the electrolyte / gas interface on both the pure and impure ScYSZ samples it must be the different levels of impurities found in the vicinity of the TPB inside the electrode / electrolyte interface (the rim zone), which accounts for the differences in electrode polarisation resistances. It seems therefore likely that the rate determining reaction path occurring in a SOFC anode leads across the electrode / electrolyte interface, and that it involves diffusion of protons through the nickel metal.

4.7 References

[1] B.A. Boukamp, Solid State Ionics 18-9 (1986) 136.

[2] K. V. Jensen, R. Wallenberg, I. Chorkendorff, M. Mogensen, Solid State Ionics 160 (2003) 27.

[3] K. V. Hansen, K. Norrman, M. Mogensen, Surf. Interface Anal. 38 (2006) 911.

[4] S. L. Webb, M. Banaszak, U. Köhler, S. Rausch, G. Raschke**,** European Journal of Mineralogy v. 19; no. 5; (2007) 681.

[5] M. Mogensen, S. Sunde and S. Primdahl, in: High temperature electrochemistry: ceramics and metals. 17. Risø international symposium on materials science. Poulsen, F.W., Bonanos, N., Linderoth, S., Mogensen, M., Zachau-Christiansen, B. (eds.), (Risø National Laboratory, Roskilde, 1996) p. 77-100.

[6] M. Mogensen, J. Høgh, K. V. Hansen, T. Jacobsen, ECS Transactions 7 (1) (2007) 1329.

[7] J. Newman, J. Electrochem Soc., 113 (1966) 501.

[8] K. V. Jensen, S. Primdahl, M. Mogensen, in: Mass and charge transport in inorganic materials: fundamentals to devices, P. Vincenzini, V. Buscagli (eds), Techna, Faenza. (2000) 1443.

5 Flattened Electrodes

In chapter 4 one of the conclusions drawn was that the nickel electrode could displace impurities that had segregated to the electrolyte interface, as the electrode expanded due to metallic creep. The expanding electrode created a rim zone where the impurity signal was weak in comparison with the core of the electrode / electrolyte interface as well as the electrolyte / gas interface. The drastic fall in electrode polarisation resistances measured on both *Pure-* and *Impure ScYSZ* electrolytes is believed to be a consequence of the electrode / electrolyte interface adjacent to the three phase boundary gradually being cleared of impurities. In order to test this hypothesis an experiment was performed in which the electrodes were flattened prior to heating and electrochemical testing. As the electrodes already were deformed little or no electrode creep was expected to occur at 850 °C with no subsequent decrease in the measured electrode polarisation resistances.

5.1 Sample preparation

Five *Impure ScYSZ* electrolyte pellets were polished and four high purity nickel wires were annealed and electropolished as described in chapter 2. *Impure ScYSZ* was selected as the impurity signal contrasts observed with ToF-SIMS between the EEI core and EEI rim zone were sharpest on the impure electrolytes. After electropolishing, the nickel electrodes were examined with SEM to ensure that a smooth surface had been obtained and thereafter mounted in two-bore alumina tubes.

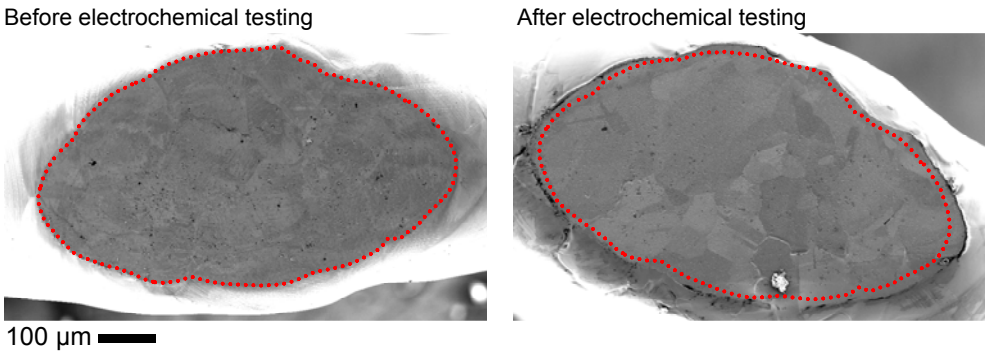

Figure 5.1: SEM images of a nickel electrode before and after electrochemical testing. The outline of the electrode before electrochemical testing is overlain the image of the electrode after electrochemical testing. The scale bar represents both images. It can be seen that the area has only increased slightly (0.3 %).

Using a pile driver technique a 315 g copper weight was lifted and released onto the alumina tube flattening the underlying electrode against one of the polished electrolyte pellets. Three electrodes tips were flattened and examined with SEM to quantify the flattened area. The three flattened electrodes and a reference electrode were then set onto the remaining four electrolyte pellets in the measurement rig. After electrochemical characterisation the nickel electrodes were examined again with SEM in order to measure the electrode / electrolyte interface area.

5.2 EIS using flattened electrodes

After the measurement rig had reached a stable temperature of 850 °C electrochemical impedance spectroscopy was performed in a 97.6 % H_2 / 2.4 % H_2O atmosphere. Impedance spectra recorded at the beginning of the measurement and after 50 hours using the reference electrode and a flattened electrode are shown in Figure 5.2 and Figure 5.3 respectively. As also described in chapter 4, the electrode polarisation resistance of the non-flattened reference electrode experienced a large drop during the first 50 hours at 850 °C. The electrode polarisation resistances measured on the flattened electrodes did not exhibit this behaviour. Figure 5.4 shows that the electrode polarisation resistances of the flattened electrodes were stable through the first ~100 hours of the measurement. Slight decreases in electrode polarisation resistances (~30 kΩ) were measured for the flattened electrodes over the length of the measurement. After 325 hours at 850 °C the electrode polarisation resistances measured on all four cells had stabilised and it was also seen that these stable values were approximately the same.

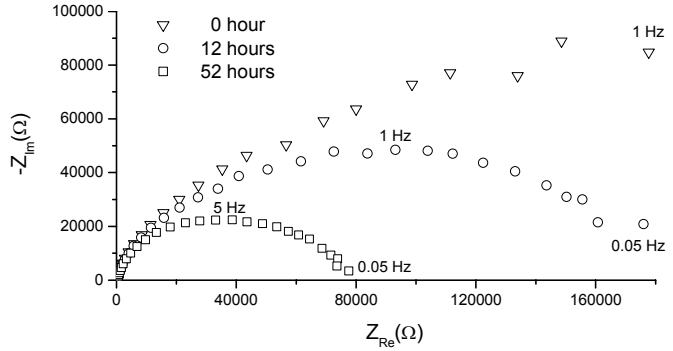

Figure 5.2: Impedance spectra recorded using the non-flattened reference electrode. A rapid decrease in electrode polarisation resistance was observed during the first 52 hours of measurements.

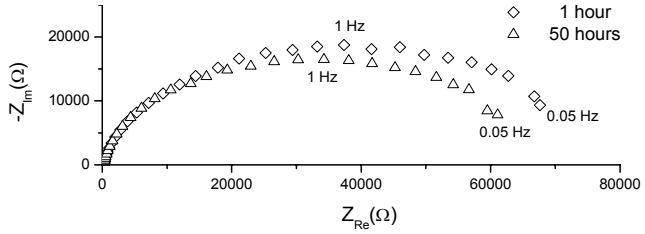

Figure 5.3: Impedance spectra recorded using a flattened electrode. Only a small decrease in electrode polarisation resistance was observed during the first 50 hours of measurements.

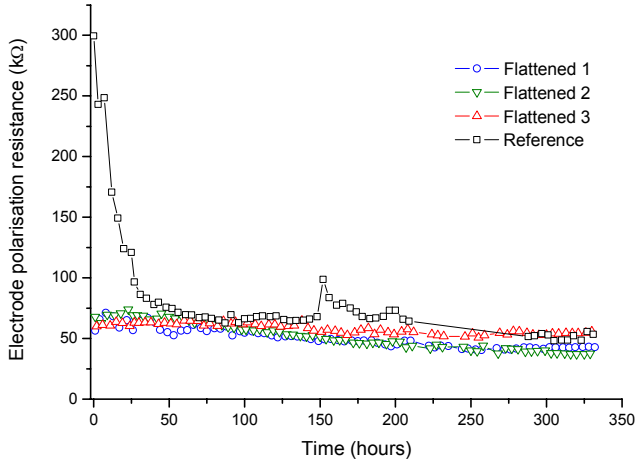

Figure 5.4: The electrode polarisation resistances measured on three flattened electrodes and one non-flattened reference electrode as a function of time at 850 °C.

As also seen in chapter 4, the series resistance of the non-flattened reference electrode showed a lag period of ~40 hours, where the series resistances did not decrease. After this lag period the series resistance decreased throughout the measurement. On the cells with flattened electrodes the series resistance increased during the first hours of measurements. As also measured using the reference electrode, a lag period of ~40 hours was measured after which the series resistances decreased steadily throughout the course of the measurements.

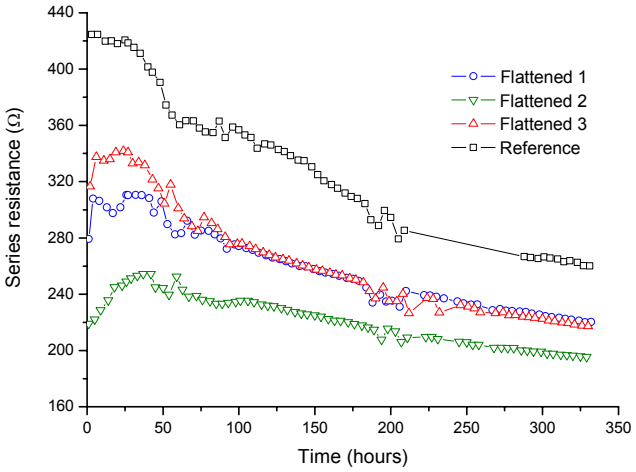

Figure 5.5: The series resistances measured on three flattened Ni electrodes and one non-flattened reference electrode as a function of time at 850 °C.

The results of the electrochemical characterisation are summarised in Table 5.1. When only considering the flattened electrodes there was a relatively small scatter, (17 %), in the area specific electrode polarisation resistances, (ASR_p). The average ASR_p of 100 Ωcm^2 was virtually the same as that measured on the non-flattened electrodes in chapter 4, 104 Ωcm^2. The length specific electrode polarisation resistances (LSR_p) were also in agreement with that measured in chapter 4, 13.5 kΩcm. It should also be noted that the calculated ion conductivities measured using flattened electrodes had a very low scatter (3 %) and were in very good agreement with the values obtained using non-flattened electrodes (45 $mScm^{-1}$). The final area

of the electrode / electrolyte interface was not always larger than the initial flattened area as is illustrated in section 5.3.

Table 5.1: Summary of the electrochemical characterisations at 850 °C of three flattened electrodes and one non-flattened reference electrode on *Impure ScYSZ*.

	Area *flattened* (μm^2)	Area *final* (μm^2)	Length *final* (μm)	R_p *start* ($k\Omega$)	R_p *final* ($k\Omega$)	ASR_p (Ωcm^2)	LSR_p ($k\Omega cm$)	σ ($mScm^{-1}$)
Flattened 1	210296	210951	2436	56.5	42.8	90	10.4	44
Flattened 2	299749	238592	3853	67.9	37.4	89	14.4	46
Flattened 3	220841	214690	3191	60.1	55.8	120	17.8	44
Reference	-	139810	1999	299.6	53.4	75	10.7	46
				Average *Flattened*		**100**	**14.2**	**45**
				Standard deviation *Flattened*		17	3.7	1
				%		17	26	3

5.3 Microstructure

Scanning electron microscopy inspection was performed on the electrode / electrolyte interfaces of the electrolytes and electrodes. SEM images of the electrodes before and after impedance measurements from cell *Flattened 1* are shown in Figure 5.1. In this case the electrode made contact with the electrolyte across the whole flattened electrode surface and expanded slightly with time. The electrode in the *Flattened 2* cell did not make contact with the electrolyte all over the flattened surface as is attempted shown in Figure 5.6. However, the contact area was to a large degree defined by the flattening before electrochemical testing and the electrode had crept across the initial perimeter as was seen at the left most edge of the electrode after testing in Figure 5.6.

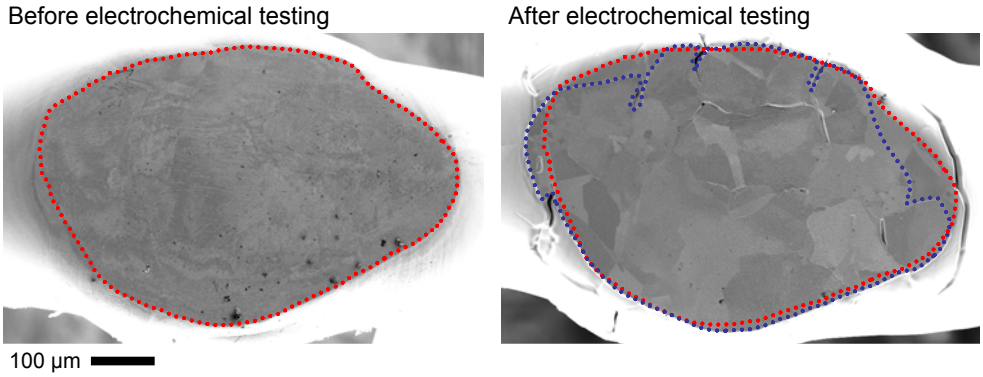

Figure 5.6: SEM images of the electrode from *Flattened 3* before and after electrochemical testing. The outline of the electrode before electrochemical testing is overlain the image of the electrode after electrochemical testing (red). The actual contact area is marked with a blue line. It can be seen that most of the flattened area was in contact with the electrolyte. The scale bar represents both images.

On all four electrolytes the hill and valley surface microstructure was observed in the EEI. A rim ridge at the perimeter of the EEI was also found on all four electrolytes. Hence the microstructures observed on the electrolyte surfaces were identical to those previously described in chapter 4.

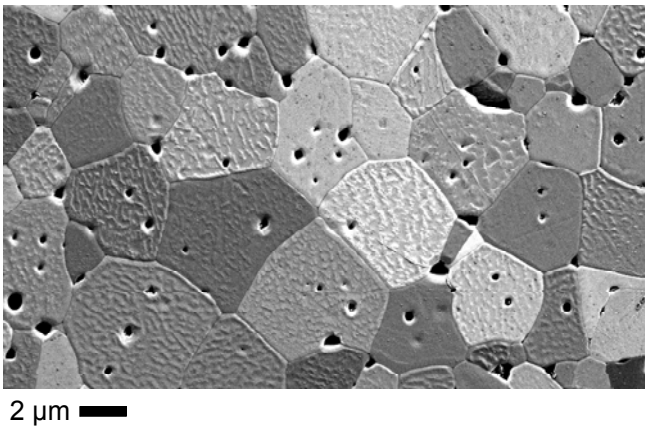

Figure 5.7: SEM image of the electrode / electrolyte interface on an *Impure ScYSZ* electrolyte where a flattened electrode had been placed. The electrolyte surface had the distinct hill and valley surface microstructure.

5.4 Chemical analysis

A ToF-SIMS scan optimised for high lateral resolution was performed on the EEI on the electrolyte of cell *Flattened 1*. The signals from impurity species K and Al as well as Ni are shown in Figure 5.8. The nickel signal was complimentary to the K and Al signals. The weak K and Al signals in the EEI relative to the EGI can be seen as an indication that the once the electrode made contact with the electrolyte during heating, impurity segregation to the electrolyte surface became energetically unfavourable.

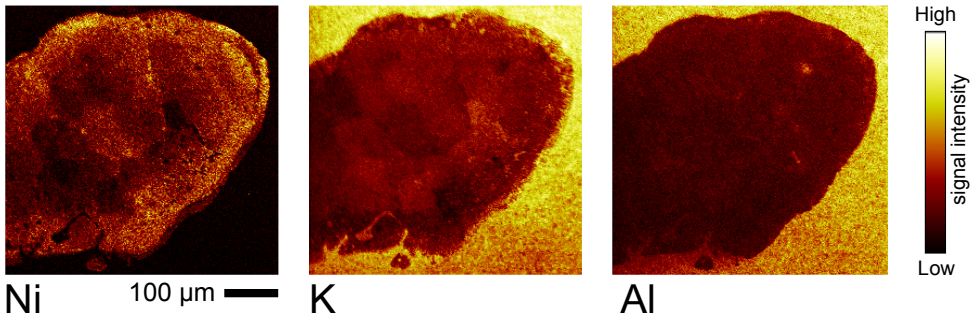

Figure 5.8: ToF-SIMS data representations showing the lateral distribution of Ni, K and Al across a 500 × 500 µm^2 area of the electrolyte which was tested with a flattened electrode.

5.5 Discussion

The behaviour of the electrode polarisation resistances measured using the flattened electrodes were remarkably different than previously observed in the measurements presented in chapter 3 and 4. A possible explanation for the fact that R_p remained stable during the first 100 hours of the measurements when using flattened electrodes is given in the following and illustrated by Figure 5.9. At room temperature the flattened electrodes are placed on a polished electrolyte surface, which is thus free of any significant impurities concentrations. The electrodes are by no means in contact with the electrolyte on the nano scale, but during heating of

the cells the electrodes set onto the electrolytes and form a gas tight bond. It is believed that the electrode is softened and sets onto the electrolyte at a relatively low temperature, i.e. before impurity segregation to the electrolyte surface begins as is indicated by ToF-SIMS. During heating to 850 °C impurities segregate to the electrolyte / gas interface to form an impurity layer. Impurity segregation to the solid / solid, electrode / electrolyte interface is energetically unfavourable and therefore the perimeter of the electrode / electrolyte interface near the three phase boundary is relatively free of impurities as impedance measurements are commenced. This in turn accounts for the low electrode polarisation resistances measured using the flattened electrodes at the start of the measurements.

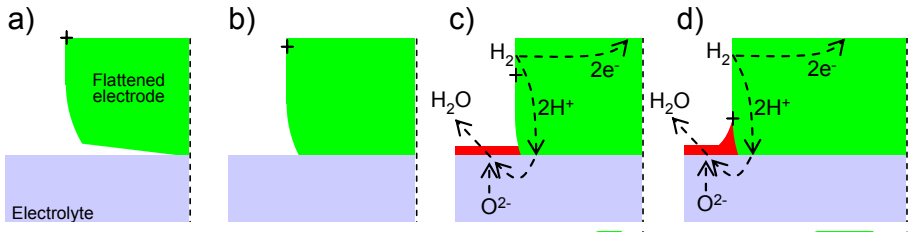

Figure 5.9: Schematic of a flattened electrode placed on an electrolyte. a) At room temperature the flattened electrode is placed on the electrolyte. Although pressed onto the electrolyte by a copper weight the flattened electrode surface is not perfectly matched (on the nano scale) with the electrolyte. b) At low temperatures the flattened electrode surface deforms to match the electrolyte surface. c) At higher temperatures, during heating and at 850 °C, impurities (red) segregate to the electrolyte / gas interface. A low polarisation resistance is measured as the EEI near the three phase boundary has a relatively low impurity concentration. d) The electrode creeps slightly during the remainder of the experiment causing the electrode polarisation resistance to decrease as impurities are displaced from the inner perimeter of the electrode at the three phase boundary. The expanding electrode causes a ridge to form at the three phase boundary.

From the measured series resistances and SEM investigations it was seen that the electrode / electrolyte interface area did increase, albeit only relatively little, during the course of the measurements. The slight decrease in electrode polarisation resistances are attributed to the expanding electrode / electrolyte interface areas and the subsequent displacement of impurities from the created rim zones. It is interesting to note that the final ASR_p, LSR_p values were by in large unaffected by flattening the electrodes.

5.6 Conclusion

The findings described in this chapter confirm the conclusions drawn in chapter 4. Impedance measurements using nickel electrodes flattened before being set onto *Impure ScYSZ* electrolyte samples showed that the electrode polarisation resistance did not decrease rapidly as it has been observed when measuring with non-flattened electrodes. The flattened electrodes did expand slightly during the measurement creating an impurity poor rim zone causing a decrease in electrode polarisation resistance.

6 Effects of Alumina doping

This chapter presents the results of the investigation of the effects of doping a ScYSZ electrolyte with alumina. The *Impure ScYSZ* electrolyte, which was analysed in chapter 4 and 5, was doped with alumina. Using a three-electrode setup the electrode polarisation resistances and series resistances were measured using impedance spectroscopy at 850 °C. Scanning electron microscopy (SEM), atomic force microscopy (AFM) and time-of-flight secondary ion mass spectrometry (ToF-SIMS) were used to characterise the surface of the alumina doped electrolyte and these results are related to the electrochemical performance. Some of the results in this chapter have been published in Solid State Ionics, appendix G.

6.1 Alumina addition to *Impure ScYSZ*

Adding alumina to stabilised zirconia used as solid oxide fuel cell electrolytes has been known to have several advantages. Alumina has been known to, act as a sintering aid [1], improve the mechanical strength of the electrolyte [2], lower the electrolyte's thermal expansion coefficient [3] and be able to act as a silica scavenger [4][5]. Alumina addition to zirconia has also been shown to have a positive effect on oxide ion conductivity across grain boundaries [4] and through the bulk [6]. However negative effects on ion conductivity through grain boundaries and the bulk as a consequence of alumina addition to the electrolyte have also been documented [7][8].

The decrease in bulk conductivity is a consequence of the mismatch in ionic radius between aluminium (with a coordination number of 6, r_{Al}^{3+} = 0.54 Å) and zirconium (with a coordination number of 8, r_{Zr}^{4+} = 0.84 Å) [9]. This causes stresses in the crystal lattice, locking vacancies thus reducing ion mobility through the bulk. The difference in ionic radii is also the reason for the low solubility of alumina in stabilised zirconia (0.1 mol % when sintered at 1300 °C) [10]. The positive effects of alumina addition are to be found at the zirconia grain boundaries. Alumina has been ascribed to scavenge impurities into crystalline particles reducing the amount of grain boundary glass phase. Changes in the chemical composition of the grain boundary glass phase and a subsequent reduction in the wetting ability of the glass phase on the grain boundary have also been attributed to alumina addition. Thus the total effect of alumina addition on the total ion conductivity through an electrolyte is sum of the combined effects of bulk and grain boundary effects.

The optimal amount of alumina to be added to the electrolyte depends on the impurity content. The decreases in ion conductivity reported in literature could thus be the result of too much alumina having been added with respect to the impurity

content of the sampled electrolyte. Excess amounts of alumina will accumulate in grain boundaries and act as a non-conducting impurity in itself. Adding too little alumina has the obvious disadvantage of not achieving the full potential increase in ion conductivity. A study performed at *Risø-DTU* has shown that an aluminium content of 2% of the metal cations in *Impure ScYSZ* is optimal [10] with respect to increasing ion conductivity. Thus AlO(OH) powder (Catapal®, *Sasol*) corresponding to a metallic cation content of 2% aluminium was added to *Impure ScYSZ* powder (called *Al-ScYSZ* in the following) and prepared into pellet samples as described in chapter 2. Using the three-electrode configuration described in chapter 2 the influence of alumina at the electrode / electrolyte interface was evaluated at 850 °C in a 97.6 % H_2 / 2.4 % H_2O atmosphere for up to 484 hours.

6.2 Electrochemical characterisation of *Al-ScYSZ*

Eight cells consisting of *Al-ScYSZ* pellets and high purity nickel electrodes were characterised using electrochemical impedance spectroscopy as described in chapter 2. Representative impedance spectra obtained during the course of measurements on one cell are shown in Figure 6.1. It is seen that the electrode polarisation resistance decreased rapidly during the first 108 hours of measurements.

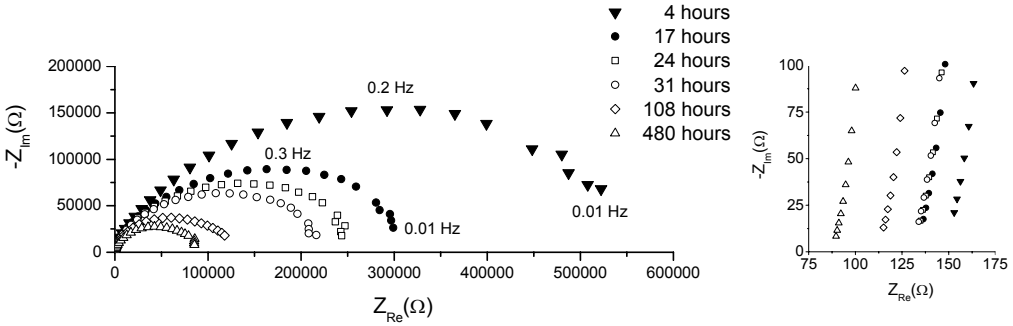

Figure 6.1: Impedance spectra recorded after 4, 17, 24, 31, 108 and 480 hours at 850 °C on a representative *Al-ScYSZ* cell. Large decreases in R_p were measured during the first 108 hours at 850 °C. The series resistances also decreased as a function of time.

The electrode polarisation resistances, measured on the same sample as shown in Figure 6.1, are plotted as a function of time in Figure 6.2. Here it is seen that R_p stabilised after ~200 hours. This trend was observed on all the tested cells using *Al-ScYSZ* electrolytes. A rapid decrease in electrode polarisation resistance followed by a stabilisation was also measured when using *Pure ScYSZ* and *Impure ScYSZ* electrolytes, as presented in chapter 4 and *YSZ* presented in chapter 3.

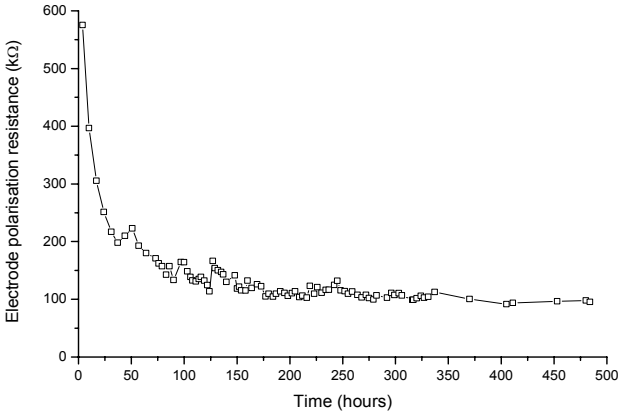

Figure 6.2: Plot of the electrode polarisation resistance as a function of time at 850 °C using *Al-ScYSZ* electrolyte. After an initial rapid decrease, R_p levelled out for the remainder of the experiment.

The series resistances measured on a cell using an *Al-ScYSZ* electrolyte is shown in Figure 6.3. Results for the same cell are also shown in Figure 6.1 and Figure 6.2. The series resistances decreased rapidly at the beginning of the measurements but the rate of decrease slowed significantly as the measurement progressed. As was stated in chapter 3 the decrease in series resistance was a consequence of an increase in electrode / electrolyte interface area caused by metallic creep of the nickel electrode.

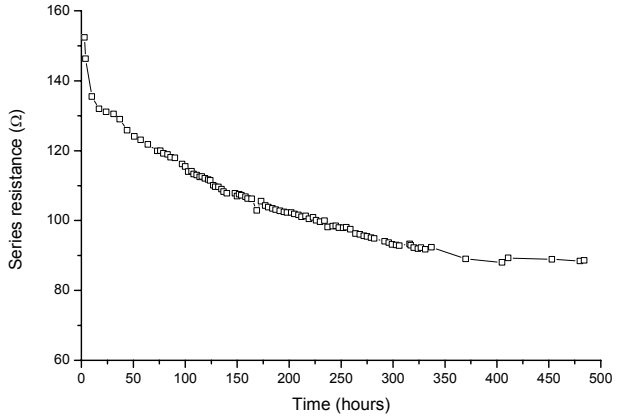

Figure 6.3: Plot of the series resistance during the course of impedance measurements of a cell with *Al-ScYSZ* electrolyte at 850 °C.

After electrochemical characterisation, the cells were dismantled and the electrode / electrolyte interface measured using SEM. The measured contact areas were used together with the last R_p measurements to calculate the area- and length specific electrode polarisation resistances. The results of the electrochemical characterisation of *Al-ScYSZ* are summarised in Table 6.1. There was a relatively large spread in ASR_p and LSR_p values. Most notably are the low values measured on sample 2 and to some extent sample 4. As will be shown in the next section, sample 2 and 4 displayed different microstructural features which could explain the deviant values. When excluding samples 2 and 4 the average ASR_p and LSR_p values increased to 134 ± 15 Ωcm^2 and 18.3 ± 2.2 kΩcm respectively. The measured contact area and the final R_s measurements were used to calculate the ion conductivity through the electrolyte, σ. An average ion conductivity value of 120

$mScm^{-1} \pm 6$ was calculated which was significantly larger than *Impure ScYSZ* with $45\ mScm^{-1} \pm 4$.

Table 6.1: Results of the electrochemical characterisation of the *Al-ScYSZ* electrolyte.

	Area (μm^2)	Length (μm)	R_s *start* (Ω)	R_s *final* (Ω)	R_p *start* ($k\Omega$)	R_p *final* ($k\Omega$)	ASR_p (Ωcm^2)	LSR_p ($k\Omega cm$)	σ ($mScm^{-1}$)
1	170243	1642	131	88	351	73.7	125	17.4	122
2*p*	123165	1750	164	114	475	34.4	42	5.8	111
3	150365	1233	154	97	521	94.8	143	17.2	118
4*p*	138926	1959	169	103	496	70.4	98	11.9	115
5	110593	1677	163	104	552	104.2	115	15.5	128
6	124588	1520	154	106	431	112.6	140	21.3	119
7	123934	1778	151	101	519	99.7	124	18.2	125
8	164265	1520	152	89	575	95.4	157	20.4	123
					Average		**118**	**16.0**	**120**
					Standard deviation		35	5.0	6
					%		30	31	5

6.3 Microstructure of *Al-ScYSZ*

The electrode / electrolyte interface was investigated by SEM and on six of the *Al-ScYSZ* electrolyte samples the observed microstructures were identical to those also observed on *Impure ScYSZ* and *Pure ScYSZ* and described in chapter 4. The electrode / electrolyte interface surface had the distinct hill and valley surface microstructure, Figure 6.4. Furthermore, the border between the electrode / electrolyte interface and the electrolyte / gas interface was marked by a 5-20 nm tall rim ridge, Figure 6.5. *Al-ScYSZ* sintered more densely than *Impure ScYSZ* as was expected. However, porosities could still be seen inside individual grains and at grain triple points.

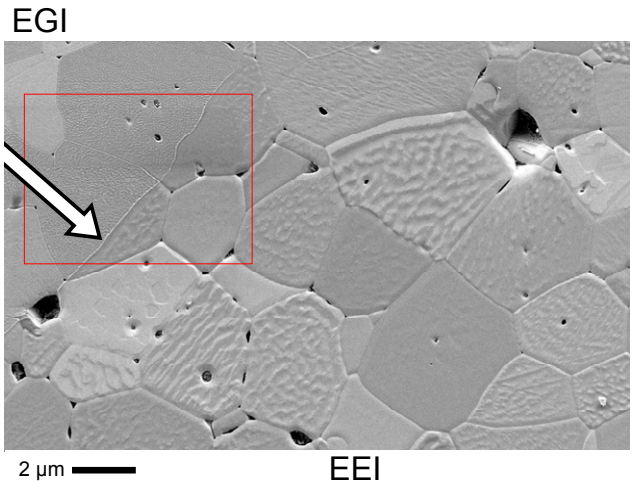

Figure 6.4: SEM image at the perimeter of the electrode / electrolyte interface (EEI) on an *Al-ScYSZ* electrolyte sample. The EEI had the distinct hill and valley surface microstructure. At the border between the EEI and the electrolyte / gas interface (EGI) a 5-20 nm tall rim ridge was observed (arrow). The red square is magnified in Figure 6.5.

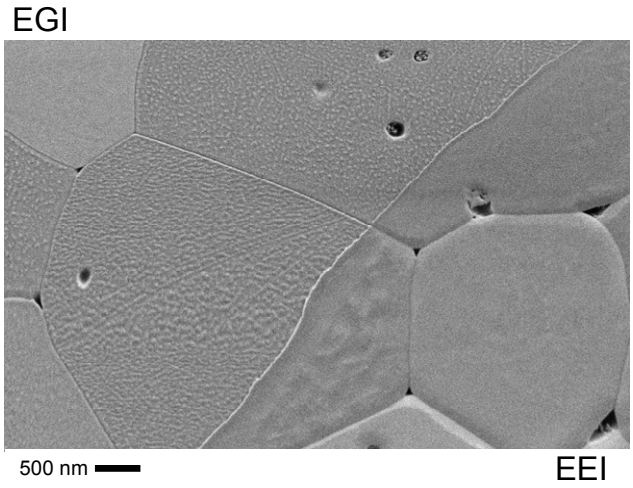

Figure 6.5: SEM image of the perimeter of the electrode / electrolyte interface (EEI). The surface of the electrolyte / gas interface (EGI) had a rough surface microstructure as is seen at large magnifications. The rim ridge is clearly seen.

Alumina rich phases were found on the surface of all eight *Al-ScYSZ* electrolytes and identified using energy dispersive X-ray spectrometry. These phases had a different secondary electron coefficient than the surrounding ScYSZ and could thus therefore easily be identified using the secondary electron signal. Examples of these alumina rich phases on the electrolyte surface are shown in Figure 6.6.

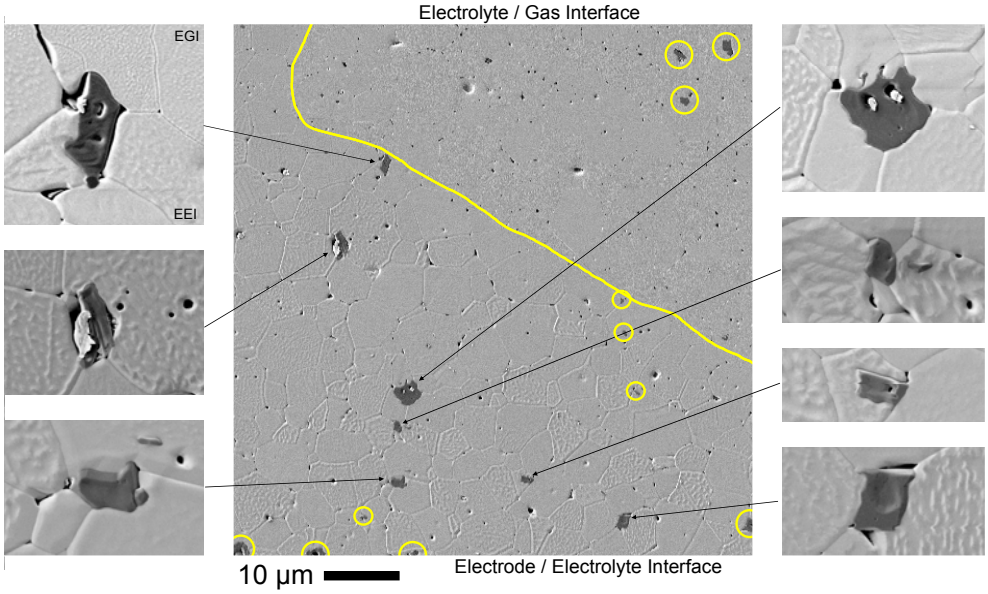

Figure 6.6: Secondary electron SEM images of the surface of an *Al-ScYSZ* electrolyte sample after electrochemical testing. The larger of the dark spots are alumina rich phases not to be mistaken for holes in the electrolyte surface. Some of the alumina rich phases are magnified around the sides of the central image and the rest are marked with circles. Nickel can be seen adhering inside holes in some of the particles (top two left and top right)

As mentioned in section 6.2, two *Al-ScYSZ* electrolyte surfaces had some unique microstructural features which might explain the improved performance of their respective cells. A SEM image of the electrode / electrolyte interface is shown in

Figure 6.7, where large areas of a layer with a porous microstructure can be seen. The porous layer rose approximately 40 nm above the plane of the hill and valley structure. Figure 6.8 shows a SEM image and an atomic force microscopy image of the same area of the porous layer. The same individual grains could be identified with both techniques. It is seen that the microstructure of the porous layer is very uneven compared to the hill and valley surface microstructure of the adjacent area.

The porous layer had flaked off in some areas Figure 6.7a) (1) exposing a very rough and coarse surface. In the corresponding areas on the nickel electrodes pieces of electrolyte were attached. Alumina rich phases such as those shown in Figure 6.6 were also observed inside the porous layer, Figure 6.7a) (2). It should be noted that the porous layer did not form on the alumina rich phase. Most of the regions with the porous layer were separated from the rim ridge by a 4-20 µm wide hill and valley belt previously referred to at the *rim zone* as exemplified in Figure 6.9. In a few areas the rim zone was not visible and the porous layer directly bordered the electrolyte / gas interface.

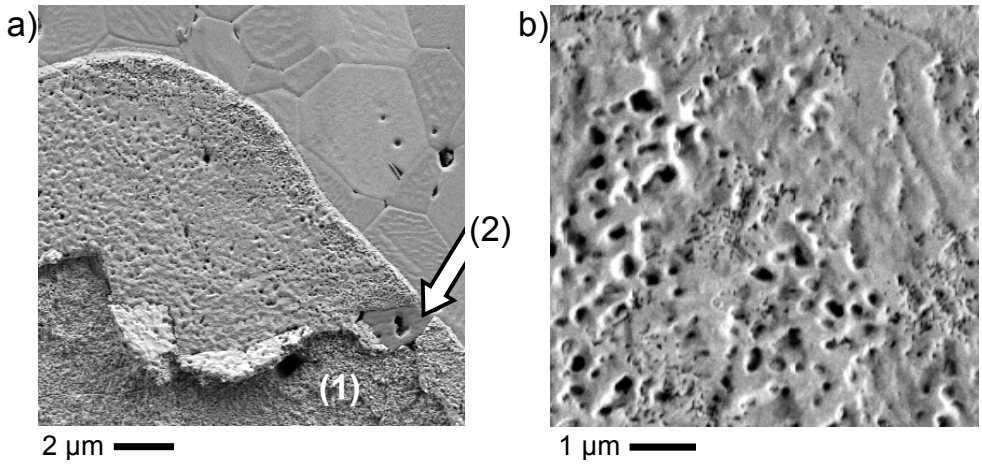

Figure 6.7: a) SEM image of an *Al-ScYSZ* electrolyte after electrochemical characterisation. Large portions of the electrode / electrolyte interface had a porous surface microstructure. Parts of the porous layer were ripped off upon removing the electrode (1). Alumina rich phases inside the porous layer remained smooth (2). b) A larger magnification of the porous layer.

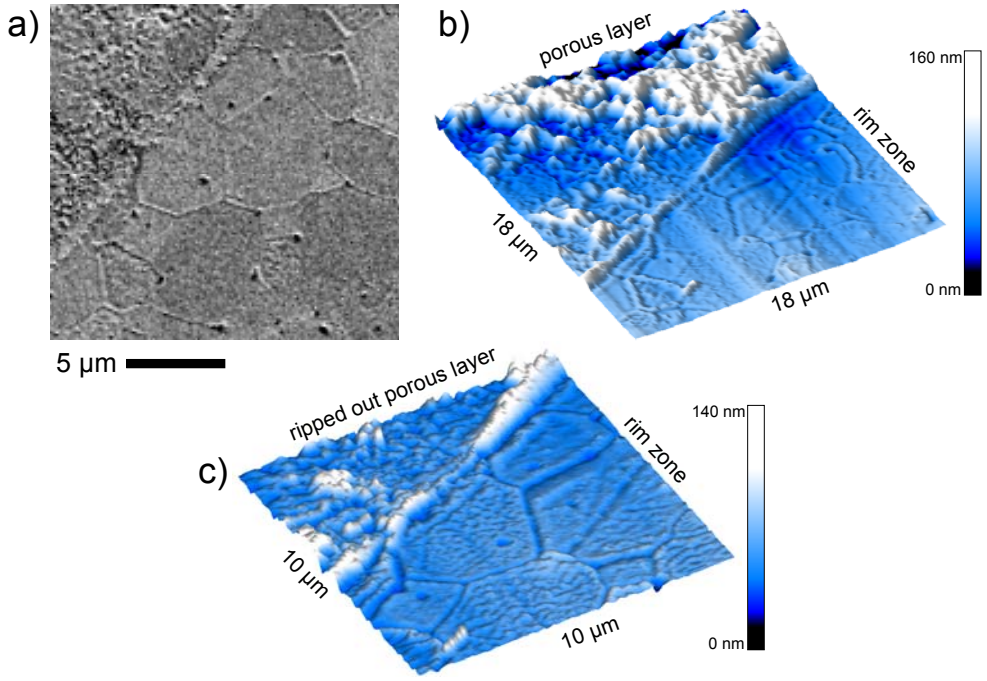

Figure 6.8: a) SEM image. b) Atomic force microscopy image of the same electrolyte area. The porous layer rose above the hill and valley surface of the rim zone. Parts of the porous layer had ripped off upon removing the electrode. c) AFM scan of a smaller area of the ripped out porous layer and the adjacent rim zone with the hill and valley surface microstructure.

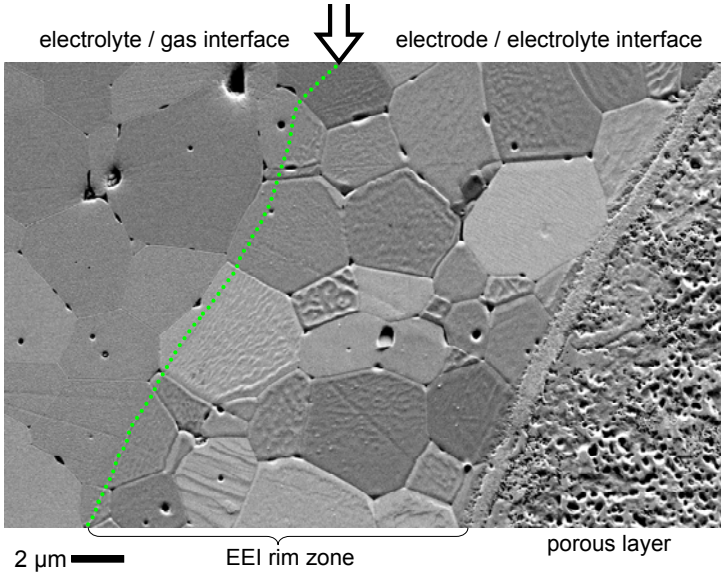

Figure 6.9: SEM image of the rim zone with the hill and valley surface microstructure surrounding the porous layers (bottom of image) observed on two *Al-ScYSZ* electrolyte samples. At larger magnifications the rim ridge could be seen and is marked here with a dotted line and an arrow.

6.4 Chemical characterisation

Chemical characterisation using ToF-SIMS was performed on one *Al-ScYSZ* electrolyte sample after electrochemical characterisation. SEM images of the electrolyte and the corresponding nickel electrode are shown in Figure 6.10. At low magnifications it was necessary to use the InLens detector in order to have enough contrast to image the electrode / electrolyte interface. The electrode / electrolyte interface on the selected sample did not have the porous layer as these were only found on a minority of the *Al-ScYSZ* samples and because a similar porous layer was analysed on an *Impure ScYSZ* sample as described in chapter 4.

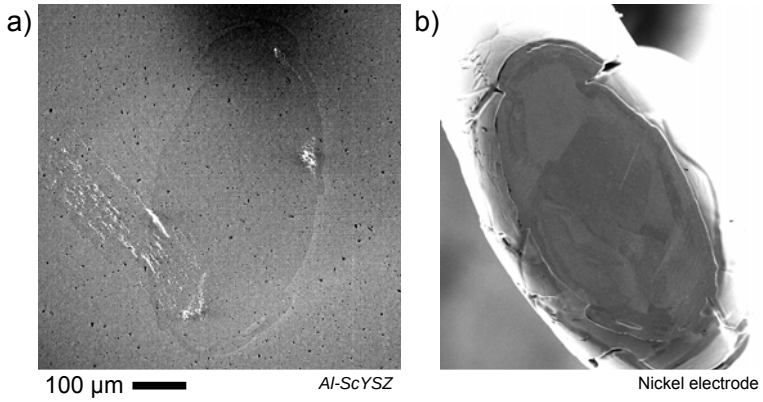

Figure 6.10: a) Secondary electron SEM image using the InLens detector, of the electrolyte surface. It was seen that the electrode had smeared the surface upon removal. b) SEM image of the nickel electrode after electrochemical measurements. The scale bare represents both images. The outline of the EEIs matched.

ToF-SIMS analysis of the electrolyte surface identified the presence of Na, Mg, K, Ca, Mn, Ni, Si in addition to Zr, Y, Sc and Al. The lateral distribution of the Si signal was representative of the locations of Na, Mg, K, Ca and Al signals and therefore the Si signal will be used to describe the location of impurity species in the following. A 500 × 500 µm^2 area was scanned with the analysis optimised for high mass resolution. The signals from impurity species were strongest from the electrolyte / gas interface and the electrode / electrolyte interface could clearly be distinguished, Figure 6.11. The impurity signal inside the electrode / electrolyte interface was strongest at the centre and decreased in intensity near the perimeter of the EEI.

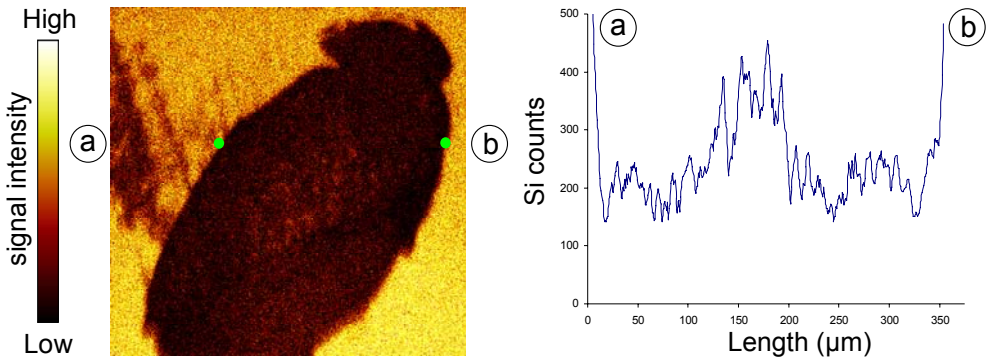

Figure 6.11: 500 × 500 µm^2 ToF-SIMS logarithmic data representation of the lateral distribution of the silicon signal on an *Al-ScYSZ* electrolyte. Inside the electrode / electrolyte interface the Si signal was strongest in the centre (EEI core). Surrounding the EEI core is an EEI rim zone with a weaker Si signal.

The Si signal along lines drawn across the electrode / electrolyte interface identified a well defined area at the centre of the EEI with a strong Si signal. As defined in chapter 4 this area was designated the *EEI core* while the surrounding area with the weaker impurity signal was called the *EEI rim zone*.

The 500 × 500 μm^2 area scan was divided in regions of interest and the Si counts from the electrode / electrolyte interface and the electrolyte / gas interface were extracted. By dividing the number of ion counts by the area of the respective regions a semi-quantitative analysis could be made, the results of which are presented in Table 6.2. The Si signal from the EEI core (0.14 counts / μm^2) was stronger than the surrounding rim zone (0.08 counts / μm^2). The ratio between the Si signal intensity in the EEI and the EGI was found to be 0.07. This was a measure of the relative silicon concentration inside the electrode / electrolyte interface. The measured values on *Pure ScYSZ* and *Impure ScYSZ* were 0.09 and 0.22 respectively.

Table 6.2: The Si signal intensity from various areas measured on an *Al-ScYSZ* sample.

	Si counts / μm^2 EEI_{Core}	Si counts / μm^2 $EEI_{Rim\ Zone}$	Si counts / μm^2 EEI_{Total}	Si counts / μm^2 EGI	$\frac{(Si\ counts / \mu m^2_{EEI})}{(Si\ counts / \mu m^2_{EGI})}$
Al- ScYSZ	0.14	0.08	0.09	1.28	0.07

A 50 × 50 μm^2 area was analysed with ToF-SIMS optimised for high lateral resolution. A SEM image of the analysed area, with the contrast adjusted so the EGI and EEI can be distinguished from each other, is shown in Figure 6.12. The same area is also shown in Figure 6.6, where alumina particles in the electrolyte surface are identified. The rim ridge, although not visible at the shown magnification, was found at the EEI perimeter and is marked with a line. As the scan was performed at the outer perimeter of the electrode / electrolyte interface the analysed area was the EEI rim zone and EGI.

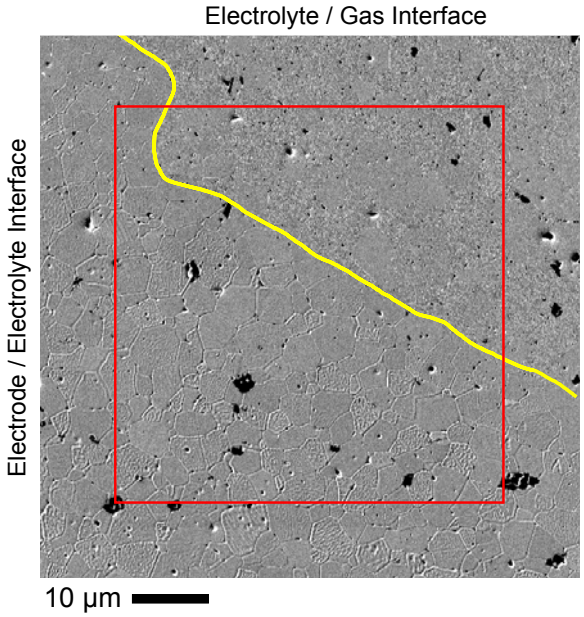

Figure 6.12: SEM image of the *Al-ScYSZ* electrolyte surface analysed by ToF-SIMS (red box). The rim ridge delimiting the EEI is marked with a yellow line.

After the initial scan of the 50 × 50 μm^2 area, a 1000 × 1000 μm^2 area centred on the scan area was sputtered with Xe^+ ions for 4 seconds and analysed again. This process was repeated for total sputter times of 16, 70 and 120 seconds. The chemical composition down through the top most surface layers could thus be monitored. As shown in Figure 6.13, the Si and Na signals were weak inside the electrode / electrolyte interface, compared to the electrolyte / gas interface. The EEI was clearly defined by the Ni signal. The signal contrast between the EEI and EGI decreased as a function of sputter time. After 70 seconds of sputtering the impurities had been removed from the EGI surface indicating that the impurities had been present as a surface layer during electrochemical characterisation. This was also observed on *Pure ScYSZ* and *Impure ScYSZ* surfaces as described in chapter 4.

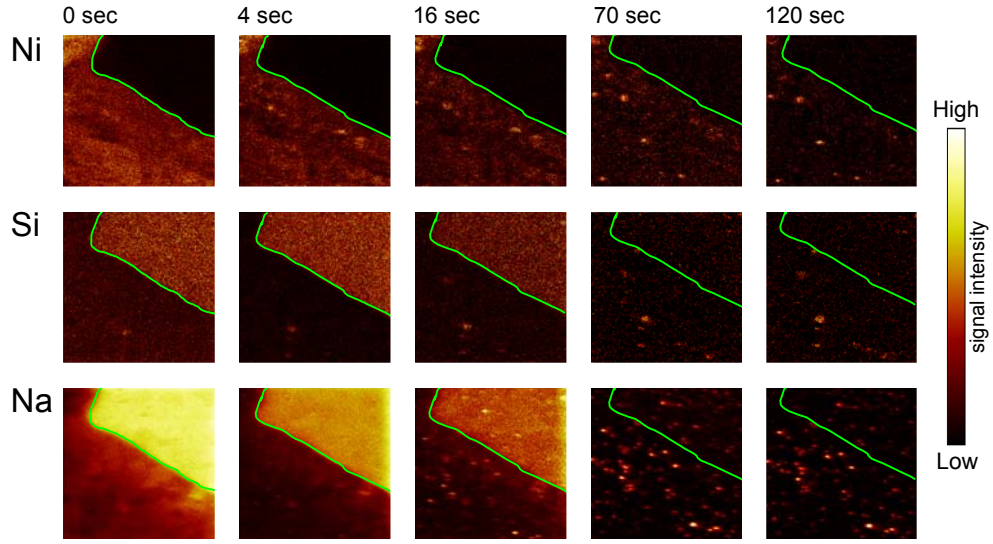

Figure 6.13: ToF-SIMS data representations of the lateral distributions of the Ni, Si and Na signal intensities on a *Al-ScYSZ* electrolyte surface as a function of Xe^+ sputter time. Before sputtering the Ni signal marked the location of the EEI. The Si and Na signals from the EEI (bottom left) were weaker than those from the EGI (top right).

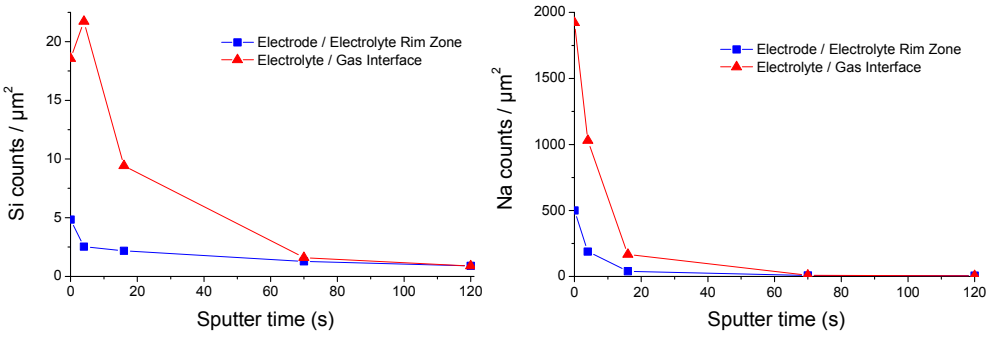

Figure 6.14: The Si and Na signal intensities obtained from a 50 × 50 μm^2 area scan at the electrode / electrolyte perimeter, inside in the EEI rim zone (□) and on the EGI (Δ), as a function of Xe^+ sputter time on *Al-ScYSZ*.

The Si and Na signal intensities measured from the EEI rim zone and EGI shown in Figure 6.13 were extracted from the spectra and plotted as a function of sputter time in Figure 6.14. It was seen that the Si and Na signals in both the EEI and EGI

decreased as a function of sputter time thus showing that the impurities had accumulated in a surface layer in both areas.

After 120 seconds of sputtering the Na signal was concentrated in particles. From SEM these particles were identified as cavities in the electrolyte surface. The Si signal was also concentrated in particles after 120 seconds of sputtering. However, the Si signal stemmed from the alumina rich particles shown in Figure 6.6 and not the cavities in the electrolyte. To further document this observation, the aluminium signal is shown together with the Si signal as a function of sputter time in Figure 6.15 and after 120 seconds of sputtering in Figure 6.16.

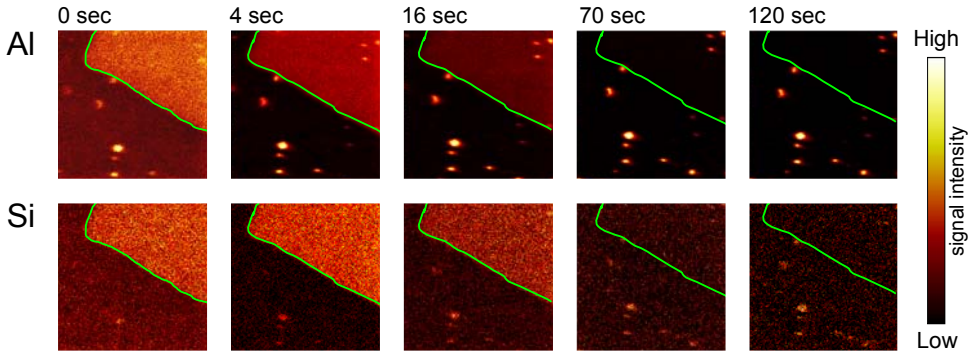

Figure 6.15: ToF-SIMS data representations of the lateral distributions of the Al and Si signal intensities on a *Al-ScYSZ* electrolyte surface as a function of Xe^+ sputter time. The EEI is at the bottom left and EGI at the top right of the images. After 120 seconds of sputtering the most intense Si signals stem from the same areas as the Al signal.

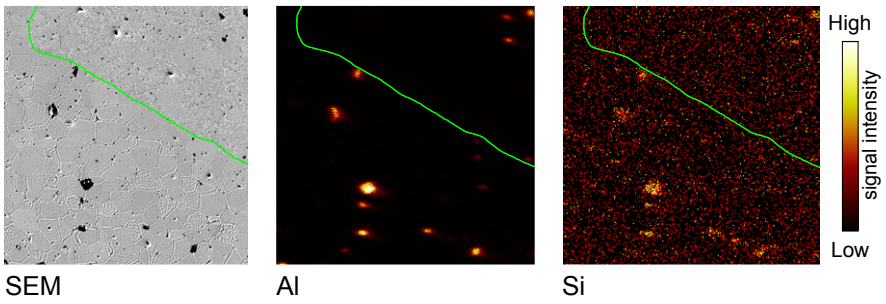

Figure 6.16: ToF-SIMS data representations of the lateral distributions of the Al and Si signal intensities on a *Al-ScYSZ* electrolyte surface after 120 seconds Xe^+ sputter time and a SEM image of the same area. The Si signal stemmed from the alumina rich phases, which were identified and located by both SEM (Figure 6.6) and ToF-SIMS.

The Al signal from the assorted areas measured on *Al-ScYSZ*, in addition to the *Impure ScYSZ* and *Pure ScYSZ* electrolytes presented in chapter 4, are shown in Table 6.3. Not surprisingly a stronger Al signal was measured from all areas of the alumina doped electrolyte than from the *Impure ScYSZ* electrolyte. Furthermore, the ratio between the Al signals from the EEI and the EGI was twice as large on *Al-ScYSZ* as on *Impure ScYSZ* indicating a relatively strong Al concentration inside the EEI of *Al-ScYSZ*.

Table 6.3: The Al signal intensity from various areas measured on *Al-ScYSZ*, *Impure ScYSZ*, and *Pure ScYSZ* samples.

	Al counts / μm^2 EEI_{Core}	Al counts / μm^2 $EEI_{Rim\ Zone}$	Al counts / μm^2 EEI_{Total}	Al counts / μm^2 EGI	$\frac{(Al\ counts / \mu m^2_{EEI})}{(Al\ counts / \mu m^2_{EGI})}$
Al- ScYSZ	2.19	1.56	1.66	13.67	0.12
Impure ScYSZ	0.35	0.77	0.60	10.79	0.06
Pure ScYSZ	0.59	0.35	0.44	4.02	0.44

6.5 Discussion and conclusion

The measured electrode polarisation resistances decreased rapidly during the first hours of measurements as exemplified by Figure 6.1 and Figure 6.2. The impurity signals from the electrode / electrolyte interface were concentrated in the EEI core and surrounded by an EEI rim zone which had low impurity concentrations. The series resistances decreased throughout the course of the measurements due to metallic creep of the nickel electrode. This was also seen, when measuring cells with *YSZ*, *Pure ScYSZ* and *Impure ScYSZ* electrolytes. As shown in chapter 4, the expansion of the EEI caused the displacement of impurities from the EEI rim zone at the three phase boundary resulting in the measured decrease in electrode polarisation resistances.

In Figure 6.16 it is shown that alumina particles at the electrolyte surface in both the EEI and EGI emitted a Si signal thus further adding to the evidence of alumina being able to act as a Si scavenger. A weaker Si signal was measured from the electrode / electrolyte interface of *Al-ScYSZ* compared to that measured on *Impure ScYSZ* and *Pure ScYSZ*. This is seen as an indication that Si was scavenged by alumina particles near the electrolyte surface under the electrode and therefore Si did not segregate to the EEI to the same degree as seen in *Impure ScYSZ*. The electrochemical characterisation of *Al-ScYSZ* showed that the ion conductivity of *Impure ScYSZ* could be increased by a factor 2.7 by adding aluminium corresponding to 2 % of the total metal cation content. This effect is attributed to the known effects of alumina towards increasing ion conductivity of ScYSZ and *Impure ScYSZ* in particular [10].

Alumina addition did not have an advantageous effect on the electrode polarisation resistance as the average area specific polarisation resistance measured on *Al-ScYSZ* was in fact slightly larger (15 Ωcm^2) than on *Impure ScYSZ*. Relatively strong concentrations of Al were measured from the EEI. As alumina acts as an impurity in itself, alumina which has segregated to the EEI is thought to inhibit the proton transfer through the electrode / electrolyte interface resulting in decreased electrochemical performance.

The porous layer observed on two *Al-ScYSZ* surfaces did not have negative consequences with respect to the area specific electrode polarisation resistance. On the contrary, the ASR_p of the electrodes with the porous layer in the EEI were the lowest of the series. It can only be speculated as to what the cause for the formation of the porous layer was. However, the porous microstructure suggested that the three phase boundary was greatly increased and hence diminished the role of impurities.

6.6 References

[1] K.C. Radford, R.J. Bratton, Journal of Materials Science, 14 (1979) 59.

[2] K. Tsukuma, E. Ueda, M. Shimada, J. Am. Ceram. Soc., 68 (1985) C4.

[3] S.P.S. Badwal, Journal of Materials Science, 18 (1983) 3230.

[4] E.P. Butler, J. Drennan, J. Am. Ceram. Soc., 65 (1982) 474.

[5] J. Drennan, E.P. Butler, Science of Ceramics 12, Faenza, Italy, (1984) 267.

[6] E. P. Butler, N. Bonanos, Mater. Sci. Ing., 71 (1985) 49.

[7] M. J. Verkerk, A.J.A. Winnubst, A.J. Burggraaf, Journal of Materials Science 17 (1982) 3113.

[8] A.J. Feighery, J.T.S. Irvine, Solid State Ionics, 121 (1999) 209.

[9] R.D. Shannon, Acta Crystallographica, A 32 (1976) 751.

[10] D. Lybye, Y.-L. Liu, J. Eur. Ceramic. Soc., 26 (2006) 599.

7 Electrode Dynamics

This chapter describes the effects of applying an anodic overpotential to the nickel electrode of the three-electrode cell. Using the three-electrode cell configuration chronoamperometry with an applied overpotential to the working electrodes was undertaken on *Pure ScYSZ* and *Impure ScYSZ* electrolytes in a wet and dry hydrogen atmospheres at 850 °C. High anodic overpotentials resulted in the occurrence of distinct sawtooth oscillation patterns in the measured current signal. The current oscillations indicated that a dynamic electrode process was taking place. Decreasing the water content in the measurement atmosphere as well as lowering the applied anodic overpotential had the effect of lowering the frequency and the amplitude of the current oscillations. Anodic polarisation had the effect of temporarily decreasing the electrode polarisation resistance measured at OCV after polarisation. A mechanism accounting for the observed phenomena and possible implications for solid oxide fuel cell operation are presented. The results presented in this chapter were submitted for publication in the form shown in appendix H.

7.1 Motivation

In the pursuit of improving SOFC performance detailed knowledge of the reaction mechanisms, reaction pathways and degradation mechanisms occurring at the anode and cathode are desirable. It has been established that continuous polarisation of the electrodes decreases interfacial impedance resulting in a temporary performance increase [1]. It has also been found that this activation during polarisation is followed by a deactivation when the electrodes are relaxed. Strong polarisations have also been found to influence the microstructure at the electrode / electrolyte interface between electrolytes and both anode and cathode materials [2][3]. The underlying mechanisms behind the observed changes in microstructure are presently not fully understood. However it is likely that they have a significant effect on the long term stability of SOFCs [4][5].

7.2 Experimental

7.2.1 Measurement setup

The custom made rig described in chapter 2 was used for electrochemical characterisation. The rig parts consisted of alumina and all electrical leads were platinum. The rig fitted four, three-electrode cells in which the Ni point-electrode was the working electrode. Figure 7.1 gives the principle and the dimensions of the three-electrode configuration. The measurements were performed in a one-

atmosphere setup. Inlet hydrogen was bubbled through a water bottle placed in a refrigerator, hence the water content in the measurement atmosphere could be controlled by varying the water temperature [6]. The oxygen potential in the measurement atmosphere versus air was monitored by a platinum electrode pair on two sides of an alumina tube closed at one end, inserted in the measurement atmosphere, Figure 7.1. The water bottle could be bypassed to create a "dry" measuring atmosphere. Some moisture was, however, present in the gas supply and based on the oxygen potential the "dry" atmosphere had a calculated water content of 54 ppm.

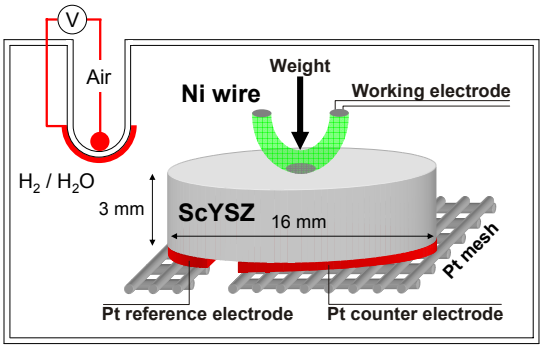

Figure 7.1: Schematic of the 3-electrode configuration. The oxygen partial pressure in the measurement atmosphere was monitored by an oxygen sensor as pictured.

The three-electrode cell configuration was a model system which studied the hydrogen reaction at the SOFC nickel anode. As the electrode could be lifted off the electrolyte surface after electrochemical measurements, the point-electrode setup enabled the study of a well defined electrode / electrolyte interface (EEI) and three phase boundary (TPB). Chronoamperometry was undertaken with an applied anodic polarisation in hydrogen atmospheres at 850 °C.

7.2.2 Electrochemical impedance spectroscopy

Four *Pure ScYSZ* pellets were prepared as described in chapter 2. Together with high purity nickel electrodes (99.999 % Ni) the electrolyte pellets were mounted in the measurement rig in the three-electrode cell configuration. With the cells mounted, the rig was heated to 850 °C at a rate of 5 °C / minute in 89 % Ar / 9 % H_2 / 2 % H_2O where after the atmosphere was switched to 97.6 % H_2 / 2.4 % H_2O (pO_2 = -1104 mV vs. air at 850 °C). Electrochemical impedance spectroscopy was performed at open circuit voltage (OCV) with an applied RMS amplitude of 7.07 mV using a *Solartron* 1250 frequency response analyser coupled with a *Solartron* SI 1287 potentiostat. The obtained impedance spectra were fitted with the equivalent circuit $R_s(R_{p1}Q_1)(R_{p2}Q_2)$ [7].

The values of the electrode polarisation resistances have previously been seen to fall rapidly during the first 50 hours. This drop was accounted for in chapter 4 and [8]. In order to ensure that the chronoamperometric measurements were performed independently of the effects described in chapter 4 the polarisation resistance values were measured at OCV until stable values were measured on all four samples.

7.2.3 Chronoamperometry

After the electrode polarisation resistance values had stabilized, chronoamperometry with applied anodic overpotentials was performed on three of the *Pure ScYSZ* cells, with the fourth cell acting as a reference. Each of the three cells were anodically polarised with an applied overpotential of 50 mV for one hour. In direct continuation of chronoamperometry, impedance measurements were performed at OCV to monitor the temporal effect of anodic polarisation on the electrode polarisation resistance. When the electrode polarisation resistances measured at OCV had stabilised the procedure was repeated by increasing the applied overpotential in steps of 50 mV until electrode potentials of -550 mV vs. Pt / air were reached.

By adjusting the temperature of the water humidifying the inlet gas, the atmosphere was changed to 99.3 % H_2 / 0.7 % H_2O (pO_2 = -1162 mV vs. Pt / air), and chronoamperometric measurements were performed on the samples with electrode potentials from -850 mV to -550 mV vs. Pt / air in steps of 100 mV.

The direct effect of water content in the atmosphere was investigated by conducting chronoamperometric measurements in a "dry" atmosphere (pO_2 = -1400 mV vs. Pt / air) lasting one hour and then increasing the H_2O content to 2.4 % whilst keeping the electrode potential constant by adjusting the set overpotential. After one hour with a wet atmosphere the incoming gas flow was switched back to a "dry" H_2 atmosphere. This procedure was repeated using a wet atmosphere with 0.7 % H_2O instead of 2.4 % H_2O.

Potential sweeps were carried out on the three samples in a 97.6 % H_2 / 2.4 % H_2O atmosphere at rate of 1 mV/s spanning the electrode potential range from -1500 mV to -550 mV vs. Pt / air at 850, 800 and 750 °C before terminating the experiment.

After completion of the above mentioned measurements, *Impure ScYSZ* cells were anodically polarised to reach electrode potentials ranging from -400 mV to -550 mV vs. Pt / air in a 97.6 % H_2 / 2.4 % H_2O atmosphere. This was done to document reproducibility of the observed microstructures independent of electrolyte material.

7.2.4 Microscopy

Following electrochemical measurements the nickel electrodes were lifted off the electrolytes. The electrodes and electrolytes were examined with a field emission gun scanning electron microscope (SEM) in order to determine the areas of the electrolyte / electrode interfaces. Secondary electrons with a 1 keV acceleration voltage were used to examine the surface microstructures on the ScYSZ without necessitating carbon coating.

7.2.5 Chemical analysis

Time-of-flight secondary ion mass spectrometry (ToF-SIMS) was performed to obtain qualitative measurements of the lateral distribution of trace elements on the electrolyte surface. ToF-SIMS images with high mass resolution but low lateral resolution were acquired using 30-ns pulses of 25-keV Bi^+, bunched to form ion packets with a nominal temporal extent of < 0.9 ns at a repetition rate of 10 kHz

yielding a target current of 500 fA. These primary ion conditions were used to scan 500 × 500 μm^2 areas of the sample surfaces. Images with low mass resolution but high lateral resolution (primary ion spot size ~150 nm) were acquired covering 75 × 75 μm^2 areas of the sample surface using 100-ns pulses of 25-keV Bi^+ at a repetition rate of 10 kHz yielding a target current of ≤ 10 fA. The high lateral resolution enabled the correlation between ToF-SIMS and SEM images. Following the 75 × 75 μm^2 area scans a 1000 × 1000 μm^2 area of the surface was sputtered for 10 or 60 seconds using 3-kV Xe^+ (sputter ions) resulting in a target current of 20 nA. After sputtering, a 500 × 500 μm^2 area scan optimised for high lateral resolution was performed. Electron bombardment (20 eV) was used to minimize charge build-up at the surface. Desorbed secondary ions were accelerated to 2 keV, mass analyzed in the flight tube, and post-accelerated to 10 keV before detection.

7.3 Results

7.3.1 Impedance at OCV and during anodic polarisation

Electrochemical impedance spectroscopy was performed at OCV in order to ensure that the electrode polarisation resistance had stabilised before performing chronoamperometry. As described in chapter 4 the large drop in electrode polarisation resistances were associated with the nickel-electrodes expanding due to metallic creep, thus displacing impurities from the three phase boundary. During the first 24 hours at 850 °C the electrode polarisation resistances of the four cells dropped from ~82 kΩ to ~40 kΩ. After 35 hours at 850 °C in the 2.4 % H_2O atmosphere the first sample was polarised with an applied overpotential of 50 mV during which chronoamperometry was performed for one hour. Impedance spectra were recorded in direct continuation of the chronoamperometric measurements while polarised. Examples of impedance spectra recorded at OCV and during anodic polarisation are shown in Figure 7.2 and Figure 7.3.

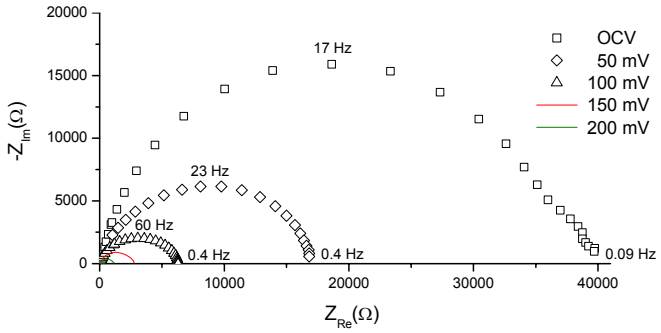

Figure 7.2: Impedance spectra recorded on a cell with *Pure ScYSZ* electrolyte at OCV and 50, 100, 150 and 200 mV anodic overpotentials. R_p decreased as a function of applied overpotential.

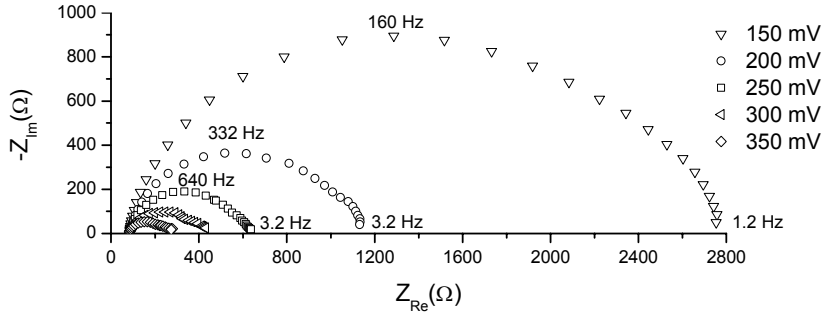

Figure 7.3: Impedance spectra recorded on a cell with *Pure ScYSZ* electrolyte at OCV and 150, 200, 250, 300 and 350 mV anodic overpotentials.

While polarised, the values of the real axis intercept decreased as a function of applied overpotential. However, at applied overpotentials of 50 mV and 100 mV, R_p returned to the levels initially measured at OCV after the applied polarisation was lifted. As the applied overpotential was increased, lasting effects to the subsequent impedance measurements at OCV were observed as illustrated by Figure 7.4. After on hour at anodic overpotentials the electrodes activated and took about 25 hours at OCV to return to stable R_p levels.

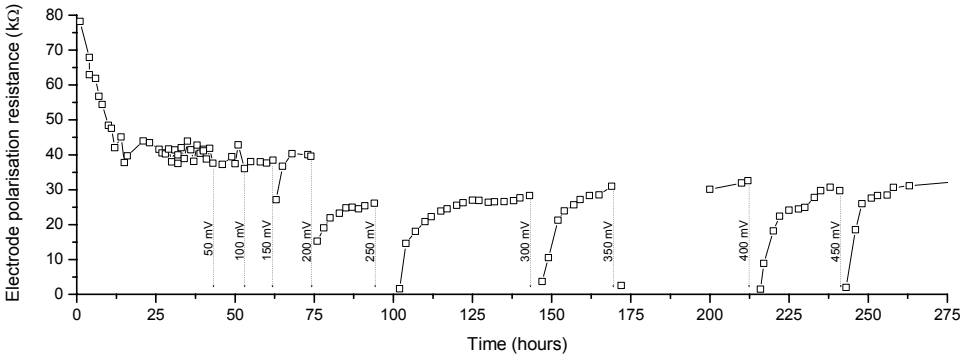

Figure 7.4: The electrode polarisation resistance measured at OCV in 2.4 % H_2O / hydrogen atmosphere on a *Pure ScYSZ* cell. After stabilising the cell was submitted to anodic polarisations (arrows).

7.3.2 Chronoamperometry in constant atmosphere

When the nickel electrodes were anodically polarised in both wet and dry atmospheres (2.4 %, 0.7 % H_2O and *dry* = 54 ppm H_2O) the measured currents were found to increase gradually until the average currents reached a constant level. The current density calculation was based on the EEI area measured by SEM after electrochemical measurements, while assuming that electrode expansion was negligible after ~50 hours. The average current levels increased as a function of applied overpotential, as shown by Figure 7.5. The equilibrium potentials of the three atmospheres were measured to be -1104 mV, -1162 mV, and -1400 mV vs. Pt / air for the 2.4 % H_2O, 0.7 % H_2O and dry atmospheres respectively.

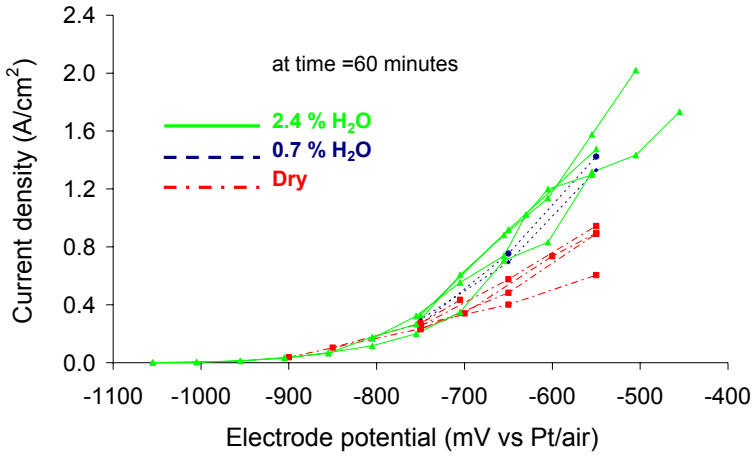

Figure 7.5: For three samples the average current density after 60 minutes of anodic polarisation is plotted as a function of the set electrode potential. It was seen that the current density increased as the water content in the measurement atmosphere was increased.

At electrode potentials over -700 mV vs. Pt / air, characteristic sawtooth oscillation patterns were measured on the three cells, Figure 7.6 and Figure 7.7. The sawtooth oscillations initially had low amplitudes but the oscillation amplitudes increased as a function of time until reaching a steady state current level, where the amplitudes remained unchanged in magnitude for the remainder of the 60 minute measurements. The sawtooth oscillation patterns can be described as a slow decline in the measured current followed by an instantaneous activation. The oscillation amplitude was approximately 30 % of the total current. The observed pattern was similar in shape to that presented in [9][10] although the frequency was several orders of magnitude larger in the present work. In [11] a similar fluctuation pattern with a similar time scale was observed using Pd electrodes.

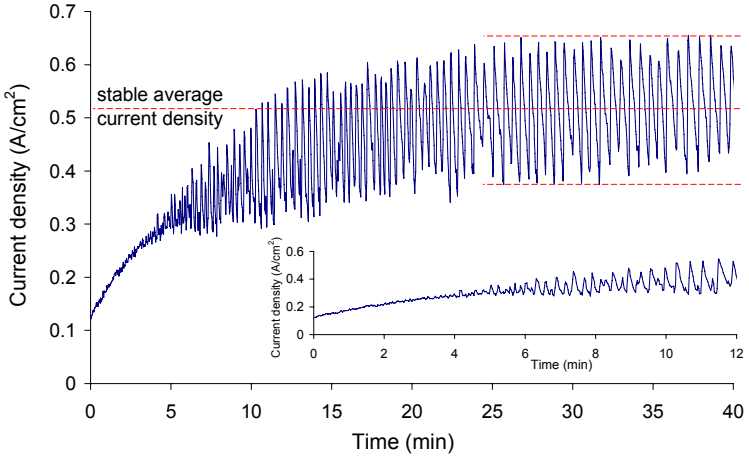

Figure 7.6: The current density as a function of time obtained from a chronoamperometric measurement of one cell in a hydrogen atmosphere containing 2.4 % H_2O. The electrode potential was set at -700 mV vs. Pt / air by anodic polarisation for 60 minutes. A distinct sawtooth oscillation pattern (insert) was observed after an initial gradual increase in current. After 25 minutes the average current density was stable for the remainder of the measurement.

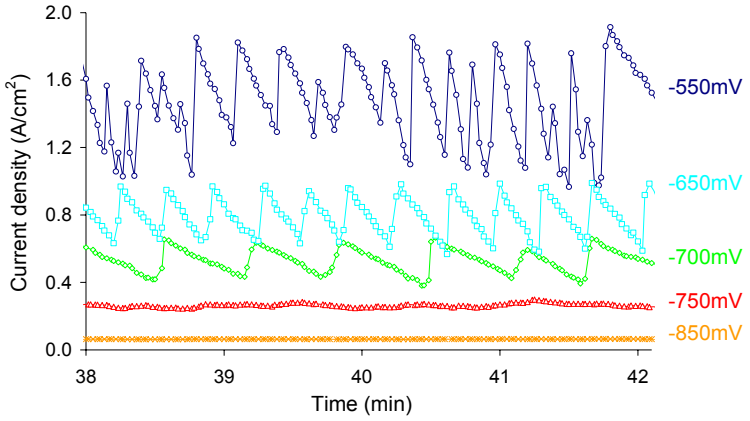

Figure 7.7: Chronoamperometric measurements in a 2.4 % H_2O atmosphere. Sawtooth oscillation patterns were observed at electrode potentials over -700 mV vs. Pt / air.

The oscillation patterns were evaluated using a fast Fourier transform analysis and a dominating frequency was found for each data set. The Fourier analysis verified that the oscillation patterns were not noise patterns and also showed that the dominating frequency of the sawtooth oscillations increased as a function of the applied electrode overpotential as is hinted in Figure 7.7. Furthermore, the amplitude of the sawtooth oscillations increased as a function of applied overpotential as can be seen from Figure 7.7 and Figure 7.8.

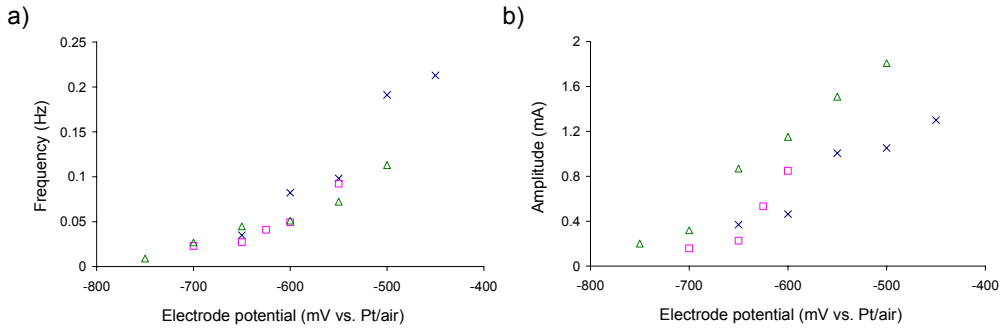

Figure 7.8: a) The dominating frequencies of the current oscillations on three cells (×,Δ,□) plotted as a function of electrode potential in a hydrogen atmosphere with 2.4 % H_2O. The oscillation frequency clearly increased as a function of anodic polarisation. b) The amplitude of the current oscillations on three cells (×,Δ,□) plotted as a function of electrode potential in a hydrogen atmosphere with 2.4 % H_2O. The oscillation amplitude clearly increased as a function of anodic polarisation.

7.3.3 Chronoamperometry in atmospheres with varying H_2O levels

The effect of varying water content in the measurement atmosphere was investigated by conducting chronoamperometric measurements with a constant applied overpotential to the working electrodes in a dry H_2 atmosphere until the average current levels had stabilised and then introducing 2.4 % H_2O into the gas flow. As a consequence of the increased water content in the atmosphere the measured equilibrium electrode potential increased from -1400 mV to -1104 mV vs. Pt / air and therefore the applied overpotential was reduced accordingly to maintain a constant electrode potential. As seen in Figure 7.9, the introduction of water into the atmosphere (II) resulted in the onset of the sawtooth oscillation

pattern. After the oscillation pattern had stabilised at new steady average current levels the atmosphere was switched back dry H_2 (III) and the applied overpotential was increased so that the electrode potential remained constant. From the measured electrode potential it was seen that it took roughly 4 hours for the atmosphere to become completely dry, which is why the measured currents took this time to decrease to new stable levels. The steady state currents measured after switching back to the dry atmosphere (III) were significantly larger than the initial measurements made in dry atmosphere (I) before introducing water to the atmosphere. However, the steady state current levels measured in the wet atmospheres were the same as those measured in the following dry atmosphere.

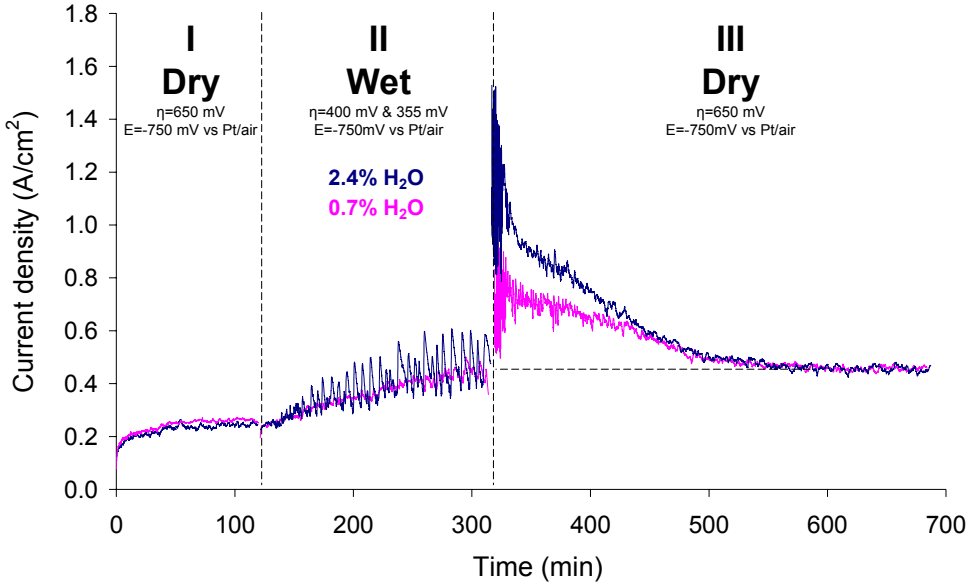

Figure 7.9: Chronoamperometric measurements on the same cell show the effect of varying water content in the measuring atmosphere by switching from a dry atmosphere (I) to wet atmospheres (II) and back again (III). A clear difference in the oscillation amplitude is seen between the 2.4 % and 0.7 % H_2O atmospheres.

The above mentioned procedure was repeated with a water content of 0.7 %. It is seen in Figure 7.9 that introducing 0.7 % water into the dry measurement atmosphere had the effect of increasing the measured current density. Sawtooth oscillations were observed in the 0.7 % H_2O atmosphere, but the onsets of the oscillations were delayed compared to the 2.4 % H_2O atmosphere. The lower water content also has the effect of reducing the amplitude of the current oscillation pattern. Furthermore, it was seen that the stabilised current levels after both 0.7 % and 2.4 % H_2O atmospheres reached the same levels in region (III).

7.3.4 Potential sweeps at different temperatures

Potential sweeps at a rate of 1 mV/s in 2.4 % H_2O at 850 °C became unstable on the upward sweeps at an electrode potential of around -770 mV, where after the measured current signals started to fluctuate, Figure 7.10. At an electrode potential of -550 mV the sweep direction was reversed and the current signals oscillated in a pattern with instant activations followed by a gradual reduction in current. As the set electrode potential reached -710 mV the current oscillations ceased for the remainder of the sweeps. This trend was also seen for sweeps made at 800 °C and

750 °C although reducing the temperature had the effect of increasing the electrode potential values needed to cause the fluctuating signals.

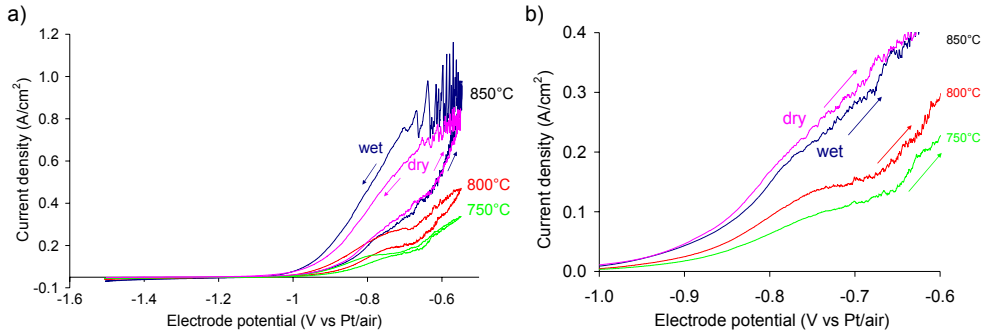

Figure 7.10: Example of cyclic potential sweeps (1 mV/second) in dry atmosphere at 850 °C and in 2.4 % H_2O atmosphere at 850 °C, 800 °C and 750 °C. b) The upward sweeps show a temperature dependence on the onset of fluctuations in the current signal.

7.3.5 Microstructure

After electrochemical measurements the electrode and electrolyte surfaces were investigated by SEM. The microstructural features observed on the reference electrolyte, which had not been polarised were identical to those previously described in chapter 4, with the main features being an undulating hill and valley microstructure in the electrode / electrolyte interface and a rim ridge delimiting the EEI. The hill and valley microstructure was also found on the EEI of the polarised *Pure-* and *Impure ScYSZ* electrolytes. However several additional microstructural features distinguished the polarised electrolyte samples from the reference sample and cells described in the previous chapters. The most noticeable feature observed on the polarised electrolytes were nickel particles (determined by EDS) lying in a 10-40 µm wide belt encircling the EEI, Figure 7.11.

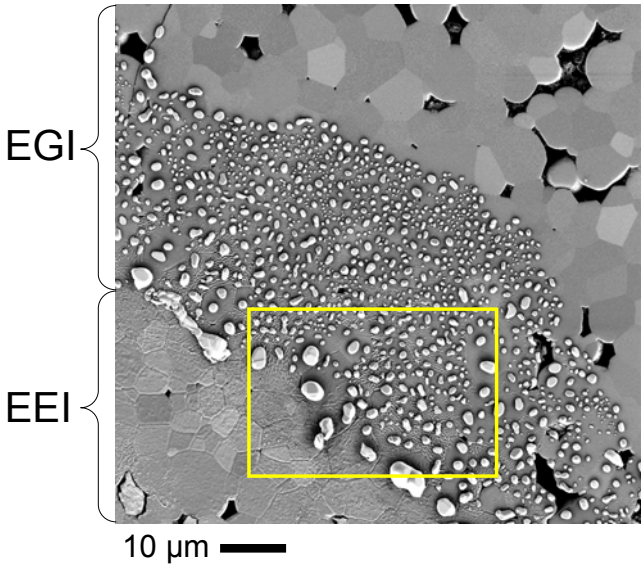

Figure 7.11: SEM image of the electrode / electrolyte interface (EEI) on a *Pure ScYSZ* electrolyte. The EEI was completely encircled by a 30-40 µm wide belt of nickel particles. Box enlarged in Figure 7.12.

The nickel particles were facetted and varied in size from 200 nm to 3 µm in diameter as shown in Figure 7.12. By comparing the EEI area on the nickel electrode with the corresponding EEI area on the electrolyte, it was established that the nickel particles lay outside the EEI, Figure 7.13. For this reason the area covered by the discrete nickel particles was not included, when calculating the EEI area. It was also noted that the Ni particles lying on the grains with flat surfaces were bigger and fewer in number than the Ni particles found on the hill and valley surfaces

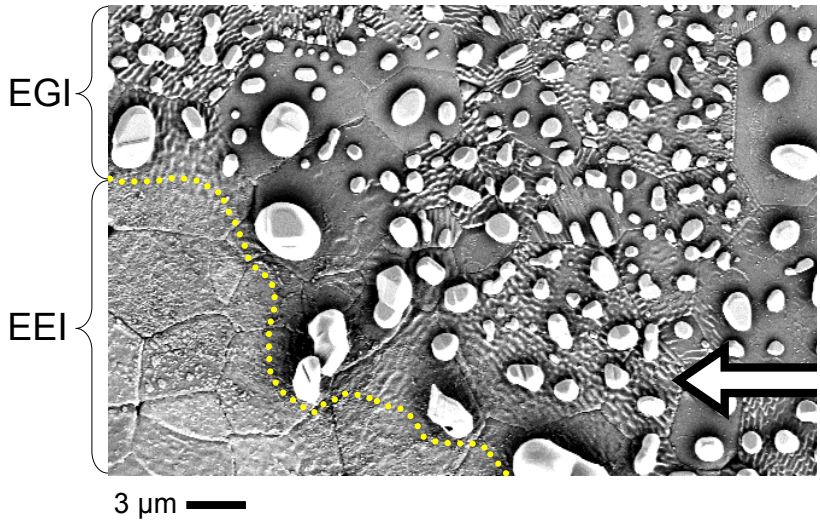

Figure 7.12: SEM image of the outer perimeter of the electrode / electrolyte interface (EEI) of a *Pure ScYSZ* electrolyte. The rim ridge, which delimited the EEI is marked with a line. Arrow: The hill and valley structure was generally much more pronounced in the electrolyte / gas interface (EGI) than in the EEI. Fewer but larger Ni particles were located on the flatter grain surfaces. The facetted nickel particles were not interconnected.

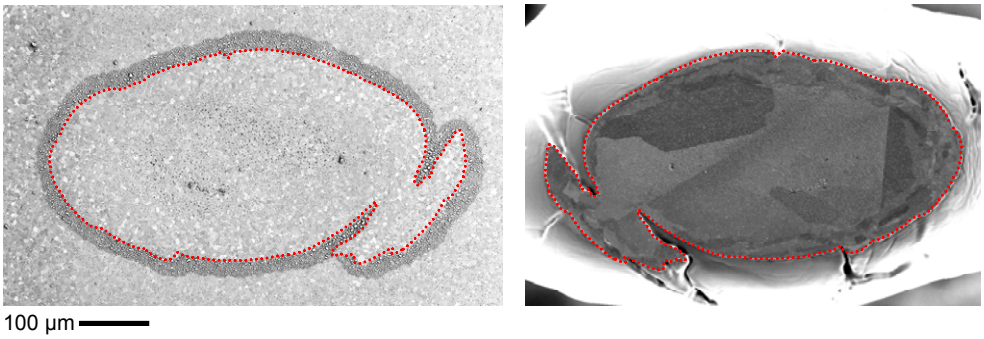

Figure 7.13: SEM images of the *Impure ScYSZ* electrolyte (left) and corresponding nickel electrode (right). The nickel particle belt is clearly seen on the electrolyte.

The electrolyte surface underneath the nickel particles nearest to the EEI also had the hill and valley microstructure, although even more pronounced than inside the EEI, Figure 7.14. The hill and valley microstructure became less pronounced, when moving towards the outer edge of the nickel particle belt as exemplified by Figure 7.15.

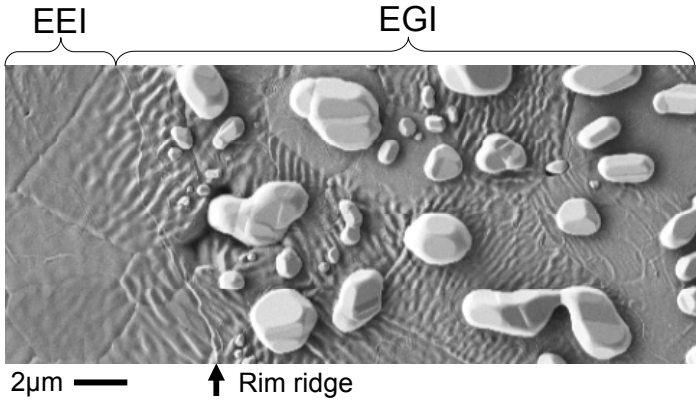

Figure 7.14: SEM image a *Pure ScYSZ* electrolyte. The electrode / electrolyte interface (EEI) outer perimeter was delimited by a rim ridge (arrow). The hill and valley surface microstructure was more pronounced in the nickel particle belt in the electrolyte gas interface (EGI) than in the EEI.

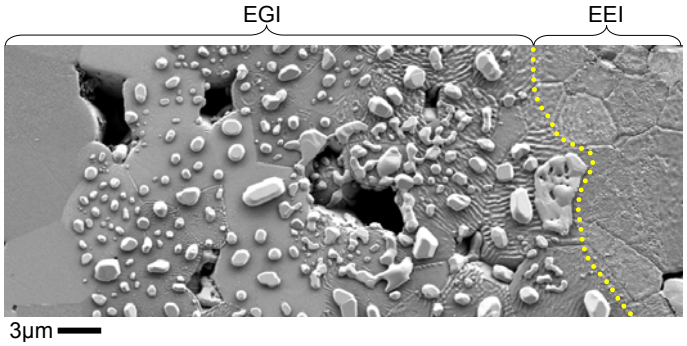

Figure 7.15: SEM image of the electrode / electrolyte interface (EEI) outer perimeter marked by a rim ridge (dotted line). The hill and valley microstructure in the nickel particle belt in the electrolyte / gas interface (EGI) became less pronounced, when moving away from the EEI.

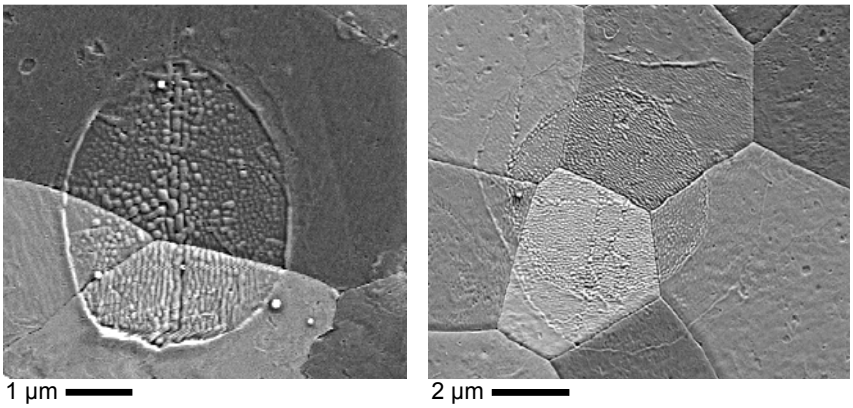

Figure 7.16: SEM image from inside the electrode / electrolyte interface showing areas with a granulated surface microstructure. These areas corresponded to cavities found in the electrodes, hence gas had been present in the cavities. A ridge, similar in appearance to the rim ridge at the outer EEI perimeter, encircled the area with the granulated microstructure.

Inside the EEI of the polarised samples, areas with a granulated surface microstructure, Figure 7.16, stood out from the hill and valley microstructure otherwise covering the EEI. The nickel electrodes had cavities in the EEI surface in

the areas corresponding to the granulated surface microstructure on the electrolytes, Figure 7.17.

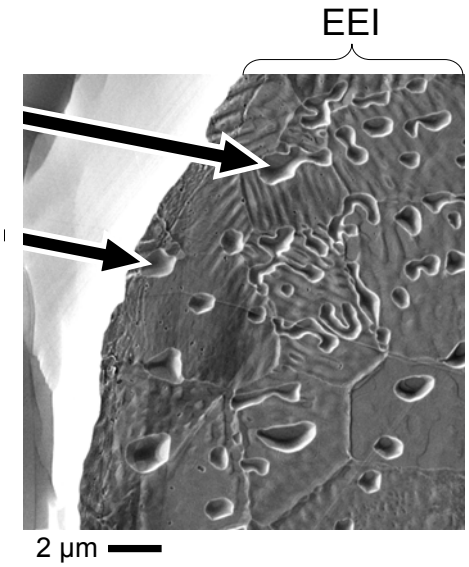

Figure 7.17: SEM image of the cavities (arrows) in the electrode / electrolyte interface (EEI) of the nickel electrode. These cavities corresponded to the areas with granulated microstructure on the electrolyte seen in Figure 7.16.

On one *Pure ScYSZ* electrolyte sample a part of the electrolyte was ripped out by the nickel-electrode when the cell was dismounted. The ripped out ScYSZ remained attached to the electrode as shown in Figure 7.18b) indicating a strong mechanical bond between the electrode and electrolyte. The exposed crater in the electrolyte was investigated and it was found that the grain boundaries had a canal like microstructure as exemplified by Figure 7.19. In the exposed cavities nickel crystallites were found, Figure 7.19 and Figure 7.20. Unlike the more rounded nickel crystals on the electrolyte surface the polyhedral structure of the nickel particles in the cavities underneath the EEI indicated that they formed in a stagnant atmosphere.

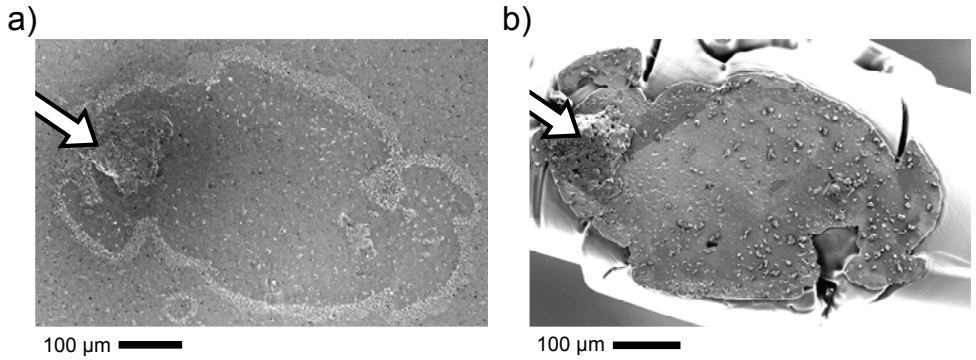

Figure 7.18: a) Secondary electron SEM image using the Inlens detector of a *Pure ScYSZ* electrolyte. The crater left by the ripped out electrolyte is marked with an arrow. b) SEM image of the corresponding nickel-electrode with the adhered electrolyte marked with an arrow.

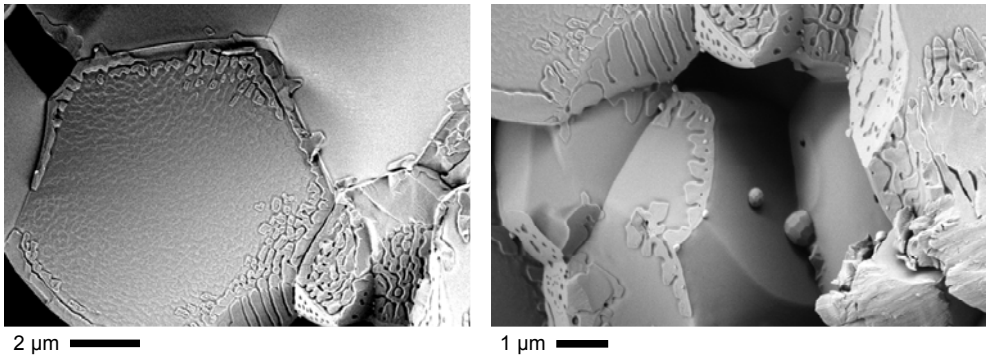

Figure 7.19: SEM images of the crater in the *Pure ScYSZ* electrolyte sample. The grain boundaries had formed a canal like microstructure. Inside the cavities nickel crystals were seen (right).

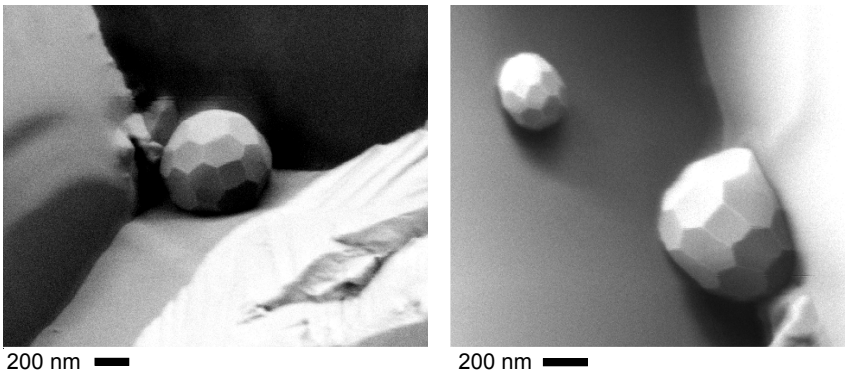

Figure 7.20: High magnification SEM images of the polyhedral nickel crystals found in the cavities in the *Pure ScYSZ* electrolyte.

7.3.6 Chemical analysis of *Pure ScYSZ*

A low magnification SEM image of the electrode / electrolyte interface on a *Pure ScYSZ* electrolyte is shown in Figure 7.21. From high magnification micrographs of the electrolyte, such as Figure 7.14, and the Ni electrode, the EEI was identified and the outline marked on the low magnification SEM micrograph in Figure 7.21.

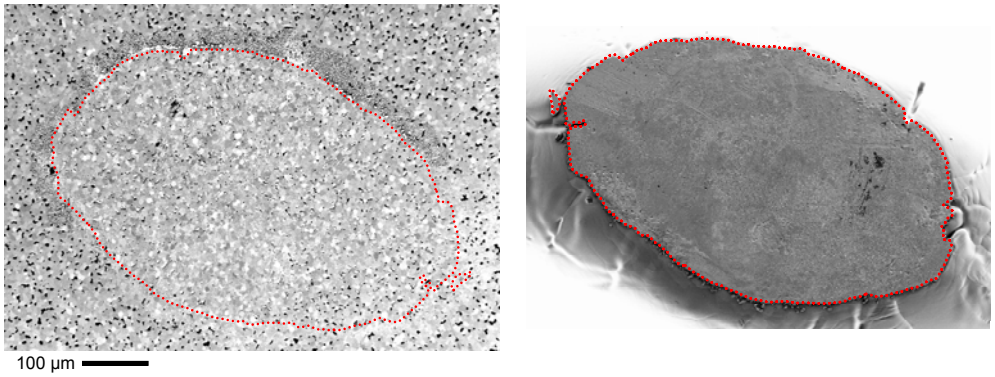

Figure 7.21: SEM images of the *Pure ScYSZ* electrolyte (left) and corresponding nickel-electrode (right). The electrode / electrolyte interface is marked with a dotted line on both images.

The results of a 500 × 500 µm^2 area ToF-SIMS analysis optimised for high mass resolution, of the electrolyte area shown in Figure 7.21, are presented in Figure 7.22. From ToF-SIMS data representations a belt of nickel particles was seen encircling the EEI. It was also found that the Si, Na, Al and K signals were weaker inside the EEI than in the EGI as also described in chapter 4. The Sc and Y signals were much stronger inside the EEI than from the EGI and correspond exactly to the EEI area established by SEM. This was not observed on samples, which were not polarised. The Zr signal seemed unaffected by polarisation.

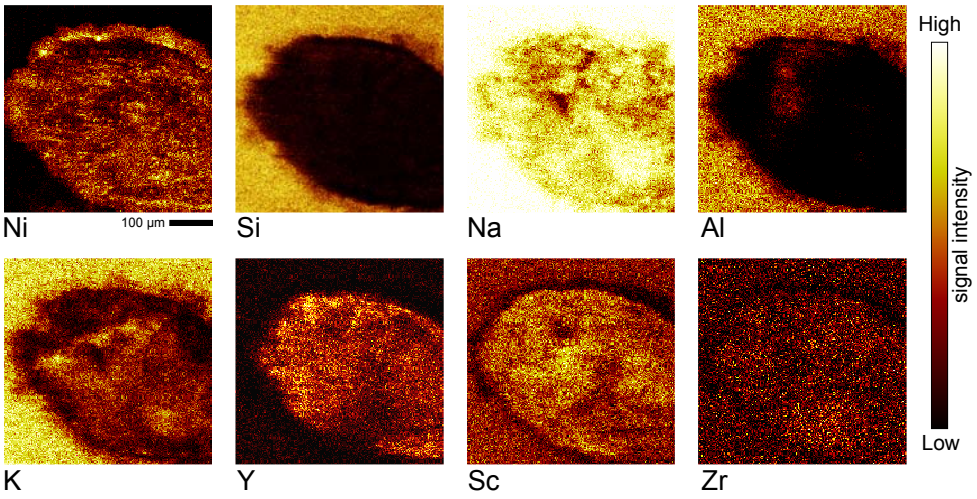

Figure 7.22: ToF-SIMS data representations of a 500 × 500 µm^2 area of the electrode / *Pure ScYSZ* electrolyte interface and surrounding electrolyte / gas interface. A nickel belt surrounded the EEI. Inside the Ni belt the Si, Na and Al signals were weaker than the rest of the EGI. Strong Sc and Y signals were measured from the EEI.

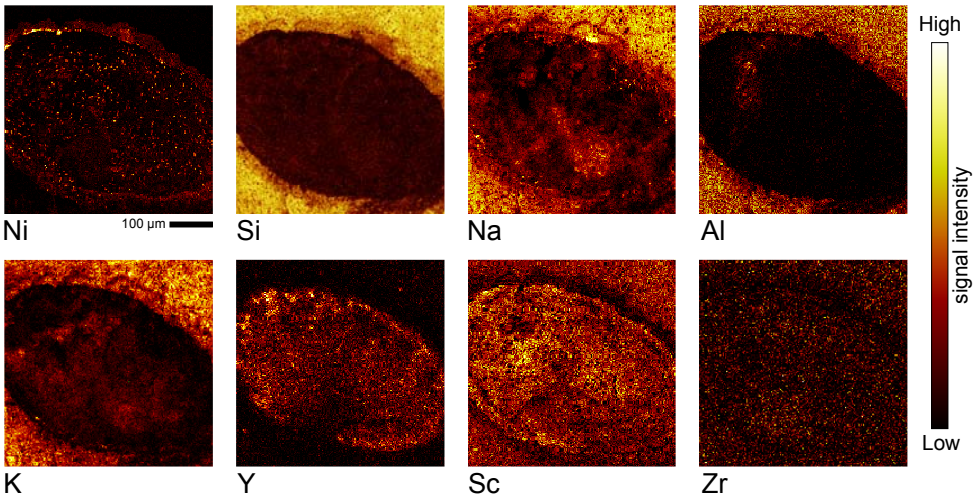

Figure 7.23: ToF-SIMS data representations of a 500 × 500 µm^2 area of the electrode / *Pure ScYSZ* electrolyte interface and surrounding electrolyte / gas interface after 10 seconds of Xe^+ sputtering. A nickel belt surrounded the EEI. Inside the Ni belt the Si, Na and Al signals were weaker than from the rest of the EGI. Strong Sc and Y signals were measured from the EEI.

After the initial 500 × 500 µm^2 area analysis, the EEI was sputtered with Xe^+ for 10 seconds. Hereafter the EEI was analysed again with the scan optimised for high

lateral resolution. The results of this scan are shown in Figure 7.23. The trends initially observed in Figure 7.22 are even more noticeable after sputtering. It was also seen that the outer perimeter of the EEI emitted stronger Sc and Y signals relative to the rest of the EEI. Again the Zr signal seemed uniform across the scan area.

Figure 7.24 shows a SEM image of an area analysed with ToF-SIMS optimised for high lateral resolution. This 75 × 75 μm^2 area at the outer perimeter of the EEI included a section of the EGI nickel particle belt. ToF-SIMS data representations of the lateral distribution of chemical species in this area are shown in Figure 7.25.

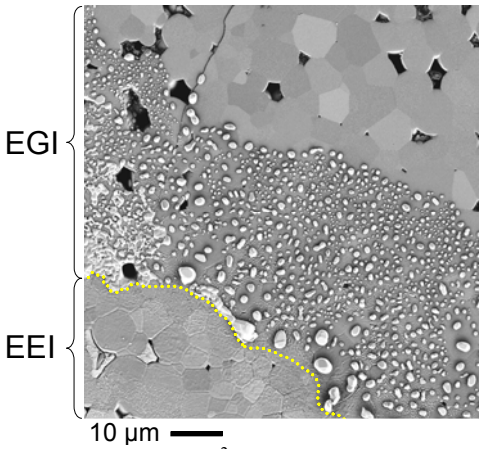

Figure 7.24: SEM image of a 75 × 75 μm^2 area at the perimeter of the electrode / electrolyte interface (EEI) on a *Pure ScYSZ* electrolyte. The nickel particle belt surrounding the EEI is clearly seen.

The Si signal from the Ni particle belt encircling the EEI was weaker than the rest of the EGI, Figure 7.25. The same effect was also observed for Na, K, and Al. Inside the nickel particle belt, the nickel particles most likely amplify the secondary ion signal by charge compensation, artificially exaggerating the measured Si signal intensity.

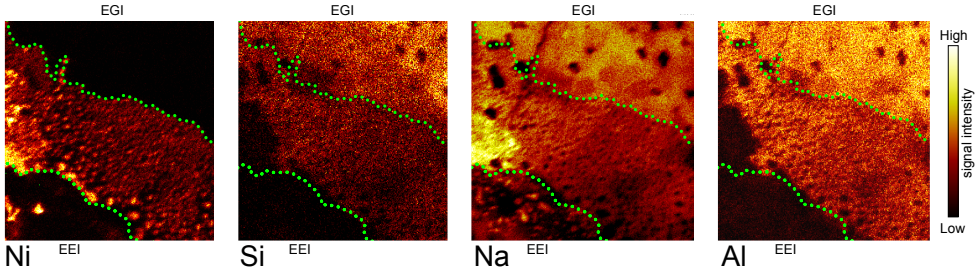

Figure 7.25: ToF-SIMS data representation of a 75 × 75 μm^2 area at the perimeter of the electrode / electrolyte interface (EEI) on *Pure ScYSZ*. Individual Ni particles could be correlated from the SEM image (Figure 7.24) to the ToF-SIMS Ni signal. The signals from the impurity species Si, Na and Al were weaker inside the Ni belt than the rest of the electrolyte/gas interface (EGI).

The 75 × 75 μm^2 area scan also showed Sc and Y concentrating at the TPB inside the EEI, Figure 7.26, and thus confirmed the observation from the sputtered 500 × 500 μm^2 area scans.

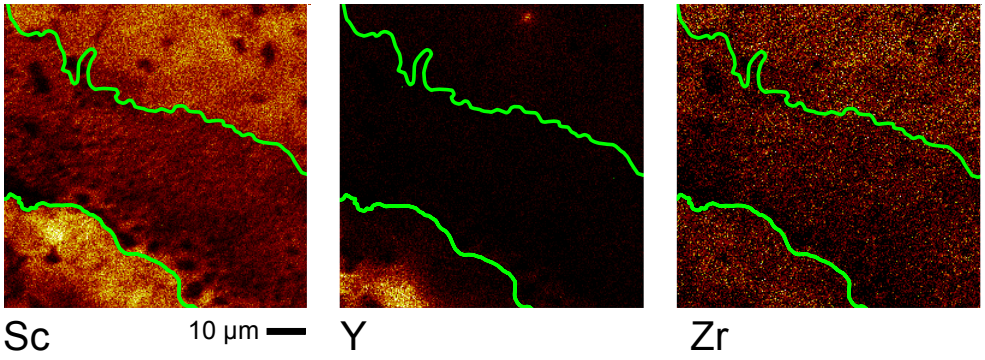

Figure 7.26: ToF-SIMS data representations of a 75 × 75 µm^2 area at the perimeter of the electrode / electrolyte interface (EEI) on *Pure ScYSZ*. The Sc and Y signals were strongest at the three phase boundary. Zr remained uniformly distributed.

7.3.7 Chemical analysis of *Impure ScYSZ*

A ToF-SIMS analysis optimised for high mass resolution was performed on a 500 × 500 µm^2 area of an *Impure ScYSZ* electrolyte. A low magnification SEM image of the analysed area is shown in Figure 7.13, where the EEI is shown to be completely encircled by a nickel particle belt. The results of the 500 × 500 µm^2 area ToF-SIMS analysis of the EEI are shown in Figure 7.27. From the Ni signal the electrode / electrolyte interface and the surrounding nickel particle belt was easily identified. Inside the electrode / electrolyte interface the Si signal was strongest in the centre in an area designated as the *EEI core* in chapter 4. The EEI core was surrounded by an area with a weaker Si signal designated as the *EEI rim zone* in chapter 4. The Sc and Y signals were significantly stronger inside the EEI than from the EGI and corresponded exactly to the EEI area established by SEM. This was not observed on samples which were not polarised. Furthermore, it was seen that the EEI rim zone emitted relatively strong Sc and Y signals.

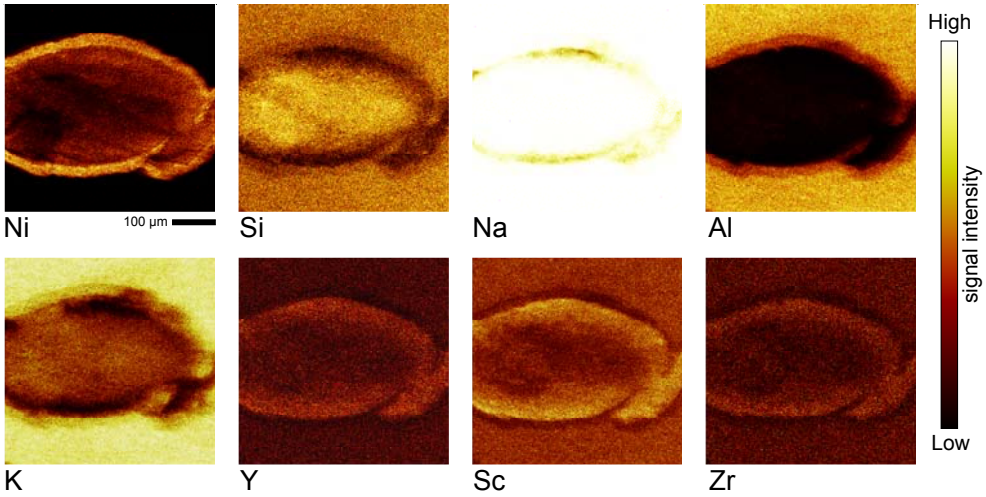

Figure 7.27: ToF-SIMS data representations of a 500 × 500 µm^2 area of the electrode / *Impure ScYSZ* electrolyte interface and surrounding electrolyte / gas interface. A nickel belt surrounded the EEI. Inside the Ni belt the Si, Na and Al signals were weaker than from the rest of the EGI. Strong Sc and Y signals were measured from the EEI.

The scanned area was sputtered with Xe^+ for 60 seconds and analysed again with the scan optimised for high lateral resolution, the results of which are shown in

Figure 7.28. The scanned area was shifted 100 µm to the left as to compare the sputtered surface to the non-sputtered surface. It was found that the Si and Na signals from inside the EEI remained concentrated in the EEI core surrounded by the impurity poor EEI rim zone. After sputtering it was also clearly seen that the Sc and Y signals from the EEI were strongest immediately adjacent to the TPB and not just in the EEI rim zone. The contrast between the non-sputtered and the sputtered areas indicated that impurities, most noticeably seen from the K signal, had segregated to form a surface layer in the electrolyte / gas interface.

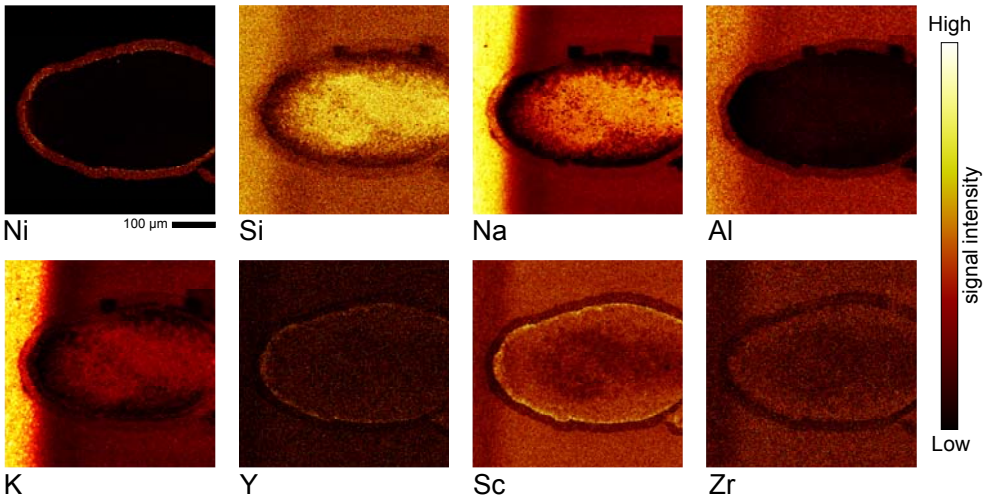

Figure 7.28: ToF-SIMS data representations of a 500 × 500 µm^2 area of the electrode / *Impure ScYSZ* electrolyte interface and surrounding electrolyte / gas interface after 60 seconds Xe^+ sputtering.

A SEM image and the results of a ToF-SIMS analysis, optimised for high lateral resolution, of a 75 × 75 µm^2 area are shown in Figure 7.29 and Figure 7.30 respectively. The analysed area was located at the outer perimeter of the EEI and included a section of the nickel particle belt. The location of individual nickel particles could be identified from the ToF-SIMS data representations and correlated to the SEM image. From the 75 × 75 µm^2 area scan it was seen that the Si and Al signals from within the nickel particle belt were weaker relative their respective signals from the rest of the electrolyte / gas interface.

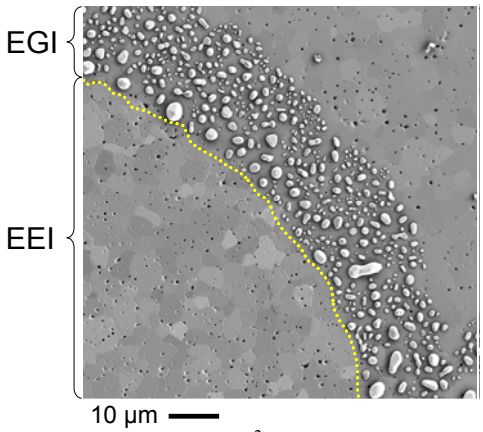

Figure 7.29: SEM image of a 75 × 75 µm^2 area at the perimeter of the electrode / electrolyte interface (EEI) on an *Impure ScYSZ* electrolyte. The nickel particle belt surrounding the EEI is clearly seen.

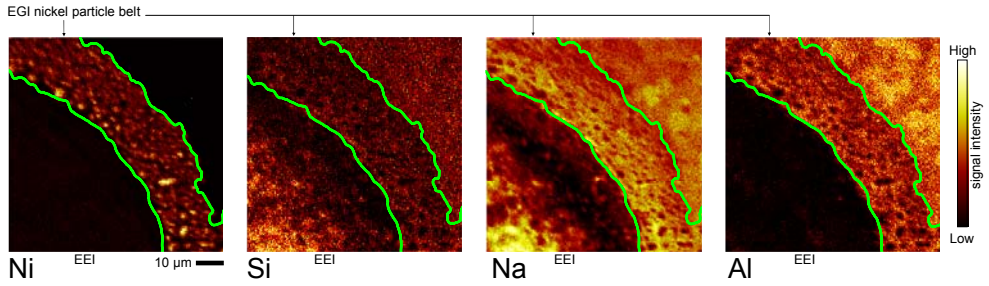

Figure 7.30: ToF-SIMS data representations of a 75 × 75 µm^2 area at the perimeter of the electrode / electrolyte interface (EEI) on *Impure ScYSZ*. Individual Ni particles can be correlated from the SEM image (Figure 7.29) to the ToF-SIMS Ni signal. The signals from the impurity species Si, Na and Al were weaker inside the Ni belt than the rest of the electrolyte/gas interface (EGI).

From the 75 × 75 µm^2 area scan the concentration of Sc and Y at the EEI side of the TPB was further documented as shown in Figure 7.31. Zr did not concentrate noticeably at the TPB and was uniformly distributed across both the EEI and EGI.

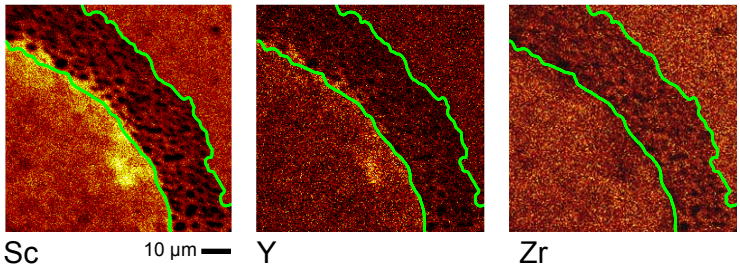

Figure 7.31: ToF-SIMS data representations of a 75 × 75 µm^2 area at the perimeter of the electrode / electrolyte interface (EEI) on *Impure ScYSZ*. The Sc and Y signals were strongest at the three phase boundary. Zr remained uniformly distributed.

7.4 Discussion

Chronoamperometric measurements with an applied anodic overpotential showed that an activation process took place before stable average current levels were reached, Figure 7.6. This was similar to that reported in [12], where an average time of 30 minutes was needed to reach stationary conditions. Impurities such as silica have been shown to react with water at high temperatures to form volatile Si-OH species [13]. At anodic overpotentials water is formed at the TPB and the water formation rate increases as a function of increasing overpotential. Thus it is likely that impurities at the TPB were, at least partially, removed by the water formed near the TPB during anodic polarisation resulting in the observed gradual increase in current until stable average current levels were reached. Impurity species such as Si were found by ToF-SIMS to have weaker signals on the EGI at the TPB. The ToF-SIMS analysis was strong evidence that Si had reacted with water and evaporated away from the TPB. It is believed that the weak Si signal in the Ni particle belt was a genuine measurement of the Si intensity on the surface between the Ni particles and not a consequence of Ni particles blocking secondary ions. This is justified by the fact that a spot size of ~150 nm was used and also that the location of individual nickel particles, and more importantly the open spaces between the particles, could be distinguished in the Si and Al signals. Furthermore, electron conducting particles on a surface tend to amplify the secondary ion signal

hence the surface concentrations could in fact be weaker than the ToF-SIMS measurements suggest.

The electrode polarisation resistances decreased by anodically polarising the electrodes as exemplified by Figure 7.2 and Figure 7.3. After applying large anodic polarisation potentials, impedance spectra measured at OCV showed that the electrodes activated temporarily followed by a slow deactivation over the course of 24 hours, Figure 7.4. The observed activation is believed to be a consequence of impurities, accumulated at the TPB, are removed by reaction with water, formed at the TPB, to form volatile Si-OH species. When the polarisation was lifted the TPB is free of impurities but impurities from the bulk will start (or continue) to segregate to the now free electrolyte surface resulting in the measured increase in polarisation resistance.

Chronoamperometry at electrode potentials above -750 mV vs. Pt / air in wet hydrogen atmospheres (2.4 % H_2O) caused the measured currents to oscillate in a distinct sawtooth pattern. The electrode potential necessary for NiO formation at 850 °C is -680 mV vs. Pt / air, and even though it has been shown that the standard Gibbs energy for oxide formation at a metal surface is lower than in the bulk [14], it is not perceived that NiO formation can fully account for the current oscillation patterns. The current oscillation amplitude and frequency decreased with reduced water content in the hydrogen atmosphere, Figure 7.9, thus clearly showing that the reaction mechanism involved water. This observation is in agreement with [15] and [16], which showed that the hydrogen oxidation reaction rate is enhanced in moist hydrogen atmospheres. The effect of water content on current density is also illustrated by Figure 7.5, where the stable average currents at the same applied electrode potentials were significantly larger in the wet atmospheres. Figure 7.7 and Figure 7.8 show that the amplitude and the frequency of the current oscillations were strongly dependent on the applied potential. This points towards a dynamic electrochemical reaction mechanism.

The facetted shapes of the Ni particles and the uniform widths of the Ni particle belts encircling the EEIs could indicate that nickel was removed from the electrode by gas phase transport and nucleated on the EGI surface, where particle growth occurred. It is also interesting to note that the Ni particles lying on the grains with a flat surface were bigger and fewer in numbers than the Ni particles found on the hill and valley surfaces, Figure 7.12. This also suggests gas phase transport of Ni to the electrolyte surface followed by growth via a surface transport mechanism since surface transport requires less energy on the smooth surfaces than on the hill and valley microstructure. Finally, the truncated octahedral shape of the nickel crystals [17] found in the crater under the EEI surface also indicated a gas phase transport mechanism. It has been reported that the Ni_2-OH complex is responsible for the mass transport at the surface of nickel particles in steam / hydrogen mixtures and that increasing the water content increases the rate of Ni particle growth [18]. Similar nickel depositions in wet hydrogen atmospheres at 1000 °C have also been reported in [19] and [20] showing that Ni particle formation is reproducible under various conditions. Potential sweeps at varying temperatures also indicated that the overpotential necessary to initiate the current oscillation patterns was temperature dependent, Figure 7.10.

Current oscillations similar to those described in the present work have also been reported in [11]. There the current oscillations measured in an air atmosphere were

attributed to migration of Pt and Ag electrode material onto the electrolyte surface to form dendritic structures resulting in an increase in EEI area. A gas phase transport mechanism of electrode species and the subsequent changes in the dendritic microstructure of the electrodes are said to cause the characteristic current oscillation pattern. In [11] the EEI and adjacent EGI areas from a Pd electrode had a remarkably similar appearance to the EEI and EGI observed in the present work, and Nielsen et al. suggest that an unknown surface transport mechanism caused Pd migration and the subsequent current fluctuations. Based on SEM investigations the present work did not find any evidence for dendrite formation having occurred. If a dendritic microstructure had been present one would expect variations in the measured current signals caused by irreversible changes in the electrode area when repeating the measurements. However, Figure 7.9 (region I) shows that the measured currents did not change, when repeating the measurement, indicating that the EEI area did not change. It has been shown that $Ni(OH)_2$ can be formed at the TPB of a SOFC anode in the presence of a high oxygen partial pressure and transported away from its formation site, where it is reduced to re-condense as Ni nanoparticles [21].

Based on the observations described above an alternative explanation for the oscillating current pattern with Ni electrodes is given in the following and illustrated by Figure 7.32. Once impurities at the TPB have been removed while the electrode is polarised and a stable average current level is reached, it is believed that nickel is oxidised to form a passivating $Ni(OH)_2$ layer at the TPB. A proton diffusion reaction mechanism through the nickel electrode has previously been suggested in [16] and supported in chapter 4. As the $Ni(OH)_2$ coverage at the TPB increases, the average proton diffusion path lengthens resulting in a slower reaction rate. The granulated surface microstructure inside the EEI cavities suggests that water formation occurred there. The granulated surface is believed to consist of impurity species mobilised by the formed water, thereafter de-wetting the electrolyte surface. The ToF-SIMS analysis, however, did not have the necessary resolution to detect this. Regardless of the chemical composition, the existence of the granulated surfaces within the EEI is additional argumentation for a “proton diffusion mechanism” through the electrode.

As the $Ni(OH)_2$ film reaches a certain electrode coverage the local H_2O partial pressure decreases, i.e. the gas diffusion of H_2O away from the TPB is faster than the H_2O formation on the electrolyte in the vicinity of the TPB, at which point the H_2 / H_2O atmosphere becomes able to reduce all of the $Ni(OH)_2$ film instantaneously. This results in an instant increase in the measured current.

The onsets of fluctuations in the potential sweeps showed that a passivation layer was formed at a threshold electrode potential value. The threshold value increased with decreasing temperature. Increasing the applied overpotential had the effect of increasing the frequency of the mechanism cycle. At overpotentials below the threshold no passivation layer was formed, hence no current oscillations were observed. Reducing the water content in the atmosphere reduced the oscillation amplitude as a lower water partial pressure slowed the rate of $Ni(OH)_2$ film build up.

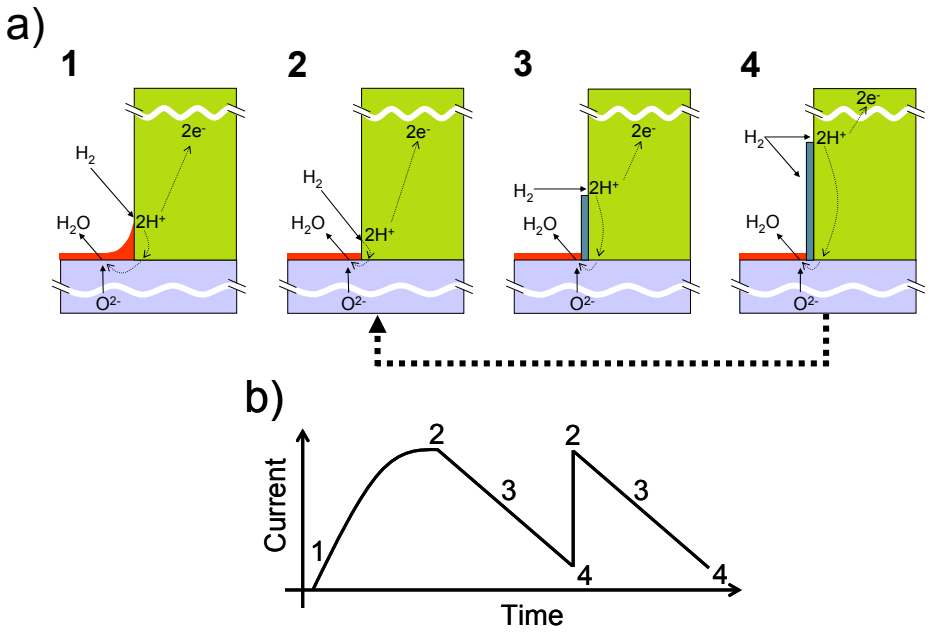

Figure 7.32: a) The suggested mechanism responsible for the occurrence of the oscillating current pattern. 1) → 2) Impurities at the TPB are mobilized by water formation at the TPB resulting in a gradual increase in measured current. 3) Strong anodic polarisation causes a high local pH_2O, which in turn causes the surface of the Ni electrode to passivate by a $Ni(OH)_2$ film. 4) The $Ni(OH)_2$ film coverage increases resulting in a continued decrease in the measured current. 4) → 2) H_2O formation slows and the H_2 atmosphere is able to reduce the $Ni(OH)_2$ film instantaneously resulting in a jump in measured current. b) Sketch of the current oscillation cycle.

The prospect of NiO formation should also be taken into account when considering explanations for the current oscillations. At electrode potentials above -680 (mV vs. Pt / air) NiO formation at the two phase boundary between the electrode and electrolyte may occur. As the proton diffusion path through the electrode is lengthened by passivation layer coverage at the electrode / gas interface the rate of NiO growth might increase. Hence NiO and $Ni(OH)_2$ formation might be coupled, where both species could contribute to the decrease in measured current.

Although the overpotentials at normal SOFC operating conditions are much lower than those applied in this work, the observations from the model system may be correlated to SOFC operation. Results from the model system presented here could explain why a SOFC cermet anode under large current load undergoes microstructural changes by nickel diffusion [5]. If the mechanism suggested above occurred in a cermet it is expected to lead to an increase in the average nickel particle size. This would result in a reduced TPB length and possibly also a loss of percolation routes for electron transport. Studies of long term tested SOFCs have shown degradations of SOFC anodes [5] and these observations are consistent with the nickel transport mechanism suggested here.

The influence of water content at the EEI on the current oscillations found in the model system could signify that high water content is undesirable in a SOFC with respect to long term microstructural stability of the anode. High water content is found near the fuel outlet in a SOFC anode and therefore it is believed that nickel particle agglomeration is most likely to occur there. In addition to this, the low H_2 concentration found at the fuel outlet would promote the growth of a $Ni(OH)_2$ film

especially at high current loads to a much larger degree than at the fuel inlet. However, a high water content may decrease the detrimental effects of impurities at the TPB.

Kinetic demixing in multicomponent solid electrolytes has been shown to occur when applying an electric potential gradient across it [22]. Hence the concentrations of Sc and Y measured at the TPB could be due to kinetic demixing of the dopants from the zirconia matrix. The location of the concentrations of Sc and Y could therefore give an indication of the depth into the EEI, of the reaction zone at the TPB.

7.5 Conclusion

Applying large anodic overpotentials to a point-electrode model of a SOFC anode showed characteristic oscillation patterns in the measured current. The water content in the atmosphere was found to have a large effect on this phenomenon. The nature of the oscillating current pattern was coupled with observations of the electrode and electrolyte surface microstructures and chemical surface analysis to develop a hypothesis for a reaction mechanism. The suggested reaction mechanism implies that proton diffusion through the nickel electrode and the electrolyte is a rate determining step for the overall anode reaction. The suggested mechanism could be taken into consideration when choosing SOFC operation conditions in order to decrease anode degradation.

7.6 References

[1] A.J. McEvoy, Solid State Ionics, 135 (2000) 331.

[2] K. Vels Jensen, S. Primdahl, I. Chorkendorff, M. Mogensen, Solid State Ionics, 144 (2001) 197.

[3] J. Nielsen, T. Jacobsen, Solid State Ionics, 178 (2008) 1769.

[4] M.J. Heneka, E. Ivers-Tiffee, 9th International Symposium on Solid Oxide Fuel Cells, SOFC IX (2005) Quebec City, 534. Singhal, S.C.; Mizusaki, J. (eds.).

[5] Karl Thyden, Ph.D. thesis, Denmark, Risø National Laboratory for Sustainable Energy, Technical University of Denmark, (2008).

[6] R. Hartung, H.H. Möbius, Chemie Ingenieur Technik, 40 (1968) 592.

[7] B.A. Boukamp, Solid State Ionics 18-19 (1986) 136.

[8] M.S. Schmidt, K.V. Hansen, K. Norrman, M. Mogensen, accepted, Solid State Ionics (2008).

[9] T. Jacobsen, K. Vels Hansen, E. Skou, J. Electrochem. Soc. 152 (2005) A2203.

[10] K. Vels Hansen, K. Norrman, M. Mogensen, J. Electrochem Soc. 151 (2004) A1436.

[11] J. Nielsen, T. Jacobsen, Solid State Ionics 178 (2008) 1769.

[12] J. Guindet, C. Roux, A. Hammou, Proceedings of the 2nd International Symposium on SOFCs, Athens, Greece, F. Grosz, P. Zegers, S.C. Singhal and O. Yamamoto, Eds.(1991) 553.

[13] E.J. Opila, J. Am. Ceram. Soc. 86 (2003) 1238.

[14] H.J. de Bruin, Nature 272 (1978) 712.

[15] S.P. Jiang, S.P.S. Badwal, J. Electrochem. Soc. 144 (1997) 3777.

[16] M. Mogensen, J. Høgh, K. V. Hansen, T. Jacobsen, ECS Transactions 7 (1) (2007) 1329, and references therein.

[17] C. L. Cleveland, U. Landman, J. Chem. Phys. 94 (1991) 7376.

[18] J. Sehested, J.A.P. Gelten, I.N. Remediakis, H. Bengaard, J.K. Nørskov, J. Catal 223 (2004) 432.

[19] M. Brown, S. Primdahl, M. Mogensen, J. Electrochem. Soc 147 (2000) 475.

[20] R.J.Aaberg, R. Tunold, M. Mogensen, R.W. Berg, R. Ødegård, J. Electrochem. Soc. 145 (1998) 2244.

[21] K. Du, F. Ernst, M. Garrels, J. Payer, Int. J. Mat. Res. 99 (2008) 548.

[22] M. Martin, J. Chem. Thermodynamics 35 (2003) 1291.

8 Summary & Discussion

In this chapter the results and conclusions from the previous chapters are summarized and drawn into context with previous studies published in literature with special focus on the work previously performed at *Risø-DTU*.

8.1 Electrochemical characterisation

In general it can be concluded that the electrochemical measurements using stabilised nickel point electrodes on stabilised zirconia electrolytes were reproducible to within 30 %. This is considered satisfactory when considering the previous studies using the three-electrode setup at *Risø-DTU*, which have reported ratios between minimum and maximum ASR_p values, measured at OCV, from 2.6 to ~200.

The discrepancies found between the various studies of the SOFC anode electrode reaction in literature most likely stem from variations in purity of the nickel electrodes and electrolyte materials in addition to variations in preparation procedures such as sintering temperature. It should therefore be stressed that identical electrodes were used for all cells and that the electrolyte pellets used in this work were prepared using identical procedures and sintered at the same time in the same oven.

From chapter 4 the effects of impurities on the electrode reaction at the nickel electrode were illustrated by comparing *Pure ScYSZ* with *Impure ScYSZ,* Table 8.1. The large differences in area specific electrode polarisation resistance (ASR_p) and length specific electrode polarisation resistance (LSR_p) clearly showed that impurities were detrimental to electrochemical performance. The high levels of impurities found in the electrode / electrolyte interface on *Impure ScYSZ* inhibited the electrode reaction at the nickel electrode as seen from the larger values of ASR_p and LSR_p. Thus the findings were in agreement with literature where the effect of impurities on electrochemical performance on YSZ electrolytes have been extensively described [1-4]. Impurities also inhibited ion transport across grain boundaries in the bulk [5], as seen from the low calculated ion conductivity values of *Impure ScYSZ*.

The effect of adding alumina to the matrix of ScYSZ has been addressed in literature [6]. Again preparation procedures as well as the need to adjust the amount of added alumina to the impurity levels present in the electrolyte determine electrolyte characteristics. Since the *Impure ScYSZ* and *Al-ScYSZ* electrolyte pellets were prepared using identical procedures a comparison as to the effect of alumina

doping was valid. In chapter 6 it was found that adding alumina did not have any effect towards decreasing electrode polarisation resistances in *Al-ScYSZ* electrolytes, Table 8.1. On the contrary, a slight increase in ASR_p and LSR_p was measured on the alumina doped ScYSZ indicating that alumina acted as an inhibiting impurity itself, when located on the electrolyte surface. The calculated ion conductivity through the *Al-ScYSZ* electrolyte did however increase by a factor 2.7 compared to *Impure ScYSZ*. This was correlated to ToF-SIMS images of sputtered electrolyte surfaces, which showed that alumina had acted as a silica scavenger in the electrolyte bulk as described in literature.

From the experiments described in chapter 3, it was found that scandia and yttria co-doped zirconia, *Pure ScYSZ*, was significantly better with respect to ASR_p and LSR_p than yttria stabilised zirconia, *YSZ*, Table 8.1. The Si content of *YSZ* and *Pure ScYSZ* were 9 and 10 ppm respectively. However there were 470 ppm Na in *YSZ* compared to 39 ppm Na in *Pure ScYSZ*. The measured differences in ASR_p and LSR_p were most likely a direct consequence of the larger Na content in *YSZ*. The calculated ion conductivity through *Pure ScYSZ* was larger than through *YSZ* and was thus in agreement with literature as to the advantageous effects of scandia doping [7].

Table 8.1: Summary of the results of the electrochemical characterisations on the four electrolyte materials using a nickel point-electrode setup at 850 °C in 97.6 % H_2 / 2.4 % H_2O atmospheres. The average values measured on each electrolyte are given.

	ASR_p (Ωcm^2)	LSR_p ($k\Omega cm$)
YSZ	75	13
Pure ScYSZ	48	7
Impure ScYSZ	104	13
Al-ScYSZ	118	16

Prolonged anodic polarisations were seen to activate the electrodes during polarisation as well as during subsequent measurements at OCV. This was believed to be caused by impurities being removed from the three phase boundary by the reaction also suggested by Høgh [8]: SiO_2 (s) + 2 H_2O (g) → $Si(OH)_4$ (g) [9]. After polarisation the anode degraded over the course of 24 hours. During this time it is believed that impurities segregated to the electrolyte surface and "wetted" the three phase boundary. The timescale of the degradation is comparable to the segregation time described in literature [10].

8.2 Microstructural and chemical characterisation

Explanations for the differences in electrochemical performance of the electrodes placed on the electrolytes described above were sought using various surface analysis techniques. In general the microstructural features found on *YSZ*, *Pure ScYSZ*, *Impure ScYSZ* and *Al-ScYSZ* were identical with the most noticeable features being the hill and valley surface microstructure on the electrode / electrolyte interface and the rim ridge surrounding it. The rim ridge height did not differ substantially between the four electrolytes and hence cannot explain the differences in electrochemical performance.

ToF-SIMS measurements confirmed the presence of an impurity layer in the electrolyte / gas interface on all electrolytes. This layer could be removed by ion sputtering. This observation was in agreement with several studies which have shown that this interface becomes covered with impurities at SOFC operation temperatures [10][11]. Attempts at quantifying the thickness of the impurity layer in the EGI were unfortunately unsuccessful in the present work, but using similar techniques Høgh [8] estimated the thickness to be in the order of 1-20 Å.

8.3 Mechanistic considerations

The electrode polarisation resistances at OCV decreased rapidly in all cells during the first 50 hours of measurements at 850 °C. This was also observed at 1000 °C by Vels Hansen (formerly Vels Jensen) [12]. As the EGIs of all electrolyte samples were covered by impurities the explanation for the large decreases in electrode polarisation resistance during the first hours of measurements is unlikely to be found at the EGI. Through ToF-SIMS analysis of the lateral distribution of chemical species on the electrolytes and electrodes, it was found that an impurity poor rim zone had formed on all ScYSZ electrolytes. The observed rim zones are believed to be formed as the electrode / electrolyte interface expanded due to metallic creep of the nickel electrode. The rate of metallic creep could be monitored by the series resistances, which decreased rapidly at the start of the measurements and flattened out as a function of time. The clearing of impurities from the reaction path in the EEI is hypothesised to be responsible for the rapid decrease in electrode polarisation resistance as presented in chapter 4. If the formation of a rim zone, relatively clear of impurities, caused the measured reductions in R_p then the conversion reaction path at the anode could perhaps be identified. Several reaction paths have been suggested in literature [13], some of which are illustrated in Figure 8.1.

In Figure 8.1b) and c) rate determining processes are related to the electrolyte / gas interface. If this interface limited the electrode reaction the R_p values measured throughout this work would be expected to increase during the first hours of measurements when correcting for EEI area expansion. In appendix B estimates of the ASR_p values at the start and end of measurements at 850 °C are presented. It has been shown in literature that 74 % of an YSZ single crystal surface was covered with impurities after one hour at 500 °C [11] and that the surface of an YSZ single crystal was fully saturated with SiO_2 after 300 minutes at 900 °C [10]. Bearing in mind that single crystals nominally have fewer impurities than polycrystals prepared from powders, the electrode polarisation resistances should increase during the course of the measurements if the electrode reaction was limited at the EGI. This was not the case. Therefore, clearing of impurities under the electrode at the three phase boundary and corresponding decrease in R_p values strongly suggested a “proton diffusion” mechanism [13] as illustrated by Figure 8.1a) with d) showing the location of impurities.

The height of the rim ridges observed in this work were comparable to those found by Høgh [8] using identical nickel electrode material (99.999 % Ni) and applied force albeit at a lower temperature (500 – 700 °C). The observed ridges were a factor of 100 smaller than those observed by Vels Hansen [12] at 1000°C on polycrystalline YSZ. Vels Hansen used less pure nickel electrodes (99.8 % and 99.995 % Ni) and impurities from the electrodes were believed to be responsible

for the large rim ridges. In an experiment presented in appendix C the same nickel wire used by Vels Hansen was placed on two *Pure ScYSZ* electrolyte samples, using 315 g weights, for 400 hours at 850 °C. The distinct microstructural features inside the EEIs in addition to well defined rim ridges described by Vels Hansen were reproduced, see appendix C. Furthermore, it was seen that up to three concentric ridges could be identified inside the electrode / electrolyte interface. In the measurements performed by Vels Hansen the weight pressing the electrode down was only 82 g hence electrode creep did not occur to the same extent and rate. As a consequence of the slower electrode expansion, impurities could accumulate at the three phase boundary and form the larger ridges seen by Vels Hansen. However, Vels Hansen did describe similar concentric ridges inside the EEI. Furthermore some indications of the hill and valley surface microstructure fading out towards the outer rim ridge were hinted from AFM and SEM images in [14]. The formation of a rim zone was most likely the cause of the measured decreases in R_p measured in [12].

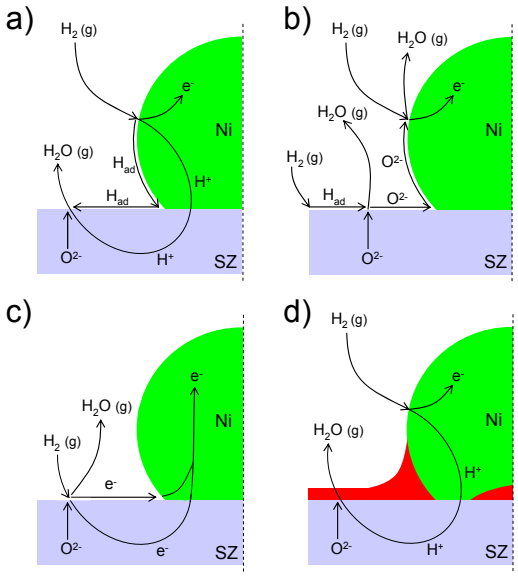

Figure 8.1: A schematic illustration of the reaction paths suggested in literature. a) H_2 adsorbs on Ni and H^+ ions diffuse on the surface or through the electrode and electrolyte to form water. b) O^{2-} migrates from and along the electrolyte surface towards water formation sites at the electrode. c) Water is formed at the electrolyte surface and electrons transported through the electrolyte or electrolyte surface. d) Only impurities adjacent to the three phase boundary influence the proton diffusion path. When an impurity poor rim zone is formed the proton diffusion path is cleared resulting in an improved conversion reaction.

Using ToF-SIMS, Vels Hansen and Høgh both measured weaker impurity signals from inside the nickel electrode / stabilised zirconia electrolyte interfaces compared to that from the electrolyte / gas interface and are thus in agreement with the present work. It appears as though the solid / solid interfaces of the stabilised zirconia electrolytes and nickel electrodes are energetically unfavourable with respect to impurity segregation compared to the stabilised zirconia / gas interface. Høgh used polished YSZ and ScYSZ single crystals. Manufacturers of single crystals take numerous precautions in attempts to eliminate impurities from the finished crystals. But despite these efforts impurities were still measured on the electrodes and electrolytes after these had been heated to elevated temperatures.

In chapter 7 the dynamic effects of sustained anodic polarisations at large overpotentials were presented. It was found that the water content in the measurement atmosphere had a large effect on the reaction rate as also presented in [8] and [15]. It was suggested that the activation of the electrodes due to anodic polarisation was caused by impurities being removed from the three phase boundary by water forming there. Furthermore, nickel was seen to be displaced from the electrode to form a belt of Ni particles surrounding the EEI. A gas phase transport mechanism away from the electrode in the form of a $Ni(OH)_2$ species was suggested. Recent studies support this perception [16]. The formation of cavities in the nickel electrode at the EEI and the surface microstructure on the electrolyte under these cavities suggests that water had been present and are thus a further indication of a "proton diffusion mechanism" through the electrode and electrolyte. The consequences of a nickel gas phase transport mechanism at large current loads in the presence of high water content such as that found at the SOFC anode, gas outlet, could contribute to coarsening of nickel particles resulting in long term degradation of anode performance.

Indications of kinetic demixing [17][18] of the electrolyte dopants Sc and Y were seen after prolonged anodic polarisation as exemplified by Figure 7.28 on page 80. The areas to which Sc and Y cations segregated are believed to indicate the areas within the EEI through which charge transport occurred.

8.4 References

[1] K. Vels Jensen, R. Wallenberg, I. Chorkendorff, M. Mogensen, Solid State Ionics, 160 (2003) 27.

[2] K. Vels Hansen, K. Norrman, and M. Mogensen, J. Electrochem. Soc., 151 (2004) A1436.

[3] K. Norrman, K. Vels Hansen, and M. Mogensen, J. Eur. Ceram. Soc., 26 (2006) 967.

[4] K. Vels Hansen, K. Norrman, and M. Mogensen, Surf. Interface Anal., 38 (2006) 911.

[5] S.P.S. Badwal, Solid State Ionics 76 (1995) 67.

[6] D. Lybye, Y.-L. Liu, J. Eur. Ceramic. Soc., 26 (2006) 599.

[7] O. Yamamoto, Y. Arati, Y. Takeda, N. Imanishi, Y. Mitzutani, M. Kawai, Y. Nakamura, Solid State Ionics 79 (1995) 137.

[8] J.V.T. Høgh, Ph.D. thesis, Risø National Laboratory, Denmark, 2005.

[9] E.J. Opila, J. Am. Ceram. Soc. 86 (2003) 1238.

[10] A.E. Hughes, Jour. American Ceramic Society, 78 (1995) 369.

[11] M. de Ridder, A.G.J. Vervoort, R.G. van Welzenis, H.H. Brongersma, Solid State Ionics, 156 (2003) 255.

[12] K. Vels Jensen, Ph.D. thesis, Risø National Laboratory, Denmark, 2002.

[13] M. Mogensen, J. Høgh, K. Vels Hansen, T. Jacobsen, ECS Transactions 7 (1) (2007) 1329.

[14] M. Mogensen, K. Vels Jensen, M.J. Jørgensen, S. Primdahl, Solid State Ionics 150 (2002) 123.

[15] S.P. Jiang, S.P.S. Badwal, Jour. Electrochem. Soc., 144 (1997) 3777.

[16] K. Du, F. Ernst, M. Garrels, J. Payer, Int. Jour. Materials Research, 99 (2008) 548.

[17] M. Martin, J. Chem. Thermodynamics 35 (2003) 1291.

[18] M. Kilo, M.A. Taylor, C. Argirusis, G. Borchardt, R.A. Jackson, O. Schulz, M. Martin, M. Weller, Solid State Ionics 175 (2004) 823.

9 Conclusions

Through the electrochemical experiments using nickel point-electrodes at 850 °C in humidified hydrogen atmospheres on ScYSZ and YSZ electrolytes followed by subsequent surface analysis as described in the present work the following conclusions could be drawn:

- Significant differences in electrode polarisation resistances were measured on ScYSZ electrolytes with different impurity levels. The highest concentrations of impurities in the electrode / electrolyte interface were measured on the electrolytes with the largest electrode polarisation resistances indicating that impurities hindered the electrode reaction.

- Displacement of impurities from the electrode / electrolyte interface to form a rim zone, with relatively few impurities, adjacent to the three phase boundary resulted in an increase in the electrode reaction rate.

- Prolonged anodic polarisation activated the electrodes. This is suggested to be due to the removal of impurities by water formed at the three phase boundary. The electrodes slowly deactivated when anodic polarisation was lifted which is believed to be a result of renewed impurity concentrations at the three phase boundary.

- Dynamic processes occurred on electrodes when subjected to strong anodic polarisation. A sawtooth oscillation pattern was observed in the measured current signal during chronoamperometry. Nickel transport away from the electrode by a gas phase mechanism was suggested.

- Water in the anode atmosphere promoted the dynamic electrode process which is believed to result in transport of $Ni(OH)_2$ away from the electrode. Such a mechanism could be responsible for the long term degradation observed in SOFC anodes.

- Alumina additions did not improve the electrode conversion reaction at the nickel anode as alumina segregated to the relevant interfaces and charge transport was thus hindered by non-conducting alumina.

- Adding alumina to the electrolyte was advantageous with respect to increasing ion conductivity through the electrolyte by acting as a silica scavenger.

10 Outlook

During the course of this project several issues and ideas for experiments arose which unfortunately could not be realised due to time constraints. It would never the less be most interesting to quantify the chemical composition of the rim ridges observed at the outer perimeter of the electrode / electrolyte interface. An initial unsuccessful attempt at using scanning auger microscopy to this end was made. It failed due to charging effects of the electrolyte surface. Further efforts with scanning auger microscopy should be made and a possible route could be the deposition of a grounded metal grid across the electrode / electrolyte interface to eliminate charging effects.

Using point electrodes in the form of nickel wires has many advantages and the expanding electrode provided interesting results. It would however also be interesting to have a stationary electrode. This could to some degree be achieved by using lighter weights to press the electrode onto the electrolyte. An ideal solution would be patterned electrodes deposited through a mask by techniques such as pulsed laser deposition or plasma enhanced chemical vapour deposition. A further advantage of patterned electrodes would be that one could tailor the three phase boundary length : EEI area ratio to give some further insight into the anode reaction mechanism. The disadvantages are that the patterned electrodes cannot be removed by simply lifting them off the electrolyte making subsequent surface analysis more challenging.

The continuous development of scanning probe microscopes able to operate at elevated temperatures opens up the possibility to conduct impedance spectroscopy on selected grains, grain boundaries of electrolytes or the three phase boundary at patterned electrodes. This technique could offer great insight into understanding electrode reactions.

Even if impurities can be prevented from wetting grain boundaries in the electrolyte bulk by adding scavengers such as alumina the solution to reducing the detrimental effects of impurities that inevitably segregate to the electrolyte surface has yet to be found. New anode composite anode materials and designs currently being researched at *Risø-DTU* and other institutions with the aim of expanding the three phase boundary length could perhaps effectively reduce the influence of impurities at the three phase boundary.

Appendices A – H

Appendix A

The electrolyte pellets were polished using the following procedure with the names referring to *Struers* consumables and discs:

Step1:	
Surface:	MD-Piano 220 (68µm)
Suspension:	-
Lubricant:	Water
Force:	10 N / sample
Direction:	with surface
Speed:	150 rpm
Time:	3:00 min

Step 2:	
Surface:	MD-Piano 1200 (15µm)
Suspension:	-
Lubricant:	Water
Force:	10 N / sample
Direction:	with surface
Speed:	150 rpm
Time:	6:00 min

Step3:	
Surface:	MD-Largo
Suspension:	DiaPro All./Lar. (9µm)
Dose:	6
Lubricant:	-
Force:	15 N / sample
Direction:	with surface
Speed:	150 rpm
Time:	6:00 min

Step 4:	
Surface:	MD-Dac
Suspension:	DiaPro Dac (3µm)
Dose:	6
Lubricant:	-
Force:	15 N / sample
Direction:	with surface
Speed:	150 rpm
Time:	8:00 min

Step5:	
Surface:	MD-Dur
Suspension:	DiaPro 1µm
Dose:	10
Lubricant:	Blue lubricant
Dose:	6
Force:	15 N / sample
Direction:	with surface
Speed:	150 rpm
Time:	8:00 min

Step6:	
Surface:	MD-Mol
Suspension:	DiaPro 1µm
Dose:	10
Lubricant:	Blue lubricant
Dose:	6
Force:	15 N / sample
Direction:	with surface
Speed:	150 rpm
Time:	8:00 min

Step7:	
Surface:	MD-Nap
Suspension:	DiaPro ¼ µm
Dose:	manual
Lubricant:	Blue lubricant
Dose:	1
Force:	25 N / sample
Direction:	with surface
Speed:	150 rpm
Time:	8:00 min

Appendix B

To illustrate that the rapid decrease in nickel electrode polarisation resistance over time on the stabilised zirconia electrolytes was not simply due to an increase in the electrode / electrolyte interface (EEI) area the following calculation is performed. Using the final series resistance measurements and the final EEI areas measured by SEM, the ion conductivity, σ, was calculated from the Newman formula:

$$r = \frac{1}{4\,\sigma\,R_s}$$

Using the average σ value calculated from each electrolyte, the area at the start of the impedance measurements was calculated from the initial measured values of R_s. The area specific electrode polarisation resistance (ASR_p) could thus be calculated at the beginning of the impedance measurements and compared with the final ASR_p. The final ASR_p was based on the final measurements of electrode polarisation resistances and the EEI areas measured by SEM. If it is assumed that the reaction zone was limited to a 10 µm wide belt inside the EEI adjacent to the three phase boundary both at the beginning and at the end of the impedance measurements the area specific polarisation resistance of the hypothetical reaction zones can be calculated. It should be noted that the belt area increased due to a general increase in EEI area. As seen from the tables below there is a general reduction in ASR_p between the start and final values when considering the hypothetical reaction belt. This effect was attributed to the clearing of impurities from the belt adjacent to the three phase boundary (*rim zone*). The shape factor introduced by Holm in Electric Contacts, Theory and Applications (1967) Springer Verlag, was not used in the calculations as the ellipticities of the EEIs were negligible with respect to the thickness of the electrolyte samples to have any consequence on the calculated ion conductivity. The results of unpublished dedicated conductivity measurements performed at *Risø-DTU* by Dorthe Lybye on the selected electrolytes are shown with the respective tables. The discrepancies could be found in the fact that the electrolyte pellets tested in this work had not sintered to completion and also the fact that the electrolyte processing was not identical.

Pure ScYSZ:

	EEI Area *final* (μm^2)	R_s *final* (Ω)	σ ($mScm^{-1}$)	R_s *start* (Ω)	EEI area *start* (μm^2)	R_p *start* ($k\Omega$)	R_p *final* ($k\Omega$)	ASR_p EEI *start* (Ωcm^2)	ASR_p EEI *final* (Ωcm^2)	belt area *start* (μm^2)	belt area *final* (μm^2)	ASR_p belt *start* (Ωcm^2)	ASR_p belt *final* (Ωcm^2)	$\frac{ASR_p \text{ belt } start}{ASR_p \text{ belt } final}$
1	122016	81	157	102	85641	113	37.8	97	46	10060	12068	**11**	**5**	**2.5**
2	125645	112	112	127	55243	124	18.7	69	23	8018	12251	**10**	**2**	**4.3**
3	69782	112	150	136	48173	121	31.7	58	22	7466	9050	**9**	**3**	**3.1**
4	151952	73	156	109	74995	131	22.1	98	34	9394	13504	**12**	**3**	**4.1**
5	125373	80	156	159	35244	141	46.1	50	58	6341	12238	**9**	**6**	**1.6**
6	135863	75	160	120	61876	113	38.4	70	52	8504	12752	**10**	**5**	**2.0**
7	129699	79	156	124	57948	120	47.5	70	62	8219	12452	**10**	**6**	**1.7**
8	112095	79	168	125	57025	111	33.5	63	38	8151	11554	**9**	**4**	**2.3**
9	163079	79	139	108	76390	71	28.7	54	47	9484	14001	**7**	**4**	**1.7**
10	188782	78	131	99	90910	101	29.9	92	56	10374	15088	**10**	**5**	**2.3**
11	154138	80	141	154	37570	63	25.1	24	39	6557	13603	**4**	**3**	**1.2**
12	174663	78	136	95	98727	77	34.1	76	60	10824	14501	**8**	**5**	**1.7**
13	92844	90	162	104	82379	126	52.9	104	49	9860	10487	**12**	**6**	**2.2**
14	95027	97	148	115	67373	155	59.9	104	57	8887	10614	**14**	**6**	**2.2**
15	100261	91	154	122	59864	171	53.0	102	53	8359	10910	**14**	**6**	**2.5**
16	89386	98	151	118	63991	236	85.1	151	76	8653	10284	**20**	**9**	**2.3**
		average:	148 ± 14					average:	48 ± 14					
	previously measured:		194											

Impure ScYSZ:

	EEI Area *final* (μm^2)	R_s *final* (Ω)	σ ($mScm^{-1}$)	R_s *start* (Ω)	EEI area *start* (μm^2)	R_p *start* ($k\Omega$)	R_p *final* ($k\Omega$)	ASR_p EEI *start* (Ωcm^2)	ASR_p EEI *final* (Ωcm^2)	belt area *start* (μm^2)	belt area *final* (μm^2)	ASR_p belt *start* (Ωcm^2)	ASR_p belt *final* (Ωcm^2)	$\frac{ASR_p \text{ belt } start}{ASR_p \text{ belt } final}$
1	155552	225	50	532	34609	387	71.1	134	111	6281	13667	**24**	**10**	**2.5**
2*p*	145362	225	52	404	60013	333	64.9	200	94	8370	13201	**28**	**9**	**3.3**
3	183486	232	45	403	60312	317	72.2	191	133	8392	14871	**27**	**11**	**2.5**
4	191924	210	48	341	84237	224	58.4	189	112	9974	15216	**22**	**9**	**2.5**
5	150385	247	46	674	21562	398	120.0	86	180	4891	13433	**19**	**16**	**1.2**
6	138245	254	47	619	25564	415	62.7	106	87	5354	12866	**22**	**8**	**2.8**
7	170984	232	46	536	34094	517	62.1	176	106	6231	14344	**32**	**9**	**3.6**
8	165950	215	51	613	26067	419	52.6	109	87	5409	14127	**23**	**7**	**3.1**
9	276920	210	40	228	188426	409	32.4	771	90	15074	18340	**62**	**6**	**10.4**
10	144037	307	38	508	37956	432	81.6	164	117	6592	13140	**28**	**11**	**2.7**
11	114724	330	40	662	22351	325	97.4	73	112	4986	11693	**16**	**11**	**1.4**
12	172083	268	40	502	38869	514	60.6	200	104	6675	14391	**34**	**9**	**3.9**
13	71169	350	47	397	62148	519	132.0	323	94	8523	9143	**44**	**12**	**3.7**
14	80348	342	46	468	44722	315	76.4	141	61	7182	9734	**23**	**7**	**3.0**
15	107256	317	43	508	37956	234	91.5	89	98	6592	11295	**15**	**10**	**1.5**
16	104098	357	38	520	36225	294	81.5	107	85	6433	11123	**19**	**9**	**2.1**
		average:	45 ± 4					average:	104 ± 26					
	previously measured:		89											

Al-ScYSZ:

	EEI Area *final* (μm^2)	R_s *final* (Ω)	σ ($mScm^{-1}$)	R_s *start* (Ω)	EEI area *start* (μm^2)	R_p *start* ($k\Omega$)	R_p *final* ($k\Omega$)	ASR_p EEI *start* (Ωcm^2)	ASR_p EEI *final* (Ωcm^2)	belt area *start* (μm^2)	belt area *final* (μm^2)	ASR_p belt *start* (Ωcm^2)	ASR_p belt *final* (Ωcm^2)	$\frac{ASR_p \text{ belt } start}{ASR_p \text{ belt } final}$
1	170243	88	122	131	79245	351	73.7	278	125	9665	14312	**34**	**11**	**3.2**
2*p*	123165	114	111	164	50563	475	34.4	240	42	7657	12127	**36**	**4**	**8.7**
3	150365	97	118	154	57342	521	94.8	299	143	8175	13432	**43**	**13**	**3.3**
4*p*	138926	103	115	169	47615	496	70.4	236	98	7421	12899	**37**	**9**	**4.1**
5	110593	104	128	163	51185	552	104.2	283	115	7706	11475	**43**	**12**	**3.6**
6	124588	106	119	154	57342	431	112.6	247	140	8175	12198	**35**	**14**	**2.6**
7	123934	101	125	151	59643	519	99.7	310	124	8343	12165	**43**	**12**	**3.6**
8	164265	89	123	152	58861	575	95.4	338	157	8286	14053	**48**	**13**	**3.6**
		average:	120 ± 6					average:	118 ± 35					
	previously measured:		113											

YSZ:

	EEI Area *final* (μm^2)	R_s *final* (Ω)	σ ($mScm^{-1}$)	R_s *start* (Ω)	EEI area *start* (μm^2)	R_p *start* ($k\Omega$)	R_p *final* ($k\Omega$)	ASR_p EEI *start* (Ωcm^2)	ASR_p EEI *final* (Ωcm^2)	belt area *start* (μm^2)	belt area *final* (μm^2)	ASR_p belt *start* (Ωcm^2)	ASR_p belt *final* (Ωcm^2)	$\frac{ASR_p \text{ belt } start}{ASR_p \text{ belt } final}$
1	122899	162	72	200	95787	125	98	120	120	10657	12113	**13**	**12**	**1.1**
2	101272	181	69	238	67641	301	89	204	90	8905	10967	**27**	**10**	**2.8**
3	113905	166	70	226	75015	150	39	112	44	9395	11650	**14**	**5**	**3.1**
4	114887	169	69	211	86060	149	40	128	46	10085	11701	**15**	**5**	**3.2**
5	100224	167	67	257	58010	221	76	128	76	8224	10908	**18**	**8**	**2.2**
6	100246	167	77	234	69974	107	67	75	67	9063	10910	**10**	**7**	**1.3**
7	81072	176	76	286	46842	172	97	81	78	7358	9779	**13**	**9**	**1.3**
8	95120	172	73	258	57561	122	83	70	79	8191	10619	**10**	**9**	**1.1**
		average:	72 ± 4					average:	75 ± 24					
	previously measured:		71											

Appendix C

In earlier studies at *Risø-DTU* low purity nickel electrodes (99.8 %) were used at 1000 °C in a similar experimental setup. Most notably the weight pressing the electrodes into the electrolyte was only 82 g. In order to compare the microstructural features found in these earlier studies the experiments were repeated at 850 °C with 315 g weights on *Pure ScYSZ* pellets. The electrodes were placed on the electrolytes for 400 hours in a 2.4 % H_2O / 97.6 % H_2 atmosphere. The electrodes remained at OCV throughout the duration of the experiment. No comprehensive electrochemical characterisations were performed with the low purity nickel electrodes. As seen from the SEM images below similar features to those described in detail by Vels Hansen are seen at the lower temperature.

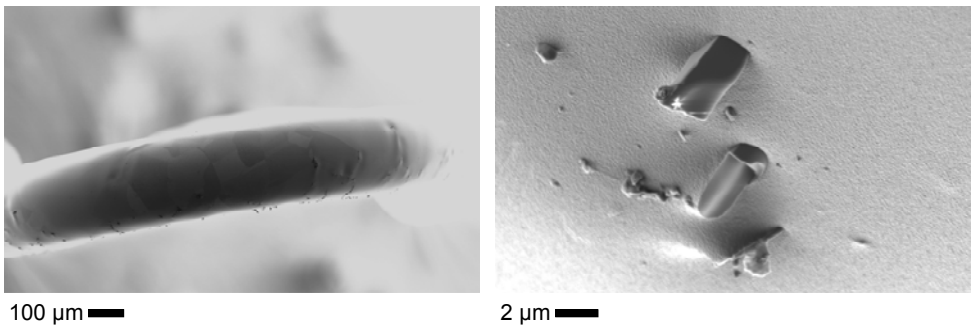

Figure C.1: SEM images of a low purity electrode after bending, annealing and electrochemical etching. Particles are seen embedded in the nickel surface.

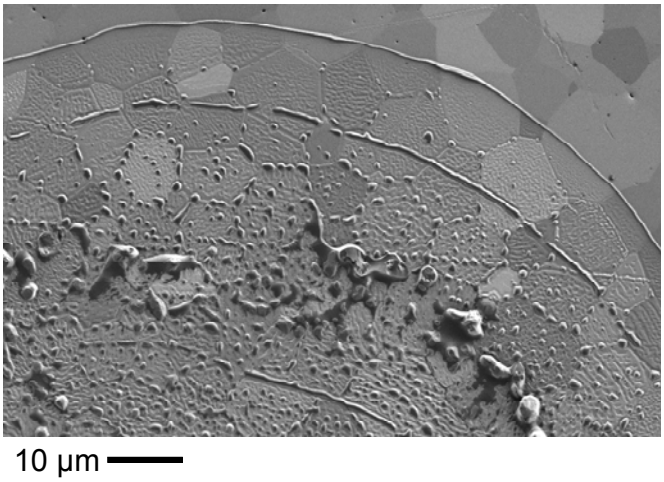

Figure C.2: SEM images of a *Pure ScYSZ* electrolyte surface after 400 hours at 850 °C with a low purity electrode placed on it. Concentric ridges are seen. The hill and valley surface microstructure fades out towards the outer rim ridge.

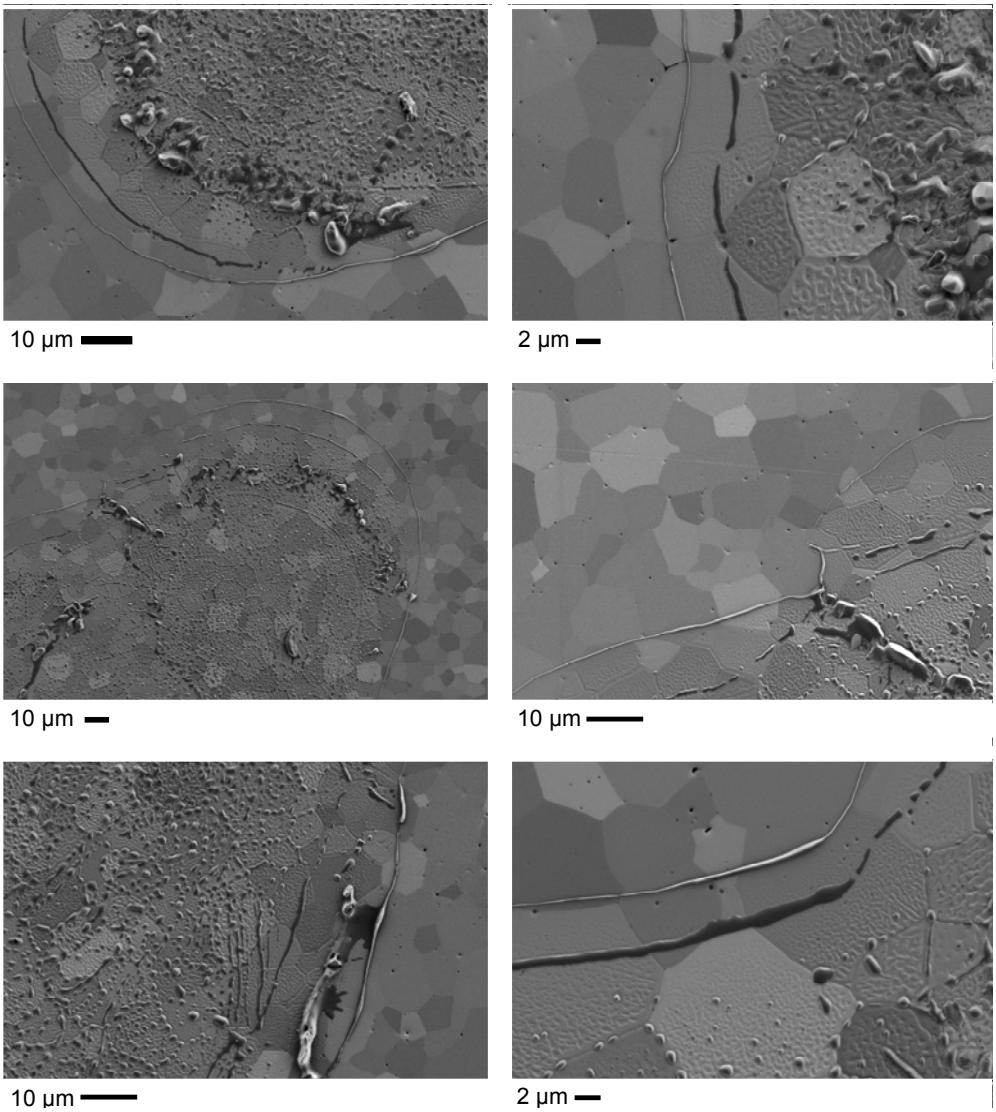

Figure C.3: Additional SEM images of a *Pure ScYSZ* electrolyte surface after 400 hours at 850 °C with a low purity electrode placed on it.

Appendix D

In an attempt to investigate whether any distinct microstructural features could be found beneath the electrolyte surface in the electrode / electrolyte interface and electrolyte / gas interface a focused ion beam (FIB) was used to mill away sections of a *Pure ScYSZ* sample. Although the rim ridge could be identified no distinct features below the electrolyte surface warranting further FIB investigations were identified.

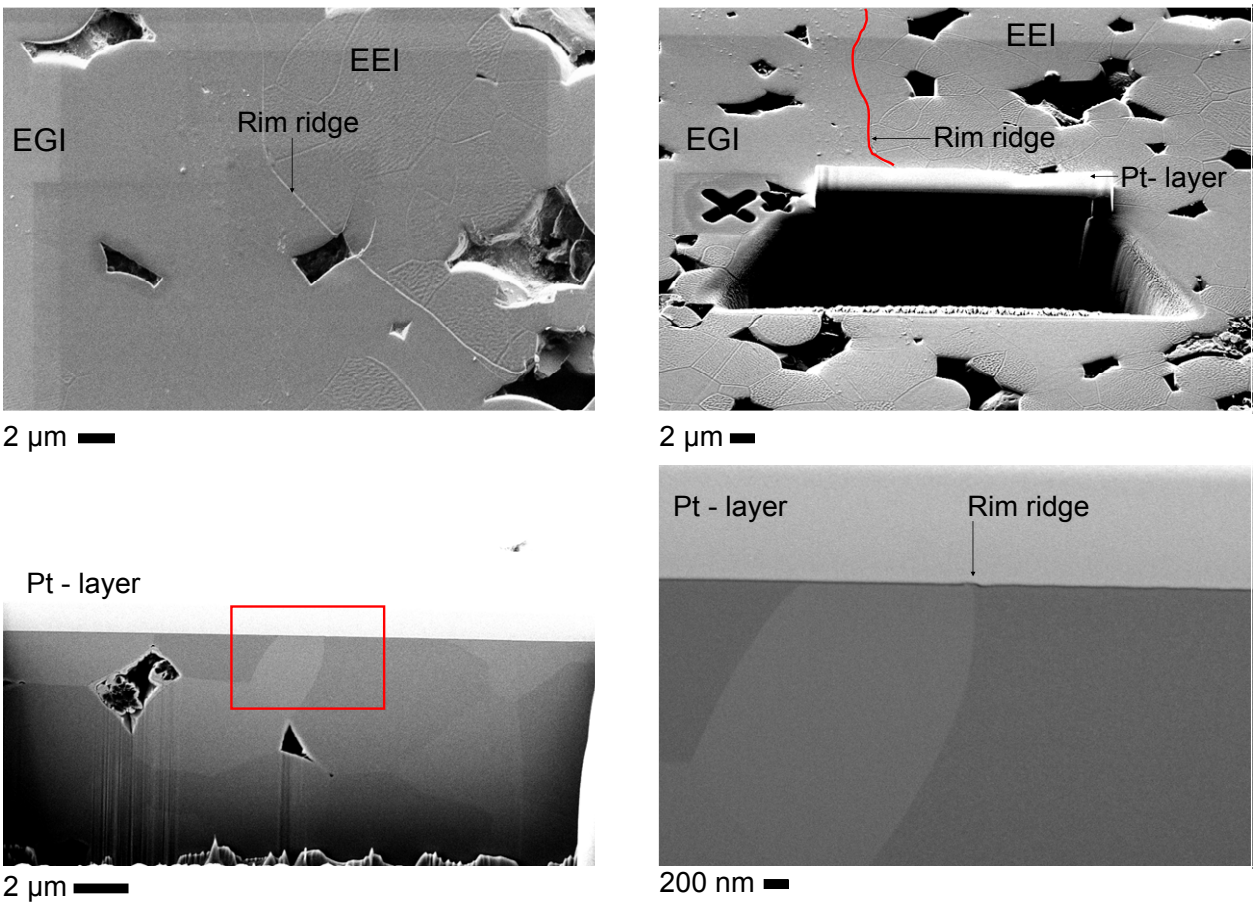

Figure D.1: FIB-SEM images of the surface of a *Pure ScYSZ* sample before and after milling. No significant microstructural features were found below the electrolyte surface under both electrode / electrolyte interfaces (EEI) and electrolyte / gas interfaces (EGI).

Appendix E

During the course of ToF-SIMS analysis it was seen that there was a correlation between the surface microstructure of grains in the electrolyte / gas interface and the measured calcium signal. Grains with more smooth surfaces emitted a stronger Ca signal relative the grains with the rougher surfaces. The degree of surface roughness is believed to be a consequence of the crystal orientation of individual grains. Hence the question remains whether the strong Ca signals are a consequence of enhanced Ca segregation rates through grains of a certain orientation while heated or a measurement artefact with respect to sensitivity factor.

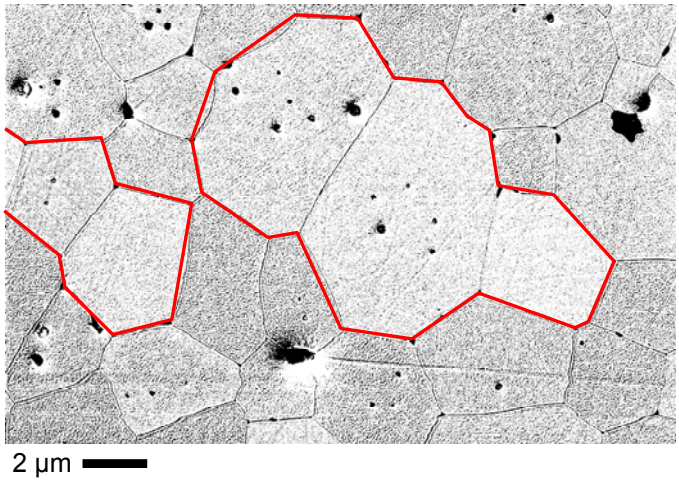

Figure E.1: SEM images of an *Al-ScYSZ* electrolyte surface. The contrast has been adjusted to emphasize the subtle differences in surface microstructure. The lighter grains (with red outline) have a smoother surface than the darker grains.

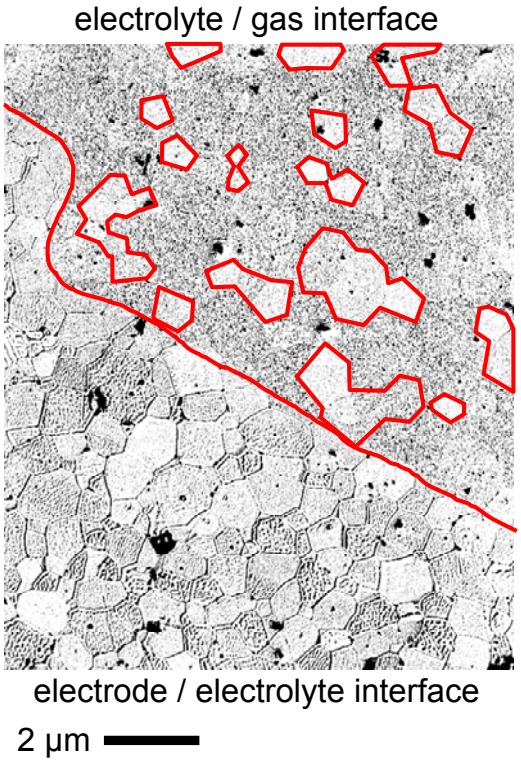

Figure E.2: SEM images of an *Al-ScYSZ* electrolyte surface. The contrast has been adjusted to emphasize the subtle differences in surface microstructure. The lighter grains (with red outline) have a smoother surface than the darker grains.

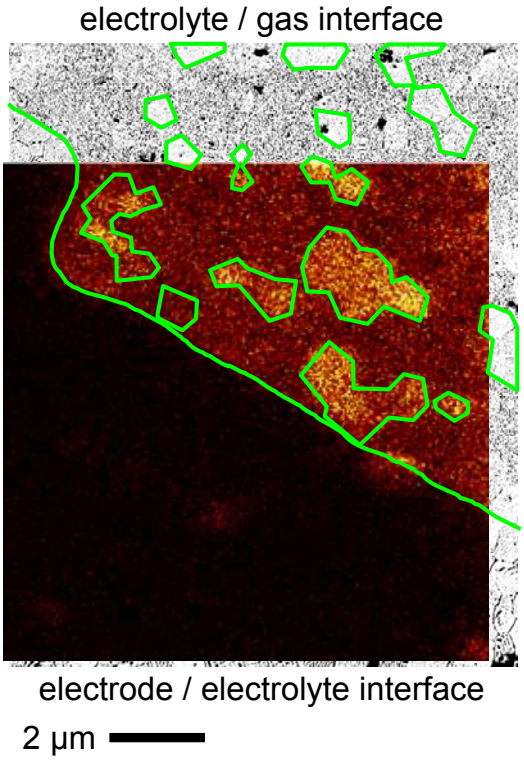

Figure E.3: ToF-SIMS data representation of the detected Ca signal after 4 seconds of Xe^+ sputtering. It is seen that the strongest Ca signals stem from the grains with the smooth surface.

Appendix F

This appendix contains a paper titled *Effects of trace elements at the Ni/ScYSZ interface in a model solid oxide fuel cell anode* which was published in Solid State Ionics. The manuscript was submitted July 13, 2007 and accepted for publication on November 21, 2007.

Appendix G

This appendix contains a paper titled *Characterisation of the Ni/ScYSZ interface in a model solid oxide fuel cell anode* which was has been accepted for publication in Solid State Ionics. The manuscript was submitted April 14, 2008 and accepted for publication on August 4, 2008.

Characterisation of the Ni/ScYSZ interface in a model solid oxide fuel cell anode.

Michael Stenbæk Schmidt[a], Karin Vels Hansen[a], Kion Norrman[b], Mogens Mogensen[a]
[a]Fuel Cells and Solid State Chemistry Department, Risø National Laboratory for Sustainable Energy, Technical University of Denmark.
[b]Polymers for Energy Technology, Risø National Laboratory for Sustainable Energy, Technical University of Denmark.
Frederiksborgvej 399, Dk-4000, Roskilde, Denmark

Corresponding author: M. S. Schmidt: e-mail: michael.stenbaek.schmidt@risoe.dk

ABSTRACT

A nickel point electrode setup was used as a model of an SOFC anode on three slightly different electrolytes of zirconia stabilised by co-doping with scandia and yttria. The effect of electrolyte impurities on the electrode polarisation resistance was investigated by correlating electrochemical impedance spectroscopy data with time-of-flight secondary ion mass spectrometry, scanning electron microscopy and atomic force microscopy data. A semi-quantitative analysis of the electrolyte surfaces showed that the levels of surface impurities inside the electrode/electrolyte interface in close proximity to the three phase boundary have a large effect on the electrode polarisation resistance.

Keywords: Solid oxide fuel cell, segregation of impurities, Ni, ScYSZ, Anode, ToF-SIMS

1. INTRODUCTION

Lowering of the operating temperature of solid oxide fuel cells (SOFC) is essential for commercialization of SOFC. However, at lower operation temperatures the detrimental effects of impurities in the SOFC become more dominant resulting in poorer performance [1]. The industrial grade materials used in SOFC today contain numerous impurities and the role of these impurities at the electrolyte/anode interface and especially at the three phase boundary (TPB), and their effect on overall SOFC performance is the subject of ongoing study [2-6].

SOFC designs commonly use cermet anodes. However, the cermet structure is impractical when studying the surface chemistry of the anode/electrolyte interface and hence a simplified point electrode model of the anode was used. This simple model anode provided a well defined electrode/electrolyte interface (EEI) making it possible to exactly measure the TPB. The model anode eased the task of examining the EEI with various surface analysis methods such as time-of-flight secondary ion mass spectrometry (ToF-SIMS) after characterisation by electrochemical impedance spectroscopy. ToF-SIMS analysis was used to examine the possible link between electrode polarisation resistance and the amount of impurity species found at the electrode/electrolyte interface.

This contribution aims to quantify the effect of impurities in scandia and yttria co-doped zirconia (ScYSZ) electrolytes on the electrode polarisation resistance at the anode of an SOFC. Previous studies have used single crystal electrolytes in an attempt to eliminate the occurrence of impurities at the electrolyte

surface [7]. Despite conducting the measurements at relatively low temperatures (500 - 700 °C) impurities were still found to segregate to the electrolyte surface. As electrolyte single crystals are not an option for commercial SOFC and since it has been shown that impurities still segregate to the surfaces of single crystals, polycrystalline electrolytes were chosen for the present study. Recently the effect of impurities were studied at relatively low (500-700 °C) [7] and high temperatures (1000 °C) [2]. An intermediate temperature of 850 °C was therefore selected for this work.

Three available ScYSZ electrolyte powders were selected for this study. The powders were custom made for Risø National Laboratory for Sustainable Energy, DTU, in previous projects that attempted to optimize the electrolyte with respect to oxide ion conductivity. One electrolyte had a relatively low impurity content compared to the two others. This difference enabled the comparison between impurity content and electrochemical performance. The effect of alumina acting as a silica scavenger in an YSZ electrolyte has been reported in literature [8]. Therefore, the effect on the electrode polarisation resistance by doping the impure ScYSZ electrolyte with alumina was also investigated.

High purity nickel electrodes were used to minimize the contamination coming from the electrode thus allowing a direct comparison of the electrolytes.

Thus, the present work is a study of the effect of impurities in the electrolyte on the polarisation resistance of the Ni – H_2 electrode.

2. EXPERIMENTAL

Pure ($Sc_{0.18}Y_{0.02}Zr_{0.80}O_{1.9}$) and impure ($Sc_{0.16}Y_{0.04}Zr_{0.80}O_{1.9}$) ScYSZ powders were analyzed by glow discharge mass spectrometry (GDMS) to determine the exact levels of impurity species, Table 1. The difference in Sc_2O_3 content between the two electrolytes was only 1.1 weight %, and thus only small differences in ionic conductivity based on doping levels were expected [9].

Table 1: Glow discharge mass spectroscopy data in ppm by weight. Note the large difference in Si, Na and Mg content.

	Li	Na	Mg	Al	Si	K	Ca	Cr	Mn	Fe	Ni	Cl
Pure ScYSZ	0.74	39	0.43	6.9	10	16	9.6	1.8	0.52	10	21	650
Impure ScYSZ	0.15	370	310	12	380	22	80	10	1.5	51	8.8	18

The ScYSZ powders were pressed into pellets and sintered at 1315 °C for 12 hours. 3 mm thick electrolyte samples with a 16 mm diameter were polished with the final step being 0.25 µm diamond particles. To investigate the effect of alumina, a third electrolyte was prepared by adding AlO(OH) powder (15 ppm wt Si) and ball milling it with the impure ScYSZ powder prior to pressing and sintering as described in [1]. AlO(OH) powder corresponding to an aluminium content of 2 % of the metal cations in the electrolyte was added.

The point electrodes consisted of high purity (99.999 %) 0.5 mm diameter nickel wire (Puratronic, Johnson Matthey). 40 mm long pieces of the wire were bent 10 mm from one end to form a point and annealed for 24 hours at 1000 °C in Ar with 9 % H_2. The annealing was performed in order to restore the Ni crystals (grains) that were damaged by deformation when the wire was bent. Finally, the nickel tips were electropolished for 4 minutes in an electrolyte consisting of alcohol and perchloric acid cooled to -5 °C.

A custom made rig was used for electrochemical impedance measurements. The rig parts consisted of alumina and all electrical leads were platinum. The rig fitted four, three-electrode cells in which the Ni point electrode was the working electrode. Figure 1 gives the principle and the dimensions of the configuration. Counter and reference electrodes were painted onto the bottom of the electrolyte with platinum slurry (Degussa-308A). The painted electrode areas were placed on two separate platinum meshes to ensure gas access to the entire area of the painted electrodes and to connect the painted electrodes to the measurement equipment. The mounting of the electrode/electrolyte pairs into the rig took place in a laminar air flow bench where particles down to 0.3 µm were filtered out. This effectively reduced dust contamination of the rig and its contents. The nickel wires acting as working electrodes were set onto the centre of the polished electrolyte surface and pressed down by 315 g copper weights via two-bore alumina tubes. Weights were necessary to ensure good physical contact between the electrode and electrolyte [7].

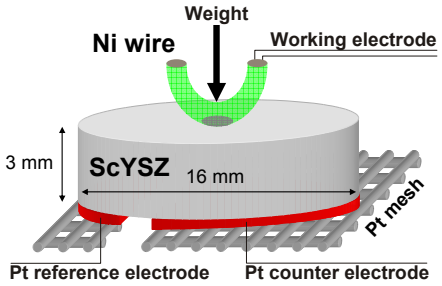

Figure 2: Schematic of the 3-electrode configuration.

2.1 Electrochemical impedance spectroscopy

After heating to 850°C by 5 °C / minute in 88 % Ar / 9 % H_2 / 2.4 % H_2O the atmosphere was switched to 97.6 % H_2 / 2.4 % H_2O. Electrochemical impedance spectroscopy was performed at open circuit voltage (OCV) with an applied RMS amplitude of 21 mV using a Solartron 1250 frequency response analyser coupled with a Solartron SI 1287 potentiostat. The measurements were started half an hour after reaching 850 °C leaving time for stabilisation of temperature and gas composition. Electrochemical measurements were made over a span of 300 and 485 hours for the two pure electrolyte series and 675 and 1125 hours for the two impure electrolyte series. Two series of alumina added electrolytes were measured over a span of 485 and 550 hours. The obtained impedance spectra were fitted to the equivalent circuit $R_s(R_{p1}Q_1)(R_{p2}Q_2)$ [10]. From the fitted circuits, average values for the exponential *n* in the constant phase element $Q^\circ (j\,\omega)^n$ were obtained for each RQ pair. These average *n*-values were locked and used to re-evaluate R_{p1} and R_{p2} for each electrolyte/electrode pair during the course of the measurement.

2.2 Microscopy

Following the impedance measurements the nickel electrodes were lifted off the electrolytes. The electrodes and electrolytes were examined with a field emission gun scanning electron microscope (SEM) (Supra 35, Zeiss) in order to determine the areas and perimeter lengths of the electrolyte/electrode interfaces. The measured EEI areas and perimeter lengths together with the final polarisation resistance values enabled the calculation of the area- and length specific polarisation resistances (ASR_p and LSR_p respectively). Secondary electrons with a 1 keV acceleration voltage were used to examine the surface microstructures on the

ScYSZ without necessitating carbon coating. Atomic force microscopy (DualScope AFM, DME Danish Micro Engineering A/S) was used in tapping mode to obtain three-dimensional images of the EEI and to quantify the microstructural features observed with SEM.

2.3 Chemical analysis

Time-of-flight secondary ion mass spectrometry (TOF-SIMS IV, ION-TOF GmbH) was performed on each electrolyte material to obtain a qualitative measurement of the lateral distribution of trace elements on the electrolytes. ToF-SIMS images with high mass resolution and low lateral resolution were acquired using 30-ns pulses of 25-keV Bi_3^+ that were bunched to form ion packets with a nominal temporal extent of < 0.9 ns at a repetition rate of 10 kHz yielding a target current of 200 fA. These primary ion conditions were used to scan up to 500×500 μm^2 areas of the sample surfaces. Additional ToF-SIMS images with low mass resolution and high lateral resolution were acquired covering areas down to 20×20 μm^2 of the sample surface using 100-ns pulses of 25-keV Bi_3^+ at a repetition rate of 10 kHz yielding a target current of ~10 fA. The high lateral resolution enabled the correlation between ToF-SIMS and SEM images. For the sputter process 3-kV Xe^+ (sputter ions) were used resulting in a target current of 19 nA. 500 × 500 μm^2 areas of the surface were sputtered for an accumulated total time of 4, 16, 40/70 and 120 seconds. Electron bombardment (20 eV) was used to minimize charge build-up at the surface. Desorbed secondary ions were accelerated to 2 keV, mass analyzed in the flight tube, and post-accelerated to 10 keV before detection.

The ToF-SIMS data analysis software enabled separate regions of interest of the same scan to be evaluated individually. The EEI could thus be singled out and compared with the electrolyte/gas interface (EGI) with respect to their signals of Si and other impurity species. A semi-quantitative analysis of the relative changes down through the top surface layers of the EEI and EGI could thus be made by ToF-SIMS and sputtering by Xe^+.

3. RESULTS

3.1 Electrochemistry

3.1.1 Pure ScYSZ

A large drop in the electrode polarisation resistance, R_p, at OCV of the Ni-electrode on the pure electrolytes was observed over the first 1 – 2 days from ~140 kΩ at t = 0 h to ~60 kΩ at t = 50 hours, Figure 2a). The polarisation resistance values fluctuated during the course of the measurement but stabilised around 40 kΩ after 350 hours. Similarly, the series resistance, R_s, decreased from an initial value of ~115 Ω at a rate of ~0.5 Ω/hour during the first 50 hours to ~100 Ω, Figure 2b). Note, however, that R_s is 3 orders of magnitude lower than R_p. After this initial rapid decrease the series resistances reached a steady rate of decrease of ~0.02 Ω/hour. The average series resistance at the end of the measurements was 90 Ω.

The polarisation resistances of the equivalent circuit $R_s(R_{p1}Q_{p1})(R_{p2}Q_{p2})$ (with locked n-values) were split up into R_{p1} and R_{p2}. A common trend was found for all eight samples. As shown in Figure 2b), the resistance corresponding to the high frequency arc (R_{p1}) after an initial stabilisation period, was about 40 kΩ larger than the low frequency arc (R_{p2}). The fluctuations in the total resistance were mainly due to changes in R_{p1}.

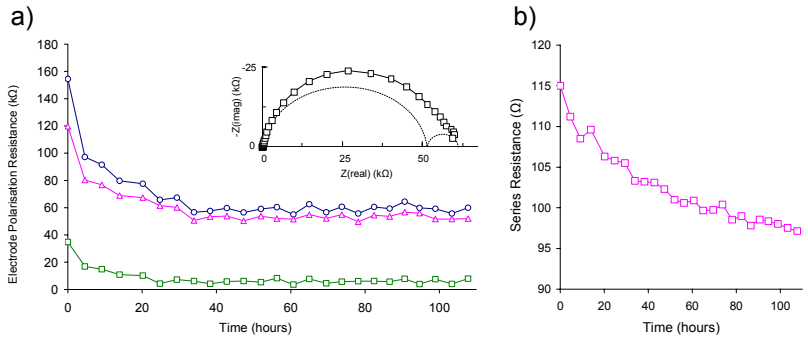

Figure 3: a) The total polarisation resistance of a Ni point electrode at OCV on a pure $Sc_{0.18}Y_{0.02}Zr_{0.80}O_{1.9}$ electrolyte (○) split up into two components R_{p1} (Δ) and R_{p2} (□) corresponding to the equivalent circuit model $R_s(R_{p1}Q_1)(R_{p2}Q_2)$. The *n*-values for this sample were locked at n_1=0.94 and n_2=0.61. The lines are simple connections between the measured values. b) The series resistance, R_s, which mainly originates from the electrolyte, as a function of time.

3.1.2 Impure ScYSZ

The polarisation resistance at OCV of the Ni-electrodes on the impure ScYSZ initially showed large drops in electrode polarisation resistance from ~500 kΩ at *t* = 0 hours to ~ 160 kΩ at *t* = 50 hours, Figure 3a). After 400 hours R_p had stabilised at ~60 kΩ. Series resistances of ~500 Ω were measured on the impure electrolytes initially, but in contrast to the case of the pure electrolyte these values did not decrease immediately. On the contrary, R_s values were stable or even increased slightly during a 20 hour period, Figure 3b). After this initial 20 hour lag period the series resistances started to decrease at an initial rate of ~0.7 Ω/h. The rate of decrease in series resistance slowed down throughout the measurement, reaching a rate of decrease of ~0.4 Ω/h at the end of the measurement. The average series resistance at the end of the measurements was 230 Ω.

The polarisation resistances of the equivalent circuit $R_s(R_{p1}Q_{p1})(R_{p2}Q_{p2})$ were split up into R_{p1} and R_{p2}, and the same common trend was found for all eight samples as shown in Figure 3a). At t=0 the resistance corresponding to the high frequency R_{p1} was four times larger than the low frequency resistance R_{p2}. R_{p1} dropped during the first 50 hours while the magnitude of the low frequency R_{p2}, remained stable during the course of the experiment. After 400 hours R_{p1} and R_{p2} had stabilised and were approximately the same size.

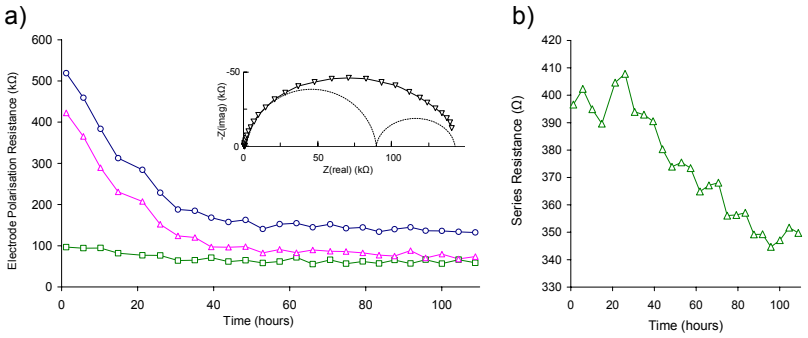

Figure 4: a) The total electrode polarisation resistance of a Ni point electrode on an impure $Sc_{0.16}Y_{0.04}Zr_{0.80}O_{1.9}$ electrolyte (○) split up into two components R_{p1} (Δ) and R_{p2} (□) corresponding to the equivalent circuit model $R_s(R_{p1}Q_1)(R_{p2}Q_2)$. The *n*-values for this sample were locked at n_1=0.85 and n_2=0.69. The lines are simple connections between the measured values. b) The series resistance, R_s, which mainly originates from the electrolyte, as a function of time.

3.1.3 Impure ScYSZ with alumina additions

The R_p of the Ni-electrodes on the alumina containing electrolyte also experienced large drops in the beginning from ~490 kΩ at t = 0 h to ~150 kΩ at t = 50 h. After 400 hours R_p had stabilised at ~95 kΩ. During the first 50 hours of measurements the series resistances measured on the alumina added electrolyte decreased from ~160 Ω at a rate of ~0.3 Ω/hour. Hereafter the rate of series resistance decrease stabilised at ~0.02 Ω/hour for the remainder of the measurement. The average series resistances measured on the impure electrolyte with added alumina was 100 Ω, about half of that measured on the samples without added alumina (230 Ω). A lag period in the course of R_s at the start of the measurement was not observed for the impure ScYSZ with added alumina. The added alumina did not reduce the electrode polarisation resistances as the final stabilised values were measured to be at the same levels as the impure electrolyte without added alumina (see Table 2).

3.1.4 EIS summary

Table 2 lists the first and the last R_p measured on each Ni-electrode together with the calculated ASR_p and LSR_p values based on SEM measurements of the EEI area and perimeter length using the last measured R_p. The relative scatter of the results for both ASR_p and LSR_p values is approximately the same for all three types of electrolyte.

Table 2: Initial and final (stabilised) electrode polarisation resistance values and corresponding area- and length specific resistances of pure- (PS), impure- (IS), and alumina added impure- (Al) electrolytes. The samples with the porous microstructure (see text) are marked with a *P*.

Pure ScYSZ

	$R_{p\text{-}start}$ (kΩ)	$R_{p\text{-}stabil}$ (kΩ)	ASR_p (Ωcm²)	LSR_p (kΩcm)
1	113	37.8	46	6.2
2	124	18.7	23	3.3
3	121	31.7	22	3.9
4	131	22.1	34	4.3
5	141	46.1	58	7.7
6	113	38.4	52	5.8
7	120	47.5	62	8.4
8	111	33.5	38	5.1
Average			**42**	**5.6**
Std. deviation			15	1.8
Std. dev. %			36	33

Impure ScYSZ

	$R_{p\text{-}start}$ (kΩ)	$R_{p\text{-}stabil}$ (kΩ)	ASR_p (Ωcm²)	LSR_p (kΩcm)
1	387	71.1	111	13.2
2	333	64.9	94	12.2 *P*
3	317	72.2	133	12.3
4	224	58.4	112	10.5
5	398	120.0	180	22.5
6	415	62.7	87	12.9
7	517	62.1	106	13.1
8	419	52.6	87	11.4
Average			**114**	**13.5**
Std. deviation			31	3.7
Std. dev. %			27	28

Impure ScYSZ + Al_2O_3

	$R_{p\text{-}start}$ (kΩ)	$R_{p\text{-}stabil}$ (kΩ)	ASR_p (Ωcm²)	LSR_p (kΩcm)
1	351	73.7	125	17.4
2	475	34.4	42	5.8 *P*
3	521	94.8	143	17.2
4	496	70.4	98	11.9 *P*
5	552	104.2	115	15.5
6	431	112.6	140	21.3
7	519	99.7	124	18.2
8	575	95.4	157	20.4
Average			**118**	**16.0**
Std. deviation			35	5.0
Std. dev. %			30	31

3.2 Microstructure

An undulating microstructure previously described as the hill and valley microstructure [2] covered the EEI on the pure and impure electrolytes. The EGIs were smooth in comparison to the hill and valley microstructure inside the EEIs. Figure 4 shows an AFM micrograph from a pure electrolyte surface, containing both some EEI and EGI. On all samples a characteristic 5-20 nm tall rim ridge separated the EEI from the EGI similar to the observations reported earlier [2, 5, 11]. Additional SEM images of the hill and valley microstructure have previously been presented elsewhere [12].

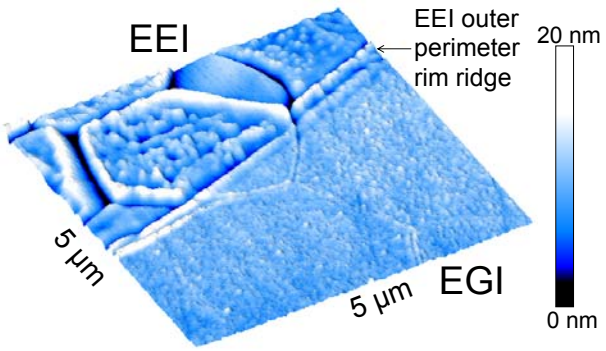

Figure 5: Atomic force microscopy image of the perimeter of the nickel electrode/electrolyte interface (EEI) on a pure electrolyte. A 5-20 nm tall ridge separated the EEI from the electrolyte/gas interface (EGI).

In addition to the hill and valley microstructure one sample of the impure electrolyte and two samples of the electrolyte with added alumina also contained large areas of a layer with a porous microstructure. The layer rose approximately 40 nm above the plane of the hill and valley structure. The porous layer had flaked off in some areas exposing a very rough and coarse surface. In the corresponding areas on the nickel electrode, pieces of electrolyte were attached. An alumina rich phase was found inside the porous layer on the electrolytes with added alumina, Figure 5a)(2). The porous layer did not form on the alumina rich phase. Furthermore, the porous structure was separated from the rim ridge by a 5-20 µm wide hill and valley belt referred to here as the *rim zone*. In a few areas the rim zone was not visible and the porous layer directly bordered the EGI. Figure 5 shows the porous layer found on the impure ScYSZ samples with added alumina. The porous layers on the impure electrolytes without alumina looked very similar to the one shown in Figure 5.

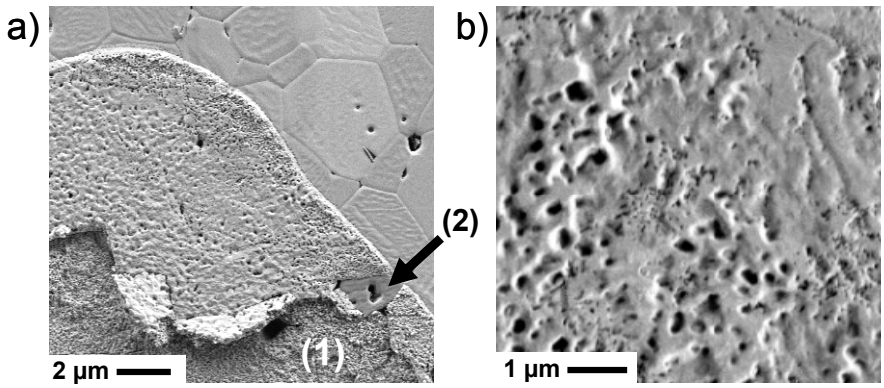

Figure 6: SEM micrograph of the electrode/electrolyte interface on an alumina doped impure electrolyte sample. a) A porous layer is seen in the centre of the electrode/electrolyte interface. Parts of the surface of the porous layer have been ripped off upon removing the electrode (1). (2) Alumina rich phase. b) A larger magnification of the porous layer.

3.3 Chemical analysis

3.3.1 Pure electrolyte

ToF-SIMS analysis of the pure electrolyte surface identified the presence of Na, Mg, Al, K, Ca, Mn, Ni, La, Si in addition to Zr, Y and Sc. The lateral distribution of the Si signal was representative of the lateral distribution of the Na,

Mg, Al, K and Ca signals, and thus Si will be used to describe the location of impurity species in the following.

An area of 500 × 500 μm^2 was scanned on the pure electrolyte prior to sputtering. Figure 6 shows the Si signal intensities. The Si counts in the whole EEI was 0.09 counts/μm^2 compared to 1.03 counts/μm^2 in the EGI, Table 3. By evaluating the Si counts along a line through the EEI it was found that the Si signal inside the EEI was most intense in the centre, referred to here as the *EEI core*, and faded towards the perimeter of the EEI, Figure 7a), (1) to (2). When evaluating the Si counts from the EEI core it was found that this area had a stronger Si signal (0.13 counts/μm^2) than the entire EEI area (0.09 counts/μm^2). The ratio between the Si signal intensity in the EEI and the Si signal intensity from the EGI is a measure of the silicon concentration in the EEI relative to the EGI and was found to be 0.09 on the pure electrolyte, Table 3.

Figure 8 shows the Si signal from a ToF-SIMS analysis of a 50 × 50 μm^2 area at the border between the EEI and EGI on the pure electrolyte plotted as a function of sputter time. The EEI signal was thus obtained from the EEI rim zone. Since the area scan was optimised for high lateral resolution it was possible to distinguish the EEI from the EGI and to correlate the ion image with SEM images of the same area [12].

Figure 8 shows that the Si signal intensity decreased in both the EEI and EGI areas as a function of Xe^+ sputter time. However, the Si signal inside the EEI was found to be lower than outside as also seen on the 500 × 500 μm^2 area scan, Figure 6 and Table 3. The fact that the silicon signal in both EEI and EGI rapidly decreased as a function of sputter time shows that the silicon impurities had accumulated in a surface layer.

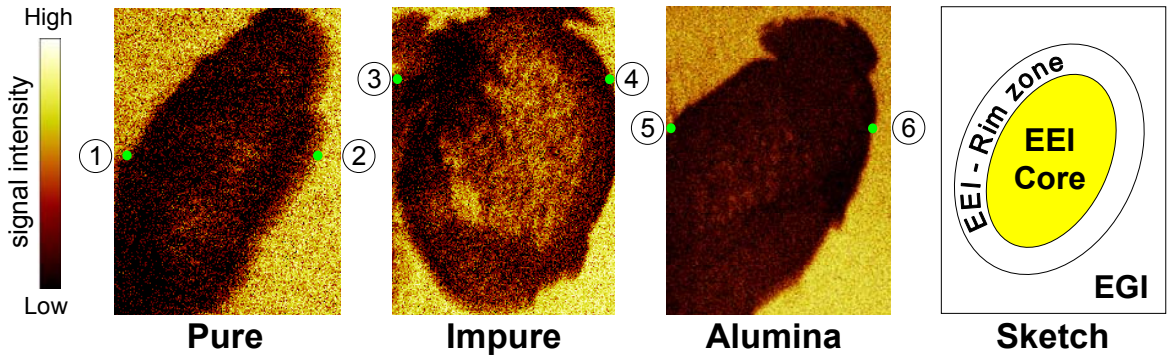

Figure 7: 350 × 500 μm^2 ToF-SIMS logarithmic data representations of the silicon signal on the pure, impure and alumina added electrolytes. The white colour corresponds to the most intense signal and black corresponds to the weakest signal. Inside the electrode/electrolyte interface (EEI) the Si signal is strongest in the centre on all three electrolytes (EEI core). Surrounding the EEI core is a rim zone with a weaker Si signal. The concepts are illustrated in the sketch to the right.

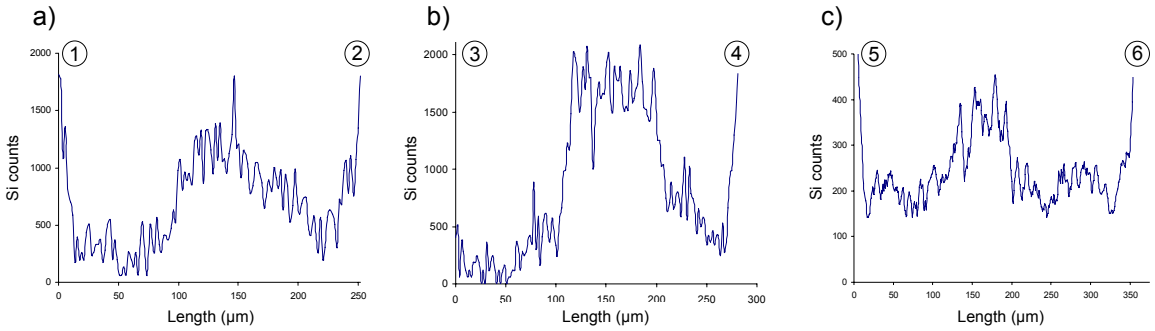

Figure 8: The Si signal across the electrode/electrolyte interface (EEI) on the pure a), impure b) and alumina added c) electrolytes. It is seen that the Si signal is strongest in the centre of the EEI and fades out towards the EEI perimeter before increasing at the EGI.

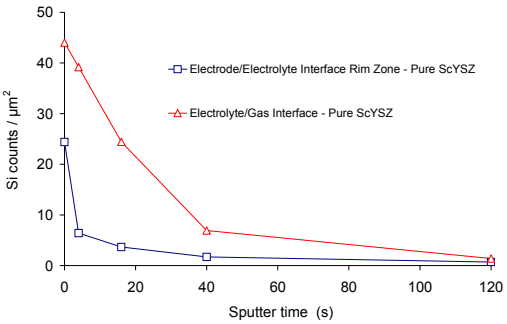

Figure 9: The Si signal intensities obtained from a 50 × 50 µm^2 area scan at the electrode/electrolyte perimeter, inside in the EEI rim zone (□) and outside, on the EGI (Δ), as a function of Xe^+ sputter time on pure ScYSZ.

3.3.2 Impure electrolyte

ToF-SIMS analysis measured significant amounts of Na, Mg, Al, Si, K, Ca, Ni, Mn, and La in addition to Zr, Y and Sc on the surface of the impure electrolyte. As on the pure electrolyte the in-plane distribution of signals from the impurity species Na, Mg, Al, K, Ca and Si overlapped and are thus described here by the representative Si signal, Figure 6. A 500 × 500 µm^2 area scan of an impure electrolyte, without the porous microstructure, showed a Si signal intensity of 0.40 counts/µm^2 in the EEI compared to 1.77 counts/µm^2 in the EGI, Table 3. As also seen on the pure electrolyte the Si signal was concentrated at the EEI core and faded out in the rim zone, Figure 6 and Figure 7b). The Si signal intensity in the EEI core was 0.66 counts/µm^2 compared to 0.40 counts/µm^2 for the entire EEI, comprising both the core and the rim zone, Table 3. The ratio between the Si signals of the EEI and the EGI from the impure electrolyte was 2.5 times larger than measured on the pure electrolyte. This indicates that a relatively high impurity level existed inside the EEI of the impure electrolyte compared to that of the pure electrolyte.

A strong ToF-SIMS nickel signal was detected in the porous layer on the impure electrolyte. Si and other impurity signals were measured on the impure electrolyte using a 20 × 20 µm^2 area scan at the perimeter of the EEI. The scan included an area with the porous layer, a hill and valley structured rim zone, and an area of the EGI. It was found that the silicon, sodium and potassium signal from the porous layer in the EEI became stronger relative to the EGI as a function of sputter time. Figure 9 gives the Si signal intensity for the porous microstructure,

the rim zone within the EEI as well as the EGI. ToF-SIMS and SEM images of the analysed area have been presented previously [12].

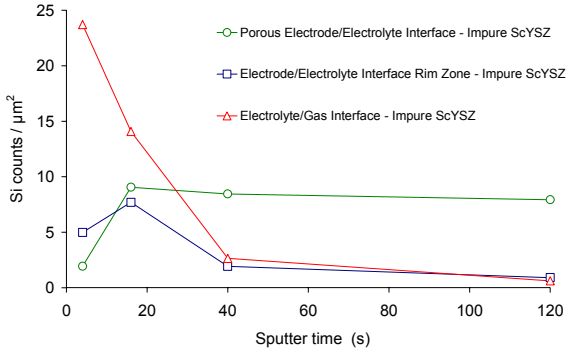

Figure 10: The Si signal intensities from a 20 × 20 µm^2 area scan at the electrode/electrolyte interface perimeter including the porous layer (○), the hill and valley rim zone inside the EEI (□) and the EGI (Δ) on an impure ScYSZ as a function of Xe^+ sputter time.

3.3.3 Impure electrolyte with alumina additions

ToF-SIMS analysis detected strong signals of Na, Mg, Al, Si, K, Ca, Ni, Mn in addition to Zr, Y and Sc on the impure electrolyte with alumina additions. In a 500 × 500 µm^2 area scan a very weak Si signal was measured inside the EEI when compared to the impure electrolyte without alumina. However, an EEI core with an increased impurity signal could be identified as seen from Figure 7. The Si signal intensity in the EEI core was 0.14 counts/µm^2 compared to 0.09 counts/µm^2 for the entire EEI, comprising both the core and the rim zone, Table 3. The ratio between the Si signal of EEI and the EGI on the impure electrolyte was 3.1 times less than measured on the impure electrolyte without added alumina. Not surprisingly a very strong Al signal was detected from the EEI where 1.7 Al counts/µm^2 were measured as opposed to 0.6 Al counts/µm^2 on the impure electrolyte without added alumina.

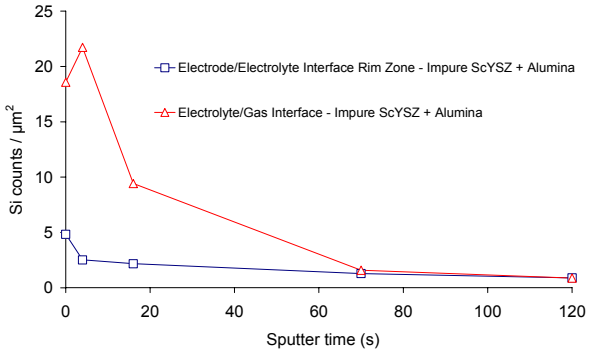

Figure 11: The Si signal intensities from a 50 × 50 µm^2 area scan at the electrode/electrolyte perimeter in the EEI rim zone (□) and the EGI (Δ) on an impure ScYSZ with alumina additions as a function of Xe^+ sputter time.

A 50 × 50 µm^2 area scan at the perimeter of the EEI was carried out. The Si signals inside and outside the EEI are plotted as a function of sputter time in Figure 10. As the scan was made at the border between the EEI and EGI, the EEI signal was obtained from the EEI rim zone.

Figure 11 shows a SEM image and two ToF-SIMS images of the corresponding 50 × 50 μm^2 area. It reveals intergranular alumina particles, 0.5 – 2 μm in diameter, dispersed throughout the electrolyte. The relative intensity of the Si signal from these alumina particles increased as a function of sputter time. While the Si signal had disappeared from the ScYSZ surface of the EEI and EGI after 120 seconds of sputtering the Si signal from the alumina particles inside and outside the EEI remained strong relative to the surrounding ScYSZ surface. This indicates that the Si does not only sit on the surface of the alumina particles but rather has dissolved into the alumina particle. This agrees with the findings that alumina acts as a silica scavenger [8,13].

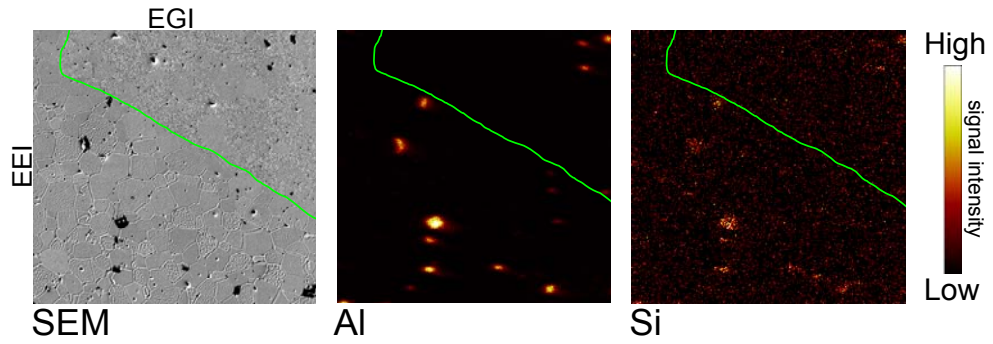

Figure 12: A SEM image of impure ScYSZ with alumina additions and ToF-SIMS images of the Al and Si signals after 120 seconds Xe^+ sputtering of the same 50 × 50 μm^2 area. The electrode/electrolyte interface lies below and the electrolyte/gas interface lies above the green line, which marks the EEI perimeter rim ridge.

The Ni-electrodes were also investigated by ToF-SIMS. Trace amounts of the impurity species Na, Al, Si, K and Ca could be detected on the EEI surface of the Ni-electrodes. However, no concentrations of impurities were found adhering to the electrodes in the areas corresponding to the rim zones measured on the electrolytes. Thus it can be concluded that the impurities essentially adhere to the electrolyte.

Table 3: The Si signal intensities on the three electrolytes from 500 × 500 μm^2 area scans. The Si signal intensity from the electrode/electrolyte interface (EEI) relative to the electrolyte/gas interface (EGI) is strongest on the impure electrolyte.

	Si counts / μm^2 EEI_{Core}	Si counts / μm^2 EEI_{Total}	Si counts / μm^2 EGI	$\frac{\text{(Si counts / μm}^2_{EEI})}{\text{(Si counts/ μm}^2_{EGI})}$
Pure ScYSZ	0.13	0.09	1.03	0.09
Impure ScYSZ	0.66	0.40	1.77	0.22
Impure ScYSZ + Al_2O_3	0.14	0.09	1.28	0.07

4. DISCUSSION

The ToF-SIMS measurements documented the existence of an impurity layer on the electrolyte/gas interface on the pure as well as on the two impure electrolytes. Although this layer did not necessarily have the same thickness and composition on the three electrolytes, the layer could be removed by 120 seconds of Xe^+ sputtering on all electrolytes. It was not possible to quantify the thickness of the impurity layer in the EGI, but the relatively short time of sputtering required to

remove the layer indicates that the layer thickness is to be measured in the order of monolayers [14]. Subtle differences in the chemical composition of glass phases, such the Na content, will affect the viscosity [15]. Since ToF-SIMS is not a quantitative method the exact chemical compositions of the detected impurity layers of the EGI is not known. However, it is noted that it is mainly the impurities that were present in the original electrolyte powders (Table 1), which were found by ToF-SIMS. Thus, it is assumed that the impurities segregated from the interior of the electrolyte to the surface, and no significant amount of the impurities originated from the cell assembly or from the hydrogen gas.

All three electrolytes displayed impurity layers similar in both composition and thickness on the free surfaces, i.e. on the EGI. Thus, the large differences in electrode polarisation resistance between the electrodes on the pure and the impure electrolytes cannot be explained by a rate determining step of the electrode reaction occurring through the EGI. It seems reasonable to assume that the rim ridges at the TPBs also have similar compositions, at least for the pure and impure electrolyte without alumina addition, and a consequence of this assumption is that the TPB is not the main place at which the electrode reaction takes place. This in turn means that the only important reaction path for charge transfer is by diffusion of protons through the Ni to the EEI near the rim ridge and further into the ScYSZ by a mechanism described previously by Mogensen et al. [16,17].

Also, in the EEIs the same elements were detected on both the pure and impure electrolytes, so the measured differences in electrode polarisation resistance must be explained in terms of surface concentration rather than chemical composition of impurity species. A relatively weaker Si signal was found in the pure electrolyte EEI compared to the EEI of the impure electrolyte. This supports the hypothesis that impurity species affect the reaction kinetics occurring through the EEI.

In the EEI of all three electrolytes the Si signal was found to be most intense in the core of the EEI. The Si signal faded out towards the perimeter of the EEI, and a contrast between the EEI core and the rim zone was observed and illustrated in Table 3 and Figure 6 and Figure 7. A possible explanation is attempted in the following and illustrated in Figure 12. At room temperature, when the electrode is set onto the electrolyte the EEI is essentially a point contact between a sphere and a flat surface. However slight plastic deformation of the Ni will occur when placing the polished electrode onto the electrolyte due to the mechanical load. Nevertheless the EEI is only a relative small fraction (ca. 25 % in case of the Ni on the pure ScYSZ) of the final area as estimated from the course of the ohmic resistances using the Newman formula, $r = 1/4\sigma R_s$ [18]. This situation is indicated in Figure 12a). As the cell is heated to the test temperature of 850 °C over a period of four hours, impurities start to segregate to the electrolyte surface and in particular to the TPB [19]. When approaching this temperature the Ni begins to creep causing the EEI area to increase. Through the creep process the first formed rim ridge impurity (glassy) phase is caught under the Ni, which is slowly pressed down almost vertically, and in this way the high concentration (particles) of impurities in the EEI core was formed, Figure 12c). If the impurity segregation is fast relative to the Ni creep rate then the EEI may be blocked to an extent that R_s increases (or decreases much slower than the actual contact area increases, Figure 3a), the impure electrolyte). Furthermore, the results indicate that the glassy impurities do not tend to segregate to the EEI as seen when comparing the Si signal from the entire EEI with the Si signal from the EGI in Table 3. This means that the interface free energy of the EEI (Ni to ScYSZ) is more negative than the total energy of the Ni to glass and glass to gas interfaces. Thus, when the TPB has scavenged most of

the impurities and these were "embedded" under the Ni, Figure 12c), the further creep of the Ni will come down on an electrolyte surface with only maybe a monolayer of silica based glass, and as this is on an unstable interface some mobile impurities may migrate to TPB outside the EEI. In this way a relatively clean EEI rim zone was formed, and outside this zone only a rather modest rim ridge was observed as sketched in Figure 12e). The fact that the EEI and TPB of the corresponding Ni-electrode surfaces did not show signs of glassy impurities of the type found on the electrolyte gives evidence that especially the interface energy of the Ni-glassy impurity interface here is very high, i.e. a free energy is gained by making interfaces to the gas instead.

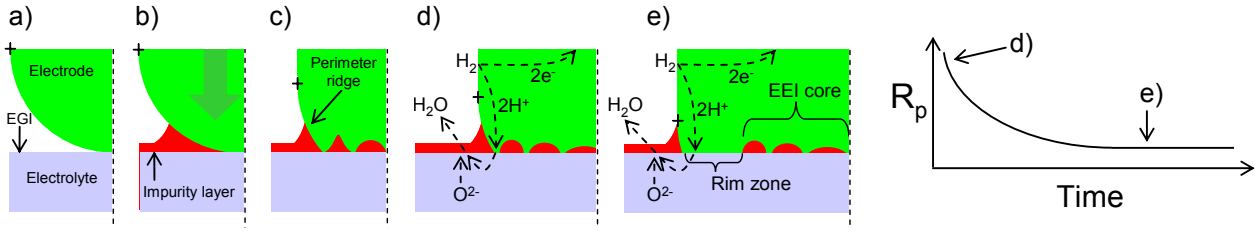

Figure 13: The proposed mechanism that creates rim zones during electrode/electrolyte interface expansion due to nickel creep. a) The electrode is set on to the electrolyte at room temperature. b) During heating to operation temperature impurities segregate to the surface of the electrolyte. c) While heating, electrode area expansion also occurs but is not able to displace impurities at low temperatures. d) At operation temperature EIS measurements are started. The EEI at the TPB is blocked by impurities resulting in a large electrode polarisation resistance (R_p). e) The electrode area continues to expand and, at the high temperature, is now able to displace the impurities resulting in a decrease in the measured electrode polarisation resistance.

Thus, it is hypothesised that the EEI at the onset of the impedance measurements corresponds to the EEI core area later measured by ToF-SIMS. The first electrode polarisation resistance measurements yield relatively large values for all three electrolytes. The large R_p values are a result of an impurity concentration at the TPB and on the EEI, Figure 12d). The rapid decrease of R_p is seen as a consequence of the formation of the EEI rim zone, Figure 12e). It is interesting to note that the time scale of the initial decrease in R_p was similar for all three electrolytes even though the detailed course was not identical. This is likely to be a consequence of the identical force applied to all of the electrodes resulting in equal creep rates. The relative decrease rate of R_p was largest for the Ni on the impure electrolyte. This electrode had a very large initial R_p, so as soon as just a small area of relatively clean EEI rim zone was formed, R_p dropped drastically.

The EIS revealed two arcs i.e. two processes contributing to the limitation of the electrode reaction rate. The fact that the high frequency arc undergoes the largest changes indicates that it is related to the expanding electrode and the formed rim zone. The hypothesis is that the high frequency arc, which seems very dependent on the size of the EEI rim zone, is associated with proton transport across the electrode / electrolyte interface. The low frequency arc is supposed to be due to the diffusion of protons through the Ni bulk metal. This conclusion is mainly taken from literature and the present findings support this picture. Proton diffusion is expected to be less dependent, but certainly not independent on the size of the EEI rim zone. The low frequency arc only changes slightly as the proton diffusion through the nickel electrode is not influenced by impurities the EEI surface. However the proton diffusion length could perhaps be influenced by the height of the rim ridge.

The rim ridges observed at the perimeters of the EEI, Figure 12e), are expected to consist of accumulated impurity species. In prior work, glassy types of impurities were found on larger ridges using energy dispersive X-ray spectroscopy (EDS) [19]. Unfortunately, the ridges observed in this work were too small to analyse with EDS and ToF-SIMS.

The reason for the occurrence of the layer with the porous microstructure found on one of the impure electrolyte samples and two of the impure electrolyte samples with alumina additions cannot be satisfactorily explained at the present moment. As with the other samples it is interesting to note that the Si signal from the porous EEI core was relatively stronger than the Si signal from the rim zone, which surrounded the porous microstructures. The fact that EEI rim zones with hill and valley structures surrounded the porous EEI cores indicates that the porous microstructures were formed at the beginning of the measurement and that the hill and valley structures formed later as the electrode slowly expanded across the electrolytes over time.

The layers with porous microstructures rich in impurities did not appear to have a negative influence on electrode polarisation resistance as seen from the samples marked with a *P* in Table 2. On the contrary, the ASR_p of the electrode with the porous layer in the EEI of the electrolyte sample with alumina were the lowest of its series. It is speculated that the formation of the porous microstructure greatly increased the TPB length, hence diminishing the role of impurities.

From the continuing decrease in R_s throughout the measurement it is clear that the EEI area was constantly increasing throughout the measurement while the electrode polarisation resistance stabilised over time. Relative to the EEI area, the EEI perimeter length does not increase as quickly when the electrode expands. This may be a further indication that it is the TPB length or rim zone length rather than the EEI area which defines reaction kinetics. This suggests that the width of the active EEI rim zone is relatively narrow compared to the size of the total area of the EEI. Thus, based on the above reasoning it can be argued that the anode reaction in these cells takes place through a rim zone of the Ni-ScYSZ interface at the inner side of the TPB as described in [17] and is therefore not influenced much by the higher impurity level located in the centre of the EEI.

The significant reduction in series (ohmic) resistance measured on the impure electrolyte with added alumina is attributed to the known effects of alumina towards increasing the ionic conductivity of ScYSZ [1]. Si concentrations were measured from alumina particles at the electrolyte surface. This became even more evident after the surface had been sputtered to remove the topmost surface impurity layer, Figure 11. We believe that the Si concentrations measured from the alumina particles are a genuine consequence of alumina acting as a Si "scavenger" as has been reported in literature [8]. This is based on the fact that the impurity content of the alumina raw material was very low (15 ppm) compared to the impure electrolyte (380 ppm). After 120 seconds of Xe^+ sputtering the surrounding electrolyte surfaces had a very weak Si signal compared to the alumina particles. This is an indication that not only the surface of the alumina particles contained Si but that Si had moved into the bulk of the alumina particles.

However, adding alumina did not decrease the electrode polarisation resistance of the impure electrolyte. This points to alumina having segregated to the EEI, and being an impurity, inhibiting proton transfer through the EEI.

5. CONCLUSION

Electrochemical impedance spectroscopy showed that the electrode polarisation resistance in a model SOFC anode greatly depends on the amount and

type of impurities found in the electrode/electrolyte interface near the three phase boundary. As impurity layers of similar compositions accumulated in the electrolyte/gas interface on both the pure and impure ScYSZ samples it must be the different levels of impurities found in the vicinity of the TPB inside the electrode/electrolyte interface (the rim zone), which accounts for the differences in electrode polarisation resistances. It seems therefore likely that the rate determining reaction path occurring in a SOFC anode leads across the electrode/electrolyte interface, and that it involves diffusion of protons through the Ni-metal.

AKNOWLEDGEMENTS

This work was carried of as part of the project "Efficient Conversion of Renewable Energy using Solid Oxide Cells" contract number 2058-03-0014, which is financially supported by The Danish Research Councils and the Danish Ministry of Science Technology and Innovation.

REFERENCES

[1] D. Lybye, Y-L. Liu, J. Eur. Ceramic Soc. 26 (2006) 599-604.

[2] K. V. Jensen, R. Wallenberg, I. Chorkendorff, M. Mogensen, Solid State Ionics 160 (2003) 27-37.

[3] M. de Ridder, A. G. J. Vervoort, R.G. van Welzenis, H. H. Brongersma, Solid State Ionics 156 (2003) 255-262.

[4] R. J. Aaberg, R. Tunold, M. Mogensen, R. W. Berg, R. Ødegård, J. Electrochem. Soc., 145 (1998) 2244-2252.

[5] K. Norrman, K. V. Hansen, M. Mogensen, J. Eur. Ceramic Soc. 26 (2006) 967-980.

[6] A. E. Hughes, S. P. S. Badwal, Solid State Ionics 46 (1991) 265-274.

[7] J. Høgh, Ph.D. thesis, (2005) Risø National Laboratory, Roskilde, Denmark

[8] J. Drennan, E. P. Butler,(1984) Science of Ceramics 12. Faenza, Italy, 267–272.

[9] O. Yamamoto, Y. Arati, Y. Takeda, N. Imanishi, Y. Mitzutani, M. Kawai, Y. Nakamura, Solid State Ionics 79 (1995) 137-142.

[10] B. A. Boukamp, Solid State Ionics 18-19 (1986) 136-140.

[11] K. V. Jensen, S. Primdahl, I. Chorkendorff, M. Mogensen, Solid State Ionics 144 (2001) 197-209.

[12] M. S. Schmidt, K. V. Hansen, K. Norrman, M. Mogensen, Solid State Ionics 179 (2008) 1436-1441.

[13] J-H. Lee, T. Mori, J-G. Li, T. Ikegami, M. Komatsu, H. Haneda, J. Am. Ceram. Soc., 83 (2000) 1273-75.

[14] K. V. Hansen, K. Norrman, M. Mogensen, Surf. Interface Anal. 38 (2006) 911-916.

[15] S. L. Webb, M. Banaszak, U. Köhler, S. Rausch, G. Raschke, *European Journal of Mineralogy* v. 19; no. 5; (2007) 681-692.

[16] M. Mogensen, S. Sunde and S. Primdahl, in: High temperature electrochemistry: ceramics and metals. 17. Risø international symposium on materials science. Poulsen, F.W., Bonanos, N., Linderoth, S., Mogensen, M., Zachau-Christiansen, B. (eds.), (Risø National Laboratory, Roskilde, 1996) p. 77-100.

[17] M. Mogensen, J. Høgh, K. V. Hansen, T. Jacobsen, ECS Transactions 7 (1) (2007) 1329-1338.

[18] J. Newman, J. Electrochem Soc., 113 (1966) 501-503.

[19] K. V. Jensen, S. Primdahl, M. Mogensen, in: Mass and charge transport in inorganic materials: fundamentals to devices, P. Vincenzini, V. Buscagli (eds), Techna, Faenza. (2000) 1443-1449.

Appendix H

This appendix contains a manuscript submitted to Solid State Ionics on July 17. 2008, titled *Three phase boundary dynamics at the Ni/ScYSZ interface*. The manuscript is presented as submitted.

Three-phase-boundary dynamics at the Ni/ScYSZ interface

Michael Stenbæk Schmidt[a], Karin Vels Hansen[a], Kion Norrman[b], Mogens Mogensen[a]
[a]Fuel Cells and Solid State Chemistry Department, Risø National Laboratory for Sustainable Energy, Technical University of Denmark.
[b]Polymers for Energy Technology, Risø National Laboratory for Sustainable Energy, Technical University of Denmark.
Frederiksborgvej 399, DK-4000, Roskilde, Denmark

Corresponding author: M. S. Schmidt: e-mail: michael.stenbaek.schmidt@risoe.dk

ABSTRACT

Chronoamperometry using a three-electrode cell configuration was undertaken with a nickel point electrode acting as the working electrode on a polished ScYSZ electrolyte in a hydrogen atmosphere at 850 °C. High anodic overpotentials resulted in the occurrence of distinct sawtooth oscillation patterns in the measured current signal. The current oscillations indicated that a dynamic electrode process was taking place. Decreasing the water content in the measurement atmosphere as well as lowering the applied anodic overpotential had the effect of lowering the frequency and the amplitude of the current oscillations. A mechanism accounting for the observed phenomena and possible implications for solid oxide fuel cell operation are presented.

Keywords: Solid oxide fuel cell, Ni, ScYSZ, polarisation, ToF-SIMS, anode dynamics

1. INTRODUCTION

In the pursuit of improving solid oxide fuel cell (SOFC) performance detailed knowledge of the reaction mechanisms, reaction pathways and degradation mechanisms occurring at the anode and cathode are desirable. It has been established that continuous polarisation of the electrodes decreases interfacial impedance resulting in a temporary performance increase [1]. It has also been found that this activation during polarisation is followed by a deactivation when the electrodes are relaxed. Strong polarisations have also been found to influence the microstructure at the electrode/electrolyte interface on both anode and cathode materials [1][2]. The underlying mechanisms behind the observed changes in microstructure are presently not fully understood. However it is likely that they have a significant effect on the long term stability of SOFC [3][4].

A three-electrode cell configuration was used as a model system to study the hydrogen reaction at the SOFC nickel anode. A nickel point electrode was used as the working electrode as a physical model of the cermet anodes presently used in SOFC. As the electrode could be lifted off the electrolyte surface after electrochemical measurements, the point electrode setup enabled the study of a well defined electrode/electrolyte interface (EEI) and three phase boundary (TPB). Chronoamperometry was undertaken with an applied anodic polarisation in a hydrogen atmosphere at 850 °C. Following electrochemical characterisation the surface microstructure of the electrode/electrolyte interface was studied by scanning electron microscopy and correlated to the electrochemical data.

2. EXPERIMENTAL

The ScYSZ powder ($Sc_{0.18}Y_{0.02}Zr_{0.80}O_{1.9}$) was pressed into pellets and sintered at 1315 °C for 12 hours. 3 mm thick electrolyte samples with a 16 mm diameter were polished with the final step being 0.25 µm diamond particles.

The point electrodes consisted of high purity (99.999 %) 0.5 mm diameter nickel wire (Puratronic, Johnson Matthey). 40 mm long pieces of the wire were bent to form a point and annealed for 24 hours at 1000 °C in Ar with 9 % H2. The annealing was performed in order to restore the Ni crystals (grains) that were damaged by deformation when the wire was bent. Finally, the nickel tips were electropolished for 4 minutes in an electrolyte consisting of alcohol and perchloric acid cooled to -5 °C.

A custom made rig was used for electrochemical characterisation. The rig parts consisted of alumina and all electrical leads were platinum. The rig fitted four, three-electrode cells in which the Ni point electrode was the working electrode. Figure 1 gives the principle and the dimensions of the configuration. Porous counter and reference electrodes were painted onto the bottom of the electrolyte with platinum paste (Degussa-308A). The painted electrode areas were placed on two separate platinum meshes to ensure gas access to the entire area of the painted electrodes and to connect the painted electrodes to the measurement equipment. The nickel wires acting as working electrodes were set onto the centre of the polished electrolyte surface and pressed down by 315 g copper weights via two-bore alumina tubes. Weights were necessary to ensure good physical contact between the electrode and electrolyte. The measurements were performed in a one-atmosphere setup. Inlet hydrogen was bubbled through a water bottle placed in a refrigerator, hence the water content in the measurement atmosphere could be controlled by varying the refrigerator temperature. The oxygen potential in the measurement atmosphere versus air was monitored by a platinum electrode pair on two sides of an alumina tube closed at one end, inserted in the measurement atmosphere, Figure 1. The water bottle could be bypassed to create a "dry" measuring atmosphere. Some moisture was however present in the gas supply and based on the oxygen potential the "dry" atmosphere had a water content calculated to 54 ppm.

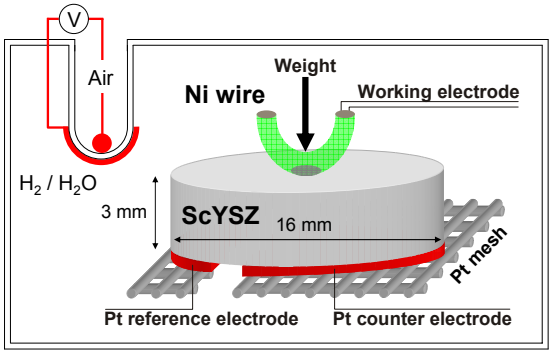

Figure 14: Schematic of the 3-electrode configuration.

2.1 Electrochemical impedance spectroscopy

With the samples mounted, the rig was heated to 850 °C by 5 °C / minute in 89 % Ar / 9 % H_2 / 2 % H_2O whereafter the atmosphere was switched to 97.6 % H_2 / 2.4 % H_2O (pO_2 = -1104 mV vs. air). Electrochemical impedance spectroscopy was performed at open circuit voltage (OCV) with an applied RMS amplitude of

7.07 mV using a Solartron 1250 frequency response analyser coupled with a Solartron SI 1287 potentiostat. The obtained impedance spectra were fitted with the equivalent circuit $R_s(R_{p1}Q_1)(R_{p2}Q_2)$ [6].

The values of the electrode polarisation resistance have previously been seen to fall rapidly during the first 50 hours. This drop is accounted for in [7]. In order to ensure that the chronoamperometric measurements were performed independently of the effects described in [7] the polarisation resistance values were measured at OCV until stable values were measured on all four samples.

2.2 Chronoamperometry

After the electrode polarisation resistance values had stabilized, chronoamperometry with applied anodic overpotentials was performed on three of the samples, with the fourth sample acting as a reference. At 850 °C the electrode potential at OCV of the Ni working electrode was measured to be -1104 mV vs Pt/air. Each of the three samples were then anodically polarised with an applied overpotential of 50 mV for one hour. Thereafter the applied overpotential was increased in steps of 50 mV until electrode potentials of -550 mV vs Pt/air were reached. Impedance measurements were recorded during chronoamperometry at overpotentials up to 400 mV.

Subsequently the atmosphere was changed to 99.3 % H_2 / 0.7 % H_2O (pO_2= -1162 mV vs Pt/air), and chronoamperometric measurements were performed on the samples with electrode potentials from -850 mV to -550 mV vs Pt/air in steps of 100 mV.

The direct effect of the water content in the atmosphere was investigated by conducting chronoamperometric measurements in a "dry" atmosphere (pO_2= -1400 mV vs Pt/air) lasting one hour and then increasing the H_2O content to 2.4 % whilst keeping the electrode potential constant by adjusting the set overpotential. After one hour with a wet atmosphere the incoming gas flow was switched back to a "dry" H_2 atmosphere. This procedure was then repeated for a 0.7 % H_2O atmosphere.

Potential sweeps were carried out on the three samples in a 97.6 % H_2 / 2.4 % H_2O atmosphere at rate of 1 mV/s spanning the electrode potential range from -1500 to -550 mV vs Pt/air at 850, 800 and 750 °C before terminating the experiment.

2.3 Microscopy

Following the electrochemical measurements the nickel electrodes were lifted off the electrolytes. The electrodes and electrolytes were examined with a field emission gun scanning electron microscope (SEM) (Supra 35, Zeiss) in order to determine the areas of the electrolyte/electrode interfaces. Secondary electrons with a 1 keV acceleration voltage were used to examine the surface microstructures on the ScYSZ without necessitating carbon coating.

2.4 Chemical analysis

Time-of-flight secondary ion mass spectrometry (TOF-SIMS IV, ION-TOF GmbH) was performed to obtain qualitative measurements of the lateral distribution of trace elements on the electrolyte surface. ToF-SIMS images with high mass resolution but low lateral resolution were acquired using 30-ns pulses of 25-keV Bi^+, bunched to form ion packets with a nominal temporal extent of < 0.9 ns at a repetition rate of 10 kHz yielding a target current of 500 fA. These primary ion conditions were used to scan 500 × 500 μm^2 areas of the sample surface.

Images with low mass resolution but high lateral resolution (primary ion spot size ~150 nm) were acquired covering 75 × 75 μm^2 areas of the sample surface using 100-ns pulses of 25-keV Bi^+ at a repetition rate of 10 kHz yielding a target current of ≤ 10 fA. The high lateral resolution enabled the correlation between ToF-SIMS and SEM images. Following the 75 × 75 μm^2 area scans a 1000 × 1000 μm^2 area of the surface was sputtered for 10 seconds using 3-kV Xe^+ (sputter ions) resulting in a target current of 20 nA.. After sputtering a 500 × 500 μm^2 area scan optimised for high lateral resolution was performed. Electron bombardment (20 eV) was used to minimize charge build-up at the surface. Desorbed secondary ions were accelerated to 2 keV, mass analyzed in the flight tube, and post-accelerated to 10 keV before detection.

3. RESULTS

3.1 Chronoamperometry in constant atmosphere

When the nickel electrodes were anodically polarised in both wet and dry atmospheres (2.4 %, 0.7 % H_2O and dry = 54 ppm H_2O) the measured currents were found to increase gradually until the average current reached a constant level. The current density calculation is based on the EEI area measured by SEM after electrochemical measurements. The same area is used for each sample while assuming that electrode expansion is negligible after 50 hours. The average current levels increased as a function overpotential as seen in Figure 2. The equilibrium potential of the three atmospheres were measured to be -1104 mV, -1162 mV, and -1400 mV vs. Pt/air for the 2.4 % H_2O, 0.7 % H_2O and dry atmospheres respectively.

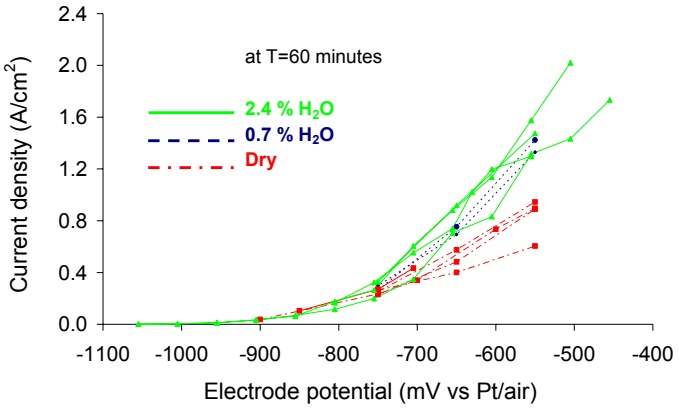

Figure 2: For three samples the average current density after 60 minutes of anodic polarisation is plotted as a function of the electrode potential. It was seen that the current density increased as the water content in the measurement atmosphere was increased.

At electrode potentials over -700 mV vs. Pt/air characteristic sawtooth oscillation patterns were observed on the three samples, Figure 3 and Figure 4. The sawtooth oscillations initially had low amplitudes but the oscillation amplitude increased as a function of time until reaching the steady state current level where the amplitude remained unchanged in magnitude for the remainder of the 60 minute measurement. The sawtooth oscillation pattern can be described as a slow decline in the measured current followed by an instantaneous activation. The oscillation amplitude was approximately 30 % of the total current. The observed pattern is similar in shape to that presented in [8][9] although the frequency is

several orders of magnitude larger in the present work. In [10] a similar fluctuation pattern with a similar time scale was observed using a Pd electrode.

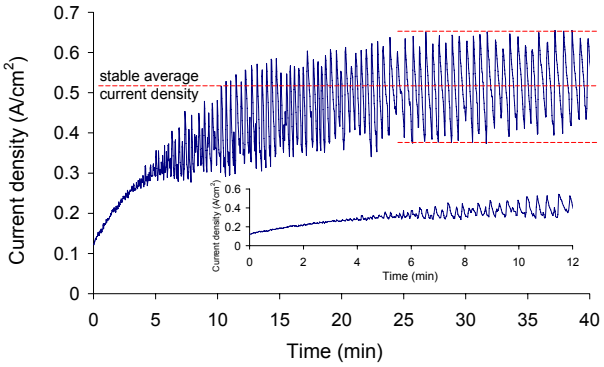

Figure 3: The current density as a function of time obtained from a chronoamperometric measurement of a single sample in a hydrogen atmosphere containing 2.4 % H2O. The electrode potential was set at -700 mV vs Pt/air by anodic polarisation for 60 minutes. A distinct sawtooth oscillation pattern (insert) was observed after an initial gradual increase in current. After 25 minutes the average current density was stable for the remainder of the measurement.

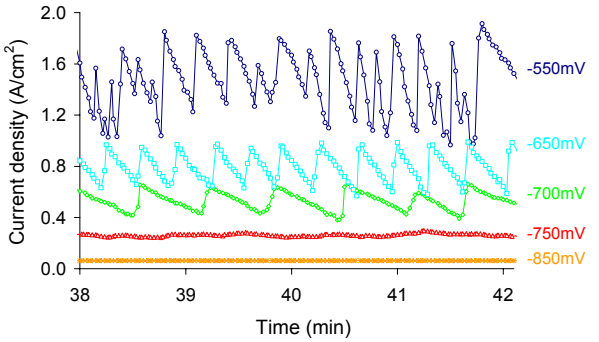

Figure 4: Chronoamperometric measurements in a 2.4 % H2O atmosphere. Sawtooth oscillation patterns were observed at electrode potentials over -700 mV vs Pt/air.

The oscillation patterns were evaluated using a fast Fourier transform analysis and a dominating frequency was found for each data set. The Fourier analysis verified that the oscillation patterns were not noise patterns and also showed that the dominating frequency of the sawtooth oscillations increased as a function of the applied electrode overpotential. Furthermore the amplitude of the sawtooth oscillations increased as a function of applied overpotential as can be seen from Figure 4, Figure 5 and Figure 6.

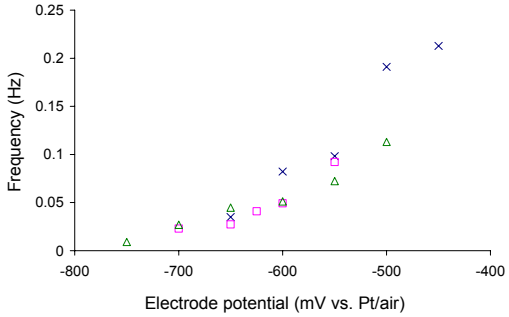

Figure 5: The dominating frequency of the current oscillations on three samples (□Δx) plotted as a function of electrode potential in a hydrogen atmosphere with 2.4 % H_2O. The oscillation frequency clearly increased as a function of anodic polarisation.

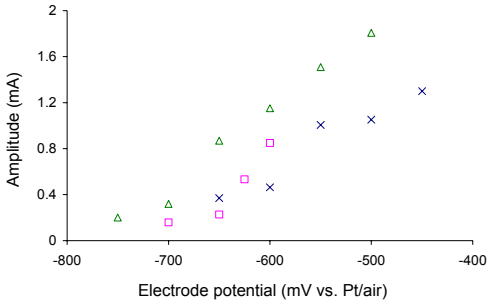

Figure 6: The amplitude of the current oscillations on three samples (□Δx) plotted as a function of electrode potential in a hydrogen atmosphere with 2.4 % H_2O. The oscillation amplitude clearly increased as a function of anodic polarisation.

3.2 Chronoamperometry in atmospheres with varying water content

The effect of varying water content in the measurement atmosphere was investigated by conducting chronoamperometric measurements with a constant applied potential to the working electrode in a dry H_2 atmosphere until the average current level had stabilised and then introducing 2.4 % H_2O into the gas flow. As a consequence of the increased water content in the atmosphere the measured equilibrium electrode potential increased from -1400 mV to -1104 mV vs Pt/air and therefore the appplied overpotential was reduced accordingly to maintain a constant electrode potential. As seen in Figure 7, the introduction of water into the atmosphere (II) resulted in the onset of the sawtooth oscillation pattern. After the oscillation pattern had stabilised at the new steady average current level the atmosphere was switched back dry H_2 (III) and the applied overpotential was increased so that the electrode potential remained constant. From the measured electrode potential it was seen that it took roughly 4 hours for the atmosphere to become completely dry which is why the measured current took this time to decrease to the new stable level. The steady state currents measured after switching back to the dry atmosphere (III) were significantly larger than the initial measurements made in dry atmosphere (I) before introducing water to the atmosphere. However the steady state current levels measured in the wet atmospheres were the same as those measured in the following dry atmosphere.

The above mentioned procedure was repeated with a water content of 0.7 %. It is seen in Figure 7 that introducing 0.7 % water into the measurement atmosphere had the effect of increasing the measured current density. Sawtooth oscillations are observed in the 0.7 % H_2O atmosphere but the onset of the oscillations is delayed compared to the 2.4 % H_2O atmosphere. The lower water content also has the effect of reducing the amplitude of the current oscillation pattern. It is also seen that the current levels in both atmospheres reach the same level in region (III).

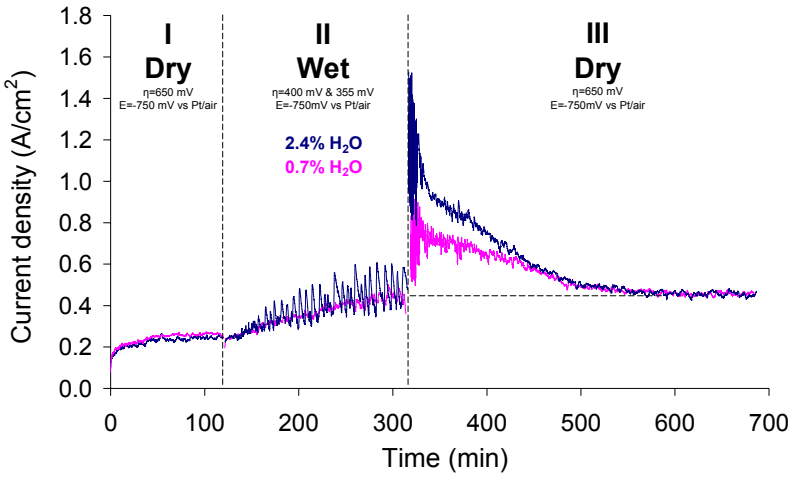

Figure 7: Chronoamperometric measurements on the same sample show the effect of varying water content in the measuring atmosphere by switching from a dry atmosphere (I) to wet atmospheres (II) and back again (III). A clear difference in the oscillation amplitude is seen between the 2.4 % and 0.7 % H_2O atmospheres.

3.3 Potential sweeps at different temperatures.

Potential sweeps at a rate of 1 mV/s in 2.4 % H_2O at 850 °C become unstable on the upward sweep at an electrode potential of around -770 mV where after the measured current signal started to fluctuate, Figure 8. At an electrode potential of -550 mV the sweep direction was reversed and the current signal oscillated in a pattern with instant activations followed by a gradual reduction in current. As the set electrode potential reached -710 mV the current oscillations ceased for the remainder of the measurement. This trend was also seen for sweeps made at 800 °C and 750 °C although reducing the temperature had the effect of increasing the electrode potential value needed to cause the fluctuating signal.

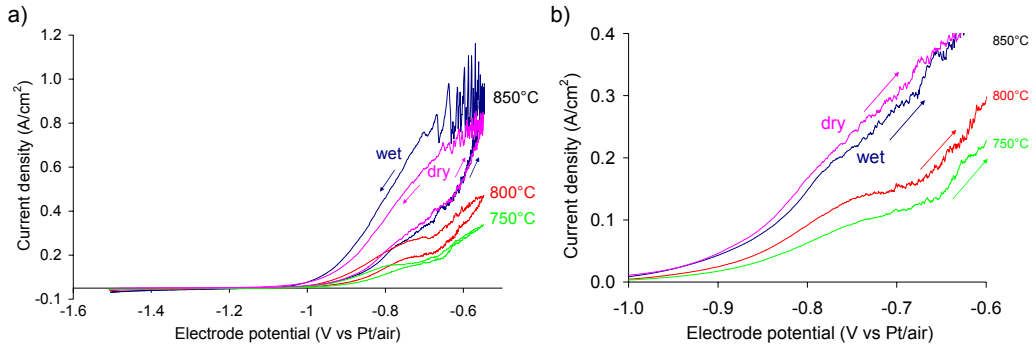

Figure 8: a) Cyclic potential sweeps (1 mV/second) in dry atmosphere at 850 °C and in 2.4 % H_2O atmosphere at 850 °C, 800 °C and 750 °C. b) The upward sweeps show a temperature dependence on the onset of fluctuations in the current signal.

3.4 Microstructure

After the electrochemical measurements the electrode and electrolyte surfaces were investigated by SEM. The microstructural features observed on the reference electrolyte which had not been polarised were identical to those previously seen and described [11], with the main features being an undulating hill and valley microstructure in the electrode/electrolyte interface and a rim ridge delimiting the EEI. The hill and valley microstructure was also found in the EEI of

the polarised electrolyte samples. However several additional microstructural features distinguished the reference sample from the polarised electrolyte samples. The most noticeable feature observed on the polarised electrolytes were nickel particles (determined by EDS) lying in a 10-40 µm wide belt encircling the EEI, Figure 9. The facetted nickel particles varied in size from 200 nm to 3 µm in diameter as shown in Figure 10. By comparing the EEI area on the nickel electrode with the corresponding EEI area on the electrolyte, it was established that the nickel particles lay outside the EEI. For this reason the area covered by discrete nickel particles was not included when calculating the EEI area. The electrolyte surface underneath the nickel particles nearest to the EEI had the hill and valley microstructure, although more pronounced than inside the EEI. The hill and valley microstructure became less pronounced when moving towards the outer edge of the nickel particle belt.

Inside the EEI of the polarised samples, areas with a granulated surface microstructure, Figure 11, stood out from the hill and valley microstructure otherwise defining the EEI. The nickel electrodes had cavities in the EEI surface in the areas corresponding to the granulated surface microstructure on the electrolytes, Figure 12.

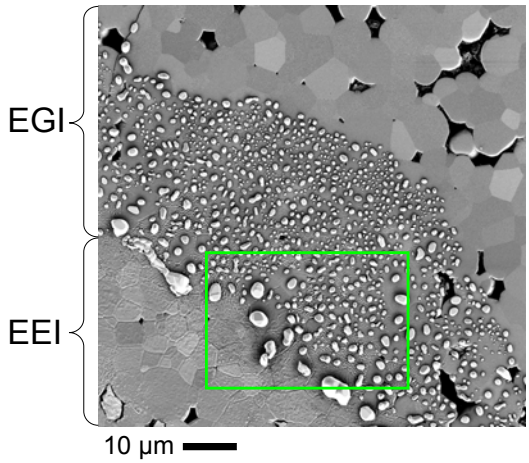

Figure 9: SEM micrograph of the electrode/electrolyte interface (EEI) surrounded by a 30-40 µm wide belt of nickel particles completely encircled the EEI. Box enlarged in Figure 10.

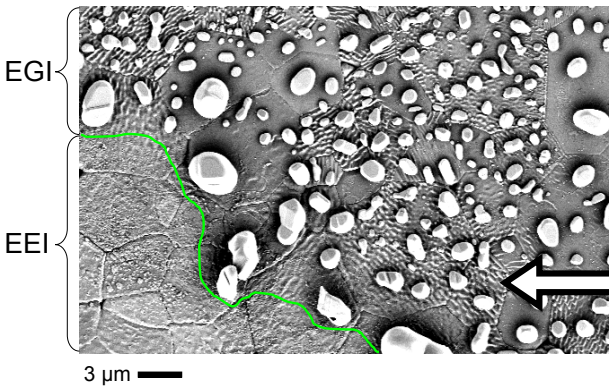

Figure 10: SEM micrograph of the outer perimeter of the electrode/electrolyte interface (EEI). The rim ridge which delimited the EEI is marked with a line. Arrow: The hill and valley structure was generally much more pronounced in the electrolyte/gas interface (EGI) than in the EEI. The hill and valley structure faded out towards the outer edge of the nickel particle belt. The facetted nickel particles were not interconnected.

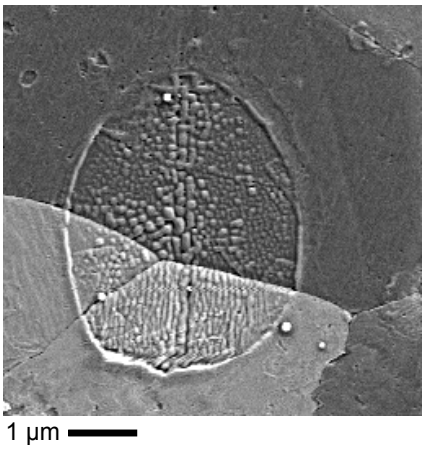

Figure 11: SEM micrograph from inside the electrode/electrolyte interface (EEI) showing an area with a granulated surface microstructure. These areas corresponded to cavities found in the electrode, hence gas had been present in the cavities. A ridge, similar in appearance to the rim ridge at the outer EEI perimeter, encircled the area with the granulated microstructure.

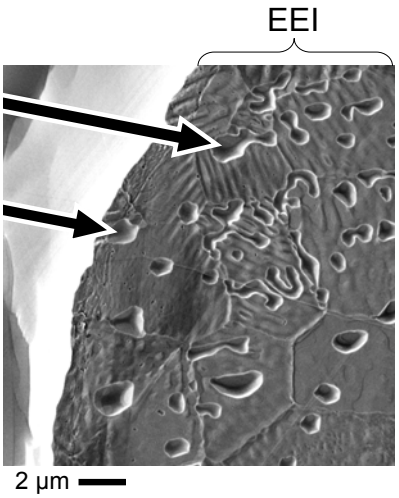

Figure 12: SEM micrograph of the cavities (arrows) in the electrode/electrolyte interface (EEI) of the nickel electrode. These cavities corresponded to the areas with granulated microstructure on the electrolyte seen in Figure 11.

3.5 Chemical analysis

From high magnification micrographs of the electrolyte, such as Figure 10, and the Ni electrode, the EEI was identified and the outline marked on the low magnification SEM micrograph in Figure 13. A 500×500 µm^2 area ToF-SIMS analysis of the EEI is shown in Figure 13 together with a SEM micrograph of the corresponding area. The belt of nickel particles is clearly seen encircling the EEI. It is also seen that the Si signal is weaker inside the EEI than in the EGI as also described in [7]. The Y signal is much stronger inside the EEI than from the EGI and corresponds exactly to the EEI area defined by SEM. This was not observed on samples which were not polarised [7]. Figure 14 shows ToF-SIMS data representations of a 75×50 µm^2 area at the outer perimeter of the EEI including the Ni particle belt of the EGI. It is seen that the Si signal from the Ni particle belt encircling the EEI is weaker than the rest of the EGI. The same effect was also observed for Na, K, and Al. The Ni particles most likely amplify the secondary ion

signal by charge compensation artificially exaggerating the measured Si signal intensity.

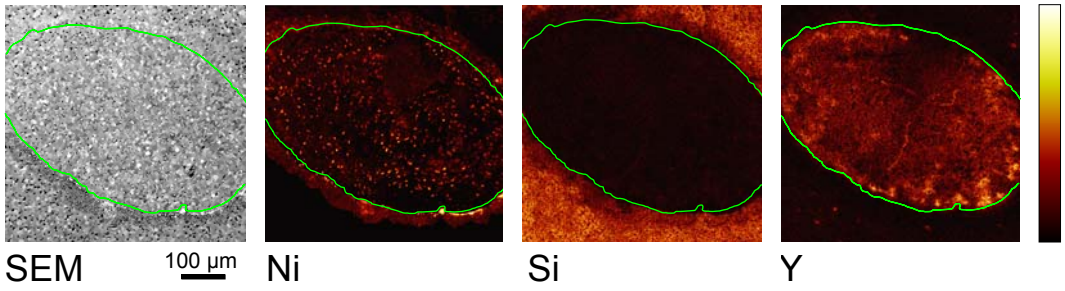

Figure 13: SEM micrograph and ToF-SIMS data representation of a 500 × 500 µm^2 area of the electrode/electrolyte interface (EEI) and surrounding electrolyte/gas interface (EGI). The white colour corresponds to the strongest signal intensity and black to the weakest. A nickel belt surrounds the EEI. Inside the Ni belt the Si signal is weaker than from the rest of the EGI. A strong Y signal is measured from the EEI.

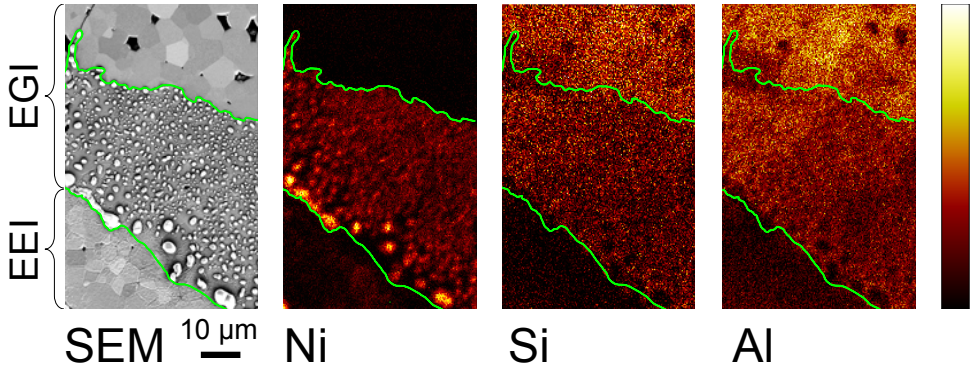

Figure 14: SEM micrograph and ToF-SIMS data representation of a 75 × 50 µm^2 area at the perimeter of the electrode/electrolyte interface (EEI). The white colour corresponds to the strongest signal intensity and black to the weakest. Individual Ni particles can be correlated from the SEM micrograph to the ToF-SIMS Ni signal. The signals from the impurity species Si and Al are weaker inside the Ni belt than the rest of the electrolyte/gas interface (EGI). Larger SEM micrographs of the analysed area seen in Figures 9 and 10.

4. DISCUSSION

Chronoamperometric measurements with an applied anodic overpotential showed that an activation process took place before stable average current levels were reached, Figure 3. This is similar to 0 where an average time of 30 minutes was needed to reach stationary conditions. Impurities such as silica have been shown to react with water at high temperatures to form volatile Si-OH species [12]. At anodic overpotentials water is formed at the TPB and the water formation rate increases as a function of increasing overpotential. Thus it is likely that impurities at the TPB were, at least partially, removed by the water formed near the TPB during anodic polarisation resulting in the observed gradual increase in current until a stable average current level was reached. Impurity species such as Si were found by ToF-SIMS to have weaker signals at the TPB. The ToF-SIMS analysis is strong evidence that Si has reacted with water and evaporated away from the TPB. We believe that the weak Si signal in the Ni particle belt is genuinely a measurement of the Si intensity on the surface between the Ni particles and not a consequence of Ni particles blocking secondary ions. This is justified by the fact that a spot size of ~150 nm was used and also that the location of individual nickel

particles, and more importantly the open spaces between the particles, could be distinguished in the Si and Al signals. Furthermore, electron conducting particles on a surface tend to amplify the secondary ion signal hence the surface concentrations could in fact be weaker than the ToF-SIMS measurements suggest.

Chronoamperometry at an electrode potential above -750 mV vs. Pt/air in wet hydrogen atmospheres (2.4 % H_2O) caused the measured current to oscillate in a distinct sawtooth pattern. The electrode potential necessary for NiO formation at 850 °C is -680 mV, and even though it has been shown that the standard Gibbs energy for oxide formation at a metal surface is lower than in the bulk [13], we do not find that NiO formation can fully account for the current oscillation pattern. The current oscillation amplitude and frequency decreased with reduced water content in the hydrogen atmosphere, Figure 7, thus clearly showing that the reaction mechanism involved water. This agrees with [14] and [12] which show that the hydrogen oxidation reaction rate is enhanced in a moist hydrogen atmosphere. The effect of water content on current density is also illustrated by Figure 2, where the stable average currents at the same applied electrodepotentials were significantly larger in the wet atmospheres. Figures 4, 5 and 6 show that the amplitude and the frequency of the current oscillations were strongly dependent on the applied potential in both wet and dry atmospheres. This points towards a dynamic electrochemical reaction mechanism.

The facetted shape and the uniform width of the Ni particle belt encircling the EEI could indicate that nickel was removed from the electrode by gas phase transport and nucleated on the EGI surface where particle growth occurred. It is also interesting to note that the Ni particles lying on the grains with a flat surface are bigger and fewer in number than the Ni particles found on the hill and valley surfaces. This also suggests gas phase transport of Ni to the electrolyte surface followed by growth via a surface transport mechanism since surface transport requires less energy on the smooth surfaces than on the hill and valley microstructure. It has been reported that the Ni_2-OH complex is responsible for the mass transport at the surface of nickel particles in steam/hydrogen mixtures [16]. It was also shown that increasing the water content increases the rate of Ni particle growth. Similar nickel depositions in wet hydrogen atmospheres at 1000 °C have also been reported in [18] and [19] showing that Ni particle formation is reproducible in various conditions. Potential sweeps at varying temperatures also showed that the overpotential necessary to initiate the current oscillation patterns was temperature dependent, Figure 8.

Current oscillations similar to those described in the present work have also been reported in [10]. There the current oscillations measured in an air atmosphere are attributed to migration of Pt and Ag electrode material onto the electrolyte surface to form dendritic structures and an increase in EEI area. A gas phase transport mechanism of electrode species and the subsequent changes in the dendritic microstructure of the electrodes are said to cause the characteristic current oscillation pattern. In [10] the EEI from a Pd electrode had a remarkably similar appearance to the EEI observed in the present work, and Nielsen et al. suggest that an unknown surface transport mechanism causes Pd migration and the subsequent current fluctuations. Based on SEM investigations the present work does not find any evidence for dendrite formation having occurred. If a dendritic microstructure were present one would expect variations in the measured current caused by changes in the electrode area when repeating the measurements. However Figure 7 (region I) shows that the measured current does not change when repeating the measurement indicating that the EEI area was unchanged. It has been shown that $Ni(OH)_2$ can be formed at the TPB of a SOFC anode in the presence of a high

oxygen partial pressure and transported away from its formation site where it is reduced to recondense as Ni nanoparticles [20].Therefore an alternative explanation for the oscillating current pattern with Ni electrodes is given in the following and illustrated by Figure 15.

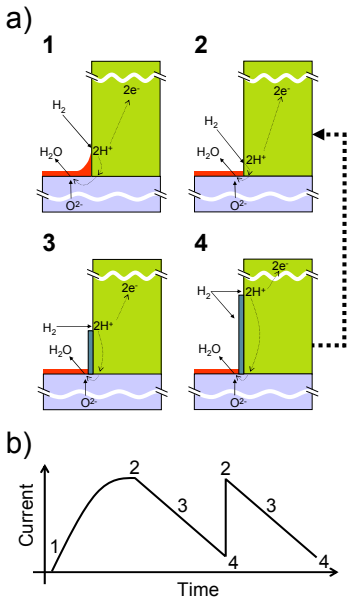

Figure 15: a) The suggested mechanism responsible for the occurrence of the oscillating current pattern. 1) → 2) Impurities at the TPB are mobilized by water formation at the TPB resulting in a gradual increase in measured current. 3) Strong anodic polarisation causes a high local pH_2O, which in turn causes the surface of the Ni electrode to passivate by a $Ni(OH)_2$ film. 4) The $Ni(OH)_2$ film coverage increases resulting in a continued decrease in the measured current. 4) → 2) H_2O formation slows and the H_2 atmosphere is able to reduce the $Ni(OH)_2$ film instantaneously resulting in a jump in measured current. b) Sketch of the current oscillation cycle.

After impurities accumulated at the TPB are removed by reaction with water to form volatile Si-OH species and a stable average current level is reached, it is believed that nickel is oxidised to form a passivating $Ni(OH)_2$ layer at the TPB. We have previously suggested a proton diffusion reaction mechanism through the nickel electrode [12]. As the $Ni(OH)_2$ coverage at the TPB increases the average proton diffusion path lengthens resulting in a slower reaction rate. The granulated surface microstructure inside the EEI cavities suggests that water formation occurred there. The granulated surface is believed to consist of impurity species mobilised by the formed water thereafter de-wetting the electrolyte surface. The ToF-SIMS analysis, however, did not have the necessary resolution to detect this. Regardless of the chemical composition the existence of the granulated surfaces within the EEI is additional argumentation for of a proton diffusion mechanism through the electrode.

As the $Ni(OH)_2$ film reaches a certain electrode coverage the local H_2O partial pressure decreases i.e. the gas diffusion of H_2O away from the TPB is faster than the H_2O formation on the electrolyte in the vicinity, at which point the H_2/H_2O atmosphere becomes able to reduce all of the $Ni(OH)_2$ film spontaneously. This results in an instant increase in the measured current.

The onsets of fluctuations in the potential sweeps show that a passivation layer is formed at a threshold electrode potential value. The threshold value increases with decreasing temperature. Increasing the applied overpotential has the effect of increasing speed of the mechanism cycle. At overpotentials below the

threshold no passivation layer is formed hence no current oscillations are observed. Reducing the water content in the atmosphere reduces the oscillation amplitude as a lower water partial pressure slows the rate of $Ni(OH)_2$ film build up.

The prospect of NiO formation should also be taken into account when considering explanations for the current oscillations. At electrode potentials above -680 (mV vs Pt/air) NiO formation at the two phase boundary between the electrode and electrolyte may occur. As the proton diffusion path through the electrode is lengthened by passivation layer coverage at the electrode/gas interface the rate of NiO growth might increase. Hence NiO and $Ni(OH)_2$ formation might be coupled where both species could contribute to the decrease in measured current.

Although the overpotentials at normal SOFC operating conditions are much lower than those applied in this work the observations from the model system may be correlated to SOFC operation. Results from the model system presented here could explain why a SOFC cermet anode under large current load undergoes microstructural changes by nickel diffusion [4]. If the mechanism described above occurred in a cermet it is expected to lead to an increase in the average nickel particle size. This would result in a reduced TPB length and possibly also a loss of percolation routes for electron transport. Studies of long term tested SOFC have shown degradations of SOFC anodes [4] and these observations are consistent with the nickel transport mechanism suggested here.

The influence of water content at the EEI on the current oscillations found in the model system could signify that a high water content is undesirable in a SOFC with respect to long term microstructural stability of the anode. High water content is found near the fuel outlet in a SOFC anode and therefore we believe that nickel particle agglomeration is most likely to occur here. In addition to this the low H_2 concentration found at the fuel outlet would promote the growth of a $Ni(OH)_2$ film especially at high current loads to a much larger degree than at the fuel inlet. A high water content may decrease the detrimental effects of impurities at the TPB.

5. CONCLUSION

Applying large anodic overpotentials to a point electrode model of a SOFC anode showed characteristic oscillation patterns in the measured current. The water content in the atmosphere was found to have a large effect on this phenomenon. The nature of the oscillating current pattern was coupled with observations of the electrode and electrolyte surface microstructures and surface chemical analysis to develop a hypothesis for a reaction mechanism. The suggested reaction mechanism implies that proton diffusion through the nickel electrode and the electrolyte is a rate determining step for the overall anode reaction. The suggested mechanism could be taken into consideration when choosing SOFC operation conditions in order to decrease anode degradation.

AKNOWLEDGEMENTS

This work was carried of as part of the project “Efficient Conversion of Renewable Energy using Solid Oxide Cells” contract number 2058-03-0014, which is financially supported by The Danish Research Councils and the Danish Ministry of Science Technology and Innovation.

REFERENCES

[1] A.J. McEvoy, Solid State Ionics, 135 (2000) 331.

[2] K. Vels Jensen, S. Primdahl, I. Chorkendorff, M. Mogensen, Solid State Ionics, 144 (2001) 197.

[3] J. Nielsen, T. Jacobsen, Solid State Ionics, 178 (2008) 1769.

[4] M.J. Heneka, E. Ivers-Tiffee, 9th International Symposium on Solid Oxide Fuel Cells, SOFC IX (2005) Quebec City, 534. Singhal, S.C.; Mizusaki, J. (eds.).

[5] Karl Thyden, Ph.D. thesis, Denmark, Risø National Laboratory for Sustainable Energy, Technical University of Denmark. (2008)

[6] B.A. Boukamp, Solid State Ionics 18-19 (1986) 136.

[7] M.S. Schmidt, K.V. Hansen, K. Norrman, M. Mogensen, Accepted for publication in Solid State Ionics (2008).

[8] T. Jacobsen, K. Vels Hansen, E. Skou, J. Electrochem. Soc. 152 (2005) A2203.

[9] K. Vels Hansen, K. Norrman, M. Mogensen, J. Electrochem Soc. 151 (2004) A1436.

[10] J. Nielsen, T. Jacobsen, Solid State Ionics 178 (2008) 1769.

[11] M.S. Schmidt, K.V. Hansen, K. Norrman, M. Mogensen, Solid State Ionics 179 (2008) 1436.

[12] J. Guindet, C. Roux, A. Hammou, Proceedings of the 2nd International Symposium on SOFCs, Athens, Greece, F. Grosz, P. Zegers, S.C. Singhal and O. Yamamoto, Eds.(1991) 553.

[13] E.J. Opila, J. Am. Ceram. Soc. 86 (2003) 1238.

[14] H.J. de Bruin, Nature 272 (1978) 712.

[15] S.P. Jiang, S.P.S. Badwal, J. Electrochem. Soc. 144 (1997) 3777.

[16] M. Mogensen, J. Høgh, K. V. Hansen, T. Jacobsen, ECS Transactions 7 (1) (2007) 1329, and references therein.

[17] J. Sehested, J.A.P. Gelten, I.N. Remediakis, H. Bengaard, J.K. Nørskov, J. Catal 223 (2004) 432.

[18] M. Brown, S. Primdahl, M. Mogensen, J. Electrochem. Soc 147 (2000) 475.

[19] R.J.Aaberg, R. Tunold, M. Mogensen, R.W. Berg, R. Ødegård, J. Electrochem. Soc. 145 (1998) 2244.

[20] K. Du, F. Ernst, M. Garrels, J. Payer, Int. J. Mat. Res. 99 (2008) 548.